

UNIVERSITY OF OKLAHOMA

GRADUATE COLLEGE

A TEMPORAL GIS APPROACH TO CHARACTERIZING GEOGRAPHIC

DYNAMICS

A DISSERTATION

SUBMITTED TO THE GRADUATE FACULTY

In partial fulfilment of the requirements for the

Degree of

DOCTOR OF PHILOSOPHY

By

JAMES BOTHWELL

Norman, Oklahoma

2011

A TEMPORAL GIS APPROACH TO CHARACTERIZING GEOGRAPHIC  
DYNAMICS

A DISSERTATION APPROVED FOR THE  
DEPARTMENT OF GEOGRAPHY

BY

---

Dr. May Yuan, Chair

---

Dr. David Karoly

---

Dr. Sally Gros

---

Dr. J. Scott Greene

---

Dr. Chris Weaver

© Copyright by JAMES BOTHWELL 2011  
All Rights Reserved

### *Acknowledgements*

Thank you to all who provided support and encouragement during my pursuit of the Doctor of Philosophy. Special thanks to my advisor, Dr. May Yuan, who has tirelessly guided me on how to approach this momentous task. Thanks to Dr. David Karoly for the guidance and encouragement that kept me going. Thanks to Dr. Sally Gros, Dr. Scott Greene and Dr. Chris Weaver for taking the time to be on my committee. Finally, a special thanks is given to my wife and three sons for accepting the turmoil of my midlife pursuit of the Doctor of Philosophy.

## ***Table of Contents***

Acknowledgements.....	iv
List of Tables .....	ix
List of Figures .....	x
Abstract.....	xiii
Chapter 1: Introduction.....	1
1.1 Introduction.....	1
1.2 Background.....	2
1.2.1 The Research Challenges in Temporal GIS.....	2
1.3 Research Goals and Dissertation Organization.....	4
1.3.1 Conceptual foundation .....	7
1.3.2 Kinematic Representation of regions.....	8
1.3.3 Quantitatively Comparing GCM output using the Kinematic Field Representation.....	9
1.4 Variability characteristics of the Kinematic Field Representation .....	10
1.5 Dissertation Organization .....	10
References.....	11
Chapter 2: Incorporating Concepts of Fluid Kinematics in Temporal GIS to Represent Continuous Geographic Fields in Space and Time.....	13
Abstract.....	13
2.1 Introduction.....	14
2.1.1 The conceptual basis to incorporate fluid kinematics into GIS representation and analysis of spatiotemporal phenomena.....	19
2.2 A Case Study to Compare Global Temperature Projections from Two General Circulation Models (GCM).....	24
2.2.1 Data and Methods .....	25
2.3 Results and Discussions.....	34
2.3.1 Velocity Fields and Vector Displacement Analysis of the CNRM CM3 Projected Temperature for Scenario A2 during the period of 2030-2090 .....	34
2.3.2 Velocity Fields and Vector Displacement Analysis of the NCAR CCSM Projected Temperature for Scenario A2 during the period of 2030-2090 .....	40
2.3.3 Comparison of the two datasets from CNRM CM3 and NCAR CCSM ....	46
2.4 Conclusion and Future Research .....	50
References.....	53
Chapter 3: A Kinematics-based GIS Methodology to Represent and Analyze Spatiotemporal Patterns of Precipitation Change .....	57

Abstract.....	57
3.1 Introduction.....	58
3.2 Conceptual Bases and Related Research .....	60
3.2.1 Information Representation .....	60
3.2.2 Elicit Spatiotemporal Patterns from Massive Data.....	64
3.3 Datasets and Methods .....	67
3.3.1 Kinematic analysis.....	74
3.3.2 Region transition tracking.....	80
3.4 Results and Discussion .....	85
3.5 Conclusion and Future Work.....	98
References.....	101
Chapter 4: Use Displacement Vectors to Discern Differences in Temperature Change in the 20th Century.....	105
Abstract.....	105
4.1 Introduction.....	105
4.2 Comparison of Model Data in Climate Change Research.....	106
4.2.1 Approaches to Analyze Temporal Gridded Datasets.....	108
4.2.2 Research Hypotheses and Goals .....	109
4.3 Data Sets used in the Study.....	110
4.4 Methods and Methodology .....	116
4.4.1 Displacement Vectors and Comparisons of Differences .....	118
4.5 Results and Discussions.....	120
4.5.1 The findings .....	122
4.5.1.1 Similarity maps.....	124
4.5.1.2 Difference maps.....	127
4.5.1.2.1 Antarctic Regions based on Differences in Displacement Vectors with CNRM data sets.....	130
4.5.1.2.2 NIÑO3.4 Region based on Differences in Displacement Vectors with CNRM datasets.....	131
4.5.1.2.3 Arabian Sea Region identified from Differences in Displacement Vectors with NCEP datasets.....	132
4.5.1.2.4 Middle East Region Identified by Differences in Displacement Vectors between ERA-40 and CNRM 20C3M datasets.....	133
4.5.1.2.5 Greenland and North Atlantic Region based on Differences of Displacement Vectors with NCAR 20C3M datasets.....	133

4.5.1.2.6	Equatorial Regions off of the northern coast of Brazil and eastern coast of Columbia Region.....	136
4.5.1.2.7	Australia and South America Regions .....	136
4.5.1.2.8	The Verkhoyansk Range in East Siberia.....	137
4.6	Summary, Intellectual Contribution and Future Study .....	137
	References.....	140
Chapter 5: The Similarity of the Variability Characteristics of Datasets Produced by Applying the Temporal Geographic Information System Framework to GCM output with that of Trends Embedded in GCM Output.....		
	Abstract.....	145
5.1	Introduction.....	146
5.2	Hypothesis.....	147
5.3	Model variable choice.....	148
5.4	Variability .....	149
5.4.1	SME versus MME.....	152
5.4.2	Scale of region, range, variability and spread.....	153
5.5	Data Sets used in the Study.....	154
5.6	Methods and Methodology .....	154
5.7	Results.....	157
5.8	Discussion.....	164
5.9	Conclusion .....	165
	References.....	167
Chapter 6: Conclusion .....		
6.1	Introduction.....	170
6.1.1	The Kinematic Representation Applied to Spatiotemporal Analysis .....	170
6.2	Summary of findings.....	171
6.2.1	Representing Continuous Temporal Geographic Fields using Fluid Kinematic Concepts .....	171
6.2.1.1	Displacement analysis of Project Temperature for Scenario A2 during the period of 2030-2090.....	172
6.2.2	Applying the Kinematics-based Methodology to Represent and Analyze Spatiotemporal Patterns of Precipitating Change .....	174
6.2.2.1	Eliciting Spatiotemporal Patterns .....	174
6.2.2.2	Results Interpretation.....	175
6.2.3	Discerning Differences in Temperature Change in the 20th Century datasets	176

6.2.4	Variability of Displacement Vectors Compared to Fixed Location Trends	179
6.3	Concluding Remarks.....	181
	References.....	186
Appendix A	.....	189
A.1	Introduction.....	189
A.2	Background.....	189
A.3	Procedure .....	192
A.4	Results and discussion .....	192
A.5	Conclusion .....	195
6.4	References.....	196



**List of Tables**

Table 2.1: Latitudinal table for CNRM displacements.....	30
Table 3.1: An example data table for a set of precipitation objects and the derived kinematic attributes.....	62
Table 3.2: Spatial Entity Evolution (Claramunt <i>et al.</i> 1997).....	67
Table 3.3: $d/dx$ kernel.....	74
Table 3.4: $d/dy$ kernel.....	74
Table 3.5: Mapping regions between time steps for CNRM.....	83
Table 3.6: Attribute table for areas of precipitation objects.....	84
Table 4.1: Datasets and their horizontal resolution.....	115
Table 4.2: The median and data range of differences in the longitudinal displacement in km/decade.....	123
Table 5.1: Grid points count for range expansion when 8th NCAR realization or CNRM realization was added.....	159
Table 5.2: Spread for the 8 NCAR and the CNRM hemisphere realization dataset in km/decade.....	162
Table 5.3: Spread for mean global, northern, and southern hemisphere displacements in km/decade.....	164
Table 5.4: Spread for land and ocean in both hemispheres.....	164

## List of Figures

Figure 1.1: Dissertation Organization and the logical connections among core chapters ..	7
Figure 2.1: An example of an isotherm moving inwards to indicate the change in a temperature field from $T_0$ to $T_1$ .....	22
Figure 2.2: Mean Temperature for the Years 2000-2030 from the CNRM CM3 GCM ..	25
Figure 2.3: Mean Temperature for the Year 2060-2090 from the CNRM CM3 GCM ....	26
Figure 2.4: Image of 16 °C isotherms from the CNRM GCM output in the 30-year mean from the period of 2000-2030. ....	27
Figure 2.5: Image of 16 °C isotherms from the CNRM GCM output in the 30-year mean from the period of 2060-2090 .....	28
Figure 2.6: Processes to create kinematics map of displacement vectors.....	32
Figure 2.7: Frequency distribution of longitudinal (y) displacements for CNRM. The displacement range of -216 to 228 is divided into 100 bars. ....	35
Figure 2.8: CNRM CM3 Longitudinal Isotherm Displacement 2030-2090.....	36
Figure 2.9: Histogram of latitudinal displacements for CNRM CM3 2030 – 2090. The displacement range of -68 to 71 is divided into 100 bars. ....	37
Figure 2.10: CNRM CM3 Isotherm Latitudinal Displacement 2030-2090.....	38
Figure 2.11: CNRM CM3 rapid displacement vectors, high convergence and high divergence areas for 2030-2090.....	39
Figure 2.12: NCAR CCSM3 longitudinal isotherm movement histogram. The displacement range of -156 to 182 is divided into 100 bars. ....	41
Figure 2.13: NCAR CCSM3 Longitudinal Displacement 2030-2090.....	42
Figure 2.14: NCAR CCSM3 Latitudinal Displacement Histogram. The displacement range of -51 to 54 is divided into 100 bars. ....	43
Figure 2.15: NCAR CCSM3 Latitudinal Displacement .....	44
Figure 2.16: NCAR CCSM rapid displacement and high convergence/divergence areas for 2030-2090.....	45
Figure 2.17: CNRM CM3 rapid displacement map for 2030-2090.....	46
Figure 2.18: NCAR CCSM rapid displacement map for 2030-2090.....	46
Figure 2.19: NCAR -16° Isotherm for the 2000-2030 mean. ....	47
Figure 2.20: CNRM -16° Isotherm for the 2000-2030 mean. ....	48
Figure 2.21: NCAR -16° Isotherm for the 2060-2090 mean .....	48
Figure 2.22: CNRM -16° Isotherm for the 2060-2090 mean .....	49
Figure 3.1: Internal kinematics is needed to determine rotation or deformation of an object.....	63
Figure 3.2: Calculating displacement vectors for the 213cm/year isohyet.....	69
Figure 3.3: Calculating displacement vectors for the 284cm/year isohyet.....	69
Figure 3.4: A manifold model to represent six basic types of spatiotemporal transitions.	72
Figure 3.5: CNRM precipitation regions greater than 213 cm/year for 2001.....	73
Figure 3.6: D1 stretching deformation along the x axis.....	77
Figure 3.7: D2 stretching deformation along the y = x axis.....	78
Figure 3.8: Deformation.....	80
Figure 3.9: Determining region associations between time instances .....	81
Figure 3.10: Gridded Region Identifiers .....	82
Figure 3.11: Merge from CNRM CM3 213 cm/year regions. ....	83

Figure 3.12: CNRM precipitation regions greater than 213 cm/year with 2001 outlined in green and 2048 in solid blue .....	87
Figure 3.13: NCAR precipitation regions greater than 213 cm/year with 2001 outlined in green and 2048 in solid blue .....	88
Figure 3.14: CNRM precipitation regions greater than 213 cm/year for 2001 with an east west expansion orientation.....	89
Figure 3.15: NCAR precipitation regions greater than 213 cm/year for 2001 expanding latitudinally (east-west).....	90
Figure 3.16: CNRM precipitation regions greater than 213 cm/year for 2001 with counter clockwise rotation .....	91
Figure 3.17: NCAR precipitation regions greater than 213 cm/year for 2001 with counter clockwise rotation .....	92
Figure 3.18: CNRM precipitation regions greater than 213 cm/year for 2001 with positive divergence .....	93
Figure 3.19: NCAR precipitation regions greater than 213 cm/year for 2001 with positive divergence .....	94
Figure 3.20: External divergence and convergence .....	95
Figure 3.21: Region from 2048 with split into three parts from one. Lower flat level is from 2001.....	96
Figure 3.22: CNRM precipitation regions greater than 213 cm/year that emerged or dissipated during the interval 2001-2048.....	97
Figure 3.23: NCAR precipitation regions greater than 213 cm/year that emerged or dissipated during the interval 2001-2048.....	98
Figure 4.1: Isotherm contour lines from the NCAR NCEP dataset for 1971 .....	116
Figure 4.2: Anomalous displacement region identification and display.....	117
Figure 4.3: Calculating displacement vectors .....	118
Figure 4.4: CNRM minus NCEP displacement map .....	121
Figure 4.5: Histogram of the NCAR minus CNRM longitudinal displacement. Other difference histograms are similar.....	123
Figure 4.6: Map of ERA40 Displacement minus NCEP Displacement where the difference is within a standard deviation. Locations with a greater difference were left blank for clarity.....	125
Figure 4.7: Map of EAR40 Displacements minus NCAR 20C3M Displacements where the difference is within a standard deviation. Locations with a greater difference were left blank for clarity.....	126
Figure 4.8: Map of NCAR 20C3M Displacement minus NCEP Displacement where the difference is within a standard deviation. Locations with a greater difference were left blank for clarity.....	126
Figure 4.9: CNRM 20C3M minus NCEP large difference regions.....	127
Figure 4.10: ERA-40 minus CNRM 20C3M large difference regions.....	128
Figure 4.11: ERA-40 minus NCAR 20C3M large difference regions.....	128
Figure 4.12: ERA-40 minus NCEP large difference regions.....	129
Figure 4.13: NCAR 20C3M minus CNRM 20C3M large difference regions.....	129
Figure 4.14: NCAR 20C3M minus NCEP large difference regions.....	130
Figure 4.15: NCAR 20C3M -20°C isotherm for 1971 .....	134
Figure 4.16: NCAR 20C3M -20°C isotherm for 1999 .....	135

Figure 4.17: CNRM 14 year mean -20°C isotherms for 1971 and 1999. ....	136
Figure 5.1: Grid points for NCAR #1 realization with calculated displacements .....	156
Figure 5.2: NCAR #1 realization North American region displacements .....	156
Figure 5.3: Displacement maps for 8 NCAR CCSM realizations and the CNRM realization.....	158
Figure 5.4: CNRM dataset values contained by SME range of data at the grid point resolution.....	160
Figure 5.5: Grid points where the MME dataset values have a larger standard deviation than the SME displacements dataset.....	161
Figure 5.6: Poleward displacement of isotherms from NCAR 20C3M SME.....	162
Figure 5.7: Poleward displacement of isotherms from NCAR/CNRM MME.....	163

## *Abstract*

Temporal GIS research has historically focused on change, motion, and events. This research introduces a framework to represent concepts of fluid kinematics with the emphasis on the concept of flows. General circulation models (GCMs) and other spatially explicit environmental models produce massive time series of geographic fields (e.g. temperature) that call for effective GIS approaches to elicit temporal information embedded in these model outputs. Common temporal GIS approaches with discrete constructs in space and time tend to overlook the spatiotemporal continuity that is fundamental to the understanding of geographic dynamic fields, such as temperature. Common methods of analyzing climatological characteristics center on trend analysis at fixed locations or monitoring meteorological phenomena, such as storm tracks, to evaluate circulation changes. The proposed temporal GIS framework, on the other hand, uses the velocity of virtual particles with fixed climatological values to capture changes in scalar continuous fields. The resulting spatiotemporal distributions of velocity suggest kinematic flows that can be used to recognize features indicative of geographic processes, such as divergence and convergence of isolines. Summative characterizations of these kinematic features highlight the embedded change and motion in these temporal sets of scalar fields and facilitate understanding and comparing model outputs.

## **Chapter 1: Introduction**

### ***1.1 Introduction***

This research focuses on the representation of kinematics and the analytical needs for grids of regularly spaced spatial data generated from environmental modelling. Manual approaches to spatiotemporal correlation analysis are easily overwhelmed by the flood of data from finite element models such as general circulation models (GCMs) and other spatially explicit environmental models. Effective spatiotemporal techniques are required to fully digest these massive amounts of data to overcome the challenges of meaningful analysis of GCM data (Sauchyn, Joss & Nyirfa, 2004). Statistical analysis of GCM data at fixed locations and fixed time intervals is currently supported with statistical and reanalysis tools at the NOAA Earth System Research Laboratory (Kalnay *et al.*, 1996). Analysis of the characteristics and dynamics of output from these sources is a daunting task due to the lack of descriptive terminology for fields of scalar data that change with time (Sauchyn *et al.* 2004). The terabytes of raster or gridded data represent snapshots or estimates of the environment, yet the key emphasis of temporal sequences of gridded data is to reveal changes over space and time. Such changes as well as the underlying processes implied by the changes cannot be fully revealed or interpreted without an effective data organization for analysis. The dissertation hypothesizes that an effective data organization for analysis is a kinematics-based framework with an explicit element representing change and motion. The research builds the conceptual framework, implements the representation in a Geographic Information System (GIS), develops algorithms to characterize kinematic patterns of change and movement of regions embedded in gridded data, and demonstrates the advantage of the kinematics-based

approach to help discover spatiotemporal patterns of events and processes. Case studies are built upon GCM outputs and compare the findings of spatiotemporal patterns of climate events from the proposed approach with discoveries in the climate literature.

## **1.2 Background**

### *1.2.1 The Research Challenges in Temporal GIS*

GIS is a spatially enabling technology with emphases on spatial components and relationships in data analysis and decision support. The spatiotemporal representation chosen to support the inclusion of time must support the storage, analysis and retrieval of information gathered from time dependent phenomena (Longley, Goodchild, Maguire, & Rhind, 2005). A temporal representation that explicitly combines time and space in a single attribute eliminates the need for a new dimension in a spatiotemporal GIS representation. A temporal representation compatible with the current spatial information representation both simplifies the extension and leverages the current GIS analytical capabilities.

The integration of time into a GIS has been a research topic for several decades. Geographical phenomena are inherently time dependent yet the current GIS representation has only rudimentary support for analysis of time varying geographical information. There are several conceptually object orientated spatiotemporal models that treat events as basic data objects such as the Event-based SpatioTemporal Data Model (Peuquet & Duan, 1995) and the Three-Domain Representation (Yuan, 1998). Some focus on structural similarities in events (Worboys, 2001), object transformations with respect to cadastral data (Sperry, Claramunt & Libourel, 2001) or the construction of a temporal topology (Marceau, Guindon, Bruel & Marios, 2001). These object oriented

constructs in discrete space and time are difficult to apply to continuous spatiotemporal fields.

For continuous spatiotemporal fields, a temporal GIS provides the ability to analyze raster based or gridded snapshots (Galton, 2004) and highlight regions meeting certain spatial and temporal criteria. This research proposes an integrated approach, based on the concepts of kinematics, that conjoins space and time into a single attribute, velocity. Specifically, the goal of the dissertation research applies the ideas of fluid kinematics to develop a new representation of spatiotemporal information for analysis. Kinematics describes the motion of the field without being concerned with the processes that affected the attribute in the past or about what process will affect the attribute in the future (Bluestein, 1992). The proposed representation of kinematics is based on the direction and amount of change in space and time e.g. velocity. Velocity explicitly pairs two snapshots by determining a field of displacements that transform a field at time  $T_0$  to the field at time  $T_1$ . Kinematics based representation, therefore, advances location based to velocity based GIS analysis.

This research applies image processing techniques to merge spatial and temporal characteristics of a spatiotemporal field into the single spatiotemporal attribute, velocity. Image processing algorithms determine motion by tracking intensity values of light across multiple snapshots (Horn & Schunck, 1981). Light intensity snapshots are similar to attribute snapshots. Images could be considered as an attribute field where the recorded attribute is the reflectance. Conceptualizing an attribute field as an image enables the application of image processing.



### ***1.3 Research Goals and Dissertation Organization***

This dissertation research hypothesizes that kinematics-based representation using displacement over time is an effective means to characterize and compare a time series of gridded data sets. Under this hypothesis, the research builds object constructs to measure kinematics with pre-defined isolines. The method is similar to the use of classifications of 500 mb heights in Huth (2000). Four objectives are identified to support this activity:

- 1) Develop a kinematics-based representation that uses displacement/velocity as the basis for spatiotemporal analysis of a time series of scalar fields (i.e. gridded data sets).

Case studies use temperature data from the Intergovernmental Panel on Climate Change (IPCC) 21<sup>st</sup> Century climate change analysis. The kinematic representation for GCM temperature data shows bimodal polar displacements in the  $y$  displacement histogram: one to the north and one to the south. Cluster analysis shows regional clusters of displacement vectors of large magnitude. Large displacement clusters are compared and contrasted to identify similarities and differences between the two GCMs. The divergence map is inspected to determine if there are regions of large positive or negative divergence. Regions exhibiting suggestive divergence are discussed.

- 2) Apply the kinematics-based representation to develop analytical methods that measure spatiotemporal characteristics of regions embedded in temporally sequenced gridded data.

Case studies use 21<sup>st</sup> Century precipitation from GCM model output. The research uses kinematic attributes of the objects to measure positive or negative vorticity, longitudinal and latitudinal deformation, and divergence. Patterns of objects with particular kinematic characteristics are examined. The deformation and divergence attributes for regions that merge or split are examined for potential drivers for the merges or splits.

- 3) Apply the kinematics-based representation to develop analytical methods to compare climate projections from two GCM models and two reanalysis datasets.

Case studies use data from the Twentieth-Century Climate in Coupled Models project and reanalysis datasets. The differences in displacement vectors from the six combinations of the four datasets are evident with distinctive expected values based on an F-test. The six combinations have different Interquartile Ranges and contain regions of differences that cluster. Clustered patterns consistent across comparison pairs with a particular dataset in common indicate locations that have fundamental modelling differences in the model. A literature review is conducted on any clustered difference regions.

- 4) Establish that the representation has different grid point value ranges by applying the F-test to the grid point range increases counts generated by adding an eighth model realization to a seven member Same Model Ensemble (SME) versus adding a different model realization. Compare and contrast the spread of the

kinematics-based representation to temperature data trends for a Same Model Ensemble (SME) and a Multiple Model Ensemble (MME).

Case study uses data from the Twentieth-Century Climate in Coupled Models project datasets. Eight permutations of eight realizations from the same model are formed with seven realizations in each one. The number of grid points with increased range when adding the eighth same model realization versus the different model realizations is calculated. An F-test is applied to the two sets of counts to determine if there is a significant difference in expected values. The variance characteristics of the kinematics-based representation and that of temperature data trends are compared for both SME and MME at the grid point resolution and the hemisphere means. Hemisphere means are further divided into land and sea hemisphere means. Temperature data trend variance characteristics for SME's and MME's are determined from a literature review.

The dissertation consists of six chapters to meet the four research goals: an introduction, four core stand-alone papers that target the four goals, and a conclusion chapter. The first objective is addressed in Chapter Two, the second in Chapter Three, the third in Chapter Four and the fourth in Chapter Five. The introduction chapter provides an overall context for the dissertation while the conclusion chapter summarizes the findings and suggests future research. Figure 1.1 highlights the structure of the four core chapters of this dissertation.

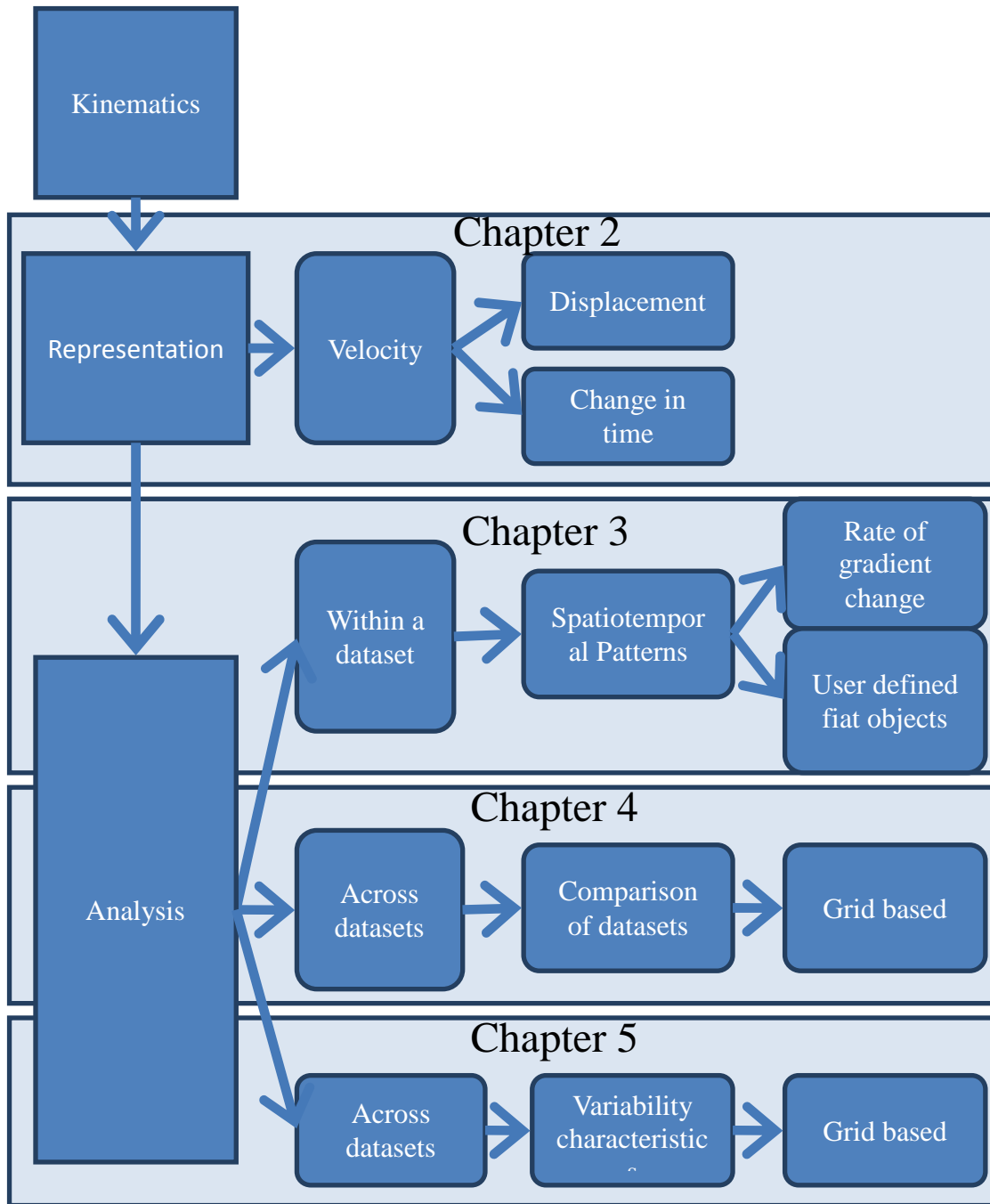


Figure 1.1: Dissertation Organization and the logical connections among core chapters

### 1.3.1 Conceptual foundation

Chapter Two lays the conceptual foundation of this research and applies the proposed representation to the output of two GCMs. A space-time integrative approach is used to

represent the spatiotemporal characteristics of gridded data. Data are used from the National Center for Atmospheric Research (NCAR) Community Climate System Model (CCSM3; Collins *et al.*, 2006) and the Center National Weather Research (CNRM) global ocean-atmosphere coupled system (CM3; Salas-Mélia *et al.*, in review). Climatic 30 year mean isotherms are used as a filter to remove short term variability. Mean isotherms are assigned displacement velocities by utilizing virtual objects defined by isotherm boundaries. An optical flow algorithm (Horn & Schenk, 1981) is applied to the boundaries at two different times. Grid points without directly calculated displacement vectors are assigned interpolated displacement values. The extracted velocity field is examined to determine if the results are in agreement with expected isotherm changes. The velocity field characteristics are compared to the expected motion of isotherms under the anthropomorphic climate change regime. Regions of unusual motion are examined for agreement with previous climate change research. Regions of unusual displacement are confirmed using others research to provide support for using displacement as a spatiotemporal characteristic of fields.

### *1.3.2 Kinematic Representation of regions*

Chapter Three demonstrates spatiotemporal database content indices that include kinematic values used to characterize a point, a region or the entire field. Spatiotemporal data mining attributes are different from spatially derived attributes as they must capture both time and space in their representation (Pfoser & Tryfona, 1998). A useful spatiotemporal database contains content based indices to support the locating of predefined patterns in time and space as well the discovery of new spatiotemporal

patterns (Stolorz *et al.*, 1995). Regions are defined using precipitation threshold values to formulate clusters of values greater than the thresholds (McIntosh & Yuan, 2005). The region's characteristics across multiple GCM output datasets are used in comparisons to demonstrate the utility of regional kinematic indices. Comparing and contrasting the difference in region shifts between datasets reveal differences in precipitation changes in space and time. Kinematic indices of divergence, rotation, and deformation support the search for precipitation regions that are influenced primarily by local conditions or by general circulation patterns of water vapor transport. The use of the internal spatial variations and external interactions among precipitation features supports the full quantification of changes in precipitation patterns.

### *1.3.3 Quantitatively Comparing GCM output using the Kinematic Field Representation*

Chapter Four demonstrates the direct comparison of the velocity field, representing the kinematics of a scalar spatiotemporal field, with fields from other times, locations or models. Differences and similarities in the velocity field highlight spatial regions where further research may determine potential underlying reason for the differences and similarities. Differences in displacement vector characterizations of GCMs and reanalysis data support the identification of regions with conflicting climate change patterns. Statistical temporal randomness is reduced using interval means while spatial filters are used to smooth small scale variation. The pattern differences in displacement vectors reveal meaningful data set differences.

#### ***1.4 Variability characteristics of the Kinematic Field Representation***

Chapter Five evaluates the effect on grid point range of combining multiple datasets from same GCM or from different GCMs. A set of eight Same Model Ensembles (SMEs), each of seven datasets, are formulated from eight NCAR datasets. An eighth NCAR dataset is evaluated for the number of grid points for which the eighth dataset is outside the range of the seven datasets in that SME. The single CNRM dataset impact on range is similarly analyzed. The F-test is then applied to the two sets of eight numbers to determine if the expected values are different.

The spread of the displacements of GCM ensembles at the grid point, hemisphere land, hemisphere sea, hemisphere and global scale are evaluated for similarity to trend characteristics. The variance of a Same Model Ensemble and a Mixed Model Ensemble are compared to the ensemble regional, hemispherical, global and grid point scale variance of temperature trends. Similar differences in scale variability for velocity vectors versus temperature trends provide evidence the spatiotemporal variability characteristics are similar to that of the temperature trends.

#### ***1.5 Dissertation Organization***

This introductory chapter outlines the research questions, objectives and plans for Chapters Two through Five as well as for the dissertation as a whole. Chapters Two through Five provide details of the conceptual context, methodology, results and interpretations for each chapter's research questions. The final chapter summarizes the findings from the research for Chapters Two through Five and proposes areas for future research.

## **References**

- Bluestein, H. (1992). *Synoptic-Dynamic Meteorology in Midlatitudes*, pg. 32. Oxford University Press, New York
- Collins, W. D., Bitz, C. M., Blackmon, M. I., Bonan, G. B., Bretherton, C. S., Carton, J. A., Chang, P., Doney, S. C., Hack, J. J., Henderson, T. B., Kiehl, J. T., Large, W. G., McKenna, D. S., Santer, B. D., & Smith, R. D. (2006). The Community Climate System Model: CCSM3, *Journal of Climate*, 19(11), 2122-2143.
- Galton, A. (2004). Fields and Objects in Space, Time and Space-time. *Spatial Cognition and Computation*, 4(1), 1-29.
- Horn, B. K. P., & Schunck, B. G. (1981). Determining Optical Flow. *Artificial Intelligence*, 17, 185-203.
- Huth, R. (2000) A circulation classification scheme applicable in GCM studies. *Theoretical Applied Climatology*, 67, 1-18
- Kalnay, E., Kanamitsu, M., Kistler, R., Collins, W., Deaven, D., Gandin, L., Iredell, M., Saha, S., White, G., Woollen, J., Zhu, Y., Leetmaa, A., Reynolds, R., Chelliah, M., Ebisuzaki, W., Higgins, W., Janowiak, J., Mo, K., Ropelewski, C., Wang, J., Jenne, R., & D. Joseph. (1996) The NCEP/NCAR 40-Year Reanalysis Project. *Bulletin of the American Meteorology Society*, 77, 437-471.
- Longley, P. A., Goodchild, M. F., Maguire, D. J., & Rhind, D. W. (2005). *Geographic Information Systems and Science*. John Wiley & Sons, Ltd. West Sussex, England.
- Marceau D. J., Guindon L., Bruel M., & Marios C. (2001). Building temporal topology in a GIS database to study the land-use changes in a rural-urban environment. *Professional Geographer*, 53, 546-58
- McIntosh, J., & M. Yuan. (2005). Assessing similarity of geographic processes and events. *Transactions in GIS*, 9(2), 223-245
- Peuquet, D. J., & Duan, N. (1995). An Event-based Spatiotemporal Data Model (ESTDM) for Temporal Analysis of Geographical Data. *International Journal of Geographical Information Systems*, 9(1), 7-24.
- Pfoser, D., & Tryfona, N.(1998) Requirements, definitions, and notations for spatiotemporal application environments. *Proceedings of the 6th ACM international symposium on Advances in geographic information systems*, (p.124-130) November 02-07, 1998, Washington, D.C., United States.



- Salas-Mélie D., Chauvin F., Déque´ M., Douville H., Gueremy J. F., Marquet P., Planton S., Royer J. F., & Tyteca, S. (in review) Description and validation of the CNRM-CM3 global climate model. *Climate dynamics*.
- Sauchyn,D.J., Joss, B. N., & Nyirfa, W.N. (2004). Sharing the geo-Referenced Results of Climate Change Impact Research. *Earth and Environmental Science*, 88(1-3), 389-397.
- Sperry, L., Claramunt, C., & Libourel, T. (2001). A Spatio-Temporal Model for the Manipulation of Lineage Metadata. *GeoInformatics 5(1)*, 51-70.
- Stolorz, P., Nakamura, H., Mesrobian, E., Muntz, R., Shek, E., Santos, J., Yi, J., Ng, K., Chien, S., Mechoso, C., & Farrara, J. (1995). Fast Spatio-Temporal Data Mining of Large Geophysical Datasets. *Proceedings of KDD-95: First International Conference on Knowledge Discovery and Data Mining*, 300–305. Menlo Park, Calif.: American Association for Artificial Intelligence.
- Yuan, M. (1998). Representing Geographic Information to enhance GIS support for complex spatiotemporal queries. *Transactions in GIS*, 3(2), 137-160.
- Worboys, M. F. 2001. Modelling changes and events in dynamic spatial systems with reference to socio-economic units. *Life and Motion of Socio-Economic Units. Life and Motion of Socio-Economic Units*, ed. Frank. Raper and Cheylan.
- Zhou, T., & Yu, R. 2006. Twentieth-Century Surface Air Temperature over China and the Globe Simulated by Coupled Climate Models. *Journal of Climate*, 19, 5843-5858.

## **Chapter 2: Incorporating Concepts of Fluid Kinematics in Temporal GIS to Represent Continuous Geographic Fields in Space and Time**

### *Abstract*

Much temporal GIS research has addressed change, motion, and events. This chapter introduces a temporal GIS framework to represent concepts of fluid kinematics with the emphasis on the concept of flows. General circulation models (GCMs) and other spatially explicit environmental models produce a massive time series of geographic fields (e.g. temperature) that call for effective GIS approaches to elicit temporal information embedded in these model outputs. Common temporal GIS approaches with discrete constructs in space and time tend to overlook the spatiotemporal continuity that is fundamental to many geographic fields. A representation is developed to capture the direction and speed of change in space and time, using velocity as the basic unit of representation. Spatiotemporal distributions of velocity suggest kinematic flows that can be further used to recognize features indicative of geographic processes, such as divergence and convergence, with attendant ideas about isoline sources and sinks. Summative characterizations of these kinematic features highlight the embedded change and motion in these temporal sets of scalar fields and facilitate understanding and comparing model outputs. The proposed kinematic representation is applied to characterize and compare climate projections based on IPCC A2 scenario from two GCMs: 1) The Center National Weather Research global ocean-atmosphere coupled system (CNRM-CM3) and, 2) the National Center for

Atmospheric Research Community Climate System Model (NCAR-CCSM3). Results from this research suggest distinct regions of rapid isotherm movement. Several of these regions appear consistent with findings from previous climate findings. The regions of convergence and divergence identified from the two GCM models are similar except for the following: a high latitude region in southern Greenland; a band of regions at  $-15^{\circ}$  latitude extending from the middle of South America to east of Madagascar; a region over the Arabian Sea; a region over Indonesia; and several regions in the tropical oceans. The case study shows that fluid kinematics approach offers an alternative means to time-stamped or event-based representations of geographic phenomena and provides a new foundation for spatiotemporal analysis of geographic fields.

**Keywords:** temporal GIS, geographic kinematics, change, motion, and climate change.

## ***2.1 Introduction***

This research applies the concepts of fluid kinematics to characterize change and motion of spatiotemporally continuous geographic phenomena by using velocity of flows. Earth Observation Systems, ground-based radar, weather networks, and environmental models generate peta-bytes of regular or irregular grid-based data daily to monitor changes to field-based geographic phenomena, such as vegetation, temperature, and land cover. Changes are commonly characterized through differences at locations over time. With the concepts of fluid kinematics, the grid-based scalar observations (such as temperature) can

be transformed to flow vectors (directions and speed of the movement of a cold front) to address how changes progress through space.

Historically, the development of temporal GIS has largely focused on the scalar component of geographic data. Yuan (1999) reviewed four main approaches to temporal GIS data modeling: snapshot model, space-time composite model, spatiotemporal object model, and event-based spatiotemporal data model. All the four approaches build upon the scalar data of locations, objects, or events. The rich amount of spatiotemporal information about change progression, however, is not readily available because the kinematics of geographic phenomenon cannot be easily recognized by discrete measurements in space and time. A space-time integrative approach is necessary to directly examine changes or movements occurring to geographic phenomena. To this end, a representation scheme is proposed based on the concept of fluid kinematics to characterize flows and movement directly. By characterizing flows and movement in two granules: (1) the phenomenon as a whole or (2) identifiable features representative of the phenomenon, the representation is able to capture both the movement of the phenomenon as an object and the change in its properties across space and time.

In contrast, most temporal GIS research efforts have been based on the object-based approach with a focus on various concepts of “events” and “change.” Langran and Chrisman (1988) proposed a GIS spatiotemporal representation, the “Space-Time Composite Model”, in which events are used as triggers to state changes in a cadastral GIS. When an event occurs and alters the spatial configuration of a cadastral system, the “Space-Time Composite Model” divides the existing spatial constructs into homogeneous spatial units and records the change through time-stamped attributes. As a result, space-

time composites are the smallest spatial units with common changes of attributes over one's life span. Other early spatiotemporal GIS database approaches stored data as snapshots of gridded data (Armstrong, 1988), yet temporal GIS analysis for gridded data was established much later (Christakos *et al.*, 2001).

In the 1990's the focus of spatiotemporal GIS research shifted to the object-based approach (Peuquet, 2001). Worboys (1994) proposed "spatiotemporal atoms" that consist of homogeneous attributes in space and time as the basic unit of representation and developed temporal lineages among spatiotemporal atoms to form spatiotemporal objects. Peuquet and Duan (1995) proposed the Event-based Spatiotemporal Data Model to assemble location-based changes that were triggered by individual events.

Furthermore, Yuan (2000) developed a representation based on hierarchies of zones, sequences, processes and events to capture the change and motion of multi-scalar spatiotemporal aggregates across space and time. Zones are footprints resulting from a process at a given instant in time, and sequences are temporal aggregates of footprints over time which represent changes in morphology and location. Processes are spatiotemporal aggregates of sequences which highlight branching and merging that occur during the process development. Finally, events are spatiotemporal aggregates of processes under common driving forces. With fields, objects, and a hierarchy of spatiotemporal aggregates, Yuan's approach applies the Hierarchy Theory (Ahl & Allen, 1996) to enable spatiotemporal analysis using a knowledge base of definitional objects to elicit empirical objects from GIS data (Yuan, 2000).

From mid the 1990's to 2000's, the emphasis on "event" or "movement" was fundamentally based on ideas of objects. The object-oriented temporal GIS research did

not lead to broad acceptance of any particular spatiotemporal data model amongst the GIS research community due largely to the mismatches between database management and application needs. More than a decade after the initial conceptualization by Langran and Chrisman (1988) challenges remain, both methodologically and technologically, when updating large cadastral databases (Sperry, Claramunt, & Libourel, 2001). The mismatches between database management and applications were echoed by Peuquet (2001) who argued that the chosen conceptualization, field or object, should depend upon the application of the database and that there is no universal spatiotemporal representation adaptable to all application needs. Managing data objects in these object-oriented GIS data models is a task in itself. Hornsby and Egenhofer (2000) developed the Identity State Change Description Language to facilitate the management of data objects and their temporal states of properties. While GIS modeling of moving objects made significant strides in recent years (Güting *et al.*, 2000; Hornsby & Egenhofer, 2002; Pfoser & Theodoridis, 2003), management of temporal objects with high dimensional complexity (such as changing shapes, spatially varying properties, and altering continuity) continues to be challenging.

Nevertheless, the new direction of moving objects in temporal GIS data modeling shows great promises with the use of movement and deformation to an object as the basis for spatiotemporal representation, such as spatiotemporal helixes by Stefanidis, Eickhorst, Agouris, & Partsinevelos (2003). The complexity of data management is only one issue with object-oriented spatiotemporal representation in GIS. Many real-world spatiotemporal phenomena go beyond the representation power of object-oriented or event-based data models (Galton, 2004).

While most research efforts on temporal GIS data modeling center on the object-view of the world, many geographic phenomena are spatially continuous with field properties that can be represented by functions of locations (Goodchild *et al.*, 2007). Field-based representation cannot be overlooked for the temporal GIS development (Christakos, Bogaert, & Serre, 2001; Mennis, Viger, & Tomlin, 2005). Researchers have proposed several hybrid approaches to combine field and the object conceptualizations. Yuan (2001) proposed the idea of “field-objects” which behave as objects but possess fields that define the internal structure and spatially varying properties of individual objects. Cova and Goodchild (2002) combined objects and fields with the idea of “object fields” where continuous fields were mapped to spatial objects, such as locations at an elevation field are mapped to respective watersheds.

Most hybrid approaches so far have emphasized storing and relating objects and fields in GIS databases and have not addressed the underlying physical mechanisms that connect fields and objects. Temporal GIS needs integrated space-time data frameworks to be compatible with physically based models, to provide the means for sound scientific inferences rather than mere statistical inferences, and moreover to support physical knowledge integration and query processing (Christakos *et al.*, 2001).

The fluid kinematics based GIS representation attempts to enable representation of manifestations of the focal phenomenon in the GIS database. Concepts from fluid kinematics are applied in the design of a hybrid field-object representation. Use cases are developed to test the proposed representation with global temperature change projected by two general circulation models (GCMs). This section highlights the development of temporal GIS representation and illustrates the need for incorporation of physical

mechanisms of geographic phenomena to improve temporal GIS support for scientific inferences and knowledge integration. Section 2 discusses the concepts and algorithms for the proposed kinematics approach. Discussions will elucidate how the concepts of kinematics are used to discern change and movement in geographic fields, and how the characterizations of change and movement can facilitate understanding the spatiotemporal properties of geographic phenomena. Section 3 presents use cases on analysis of climate change scenarios to illustrate the capabilities of the proposed representation and analytical approaches. In particular, emphasis are placed on the spatiotemporal information that can be elicited from the kinematics approach but may be cumbersome to discern or even overlooked by other existing methods. Finally, the key features of the proposed kinematics approach are summarized with regards to enriching temporal GIS for geographic fields.

### *2.1.1 The conceptual basis to incorporate fluid kinematics into GIS representation and analysis of spatiotemporal phenomena*

The proposed kinematics-based representation facilitates analysis of how geographic phenomena change over space and time. A precursor to analysis of change or movement is to identify an object or a feature that experiences the change or carries out the movement. Identification of objects or features in a geographic field depends on human cognition and problem domains of interest. Once identified, the object or feature becomes a surrogate of analysis for the geographic phenomenon of interest. For example, isobars in an air pressure field can be used as surrogates to characterize the distribution of the pressure field and how the pressure changes over space and time. The faster the isobars move outwards the greater the divergence of the respective air mass.



At the finest granule, individual grid cells are surrogate objects of a geographic field in a grid-based data set, where each grid cell serves as the minimum observable unit of property change to the geographic phenomenon of interest. Kinematics analysis examines not only change in cell values but the direction of change based on the gradient among surrounding cells. Different levels of spatial and temporal aggregation can create additional surrogate objects to meet application needs.

At the feature level, kinematic analysis operates on the points along each surrogate object boundary (such as along an urban-wildland interface or an isotherm). Movement of these points, which may or may not be uniform, reflect the overall motion of the surrogate object. Collective patterns of all surrogate objects represent spatiotemporal characteristics of the geographic field in consideration.

From grid cells to features, the proposed kinematics-based representation incorporates both field- and object-based approaches to analysis of change and movement by constructing surrogate objects in geographic fields and tracing such objects in a temporal sequence in which the geographic field has been observed. Kinematic behavior of these surrogate objects characterizes the change and movement resulting from the geographic phenomenon. For terrain analysis, ontological features, such as mountains or slopes, can serve as surrogate features. For land cover analysis, different land cover types may be used for surrogate objects. For climate, isolines of atmospheric properties, such as isotherms or isobars, are good candidates for surrogate objects.

For analysis, the proposed kinematic approach applies concepts from Lagrangian and Eulerian systems for fluid flow. In an Eulerian system, kinematics is measured by the velocity at fixed locations and time, which is analogous to cell-based velocity analysis of

property change in a geographic field. Complimentarily, a Lagrangian system addresses kinematics through tracing a fluid parcel over space and time, which is comparable to tracing feature-level surrogate objects over space and time in a geographic field. Eulerian kinematics captures local change, and Lagrangian kinematics reflects change or movement at the regional level or at a larger scale. The two distinct perspectives to kinematics analysis allow flexibility to facilitate understanding of fluid flows through spatial gradient (an Eulerian property) or based on parcel trajectory (a Lagrangian property).

The proposed kinematics-based analysis utilizes Eulerian and Lagrangian concepts in two stages. First, surrogate objects are identified, and fluid velocity is calculated at locations along each of the surrogate objects to determine kinematics at a given time. The Lagrangian approach considers a parcel as a whole moving at a uniform speed. Surrogate objects for geographic fields may not exhibit such uniformity due to spatial variability and deformation. Therefore, the second step involves identification of points along the surrogate objects and calculates velocity values at these points. At a conceptual level, the kinematic nature of a geographic phenomenon is then represented by surrogate objects that move across space in temporally sequenced scalar fields. For example, surrogate objects of a temperature field may be isotherms. The Lagrangian approach characterizes the “temperature flow” by how fast these isotherms move and to what direction they move. Alternatively, the Eulerian approach determines the amount of temperature change and the direction of change gradient at grid points in the scalar fields.

For proof of concepts, isotherms are chosen to be surrogate objects that characterize temperature fields projected by two general circulation models. In particular,

temperature thresholds are selected to identify isotherms of interest. Image processing techniques are applied to analyze the change and movement of these isotherms by tracing these surrogate objects over space and time (Figure 2.1).

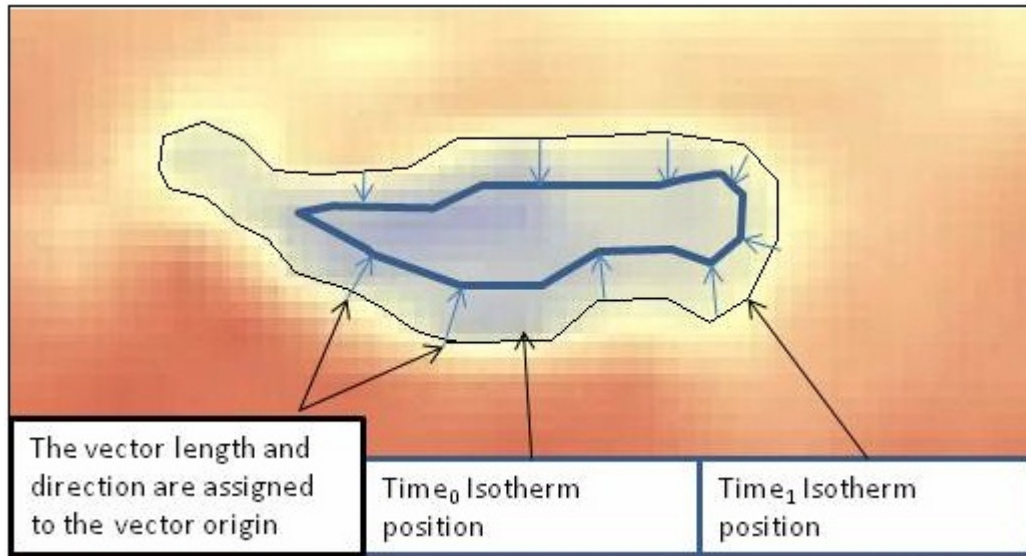


Figure 2.1: An example of an isotherm moving inwards to indicate the change in a temperature field from  $T_0$  to  $T_1$ .

The vector calculation algorithm is run for all grid points on an isotherm. The vectors are oriented with the local gradient, usually perpendicular to the  $T_0$  isotherm, if the  $T_1$  value is less than  $T_0$  value, or opposite to the gradient if the  $T_0$  value is less than the  $T_1$  value. The vector is assigned a length equal to the distance in line with the gradient to the nearest equivalent  $time_1$  isotherm. The algorithm does not calculate a vector to the  $T_1$  isotherm if the difference between the current grid point and the previous has a sign opposite of the gradient's sign somewhere along the vector.

Isotherms are effective means to capture the transitional and continuous nature of temperature fields. Certain isotherms carry strong physical implications, e.g.,  $0^\circ\text{C}$ , and shifts of these isotherms may have further implications on ecological systems. Analysis

of positions and movements of isotherms over time can provide summative assessment of climate trends. Comparison of temperature fields estimated from different climate change models can suggest the discrepancies in spatial and temporal trends of the model outputs as well as areas and periods of high discrepancies for further investigations.

Furthermore, this study tracks motion of surrogate objects, calculates velocity, and assigns velocity to the properties of the surrogate objects. Velocity is treated as a part of an isotherm's properties. Velocity is the first derivative of space by time and is required to calculate the second order, acceleration, and higher order derivatives. In addition velocity is intuitively understood by a higher percentage of the population and is easier to conceptually understand (Rosenblatt, Sayre, & Heckler, A., 2009; Trowbridge, & McDermott, 1981). Velocity is the simplest conjoining of space and time and is directly calculated with optical flow. This study applies algorithms used to analyze optical flows in image processing (Horn & Schunck, 1981) and stores the flow field with velocity and displacement in GIS grid data. Kinematics maps are used to analyze spatiotemporal fields in the following three ways: identifying statistical outliers in the flow field that highlight unique areas, examining autocorrelation in displacement vectors that identify cohesive fluid objects and comparing flow fields from different data sources. Moreover, a 2D continuous field, such as temperature, can be perceived with flows of convergence and divergence. Regions of convergence and divergence may suggest areas of interesting processes driving the dynamics of the scalar field. Diffusive flow generates isoline fiat objects that maintain an outflow boundary. Such outflow boundaries across time slices are tracked to elicit the patterns of diffusive flows.

## **2.2 A Case Study to Compare Global Temperature Projections from Two General Circulation Models (GCM)**

Previously GCM projections have been compared using spatial metrics and patterns. Hulme *et al.* (1993) used precipitation and mean temperature along with gale frequency to compare the output of multiple GCMs. Felzer and Heard (1999) looked at the weather pattern storm tracks that affect precipitation in the southwestern United States to assess output of different GCMs. Pepin (1995) examined the spatial increase in the annual temperature accumulation, days multiplied by Celsius temperature, of 1000 degree days or more in the Northern England area to compare and contrast the UKHI (United Kingdom Meteorological Office High Resolution GCM Equilibrium Experiment) and GISS (Goddard Institute for Space Studies) GCMs. Sengupta and Boyle (1993) used a limited number of independent time sequences of equatorial Pacific spatial patterns to differentiate the performance of two GCMs. Huth (2000) used classification of 500mb heights to determine patterns used for T-mode PCA analysis of the GCM output. These studies all used temporal sequences of observed attribute patterns to analyze the spatiotemporal projections of GCMs. The largest spatial extent in these studies is a region extending 15°S-15°N by 120°E-255°E. These studies all determined that there is a good match between different GCM's output.

Departing from these mostly trend based approaches, this research compares GCM outputs using GIS representation and analysis based on fluid kinematics. This research uses the full global extent with a temporal dimension of limited resolution, i.e. the changes between the climatic averages of two 30 year periods with a 30 year gap in between. The approach in this research adds a pattern of change analysis that does not require the use of meteorological phenomena such as storm tracks or gale frequency.

### 2.2.1 Data and Methods

Two GCMs are selected, based on availability, from the group of GCMs used by the IPCC for climate change analysis: National Center for Atmospheric Research Community Climate System Model (NCAR CCSM3) (Collins *et al.*, 2005) at  $1.4^{\circ} \times 1.4^{\circ}$  resolution and the Center National Weather Research Global Coupled System (CNRM CM3) (Salas-Mélia *et al.*, in review) with  $2.8^{\circ} \times 2.8^{\circ}$  resolution. The kinematics representation is shown to be insensitive to differences in grid sizes (See appendix A) because the emphasis is on the general pattern of flows rather than absolute properties at location.

The case study extracts two climatological means from 95 years (2000-2095) of monthly meteorological data using 30 year moving averages ending in 2030 and 2090. The distribution of CNRM CM3 30-year mean temperatures in 2030 is shown below in Figure 2.2.

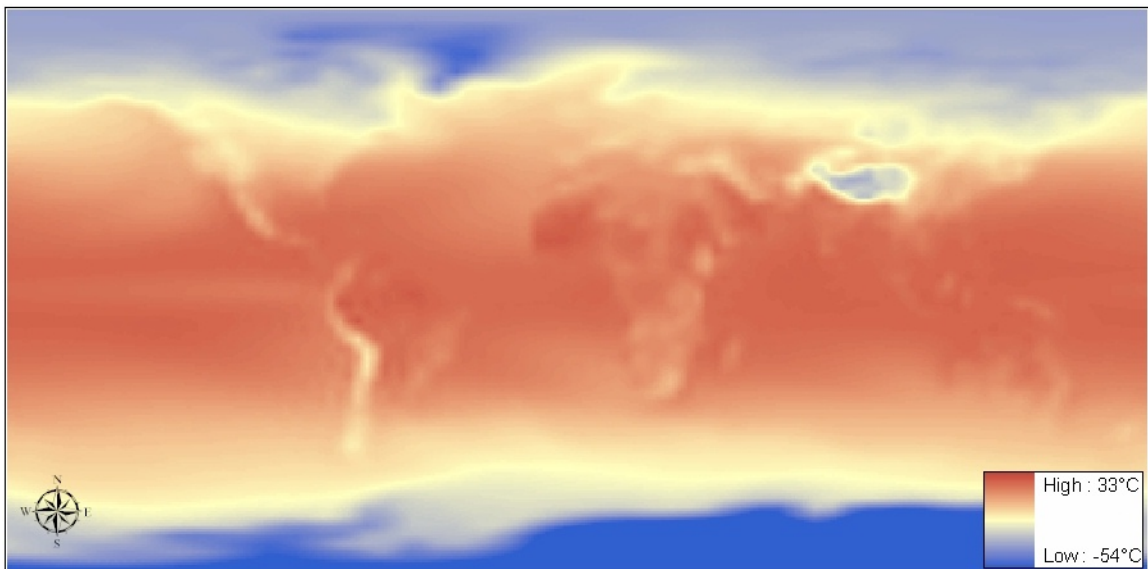


Figure 2.2: Mean Temperature for the Years 2000-2030 from the CNRM CM3 GCM

Projected monthly temperature data for the period of 2030– 2090 from the CNRM CM3 and the NCAR CCSM3 for IPCC scenario A2 are obtained from the World Climate Research Program’s Coupled Model Inter-comparison Project Multi-Model Dataset Archive. The A2 scenario is chosen because it follows more closely the actual rate of change during the years available than the other scenarios. The yearly mean of GCM surface temperature data is calculated for the years 2000-2030 and 2060-2090.

The grid dimension of the CNRM CM3 model is 128 by 64 units of approximately 2.8° latitude and longitude, and for the NCAR CCSM GCM, 256 by 128 units of approximately 1.4°. The projected temperature data is used to create 30-year mean monthly temperature data for 2000- 2030 and 2060- 2090. To facilitate comparisons, the temperature range for all displays is set to the range of -54 °C to 33 °C. Maps based on projected temperatures show dependence of temperature on latitude and elevation (Figures 2.2 and 2.3 for CNRM CM3). The Himalayan Mountain range is particularly noticeable in the Asian continent.

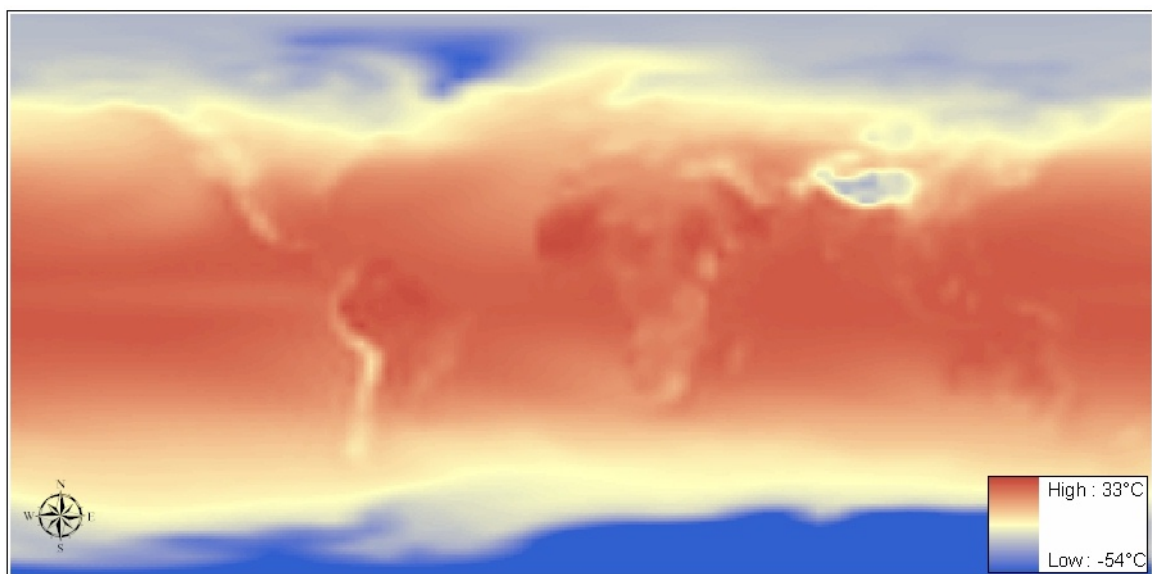


Figure 2.3: Mean Temperature for the Year 2060-2090 from the CNRM CM3 GCM

Visualization alone is not powerful enough to identify differences between figures Figure 2.2 and Figure 2.3 to determine spatial shifts of temperature between the two 30-year periods. Isotherms for the two periods are generated at the chosen temperature thresholds (-20, -16, -12, -8, -4, 0, 2, 4, 6, 8, 10, 12, 14, 16, 18, 20, 22, and 26 °C). These thresholds are based on Koppen Climate Classification (Lamb, 1972) boundary temperatures with subdivisions to insure a dense spatial sample of the temperature field. Binary boundary images were created for each isotherm (Figures 2.4 and 2.5).

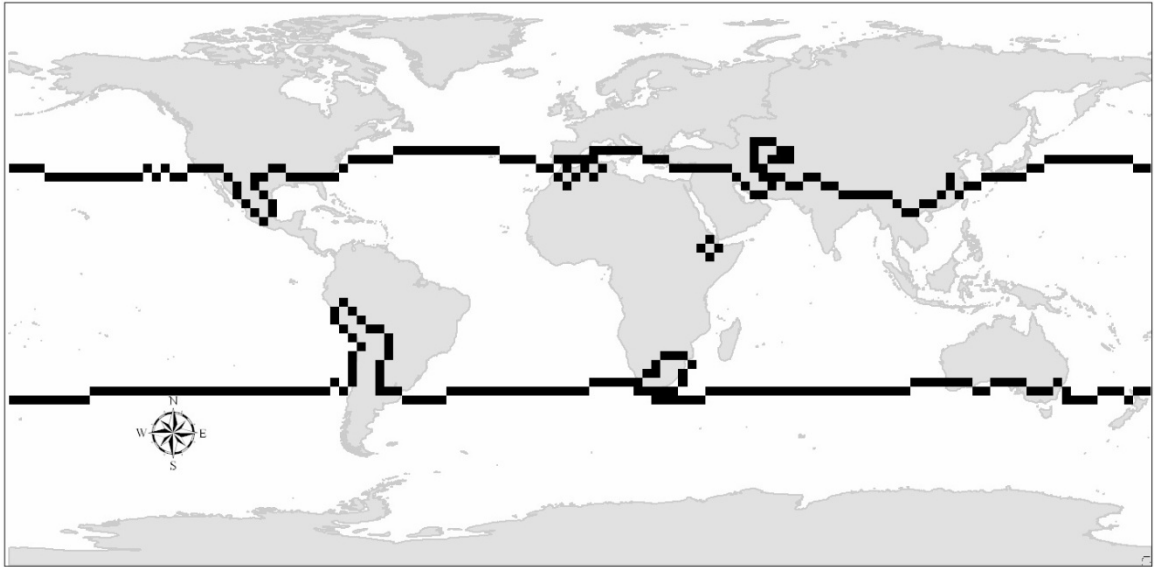


Figure 2.4: Image of 16 °C isotherms from the CNRM GCM output in the 30-year mean from the period of 2000-2030.



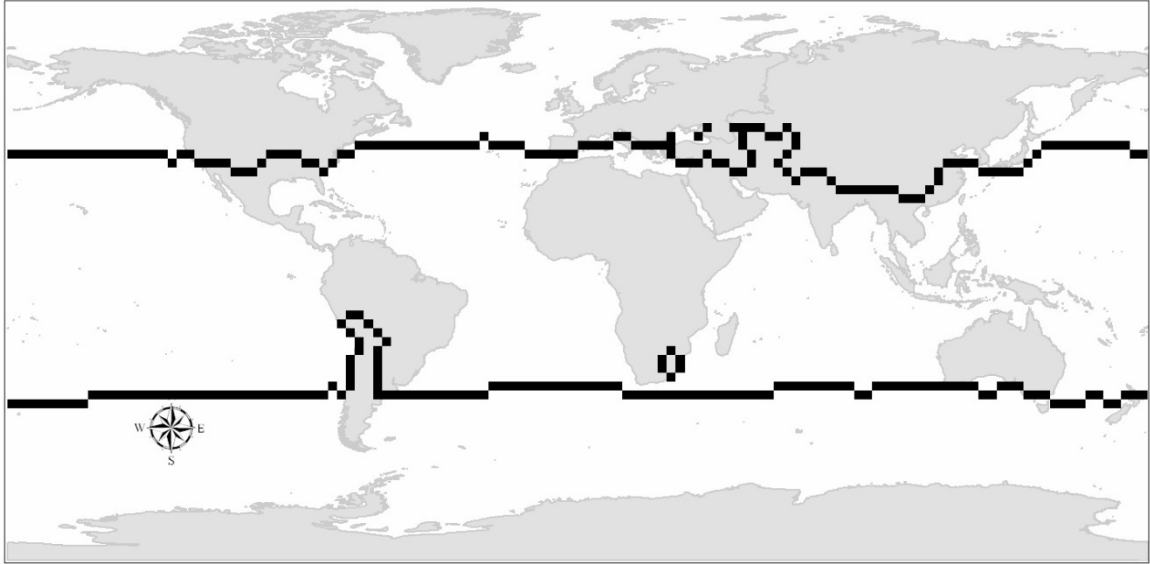


Figure 2.5: Image of 16 °C isotherms from the CNRM GCM output in the 30-year mean from the period of 2060-2090

While the isotherm of 16 °C shows differences in locations and shapes between the two 30-year periods, the differences for other isotherms were less obvious. Velocity maps are generated to show the spatial distribution of change vectors (i.e. displacement and direction) with x displacements and y displacements to portray the magnitude and direction of shifts in isotherms. Kinematics states that the change rate of flow at a fixed point ( $\frac{\partial F}{\partial t}$ ) is equal to the total rate of change of fluid particle ( $\frac{dF}{dt}$ ) minus the flow velocity at a location ( $V$ ) multiplied by the field's gradient (material derivative or advection term).

$$\frac{\partial F}{\partial t} = \frac{dF}{dt} - V \cdot \nabla F \quad \text{Eq. 2.1 (Bluestein 1992)}$$

This research makes the assumption that the attribute values are transported by constant value particles and thus there is no change in the rate of flow; i.e.  $(\frac{dF}{dt})$  is equal to zero.

$$\frac{dF}{dt} = 0 \quad \text{Eq. 2.2 (Bluestein 1992)}$$

All change at a given location,  $(\frac{\partial F}{\partial t})$ , is the result of the advection,  $(-V \cdot \nabla F)$ , of constant value particles.

$$\frac{\partial F}{\partial t} = -V \cdot \nabla F \quad \text{Eq. 2.3 (Bluestein 1992)}$$

Determination of  $V$  requires locating the most likely location from which the new value of  $F$  is advected. The velocity field ( $V$ ) is determined through the use of surrogate objects with boundaries defined by a range of threshold values. From the temperature grids, the borders of multiple surrogate objects are defined using isotherms of annual mean temperature. The assumption of particles with unchanging attribute values leads to Eq. 2.3 which is equivalent to the Optical Flow Constraint equation (Horn & Schunck, 1981) where  $I$  represents the image intensity.

$$(\frac{\partial I}{\partial t} + V \cdot \nabla I = 0) \quad \text{Eq. 2.4 (Bluestein 1992)}$$

Using attribute value instead of intensity enables the determination of the velocity of the isotherm aligned with the local gradient ( $\nabla F$ ) using the optical flow approach (Horn and Schunck 1981) with modifications for the use of the isotherm location at the next time instance. The magnitude of the displacement is determined by following the local gradient to a point on the isotherm in the next time slice.

The velocity of isotherm movement (following the local gradient) is calculated and mapped to form a global distribution of the velocity field. The local gradient is

determined using a local estimate based on a configurable window size. Four windows of size 3×3 are defined, one on each side of the point. The average value of the attribute for each window is determined and then the horizontal and vertical difference calculated using the window's means (Konrad, 2005). The velocity is represented as two scalar measures,  $u = (x \text{ displacement})/\Delta t$  and  $v = (y \text{ displacement})/\Delta t$ .  $x \text{ displacement}$  and  $y \text{ displacement}$  are the isotherm displacement in the latitudinal and longitudinal direction while  $\Delta t$  is the interval between time instances. The displacement vectors are represented as two point data tables, one for the longitudinal component and the other for the latitudinal component. A latitudinal table is show in table 2.1.

latitude	Longitude	value
76.71	-132.19	8.00
73.92	177.19	0.99
73.92	174.38	1.22
73.92	171.56	1.00

Table 2.1: Latitudinal table for CNRM displacements

Each point is represented by latitude, longitude, the latitudinal velocity and longitudinal velocity. The displacement point tables contain values for points on the isotherms for the chosen thresholds. The isotherms used for this study (-20, -16, -12, -8, -4, 0, 2, 4, 6, 8, 10, 12, 14, 16, 18, 20, 22, and 26 °C) are a subdivision of the mean yearly temperature values used in the Koppen Climate Classification (Lamb, 1972), Additional isotherms can be used to assign displacements to more points in the area of interest. A denser array of grid points with assigned displacements enables the identification of finer details in flow as can be seen in appendix A. The large regional features remain consistent with different sampling percentages. GIS provides a means for spatial interpolation of spatial pattern realizations (Burrough, 2001). Interpolation determines the values for the approximately

three quarters of the total points without calculated values. The values are interpolated using the Environmental Systems and Research Institute (ESRI) Natural Neighbor Algorithm. The Natural Neighbor Algorithm uses a set of points within a given distance of the new point and applies a weighting based on the area overlap of a Thiessen polygon associated with the new points and Thiessen polygons associated with the current points (Gold 1989). Natural Neighbor interpolation does not produce minima or maxima that are not present in the input samples (Gold 1989).

The kinematic map is created by using point sets containing both the displacement and direction attributes generated from the grids of displacement components. The grids of longitudinal and latitudinal components are processed to create values of magnitude, direction and convergence. The direction and magnitude of resultant vectors are calculated using the distance formula and arctangent functions. The direction and magnitude attributes are then used to create the kinematic map consisting of displacement arrows of size proportional of the magnitude at the location. (Figure 2.6).

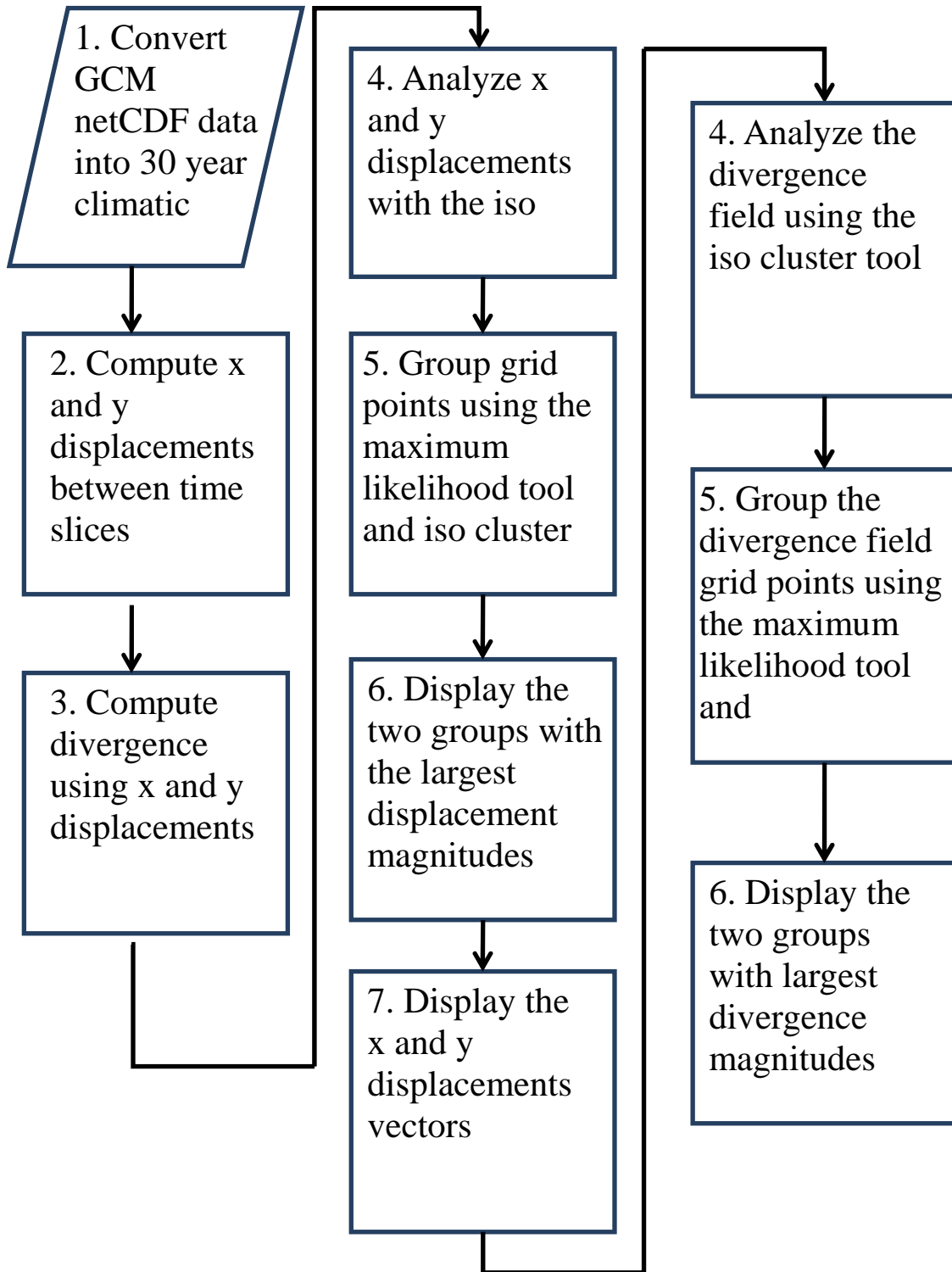


Figure 2.6: Processes to create kinematics map of displacement vectors

The final step in kinematic mapping is to identify regions of high convergence and divergence. Divergence is calculated based on longitudinal velocity ( $v$ ) and

latitudinal velocity ( $u$ ) using the centered difference formula. For location  $(i,j)$

divergence is:

$$Divergence(i,j) = \left( \frac{u(i+1,j) - u(i-1,j)}{2\Delta x} \right) + \left( \frac{v(i,j+1) - v(i,j-1)}{2\Delta y} \right) \quad \text{Eq. 2.5 (Bluestein 1992)}$$

$\Delta x$  is the grid spacing in the latitudinal direction, and  $\Delta y$  is the grid spacing in the longitudinal direction. Convergence occurs when the divergence value is less than zero. The resulting field has no discernible spatial structure due to spatial variability of the divergence values. Instead, this case study took another approach that used an areal average. The areal average is calculated using the average of the area's change in flow directly by using an area integral over a region ( $R$ ) bounded by a curve ( $C$ ):

$$\iint_R \nabla_h \cdot V \, dA \quad \text{Eq. 2.6 (Bluestein 1992)}$$

$\nabla_h$  is the horizontal divergence and  $V$  is the displacement vector with components  $u$  and  $v$ . The use of a closed contour integral can be substituted for the area integral by application of Green's theorem:

$$\iint_R \nabla_h \cdot V \, dA = \oint_C V \cdot \hat{n} \, ds \quad \text{Eq. 2.77 (Bluestein 1992)}$$

$\hat{n}$  is the vector normal to the curve  $C$  and  $ds$  traverses the curve in a counter clockwise direction. While the contour integral approach appeared challenging for regions with irregular boundaries, the case study uses moving square windows of various sizes to generate mean divergence values. A moving window is used to smooth spatial variability and produce discernible regions of divergence. Through trial and error, a  $7 \times 7$  moving window is found to produce aggregated regions convergence and divergence.

When cool regions are embedded in a warmer field the regions isotherms converge towards the interior as the overall field warms up. Expanding warm regions embedded in a cooler field produce divergence as new isotherms emerged in the warm region and move outwards into the surrounding cooler field. Convergence and divergence are also identified in regions of large displacements embedded in a field of more moderate displacements. The leading edge of the larger displacement compresses isotherms producing convergence while the trailing edge produces larger spacing between isotherms leading to divergence.

## **2.3 Results and Discussions**

### *2.3.1 Velocity Fields and Vector Displacement Analysis of the CNRM CM3 Projected Temperature for Scenario A2 during the period of 2030-2090*

Distributions of displacements in latitudinal ( $x$ ) and longitudinal ( $y$ ) directions provide insights into the trends in temperature change. The CNRM displacements show a bimodal distribution of longitudinal displacements for the 30-year means of the years 2000-2030 and 2060-2090 (Figure 2.7).

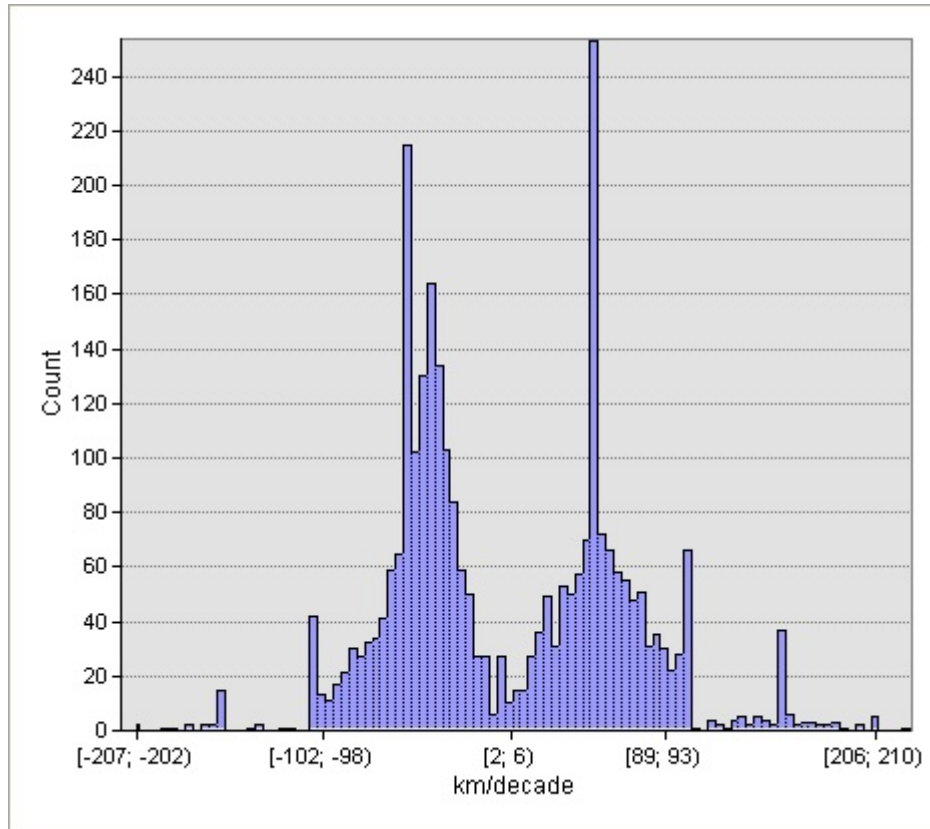


Figure 2.7: Frequency distribution of longitudinal (y) displacements for CNRM. The displacement range of -216 to 228 is divided into 100 bars.

The most frequent longitudinal displacements in the southern hemisphere occur at a rate of approximately 40 km/decade (third tallest bar in Figure 2.7) and 60 km/decade (second tallest bar in Figure 2.7) over the 60-year period. In the northern hemisphere, however, the most frequent longitudinal displacements occur around 50 km/decade (tallest bar in Figure 2.7) over the 60 years. The greater displacement towards the polar region correlates to a faster rate of isotherm shift.

Figure 2.8 shows the spatial distributions of longitudinal displacements from 2030 to 2090.



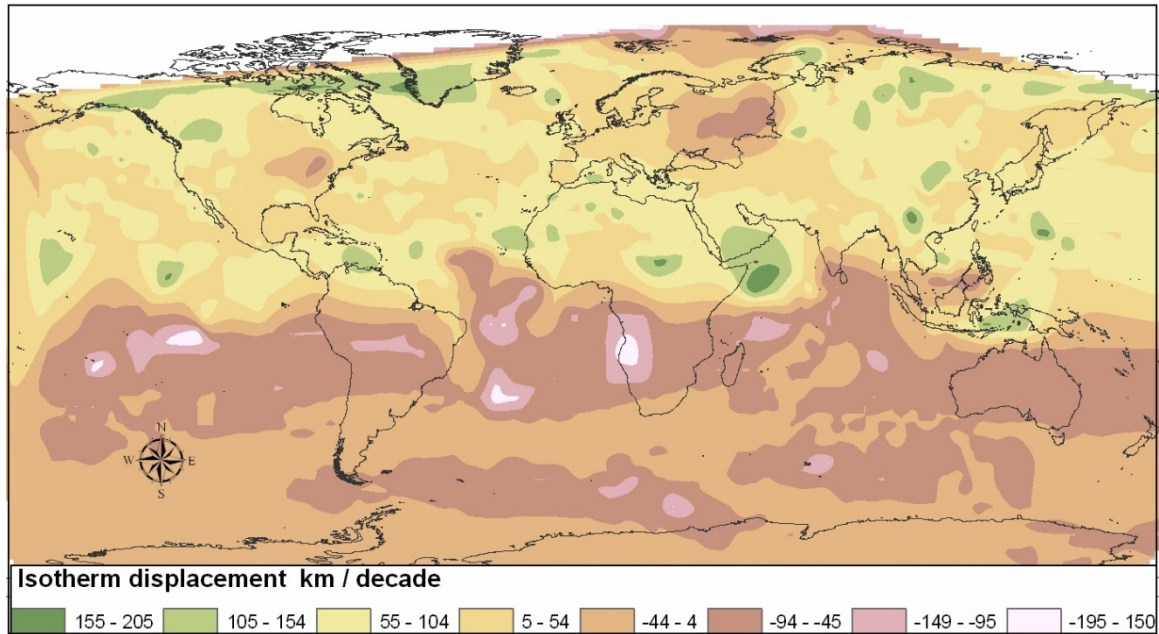


Figure 2.8: CNRM CM3 Longitudinal Isotherm Displacement 2030-2090

Figure 2.8 shows a clear trend of isotherms moving towards the polar regions. Large movements towards the north (“green spots”) occur around the equatorial region. In the northern hemisphere, most isotherms move at a similar rate towards the north (in yellow and beige colors), suggesting a wide spread moderate warming trend. However, areas in the mid-section of the U.S., Russia, Euroasia, and Siberia show isotherms moving toward the south, suggesting the presence of local temperature minima. In comparison, spatial patterns of isotherm displacements are much more fragmented in the southern hemisphere than in the north. While the general trend is warming in the southern hemisphere, regional patches of higher warming areas are almost continuous in the subtropical and temperate zones, and in a strip of area near the polar region. The lack of higher warming areas in the higher southern latitudes is a possible result of Southern Ocean heat uptake.

The CNRM CM3 latitudinal displacement histogram has a leptokurtic distribution with a dominant peak at approximately -2 km/60 years (Figure 2.9).

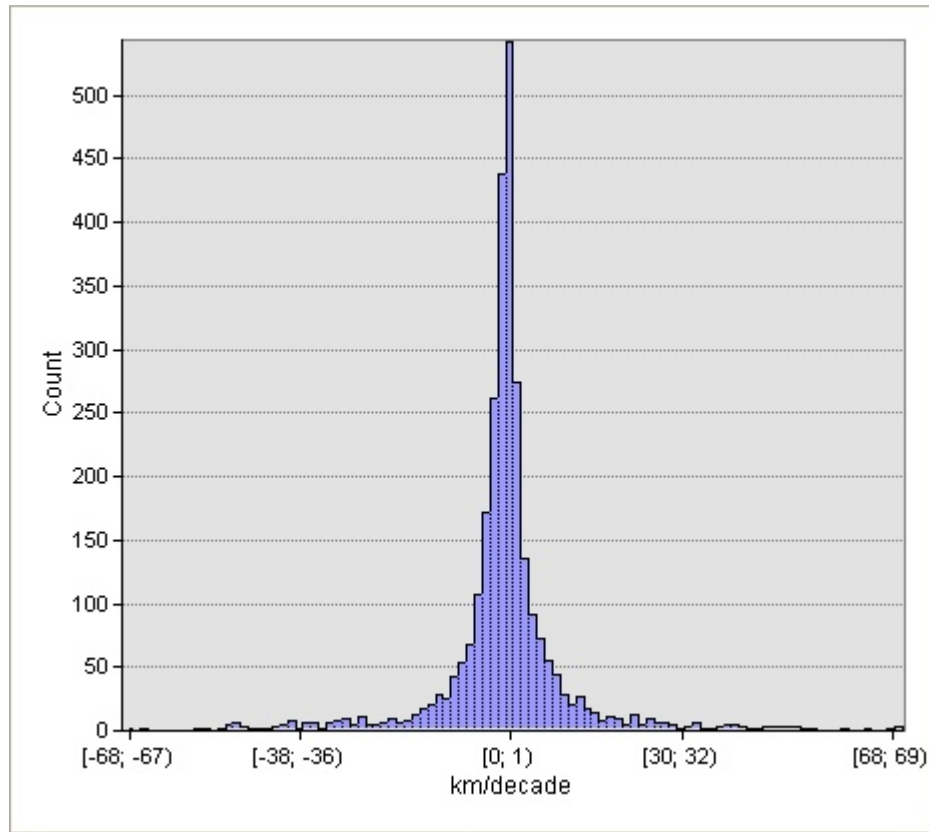


Figure 2.9: Histogram of latitudinal displacements for CNRM CM3 2030 – 2090. The displacement range of -68 to 71 is divided into 100 bars.

The latitudinal displacement distribution is centered around the zero displacement and is the possible result of the majority of isotherms having a dominantly east west orientation. The distribution of displacement in the minus or plus x direction is not spatially restricted to a particular hemisphere but rather is distributed across the globe (Figure 2.10).

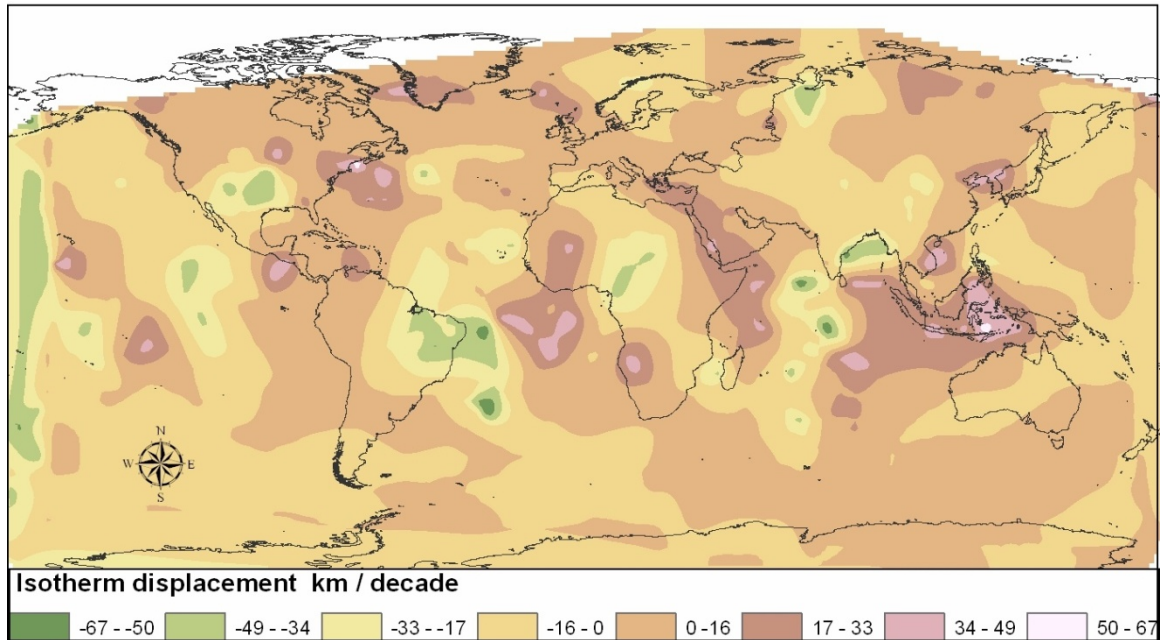


Figure 2.10: CNRM CM3 Isotherm Latitudinal Displacement 2030-2090

The displacement pattern in the latitudinal direction suggests that most of the world experiences small shifts (in beige and light brown colors). Regional patches show isotherms moving towards the east, and by large these patches occur in or around the zones of easterlies. Comparably smaller and more isolated areas show isotherms shifting towards the west (in green and light yellow colors).

The iso cluster analysis identifies clusters of large displacements and the large convergence/divergence. The iso cluster analysis makes an initial assignment using histogram peaks and then modifies the assignments using variance and covariance based on an assumed normal distribution (de Smith *et al.*, 2007). The analysis modifies the cluster assignment after each iteration using two criteria: (1) two cluster centers which are closer than a set tolerance level are combined and (2) clusters without a minimum number of members are dissolved with members assigned to surviving clusters. Clusters are broken up when they are overly large, have excessive standard deviation or when the

average distance from cluster center is excessive. The CNRM GCM kinematic map (Figure 2.11) has multiple locations of large convergence/divergence and of large displacement vectors.

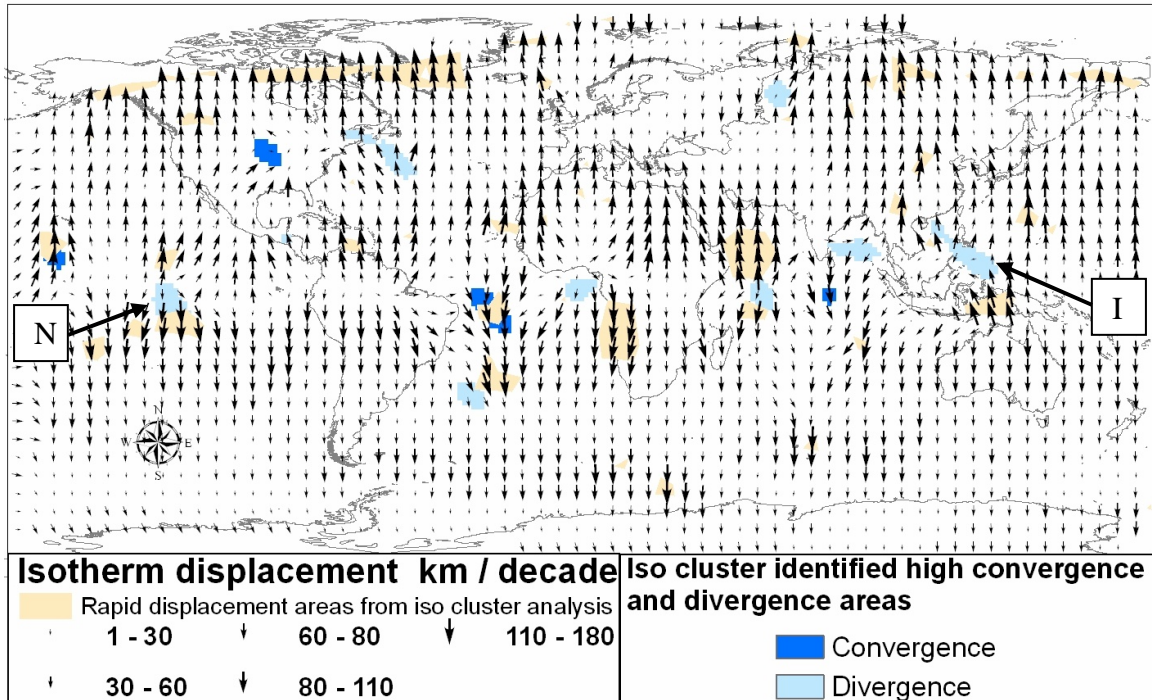


Figure 2.11: CNRM CM3 rapid displacement vectors, high convergence and high divergence areas for 2030-2090.

Divergence regions are scattered, but two interesting regions appear over Indonesia (I in Figure 2.11) and at the center of the Niño 3 region (N in Figure 2.11). These locations for divergence hint that ENSO processes may be changing due to anthropomorphic climate change (IPCC 2001). A band around  $67^\circ$  across the North American Continent with clusters in southern Greenland, a region in the western Indian Ocean and the southwest coast of Africa shows suggestively large isotherm movement. The band at  $67^\circ$  is likely related to rapid climate change at polar areas (Holland and Bitz 2003). The high change rate over the Arabian Sea is possibly due to an increase in

monsoon strength leading to cooler than normal SSTs in the Arabian Sea and the influence of a strengthening Indian Ocean Dipole which affects zonal SST gradients along the Equator (Saji *et al.*, 2006). The divergence region over the Arabian Sea indicates a possible warming region with rapid isotherm outflows in both the northern and southern directions. The rapid change in the south western coastal region of Africa may be the result of an increase in the western flow from the Sahara during summer brought about by global warming as suggested by Semazzi and Song (2001).

### *2.3.2 Velocity Fields and Vector Displacement Analysis of the NCAR CCSM Projected Temperature for Scenario A2 during the period of 2030-2090*

The histogram of NCAR CCSM longitudinal displacement for the 30-year mean shift for the years 2030-2090 shows a bimodal distribution similar to the CNRM-CM3 model output but with different modal values (Figure 2.12).

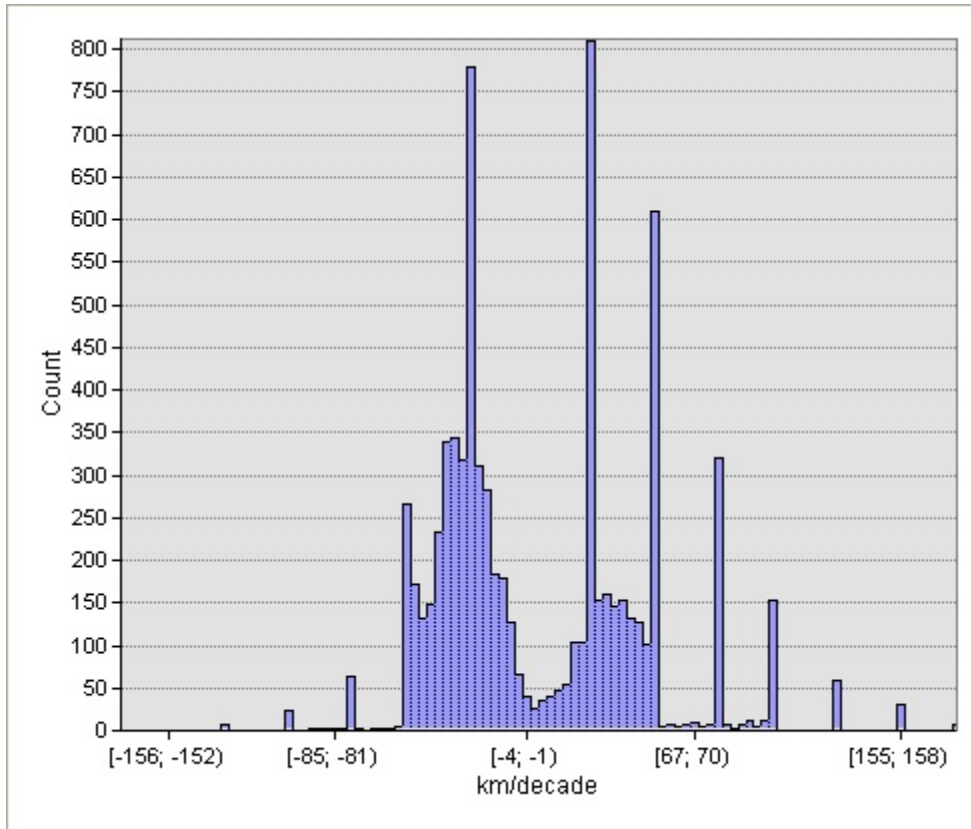


Figure 2.12: NCAR CCSM3 longitudinal isotherm movement histogram. The displacement range of -156 to 182 is divided into 100 bars.

Spatially, the longitudinal displacement shows a dominant polar motion of approximately equal magnitude in the temperature shifts for both hemispheres.

The southern displacement is characterized by a mode centered on a displacement of 105 km/decade over the 60-year period. The northern displacement mode is dominated by a north-bound displacement of approximately 25 km/decade over the 60 year period with other lesser peaks at larger displacement values.

Figure 2.13 shows the velocity field of isotherm movements projected by the NCAR CCSM.

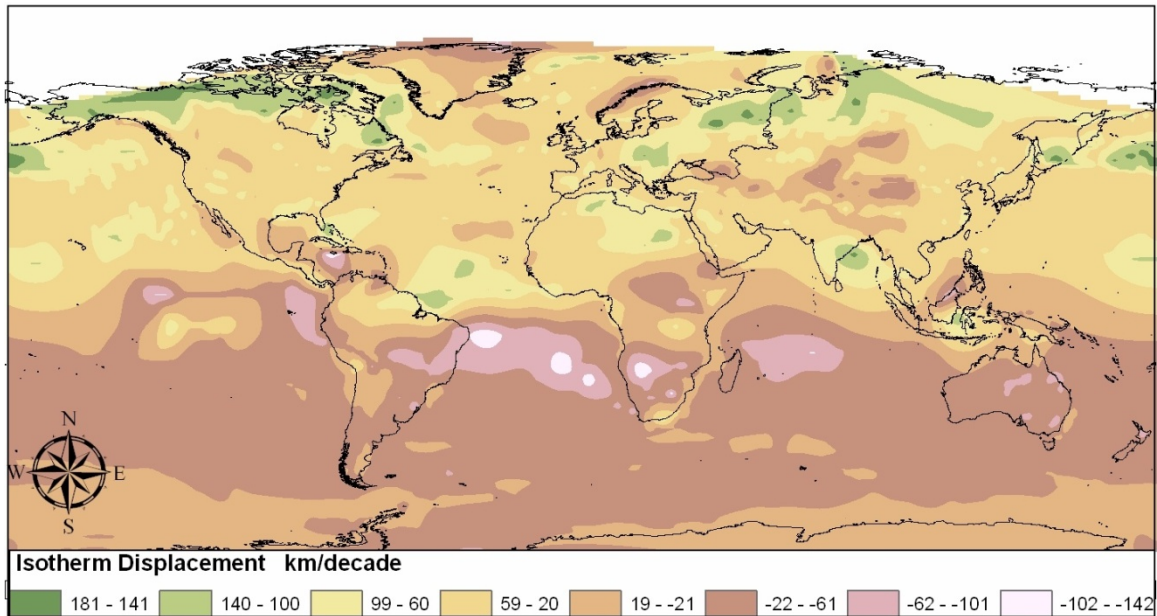


Figure 2.13: NCAR CCSM3 Longitudinal Displacement 2030-2090

The Northern Hemisphere displacement is almost exclusively towards the North Pole with the exception of the following regions; on the northwest Scandinavian coast, northern Greenland and in the vicinity of the Tibetan Plateau. The Tibetan Plateau is predicted to be cooler than the surrounding region in 2030 and acts as a local temperature minimum and thus a sink for isotherms. Regions of the most rapid northern movement occur at approximately 67°N. A different pattern is seen in the southern hemisphere where the locations with the most rapid southerly motion are just south of the equator.

The longitudinal isotherm displacement map from NCAR CCSM data shows large displacements in two north-eastern regions of Russia and a band of large displacement vectors at approximately 68°N in the North American continent. In contrast the southern regions of the Southern Hemisphere have very low values for displacement

vectors. This is expected as the large amount of thermal mass in the Southern Hemisphere oceans moderate the temperature changes resulting from anthropomorphic climate change (IPCC 2001).

The NCAR CCSM3 latitudinal displacement histogram (Figure 2.14) has a leptokurtic distribution with a dominate peak at approximately -0.5 km.

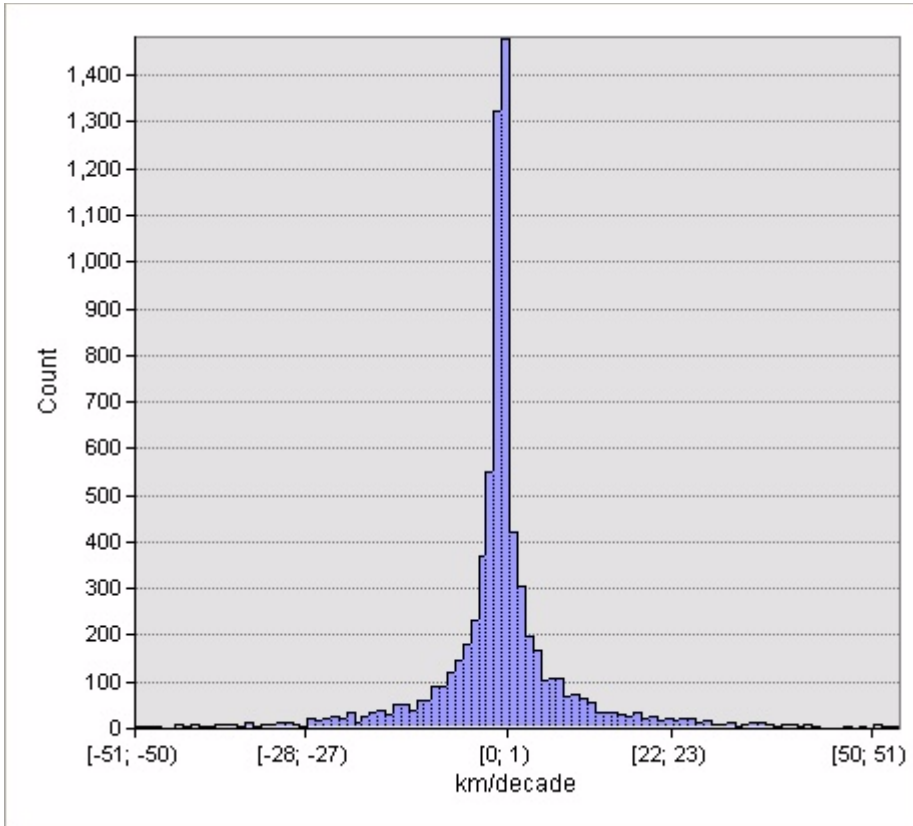


Figure 2.14: NCAR CCSM3 Latitudinal Displacement Histogram. The displacement range of -51 to 54 is divided into 100 bars.

The distribution of displacement to the east or west is not spatially restricted to a particular hemisphere but rather is distributed across the globe. Figure 2.15 displays the NCAR CCSM3 output latitudinal displacement across the globe.



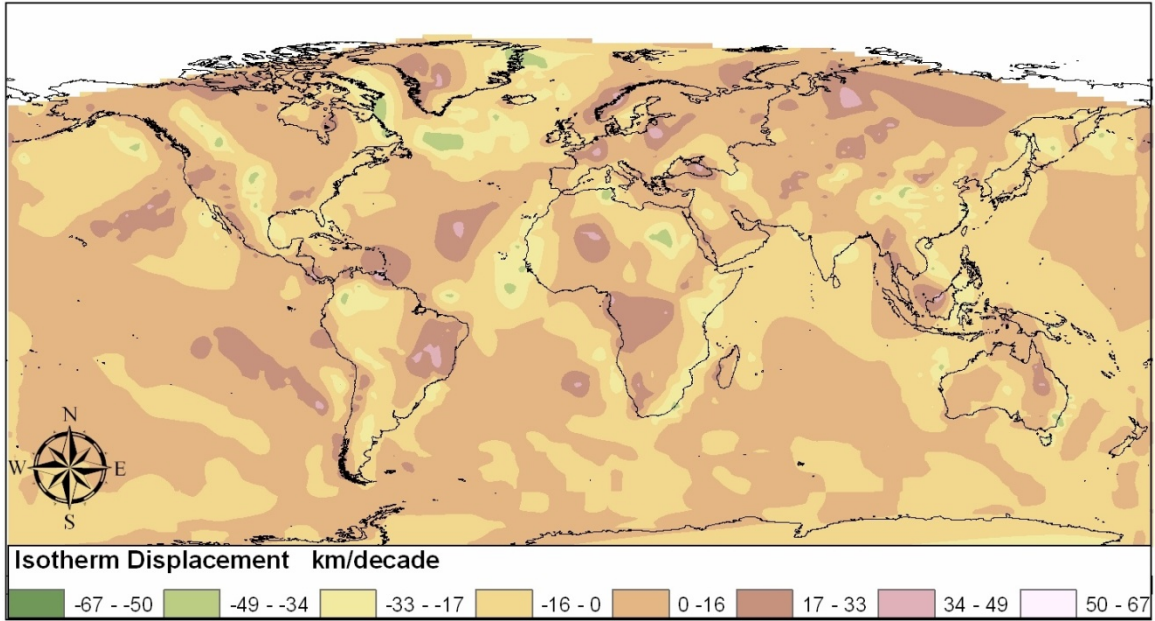


Figure 2.15: NCAR CCSM3 Latitudinal Displacement

The displacement pattern at the latitudinal direction suggests that most of the world will experience small shifts (in beige and light brown colors). Regional patches show isotherms moving towards the east with patches occurring in or around the zones of easterlies and throughout most of the Northern Hemisphere. Considerably smaller and more isolated areas in the Northern Hemisphere alone show isotherms shifting towards the west (in green and light yellow shades). Multiple concentrations of large isotherm displacements and the high convergence/divergence areas are identified by the iso cluster algorithm in the NCAR CCSM3 projections (Figure 2.16).

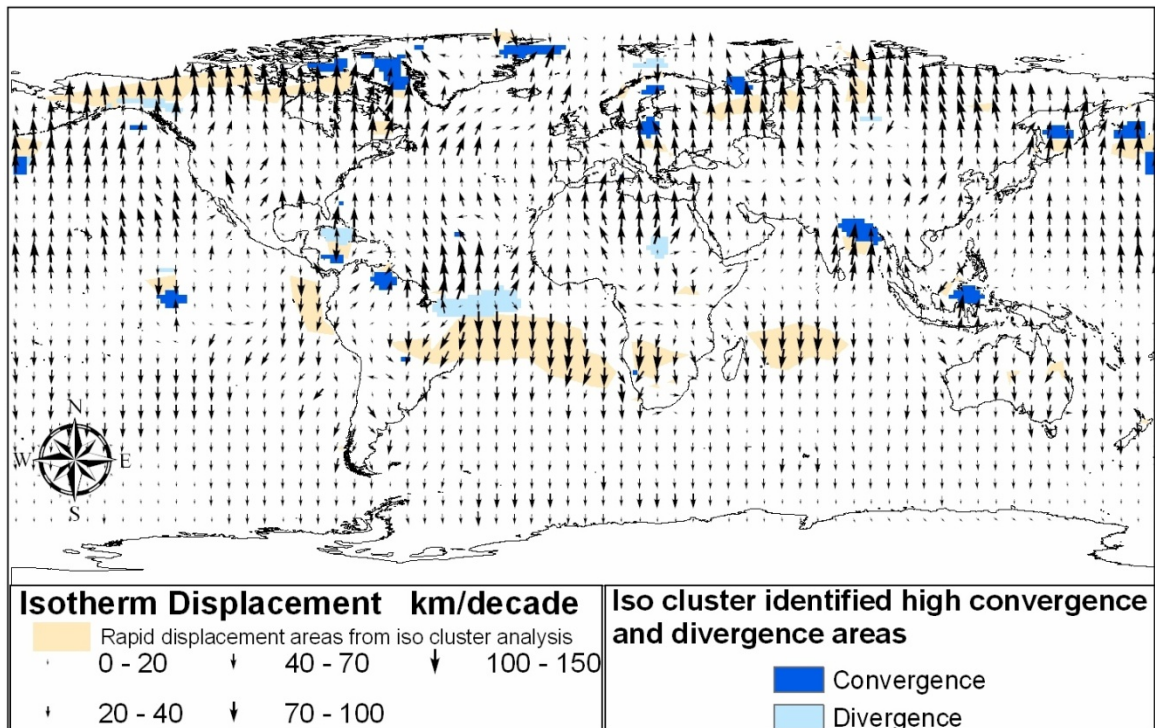


Figure 2.16: NCAR CCSM rapid displacement and high convergence/divergence areas for 2030-2090.

Bands of rapid displacement northward are found at approximately  $67^\circ$  latitude across North America and on the northern portion of central Eurasia in the NCAR CCSM3 dataset. These regions are at the boundary of the polar amplification mentioned by Holland and Bitz (2003). A region in the western Indian Ocean and the southwest coast of Africa show rapid isotherm movement southward. However, no support was found for the band of comparatively more rapid warming over the South Atlantic, Africa and the Indian Ocean east of Madagascar at approximately  $15^\circ\text{S}$  that corresponds to the region of rapid isotherm movement. Nevertheless, Carril *et al.* (1997) using an earlier version of the NCAR CCSM GCM identified an area of more rapid warming in the south Atlantic just south of the region at approximately  $15^\circ\text{S}$ . Divergence regions are scattered, and one area appears substantial: a tropical ocean region east of Brazil. The region east of

Brazil is possibly a result of a shift in the Inter-Tropical Convergence Zone (ITCZ) due to changes in the Atlantic Ocean (Labraga, 1997). The ITCZ penetrates further and more quickly to the south during the southern season due to pressure differences between the equatorial Pacific and Atlantic oceans (Labraga, 1997).

### 2.3.3 Comparison of the two datasets from CNRM CM3 and NCAR CCSM

The two datasets share several regions of rapid movement including the higher latitudes in both North America and Eurasia (Figure 2.17 and Figure 2.18).

Figure 2.17: CNRM CM3 rapid displacement map for 2030-2090.

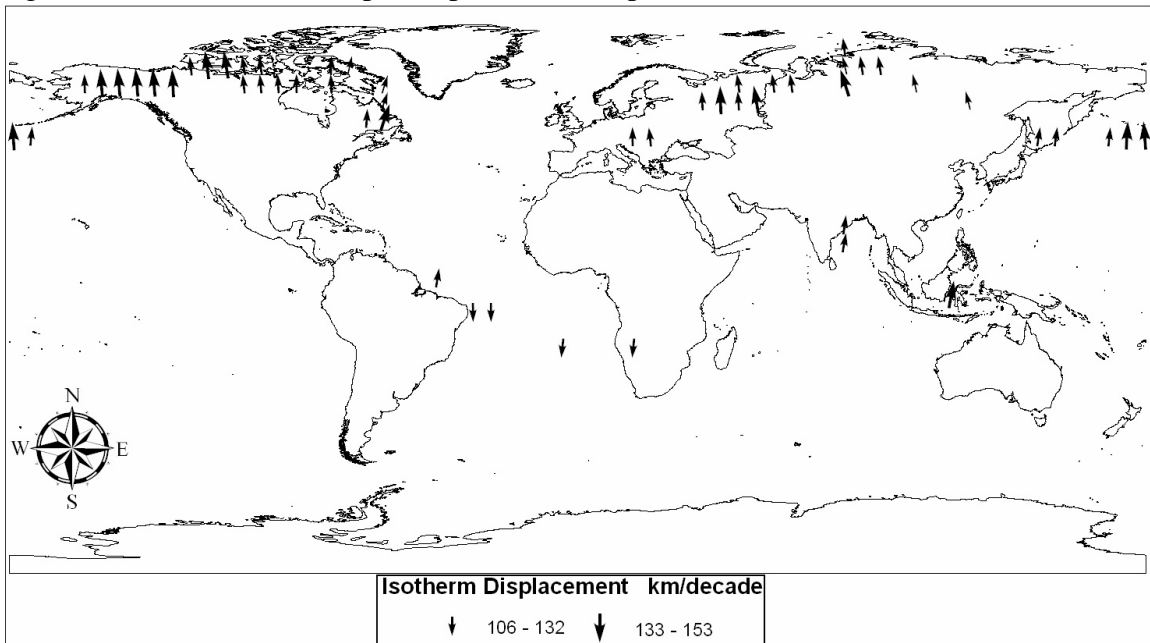


Figure 2.18: NCAR CCSM rapid displacement map for 2030-2090.

Classification as rapid is determined by applying Jenks Natural Breaks algorithm to both distributions and using the lower value of the next to highest classification of the two datasets as the threshold. The absence of a region of rapid isotherm movement in the high southern latitudes is as expected as there will be minimal warming due to ocean heat

uptake (IPCC 2001) resulting in minimal isotherm shifts. Both model's maps have rapid displacement in North America and Asia. The CNRM model had unique regions in the vicinity of Greenland, the Arabian Sea, southwest Africa and the ENSO region in the Pacific (Figure 2.17).

The difference in the shared rapid displacement locations of the high northern latitudes is examined using the positions of an isotherm confined to the Polar Regions,  $-16^{\circ}\text{C}$ . The NCAR CCSM model suggests rather different patterns of  $-16^{\circ}\text{C}$  isotherm movement than the CNRM model. In the northern hemisphere, the NCAR isotherm in the north is small and localized to a region over Greenland (Figure 2.19); whereas, the CNRM CM-3 model suggests the  $-16^{\circ}\text{C}$  isotherm spans the globe (Figure 2.20).

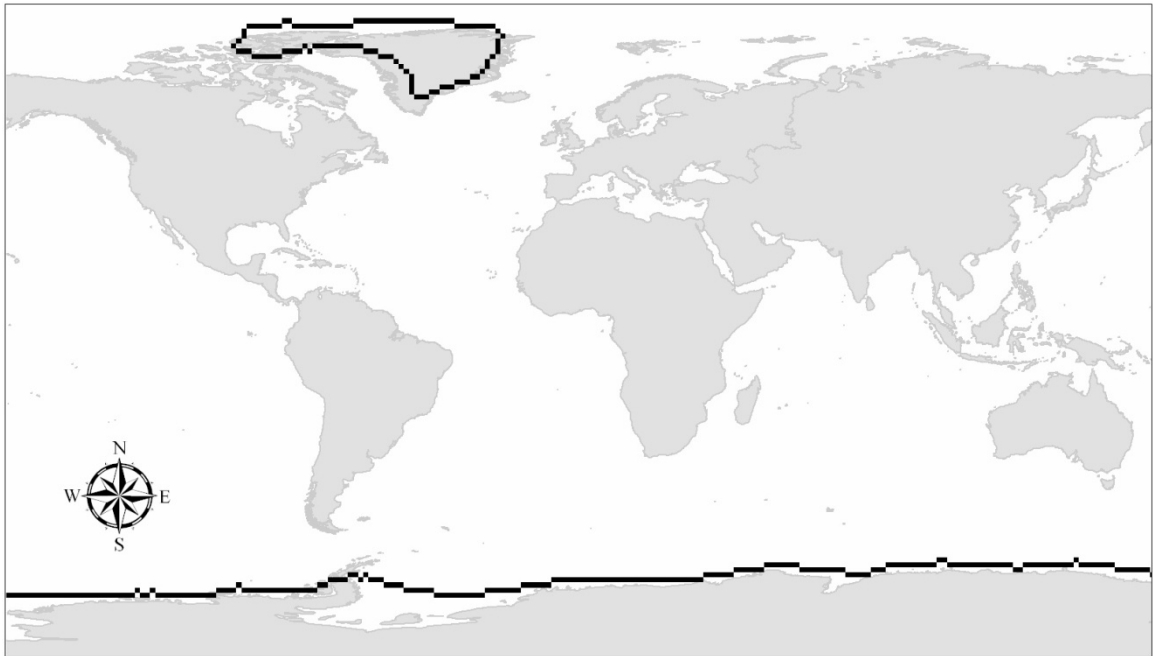


Figure 2.19: NCAR  $-16^{\circ}$  Isotherm for the 2000-2030 mean.

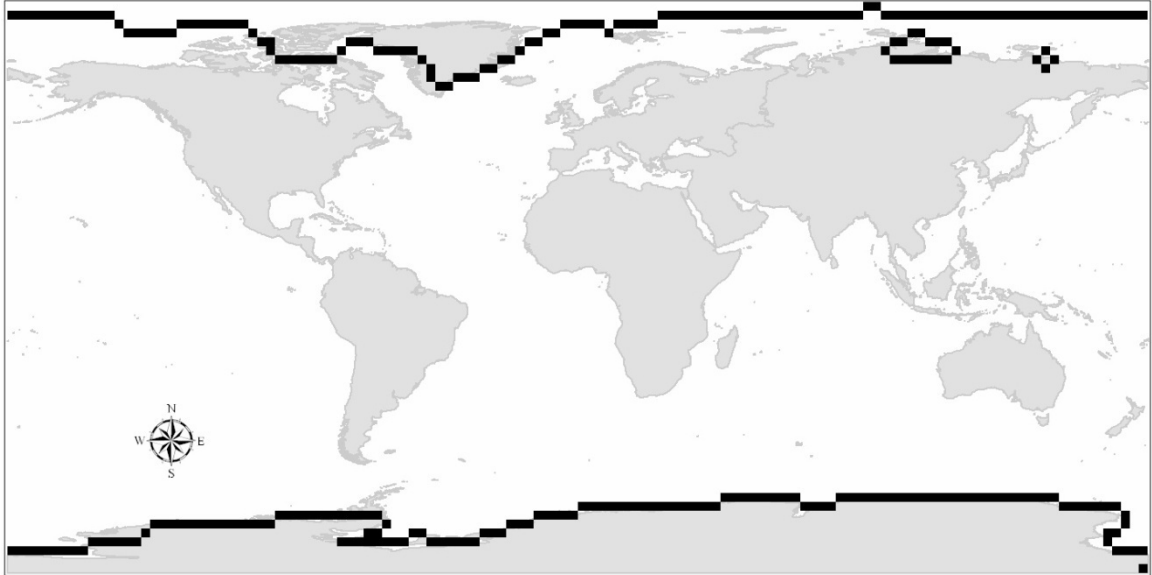


Figure 2.20: CNRM -16° Isotherm for the 2000-2030 mean.

The NCAR -16 °C 2060-2090 mean isotherm in the north remains over Greenland and is smaller than the 2000-2030 isotherm (Figure 2.21) while the CNRM CM-3 model -16 °C isotherm shrinks to Greenland over Greenland only (Figure 2.22).

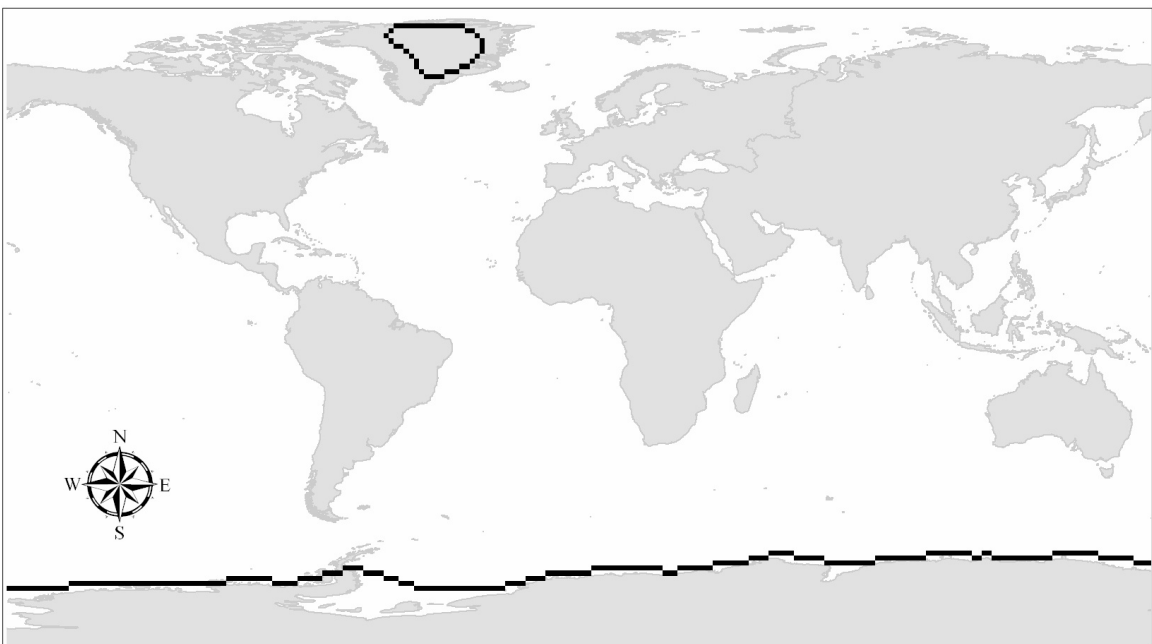


Figure 2.21: NCAR -16° Isotherm for the 2060-2090 mean

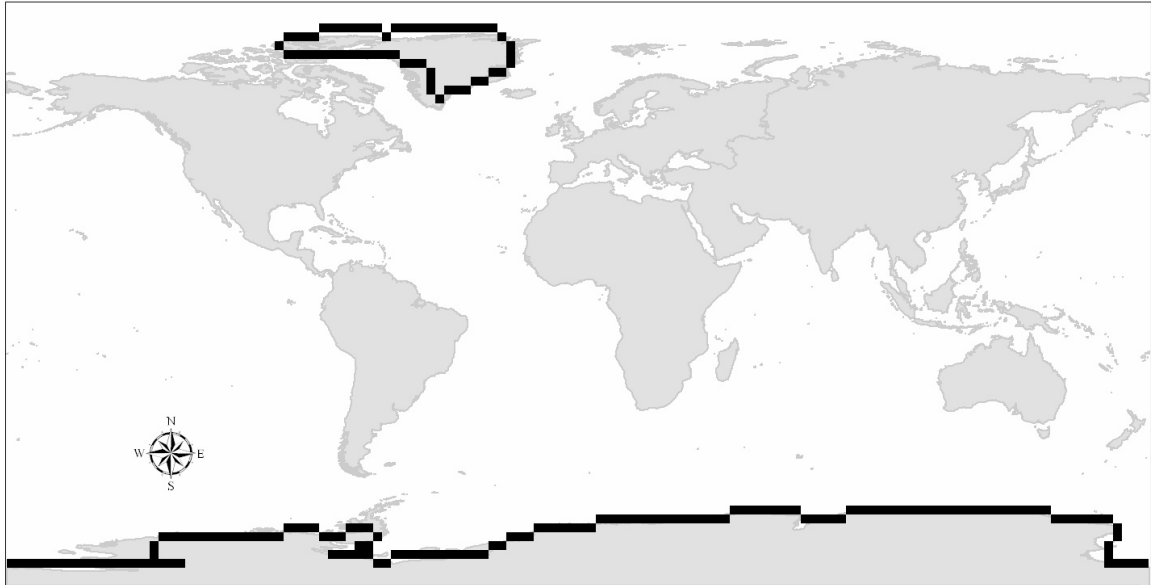


Figure 2.22: CNRM -16° Isotherm for the 2060-2090 mean

While both models suggest the -16 °C isotherms span the globe in the southern hemisphere, the initial isotherm pattern suggested by CNRM elicits a stronger warming trend about Greenland than the one by NCAR CCSM.

The Greenland differences are the possible result of sea ice model differences as the extent of the -16°C isotherms in NCAR is less than the extent in the CNRM model. Holland and Bitz (2003) determined that in the earlier versions of these two GCMs the CNRM model produced a slower sea ice melt rate than the NCAR model and it is likely that this difference persists in the current model versions. The -16°C isotherm from the two models show that the Arctic ice in the NCAR model has melted to a greater extent than in the CNRM CM3 model. The maximum warming that occurs at the latitude of the sea ice extent (Holland and Bitz 2003) is captured by the kinematic map representation.

The equatorial differences seen between the two datasets are the possible result of cloud modelling and the El Niño - Southern Oscillation (ENSO) modelling in the El Niño region. The ENSO modelling is a possible underlying cause for GCM output differences

as the Niño 3 region, an area over Indonesia, and an Indian Ocean area all have differences.

#### ***2.4 Conclusion and Future Research***

GIS support for scientific inferences and knowledge integration is limited by the lack of spatiotemporal kinematic descriptors for geographic phenomena. Kinematics describes the motion of phenomena without attempting to capture the dynamics underlying the motion. The development of a kinematic approach within the GIS enabled the spatiotemporal analysis of the output of dynamics models including General Circulation Models.

The concepts of kinematics are used to capture change and movement in geographic fields in this research. The change and movement is captured by the application of image processing approaches (Horn & Schenk, 1981). Change and motion is characterized utilizing velocity as the basic unit of change.

Grid-based scalar observations (such as temperature) are transformed to displacement vectors (directions and speed of the movement of an isoline) to describe how changes progress through space and time. The approach integrates Eulerian and Lagrangian approaches by following moving virtual object's boundaries and assigning the boundary displacements to field locations. Optical flow is applied to the surrogate virtual objects' boundaries in order to characterize the scalar field's spatiotemporal changes. The majority of locations in a field are calculated directly using multiple virtual objects with missing locations assigned values using interpolation. The resulting spatiotemporal representation of change and movement facilitates the understanding of the spatiotemporal properties of geographic phenomena.

The capabilities of the proposed representation and analytical approach are demonstrated by its application to the analysis of IPCC A2 climate change scenario as depicted in two GCM's: the NCAR CCSM3 and the CNRM CM3. The analysis focused on spatiotemporal information more easily elicited by the kinematic approach than by current GIS supported methods. The enhancements to spatiotemporal GIS analysis provided by the integrated space and time kinematics approach were summarized. Maps of the displacement portrayed the spatial pattern of the spatiotemporal changes.

A migrating means algorithm (Ball & Hall, 1965) was used to identify statistical outliers in the flow field that highlighted unique areas, examining autocorrelation in displacement vectors that identify cohesive fluid objects and comparing flow fields from different data sources. Movement extremes exhibited autocorrelation beyond the magnitude expected from an artifact from the natural neighbor tool. A 2D continuous field, such as temperature, can additionally be perceived with flows of convergence and divergence. Regions of convergence and divergence may suggest areas of interesting processes driving the dynamics of the scalar field as well as highlight local minima and maxima due to elevation or other geographic factors.

The distribution of northward and southward velocities show the poleward motion discussed in the IPCC reports (IPCC 2001). Additional areas exhibited flow convergence and divergence due to local minima and maxima. The distribution of motion amplitude in the longitudinal histograms hinted that the warming in the Northern Hemisphere is less homogeneous than in the Southern Hemisphere. The polar amplification of Holland and Bitz (2003) is captured in both GCM model's outputs by the representation in this research.



Duplicating the analysis in this paper without the spatiotemporal representation would have required manual sampling of the climate values at the two time instances for a grid point, the scaling of the change rate at the point by the spatial derivative and finally the grouping of the changes that were statically significant. The representation in this research enables users to easily spot areas of unusual spatiotemporal change and then compare the regions of unusual movement between different GCMs. Regions exhibiting differences hinted at the fundamental difference in sea ice models between the NCAR and CNRM GCMs as described by Holland and Bitz (2003). The general pattern of polar amplification stood out in both models.

The approach developed in this research could not calculate displacement vectors for complex shapes with multiple concavities. Displacement vectors for complex changes such as merges and splits in the isotherms are also not accurately captured. An isotherm ring that disappears by the next interval leads to displacements that cannot be calculated by the algorithm as no ending location for the vectors can be determined. Similarly, an isotherm near the boundary of the globe that disappears by the next sample interval leads to failed attempts to quantify the change. The inability to track complex shapes and transitions leads to loss of some of the fine grain displacements. One approach to tracking complex shapes worth further study is to use active contours ( Kass, Witkin & Terzopoulos, 1987).

## **References**

- Ahl, V., & Allen, T.F.H. (1996). *Hierarchy Theory: A Vision, Vocabulary, and Epistemology*. Columbia University Press, New York.
- Armstrong, M. P. (1988). Temporality in spatial databases. In Proceedings of GIS/LIS'88, 2. Bethesda, MD, *American Congress of Surveying and Mapping*: 880-9.
- Ball, G. H., & D. J. Hall. (1965). *ISODATA, A Novel Method of Data Analysis and Pattern Classification*. Menlo Park, California: Stanford Research Institute.
- Bluestein, H. B. (1992). *Synoptic-Dynamic Meteorology in Midlatitudes*. Oxford University Press, New York.
- Konrad, J. (2005). Handbook of image and video processing. In A. C. Bovik (Eds.) *Motion Detection and Estimation* (pp 253-274). Burlington, MA: Elsevier Academic Press.
- Burrough, P. A. (2001). GIS and geostatistics: Essential partners for spatial analysis. *Environmental and Ecological Statistics*, 8, 361-377.
- Carril, A. F., Menede, C. G., & Nunez, M. N. (1997). Climate Change Scenarios Over the South American Region: an Intercomparison of Coupled General Atmosphere-Ocean Circulation Models. *International Journal of Climatology*, 17, 1613-1633.
- Christakos, G., Bogaert, P., & Serre, M. (2001). *Temporal GIS Advanced Functions for Field-Based Applications*. Springer-Verlag Berlin Heidelberg New York.
- Collins, W. D., Bitz, C. M., Blackmon, M. I., Bonan, G. B., Bretherton, C. S., Carton, J. A., Chang, P., Doney, S. C., Hack, J. J., Henderson, T. B., Kiehl, J. T., Large, W. G., McKenna, D. S., Santer, B. D., & Smith, R. D. (2005). The Community Climate System Model: CCSM3, *Journal of Climate*, 19, 2122-2143.
- Cova, T. J. & Goodchild, M. F. (2002). Extending geographical representation to include fields of spatial objects. *International Journal of Geographical Information Science*, 16(6), 509-532.
- de Smith, M.J., Longley, P.A. & Goodchild, M.F. (2007). *Geospatial analysis: A comprehensive guide to principles, techniques and software tools* (pp 105). Winchelsea: Winchelsea Press.
- Felzer, B. & Heard, P. (1999). Precipitation Differences Amongst GCMs Used For The U.S. National Assessment. *Journal of the American Water Resources Association* 35 (6), 1327-1339.
- Galton, A. (2004). Fields and Objects in Space, Time and Space-time. *Spatial Cognition and Computation*, 4(1), 1-29.

- Gold, C. M. (1989): Surface interpolation, spatial adjacency and G.I.S. in: J. Raper (ed.): *Three Dimensional Applications in Geographical Information Systems* (pp. 2 1-35). London: Taylor and Francis Ltd. 1989.
- Goodchild, M. F., Yuan, M., & Cova, T. (2007). Towards a general theory of geographic representation in GIS. *International Journal of Geographic Information Science* 21(3): 239.
- Güting, R. H., Böhlen, M. H., Erwig, M., Hensen, C. S., Lorentzos, N. A., Schneider, M., & Vazirgiannis, M. (2000). A foundation for representing and querying moving objects. *ACM Transactions on Database Systems*, 25(1), 1-42.
- Horn, B. K. P., & Schunck, B. G. (1981). Determining Optical Flow. *Artificial Intelligence*, 17, 185-203.
- Hornsby, K., & Egenhofer, M.J. (2000). Identity-based change: A foundation for spatio-temporal knowledge representation. *International Journal of Geographical Information Science*, 14(3):207–204.
- Hornsby, K., & M. Egenhofer. (2002). Modeling Moving Objects over Multiple Granularities. *Annals of Mathematics and Artificial Intelligence* 36(1-2), 177-194.
- Hulme, M., Briffal, K. R., Jones, P. D., & Senior C. A. (1993). Validation of GCM control simulations using indices of daily airflow types over the British Isles. *Climate Dynamics*, 9(2), 95-105.
- Huth, R. (2000). A circulation classification scheme applicable in GCM studies. *Theoretical Applied Climatology*, 67, 1-18.
- IPCC, Climate Change (2001). *The scientific basis. Contribution of Working Group I to the Third Assessment Report of the Intergovernmental Panel on Climate Change*. Albritton, D. L., Meira Filho, L. G., Cubasch, U., Dai, X.; Ding, Y., Griggs, D. J., Hewitson, B., Houghton, J. T., Isaksen, I., Karl, T.; McFarland, M., Meleshko, V. P., Mitchell, J. F. B., Noguer, M., Nyenzi, B. S., Oppenheimer, M., Penner, J. E., Pollonais, S., Stocker, T., Trenberth, K. E., Maskell K., & Johnson C.A. (eds) Cambridge University Press, Cambridge, UK pp 881
- Holland, M.M., & Bitz, C.M. (2003). Polar amplification of climate change in coupled models. *Climate Dynamics*, 21(3-4), 221-232.
- Kass, M., Witkin, A., & Terzopoulos, D. (1987) Snakes: Active contour models, *International Journal of Computer Vision*. 1(4), 321-331.
- Lamb, H. H. (1972). *Climate: Present, Past and Future, vol. 1, Fundamentals and Climate Now* (pp 613), Methuen, New York.
- Langran, G. and Chrisman, N. R. (1988). A Framework for Temporal Geographic Information. *Cartographica*, 25(3), 1-14.

- Labraga, J. C. (1997). The Climate Change in South America Due to a Doubling in the CO<sub>2</sub> Concentration: Intercomparison of General Circulation Model Equilibrium Experiments. *International Journal of Climatology*, 17, 377–398
- Mennis, J., Viger, R., & Tomlin, C. D. (2005). Cubic Map Algebra Functions for Spatio-Temporal Analysis. *Cartography and Geographic Information Science*, 32(1), 17-32.
- Pepin, N.C. (1995). The Use of GCM Scenario Output to Model Effects of Future Climatic Change on the Thermal Climate of Marginal Maritime Uplands. *Geografiska Annaler. Series A, Physical Geography*, 77(3), 167-185
- Peuquet, D. J., & Duan, N. (1995). An Event-based Spatiotemporal Data Model (ESTDM) for Temporal Analysis of Geographical Data. *International Journal of Geographical Information Systems*, 9(1), 7-24.
- Peuquet, D. J. (2001). Making space for Time: Issues in Space-Time Data Representation. *GeoInformatica* 5(1), 11-32.
- Pfoser, D., & Theodoridis, Y. (2003). Generating Semantics-Based Trajectories of Moving Objects. *Intl. J. of Computers, Environment and Urban Systems (Special issue on Emerging Technologies for Geo-Based Applications)*, 27(3), 243–263.
- Rosenblatt, R., Sayre, E. C., & Heckler, A. F. (2009). Modeling students' conceptual understanding of force, velocity, and acceleration. *AIP Conference Proceedings*, 245-248.
- Saji, N. H., Xie, S.-P., & Yamagata, T. (2006). Tropical Indian Ocean Variability in the IPCC Twentieth-Century Climate Simulations. *Journal of Climate*. 19, 4397-4416.
- Salas-Mélia D., Chauvin F., Déque´ M., Douville H., Gueremy J. F., Marquet P., Planton S., Royer J. F., & Tyteca S. (in review) Description and validation of the CNRM-CM3 global climate model. *Climate dynamics*.
- Semazzi, F. H. M. and Song, Y. (2001). A GCM study of Climate Change induced by Deforestation in Africa. *Climate Research* 17, 169-182.
- Sengupta, S. K., & Boyle, J. S. (1993). Statistical intercomparison of global climate models: A common principal component approach with application to GCM data. UCRL-ID—114222. Downloaded 10/04/07 from [http://www.osti.gov/energycitations/product.biblio.jsp?osti\\_id=10173301](http://www.osti.gov/energycitations/product.biblio.jsp?osti_id=10173301).
- Sperry, L., Claramunt, C., & Libourel, T. (2001). A Spatio-Temporal Model for the Manipulation of Lineage Metadata. *GeoInformatics* 5(1): 51-70.
- Stefanidis , A., Eickhorst , K., Agouris , P., & Partsinevelos, P. (2003). Modeling and comparing change using spatiotemporal helixes. *Proceedings of the 11th ACM*

*international symposium on Advances in geographic information systems*, pg. 86-93, November 07-08, 2003, New Orleans, Louisiana, USA.

- Trowbridge, D. E., & McDermott, L. C. (1981). Investigation of student understanding of the concept of acceleration in one dimension. *American Journal of Physics*, 49(3), 242-253.
- Worboys, M. F., (1994). Object-oriented approaches to georeferenced information. *International Journal of Geographical Information Systems*, 3: 385-399.
- Yuan, M. (1999). Representing Geographic Information to enhance GIS support for complex spatiotemporal queries. *Transactions in GIS*, 3(2):137-160.
- Yuan, M. (2000). Representation dynamic geographic phenomena based on hierarchical theory. Proceedings: 9th International Symposium on Spatial Data Handling Spatial Data Handling, P. Forer Eds. Pp. 2a.19-2a.29.
- Yuan, M. (2001). Representing Complex Geographic Phenomena with both Object- and Field-like Properties. *Cartography and Geographic Information Science* 28(2): 83-96.

### **Chapter 3: A Kinematics-based GIS Methodology to Represent and Analyze Spatiotemporal Patterns of Precipitation Change**

#### ***Abstract***

A kinematics-based GIS methodology is applied to identify, represent, and analyze spatiotemporal patterns and pattern transitions in very large data sets. A use case is built from two precipitation data products projected for the A2 scenario by the International Panel for Climate Change (IPCC): (1) the Community Climate System Model (CCSM3) from the National Center for Atmospheric Research (NCAR, USA, Boulder Colorado) and, (2) the global ocean-atmosphere coupled system (CM3) from the Center for National Weather Research (CNRM, METEO-France, Toulouse). The study takes a predefined threshold to delineate regions of interest, calculates shifts of the regions between years, and characterizes the pattern change. The research focuses on the topics as changes in the tropics affect extra-tropical climate. The study uses precipitation over 213 cm/year in 2001 and 2048 to illustrate the kinematics approach to comparing precipitation patterns predicted from the CCSM3 and CM3. Even though the precipitation data in 2001 and 2048 cannot be considered temporally continuous, the differential used here was to simulate the transition of precipitation patterns between the two years under the assumption that changes to spatial patterns of precipitation for 213 cm/year were gradual from 2001 to 2048. The 213 cm/year precipitation threshold is met when a large number of precipitation events occur during the year. The 213 cm/yr threshold is stable from year to year versus lesser thresholds which may be discontinuous and require temporal averaging to smooth the rapid variation.

The kinematics approach quantifies divergence, rotation, and deformation about changes to precipitation patterns and enables the search for precipitation regions influenced primarily by local conditions or by general circulation patterns of water vapor transport. The study demonstrates that the kinematics approach is able to discern transitional patterns from a continuous field of geographic properties over time by defining objects through thresholds and analyzing the object's internal and external movement patterns in space and time.

**Keywords:** temporal GIS, objects, geographic kinematics, internal change, motion, and climate change.

### ***3.1 Introduction***

Many climatological studies examine aggregated patterns from climate events to generalize spatially the overall outcome of climate change at the regional or global scales (Carelton, 1999). Van Ulden and Oldenborgh (2006) studied five GCMs and discovered significant differences in circulation patterns leading to differences in precipitation patterns. This research continues the tradition of seeking effective ways to address spatiotemporal patterns, specifically, precipitation patterns projected in A2 scenario defined by the International Panel for Climate Change (IPCC). Instead of examining precipitation patterns at individual time frames, the research applies a method based on kinematics, originally designed for the analysis of changes in temperature patterns, to emphasize spatiotemporal transitions of precipitation. By adopting the idea of kinematics, the GIS method identified areas of high precipitation and characterized the direction and distance of movement for these areas over space and time. Measures for the area's internal spatiotemporal characteristics and transitions provide new insights into

precipitation patterns projected by two General Circulation Models (GCMs). All GCMs produce massive climate projection products, and the essence of predicted climate patterns and the differences among data outputs from models are difficult to discern. The study shows how the kinematics approach can facilitate the elicitation and summary of changes in spatiotemporal precipitation patterns from volumes of GCM data products.

Elicitation of precipitation patterns out of massive GCM data products is non-trivial. Effective detection of patterns relies heavily on the design of representation schemes and analytical methods (Yuan, Mark, Egenhofer, & Peuquet, 2005). To this end, the applied method adopts the concepts of kinematics to represent areas of high precipitation as individual objects and track the direction and movement of these objects over space and time. The shift patterns of precipitation are then examined through linking these objects across time steps as in a flow field defined by Theisel and Seidel (2003). Shifts measured by the rates of emergence, dissipation, splitting and merging may be indicative of the effects of large scale circulation patterns on precipitation. The near fifty year interval revealed movement in tropical precipitation that resulted in changes that can be analyzed for isohyet shifts. Climatic data are analyzed to determine the location, type and rate of internal change of precipitation objects. These measures can effectively summarize and contrast precipitation patterns suggested by different GCM models or for different climate change scenarios. Furthermore, the summative shift patterns may help formulate hypotheses about forcing functions or environmental variables responsible for precipitation change.

This research applies the method developed previously for analysis of changes to temperature patterns, but adds a new dimension in the measure of internal changes to



individual objects (i.e. precipitation areas) to enable insights into changes in precipitation patterns. Expanding upon the concepts of kinematics with measures of direction and movement, the research quantifies the rate of change internally and externally to the identified feature. Precipitation features defined by a given threshold, such as 213 cm/year, include areas with annual precipitation at the threshold or greater. Precipitation objects may merge, split, emerge or dissipate as change progresses. The research posits the hypothesis that changes to precipitation patterns can be represented with both internal and external kinematic measures. With the proposed quantitative measures, the chapter presents the kinematics-based method and demonstrates the application of the method to spatiotemporal analysis of precipitation patterns suggested for the IPCC A2 Scenario.

This chapter is divided into four sections: introduction; conceptual bases and related research; datasets and methods; and results and discussions. The introductory section overviews the research goal, problem context, and approach. The next section highlights the underlying conceptual frameworks and related studies that support the development of the proposed method. The section on datasets and methods discusses the GCM data products used in the case study and procedures that implement the kinematics-based GIS method to elicit spatiotemporal patterns of precipitation. Finally, the section on results and discussions presents the findings and elaborates on broader implications and directions for future research.

## ***3.2 Conceptual Bases and Related Research***

### ***3.2.1 Information Representation***

In an information system, representation is the key to effective information analysis (Yuan, Mark, Egenhofer, & Peuquet, 2005). This is particularly true for very large time-

series data sets from General Circulation Models (GCM). In the context of representation, these data products are compatible to temporal sets of snapshots that show spatial distributions of climate variables. By examining one snapshot at a time, analysis is limited to spatial characterization rather than change over space and time (Chrisman, 1998). Due to spatial and temporal autocorrelation, neighboring properties are critical to pattern analysis of geographic phenomena, including climate change (Shekhar, Zhang, Huang, & Vatsavai 2003).

Past approaches used spatial grouping to identify regions of cells that show similar temporal trends. For example, Tan, Steinbac, Kumar, Potter, and Klooster (2002) applied temporal classification to data at each grid location to determine the temporal pattern and then grouped similar patterns. Another approach took pair-wise correlations between time series at different geographical locations and found regions exhibiting spatial autocorrelation with each member of the pairs (Steinbach *et al.*, 2001).

Alternatively, this research aggregates grid points based on a threshold value into an object and then characterizes the spatiotemporal behavior of each object. Calculated change rates are in contrast to the spatiotemporal helix model proposed by Stefanidis, Eickhorst, Agouris, and Partsnevelos (2003), which requires the user to infer the rate change. The kinematics-based GIS method stores (Table 3.1) the divergence rate (divergobj), dominate axis of deformation (deforming ), deformation expansion or contraction (deform\_pri) and rotation (vorticobj) information to enable database queries regarding any of these spatiotemporal growth characteristics.

FID	Shape	VALUE	SUM_F_AREA	vorticobj	divergobj	deform_ang	deform_pri
1	Polygon	14	210474641678	2.79722	-10.3926	-0.610692	12.8152
5	Polygon	42	303645330016	3.03235	-4.43075	1.31644	-9.17179
6	Polygon	49	230971706954	14.9402	27.063101	-0.883933	-32.1581
8	Polygon	63	155491267327	83.570503	70.074097	-0.653175	-66.630699
14	Polygon	105	316108606580	17.2857	-18.475401	-0.027835	12.7012
18	Polygon	133	9442722756640	48.2953	23.5177	-0.60063	-31.692499
20	Polygon	147	78895005796.9	49.388901	4.45629	-0.648897	-32.236099
24	Polygon	175	78738331361	57.423	64.971397	-0.688072	-55.342701
28	Polygon	203	78527444356	35.223598	-43.380199	0.966261	-51.030102
29	Polygon	210	78527444356	31.415501	-20.257799	0.909806	-18.234301
31	Polygon	224	76082636957.1	22.756599	-3.12602	1.05944	-150.146
32	Polygon	231	76082636957.2	45.472	-8.49036	0.174714	-23.957399
33	Polygon	238	207009538234	36.688999	21.4611	-0.544093	-26.355301

Table 3.1: An example data table for a set of precipitation objects and the derived kinematic attributes

Using kinematic concepts incorporates the rich history of kinematic analysis in Meteorology. The basis of kinematic analysis is the change in velocity for both latitudinal flow and longitudinal flow (Bluestein, 1992). Kinematics is usually applied to real fluid flow, but this research applies the concept to a virtual flow that reflects the changes in scalar attribute values over the Earth's surface. The kinematic representation combines Lagrangian and Eulerian concepts of fluid kinematics to effectively capture the direction and amount of change in space and time of a field. The spatiotemporal distributions of velocity define kinematics. In addition to the velocity that measures the direction and movement of an object, the research considers the following as measures for internal kinematics to the object: divergence, deformation and rotation. Divergence is the fractional rate of area change to the object, deformation captures an object's rate of expansion or contraction, and rotation addresses changes in orientation due to differential velocity (Figure 3.1). Once calculated, the three measures are stored in a database and

used to differentiate regions that may have the same shape and change to shape but exhibit very different patterns of kinematics.

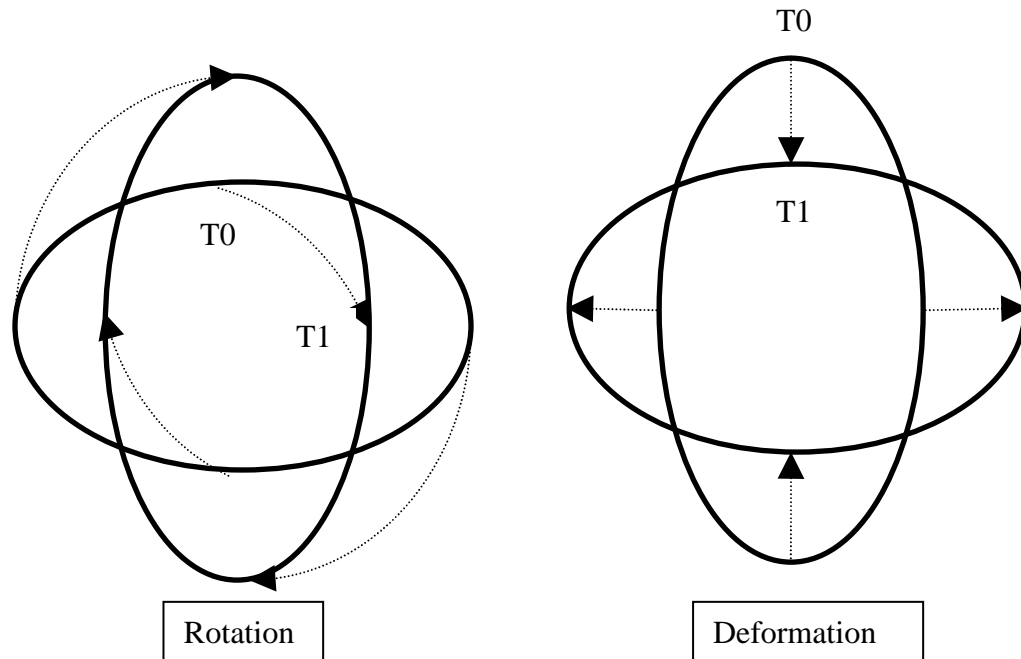


Figure 3.1: Internal kinematics is needed to determine rotation or deformation of an object.

The first step to apply concepts of kinematics to a dataset representing a scalar field of geographic properties is to construct objects in the scalar field. The continuous field representation is converted to an object-base representation (Peuquet 2001) using bona-fide or fiat boundaries to demarcate the objects' extent (Smith and Mark 1998). Bona-fide boundaries are defined by natural discontinuities in a geographic phenomenon (such as watershed divides), whereas a fiat boundary is based on subjective criteria to spatially delineate geography (such as county boundaries to delineate land administration). The creation of conceptual objects (e.g. precipitation areas) from fields in this study is based on fiat boundaries defined by a subdivision of the isohyet range

used in the Koppen climate classification (10, 20, 30, 40, 50, 60, 70, 80, 90, 100, 110, 120, 130, 140, 150, 161, 178, 213, and 284 cm/year). The discrete nature of precipitation fundamentally fits well with the object-based conceptualization. The kinematic measures are then used to summarize spatiotemporal patterns of precipitation exhibited by these conceptual objects individually and collectively.

A data model, expanding upon the three-domain model (Yuan 1999), was used for storing and analyzing the conceptual objects of precipitation areas. Three domains of semantics, space, and time provide the basis for digital representations of histories at location as well as lifecycle of geographic objects. Yuan (2001) further incorporated concepts of hierarchies into the three-domain model to facilitate the representation of events and processes across multiple levels of spatial and temporal scales. The kinematics-based method further incorporates the concepts of kinematics to expand the three-domain model with quantitative values for the internal kinematics of fiat objects identified through defined thresholds in a field.

### *3.2.2 Elicit Spatiotemporal Patterns from Massive Data*

Spatiotemporal analytical methods, traditionally developed for sampled data, are incapable of dealing with large heterogeneous geographic databases (Miller and Han 2001). The field of Knowledge Discovery in Databases (KDD) aims to develop methods that can elicit non-trivial patterns from ever increasing databases. Utilizing a KDD for analyzing large geographic databases must be done carefully as KDD systems tend to generate correlation patterns of little interest (Silberschatz & Tuzhilin 1996; Padmanabhan 2004), unless the KDD process is guided interactively or restricted by the

underlying abstract data representation. One key KDD step is data mining, the analysis of low level abstract data to produce a set of patterns from the data (Chen *et al.* 1996, Fayyad *et al.* 1996, Padmanabhan 2004). Spatiotemporal data mining requires considering what to mine from the spatiotemporal database and how the data of interest are formatted in the database (Abraham and Roddick 1998). The goal of a data mining activity should guide the creation of representation and tailor the representation to the production of summative information from massive databases (Roddick and Lees 2001).

The kinematics-based method is one approach to offer GIS support for data mining of meaningful spatiotemporal patterns by leveraging the kinematics measures to characterize spatiotemporal patterns. A spatiotemporal database should be able to describe how an object is changing in a manner that provides insight to spatial processes that lead to pattern change. A similar approach was taken by Thompson *et al.* (2002) who utilized point-level vortexes to identify physics-based objects through data mining. This research quantifies kinematics within precipitation objects defined by thresholds to identify precipitation patterns. Spatiotemporal characteristics of a precipitation object are determined by aggregating the mean spatiotemporal characteristics at grid-points within the region. The points identified as being in an object are aggregated similarly to Yip and Zhao's (1996) work on 2D fields, but, in contrast to Yip and Zhao, precipitation objects are determined by pre-defined thresholds. The aggregated characteristics at these points become attributes for the region, and the region is then conceptualized as an object. The collection of objects with their internal and external characteristics of change enables the analysis of differences and similarities between datasets and allows users to locate interesting spatiotemporal regions.

Six descriptors are required to adequately describe object spatiotemporal dynamics:

- location (Abraham and Roddick 1998);
- attribute or theme representing a characteristic assigned a value at a location (Sinton as quoted by Abraham and Roddick 1998);
- extent: the static spatial boundary of an object;
- mutation: the change in an object's attributes such that an object is assigned a new classification;
- movement: a change in the location of an object; and
- evolution: the change in an object's internal structure.

The formulation used by Abraham and Roddick (1998) to determine the six descriptors is object centric. This study extends the descriptors to field-based (or gridded) data by considering the spatiotemporal behavior of fiat objects delineated from set values in a field.

Claramunt, Parent and Theriault (1997) proposed an object-relationship data model that includes six basic extent evolutions of a spatial object: stability, deformation, expansion/contraction, and rotation and translation (Table 3.2).

Spatio-Temporal Process	Geometric types	Shape	Size	Orientation	Location
Stability	Any	constant	constant	constant	Constant
Deformation	any but point	changed	constant	constant	Constant
Expansion	Any	constant	growing	constant	Constant
Contraction	any but point	constant	shrinking	constant	Constant
Rotation	any but point	constant	constant	changed	Constant
Translation	Any	constant	constant	constant	Changed
Branching	Any	constant	merging/ splitting	constant	Constant

Table 3.2: Spatial Entity Evolution (Claramunt *et al.* 1997)

An additional index, extent evolution branching (merging or splitting), was previously suggested by Peuquet (1994). The kinematics-based method supports all seven classifications. The method computes the fluid kinematics deformation and assigns deformation rates along with the orientation of the expansion axis and the contraction axis. The divergence determines the overall rate of expansion or contraction while vorticity assigns a rotation rate. Branching is determined by tracking objects across two or more time instances and noting objects that divide into many or merge into one.

### 3.3 *Datasets and Methods*

This research applies two GCM datasets for IPCC climate change analysis: the National Center for Atmospheric Research Community Climate System Model (NCAR-CCSM3)



from the United States at  $1.4^\circ \times 1.4^\circ$  resolution (Collins *et al.* 2005) and the Center National Weather Research global ocean-atmosphere coupled system (CNRM-CM3) from France (Salas-Melia *et al.* 2005) at  $2.8^\circ \times 2.8^\circ$  resolution. Over the global coverage, the NCEP/NCAR output is in a  $256 \times 128$  grid, whereas the CNRM-CM3 output is in a  $144 \times 73$  grid. Precipitation data out of the GCM products for IPCC scenario A2 were obtained from the World Climate Research Program's Coupled Model Inter-comparison Project Multi-Model Dataset Archive. The A2 scenario was chosen as a case to demonstrate the kinematics approach. The A2 scenario more closely follows the actual rate of change during the last 5 years than the other scenarios.

Isohyets of annual precipitation were delineated from the climate data for 2001 and 2048. Mean annual isohyets over three or more years showed too little difference over the intervening (47) years to produce a sufficient number of calculated displacement vectors. The yearly isohyets from 2001 and 2048 have enough differences to have transitions while exhibiting enough continuity to allow the Optical flow analysis to succeed. The analysis was applied to annual isohyets of the values 10, 20, 30, 40, 50, 60, 70, 80, 90, 100, 110, 120, 130, 140, 150, 161, 178, 213 and 284 cm/year in years 2001 and 2048 and displacement vectors were calculated along each of the defined isohyets (Figure 3.2 and 3.3).

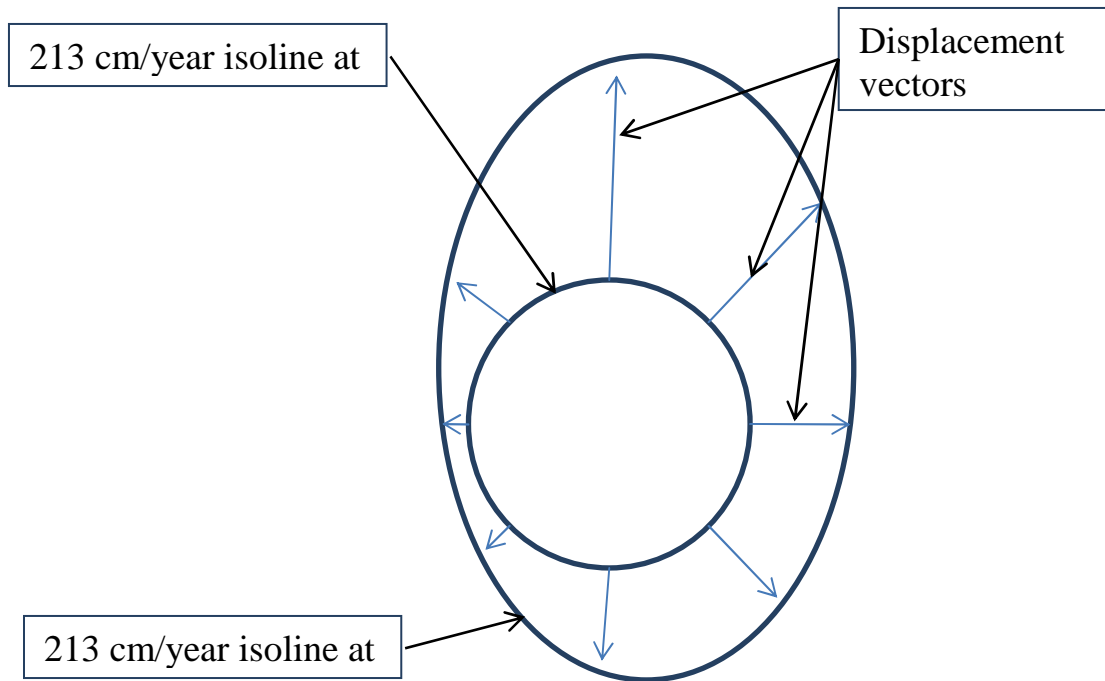


Figure 3.2: Calculating displacement vectors for the 213cm/year isohyet

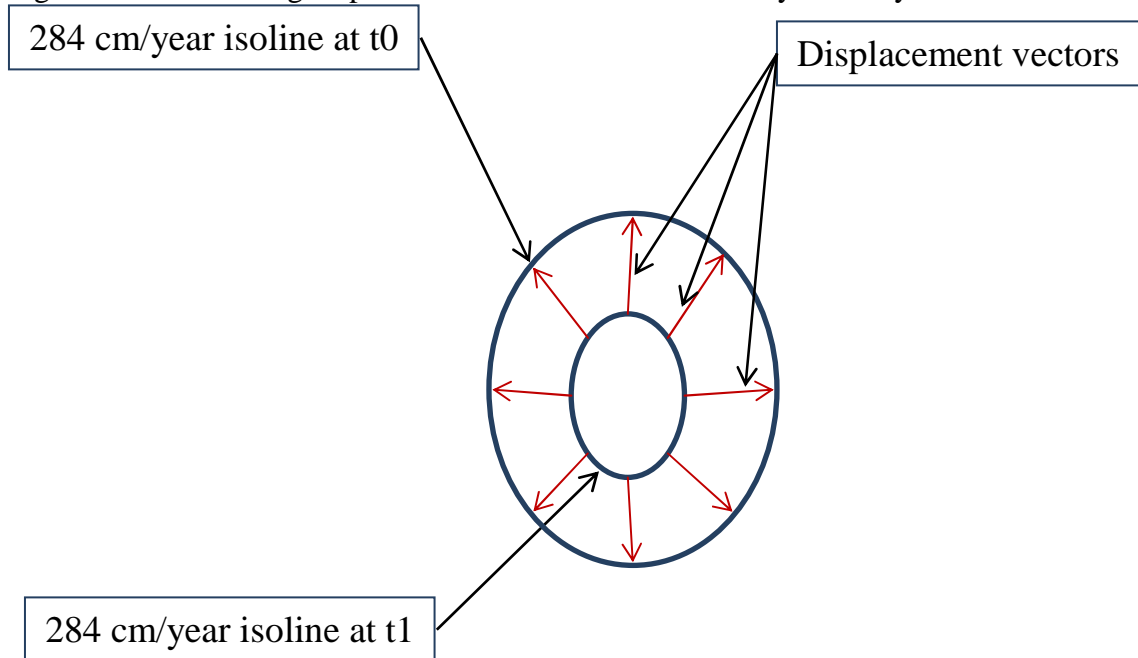


Figure 3.3: Calculating displacement vectors for the 284cm/year isohyet

Displacement vectors were spatially interpolated using the ESRI natural neighbour interpolation function to estimate displacement vectors for the remaining approximately 70% of the grid points. The natural neighbour interpolation determines the

set of points with Thiessen polygons overlapping the polygon of the new point and applies proportionate weights based on the overlap (Gold 1989). Natural Neighbor interpolation does not produce minima or maxima that are not present in the input samples (Gold 1989). The absence of interpolated minima and maxima insures any minima and maxima found are from calculated data.

This case study extends Claramunt *et al.*'s (1997) extent evolution classifications utilizing displacement vectors along precipitation object boundaries and within the object itself. An object with boundary displacement vectors equal to 0 has a stable and unchanging extent. Claramunt *et al.*'s deformation extent evolution has non zero boundary displacement vectors but the areas within the object remains constant. For this study the deformation axis of expansion and contraction were calculated using internal flow field kinematics. Claramunt *et al.*'s expansion evolution classification has an extent increase captured by outward oriented displacement vectors along the object's boundary that conserve the shape. The contraction evolution conserves the shape but has a decreased extent captured by inward displacement vectors along the object's boundary. Incorporating concepts of fluid kinematics, the study uses divergence to quantify the increase in size due to expansion and convergence to quantify the size decrease due to contraction while ignoring shape conservation. Convergence and divergence are calculated using an area integral of the net flow defined Greene's theorem equivalent to the contour integration of the boundary vectors (Bluestein 1992).

$$\iint_R \nabla_h \cdot V \, dA = \oint_C V \cdot \hat{n} \, ds \quad \text{Eq. 3.1}$$

In equation 3.1  $\nabla_h$  is the horizontal divergence,  $V$  is the vector function and  $\hat{n}$  is the vector normal to the curve  $C$  and  $ds$  traverses the curve in a counter clockwise

direction. Rotation is suggested by a divergence value of zero and all displacement vectors with the same magnitude and angle in reference of the respective normal vector at the boundary. In other words, rotation is measured by evaluating the internal shear and the resulting vorticity inside each object. Translation is determined by displacement vectors with a divergence value of 0 and equal magnitude and equal angle with respect to the coordinate system. Branching includes both merging and splitting. Branching is determined through assigning regions from a time instance to corresponding regions in the next time instance using a tracking algorithm detailed in the later session.

When transitions can be considered spatially and temporally continuous, a moving object can be conceptualized as a manifold in a two-dimensional space (x,y) with one-dimensional time (t) in six possible transitions: emergence, dissipation, convergence, divergence, merging and splitting (Figure 3.4).

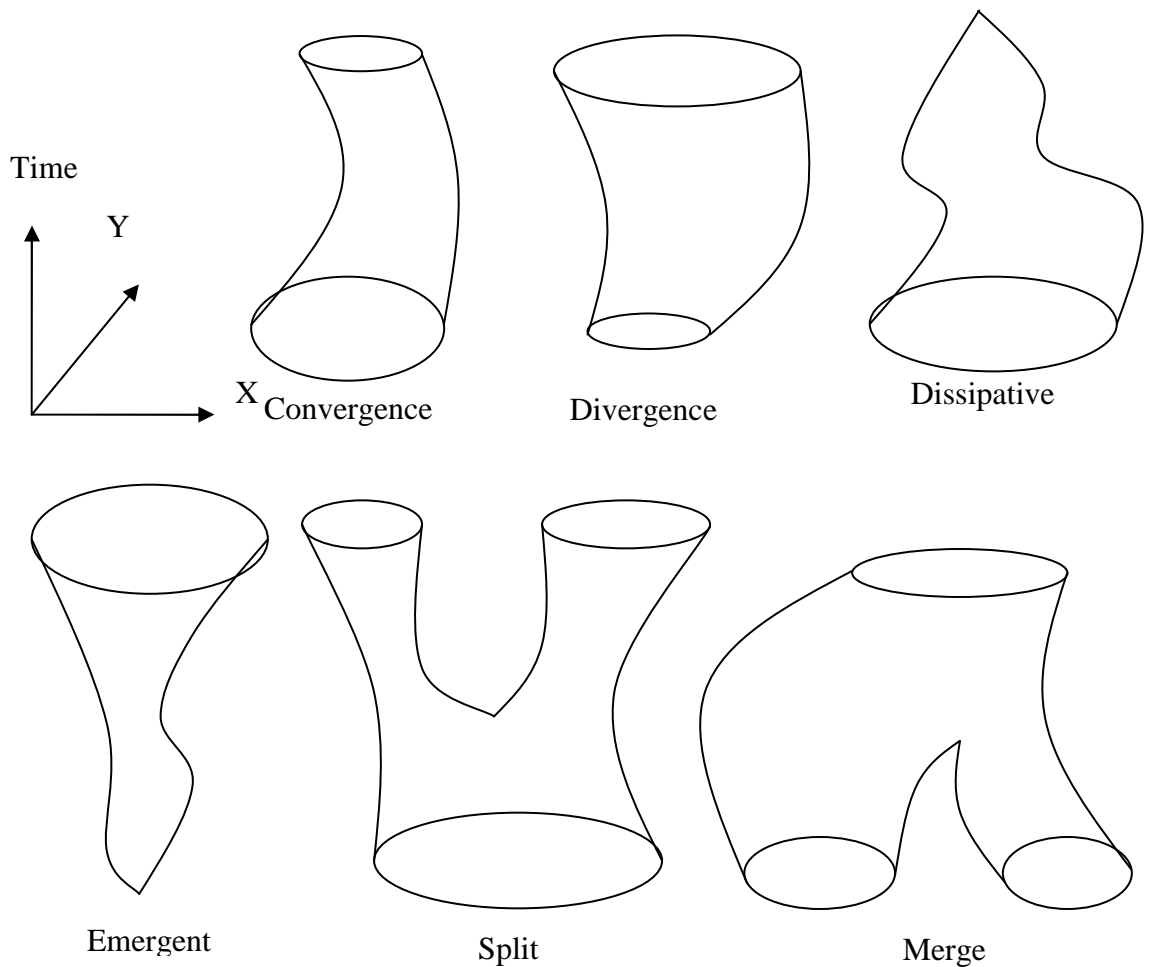


Figure 3.4: A manifold model to represent six basic types of spatiotemporal transitions.

Emergent spatiotemporal objects are those initially do not exist and then appear later in the data. Dissipative spatiotemporal objects exist at the initial time but disappear in a later time. Convergent objects are shrinking versus divergent objects which are expanding. Merging objects join into one object whereas splitting objects form multiple objects.

Regions are defined from chosen isohyets values that represent further divisions of the Koppen climate classification precipitation levels. In particular, isohyets of 213cm/year are used to delineate regions contained within the Koppen tropical wet or monsoonal climate classification. The 213cm/year regions are restricted to the tropics but

tropical changes are of interest as they affect global climate (Selten, Branstator, Dijkstra & Kliphuis, 2004). Precipitation rates lower than 213 cm/year generate only one or two large equatorial regions along with smaller mid latitude regions. The equatorial regions are of little interest because these precipitation regions mostly ran east-west, and, as a result, all divergence and deformation would be in poleward direction. Additionally the equatorial regions do not exhibit any of the six spatiotemporal transitions. The smaller regions of less than 213cm/year precipitation are too discontinuous for the optical flow algorithm to trace. The use of 213 cm/year delineates 20-40 regions in both years of study, allowing for proper comparisons of shifts in precipitation distributions. Regions enclosed by isohyets are created by identifying areas with attribute values greater than or equal to the threshold value of 213 cm/year of precipitation (Figure 3.5).

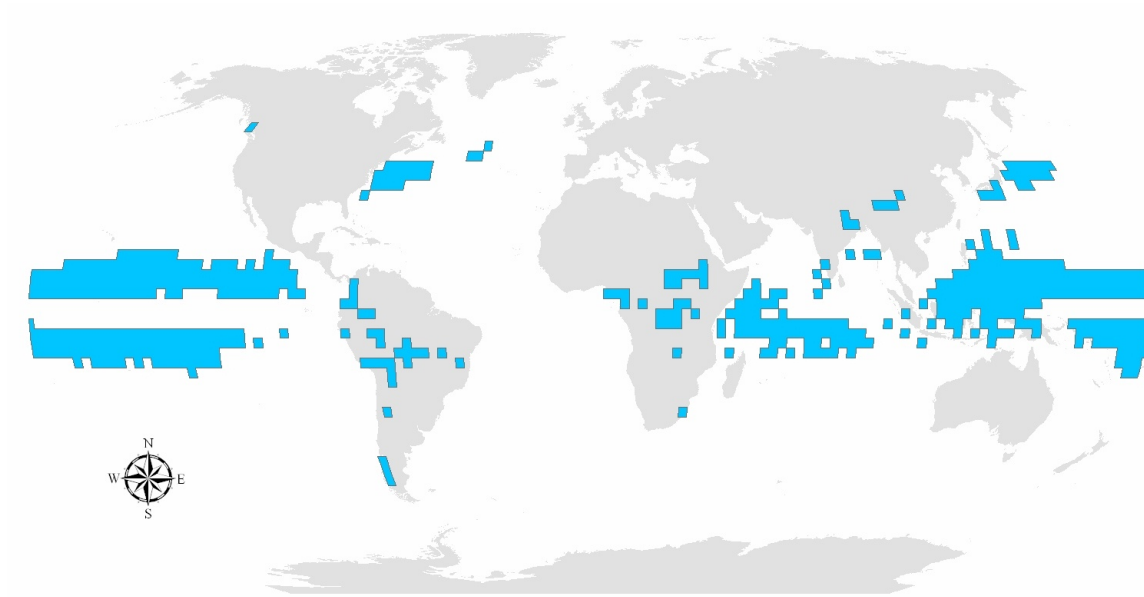


Figure 3.5: CNRM precipitation regions greater than 213 cm/year for 2001

### 3.3.1 Kinematic analysis

Only grid points within regions enclosed by 213cm/year isohyets are retained for the following analysis. The displacement in the x direction is denoted by  $u$  and in the y direction by  $v$ . Displacement vectors are used to calculate kinematic parameters at each grid point:  $\partial u/\partial x$ ,  $\partial u/\partial y$ ,  $\partial v/\partial x$  and  $\partial v/\partial y$  to determine divergence, deformation and rotation at each point location (Equations 3.1-5) where  $\partial/\partial x$  and  $\partial/\partial y$  represent changes in velocity in the x and y direction, respectively. The calculation of  $\partial u/\partial x$ ,  $\partial u/\partial y$ ,  $\partial v/\partial x$  and  $\partial v/\partial y$  is done by applying a kernel of a  $3 \times 3$  window for each differentiation (Table 3.3 shows the  $\partial/\partial x$  kernel).

0	0	0
-0.5	0	0.5
0	0	0

Table 3.3:  $d/dx$  kernel

A different kernel is applied to compute the finite differences differentiation with respect to y (Table 3.4).

0	0.5	0
0	0	0
0	-0.5	0

Table 3.4:  $d/dy$  kernel

The kernels are applied to each grid point to calculate the finite differences in velocity in the x direction and the y direction at the grid's center location for both  $u$  and  $v$ . The kernel results are divided by the distance between the grid locations in the x and y

orientations to get the finite differences that correspond to equations 3.2-5 (Bluestein 1992):

$$\frac{\partial u}{\partial x} = \frac{u(i+1,j)-u(i-1,j)}{x(i+1,j)-x(i-1,j)} \text{ Eq. 3.2}$$

$$\frac{\partial u}{\partial y} = \frac{u(i,j+1)-u(i,j-1)}{y(i,j+1)-y(i,j-1)} \text{ Eq.3.3}$$

$$\frac{\partial v}{\partial x} = \frac{v(i+1,j)-v(i-1,j)}{x(i+1,j)-x(i-1,j)} \text{ Eq.3.4}$$

$$\frac{\partial v}{\partial y} = \frac{v(i,j+1)-v(i,j-1)}{y(i,j+1)-y(i,j-1)} \text{ Eq. 3.5}$$

Even though the precipitation data in 2001 and 2048 cannot be considered temporally continuous, empirical measurements of the pattern transitions determine that changes were gradual from 2001 to 2048. Hence, the concept of fluid kinematics is applied.

The kinematic equations below (Equations 3.6-13) are applicable to any fluid regardless of scale (Warsi 2006). Divergence measures the change in area over time (Eq. 3.6). In a transition, area change is determined by the differences in movement inward and outward in respect to the area. A negative  $\partial u/\partial x$  along the boundary of an object suggests an inward move toward the object, and therefore results in reduction of area in the  $x$  direction. Similarly, a negative  $\partial v/\partial y$  suggests a contraction in  $y$  direction. Hence, positive divergence represents an increase in spacing between different isolines or an increase in the region enclosed by an isoline. Negative divergence, convergence, represents a decrease in spacing between different isolines or a decrease in the region enclosed by an isoline.



$$\text{divergence} = \frac{\partial u}{\partial x} + \frac{\partial v}{\partial y} \text{ Eq. 3.6 (Bluestein 1992)}$$

Rotation represents the angular change counter clockwise (positive) or clockwise (negative) of an isohyet region over time. Larger vertical flow at the east end of a boundary than the west side of that boundary indicates counter clockwise rotation as is a lesser flow on the northern boundary versus the southern boundary.

$$\text{rotation} = \frac{\partial v}{\partial x} - \frac{\partial u}{\partial y} \text{ Eq. 3.7 (Bluestein 1992)}$$

Deformation includes two types of spatial changes in flow patterns : the stretching difference, the change in isoline spacing parallel to the change in position; and shear, the change in isoline spacing perpendicular to the change in position. The  $D_1$  term in Eq. 3.8 describes the orientation of the region's most rapid extent increase with the  $x$  axis and of the most rapid decrease due to stretching with the  $y$  axis. Shear in the  $D_1$  term acts along the  $y = x$  and  $y = -x$  lines.

$$D_1 = \frac{\partial u}{\partial x} - \frac{\partial v}{\partial y} \text{ Eq. 3.8 (Bluestein 1992)}$$

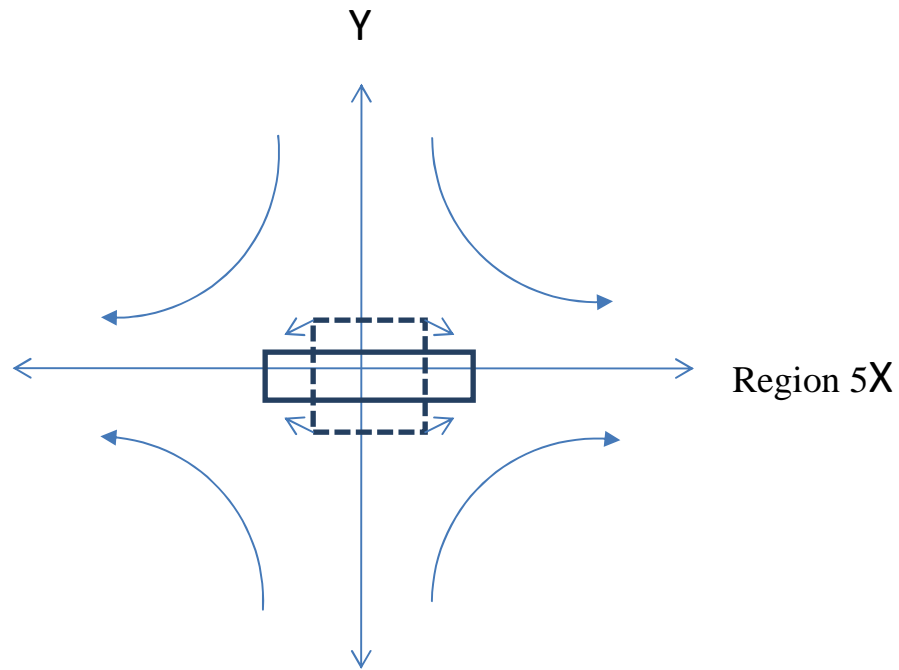


Figure 3.6: D1 stretching deformation along the  $x$  axis

The D2 term describes the orientation of the region's most rapid increase due to stretching along the  $x = y$  line and decrease along the  $y = -x$  line. The D2 term quantifies shear with respect to the  $x$  and  $y$  axis.

$$D_2 = \frac{\partial v}{\partial x} + \frac{\partial u}{\partial y} \text{ Eq. 3.9 (Bluestein 1992)}$$

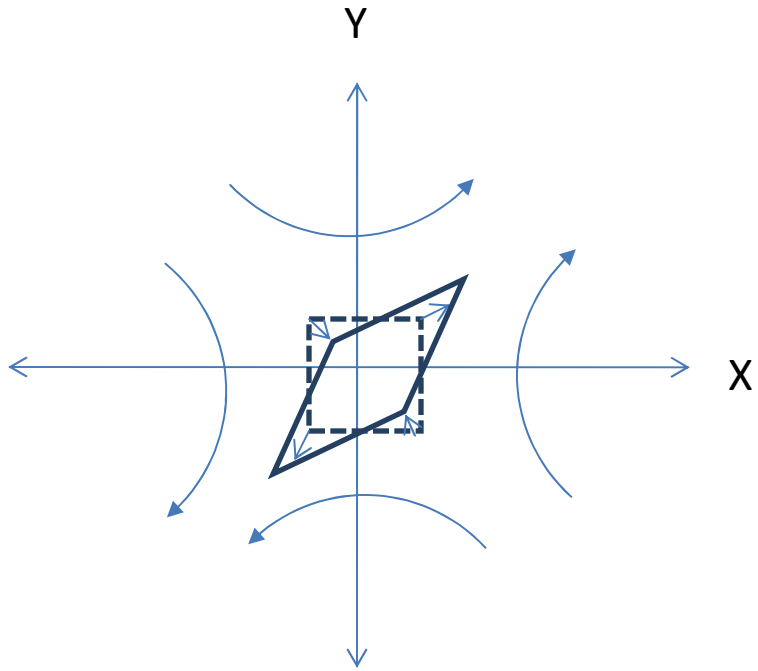


Figure 3.7: D2 stretching deformation along the  $y = x$  axis

Combining these two terms and obtaining a single axis of deformation simplifies the comparison of the deformation orientation and rate among objects. The deformation terms is combined by changing the coordinate system so that there is only a single non zero term. The deformation angle ( $\theta_D$ ) is the angle at which the coordinate system must be rotated counter clockwise so that the new coordinate system only retains a single non zero deformation term (ie.  $D_0 = 0$  leaving the  $D_1$  measure only). The deformation terms for the new coordinate system are:

$$D'_1 = \frac{\partial u'}{\partial x'} - \frac{\partial v'}{\partial y'} \quad \text{Eq. 3.10 (Bluestein 1992)}$$

$$D'_2 = \frac{\partial v'}{\partial x'} + \frac{\partial u'}{\partial y'} \quad \text{Eq. 3.11 (Bluestein 1992)}$$

The coordinate system rotation angle is determined by setting  $\frac{\partial v'}{\partial x'} = -\frac{\partial u'}{\partial y'}$  in the new coordinate system so that the  $D'_2$  term  $D'_2 = 0$  is eliminated. The remaining term  $D'_1$  now completely describes the deformation of the boundary under the influence of the displacement field whereas before  $D_1$  and  $D_2$  were both required.

$$\text{deformation angle} = \theta_D = \frac{1}{2} \tan^{-1} \frac{D_2}{D_1} \quad \dots \text{Eq. 3.12}$$

The resultant deformation  $D'_1$  summarizes the difference between the expansion in the  $x'$  direction and in the  $y'$  direction due to stretching and the  $x = y$  line and  $y = -x$  line due to shear.

$$\text{resultant deformation} = D'_1 = \frac{D_2}{\sin 2\theta_D} \quad \dots \text{Eq. 3.13}$$

The axis with the larger rate of increase is the axis of expansion, while the axis with the lesser rate is the axis of contraction (Figure 3.8).

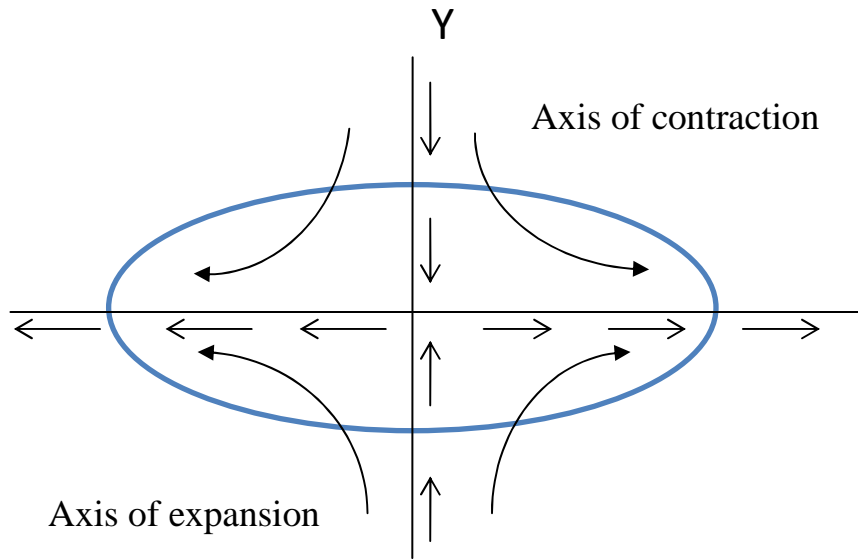


Figure 3.8: Deformation

### 3.3.2 *Region transition tracking*

The virtual particle hypothesis associates a region enclosed by an isohyets  $P_i$  to a region of the same isohyet value in the time instance. Displacement vectors between the two region's boundaries (Figures 3.2 and 3.3) represent precipitation transitions over space and time. The displacement vectors are used to associate isohyet threshold defined regions from one time to another (Figure 3.9).

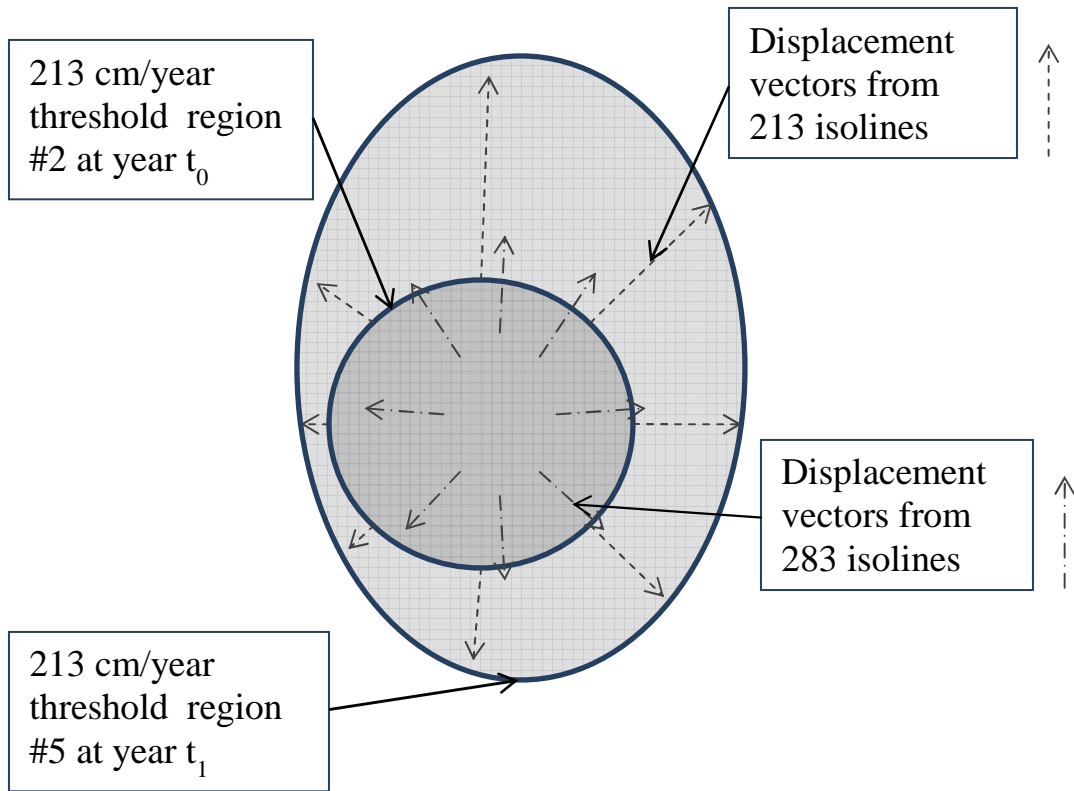


Figure 3.9: Determining region associations between time instances

Figure 3.9 shows the mapping of region 2 to region 5. All time  $T_0$  grid points with a displacement origin are associated with the time  $T_1$  grid point at the end of the displacement. Grid locations within regions bounded by the threshold isohyets are given unique gridded region identifiers for both 2001 (Figure 3.10) and 2048 data.

In Figure 3.10 there are three regions of varying sizes with ID 21, 28 and 35.

		21					
	21	21	21				
	21	21	21				
	21	21	21				
		21					
					28	28	
		35	35		28	28	
	35	35	35	35			
	35	35	35	35	35		
	35	35	35	35	35		
		35	35	35			

Figure 3.10: Gridded Region Identifiers

Regions at time  $T_1$  that spatially overlap regions at time  $T_0$  are also associated with the  $T_0$  regions. The associations are summarized in a table of time region IDs for  $T_0$  and the  $T_1$  regions associated by following displacement vectors (Table 3.5). Each row in the table is associated with a region ID in year 2001 and a region ID in year 2048. The example table contains a merge as several different region IDs from year 2001 are associated with a single year 2048 region (9 regions [28,35,49, 56, 63, 70, 77, 84 and 98] in the grey 2001 table cells merge into a single 2048 cell with the ID of 24).

region ids 2001 ( $T_0$ ) 213cm/year	region ids 2048 ( $T_1$ ) 213cm/year
21	32
28	24
35	24
42	64
49	24
56	24
63	24

70	24
77	24
84	24
91	80
98	24
105	96

Table 3.5: Mapping regions between time steps for CNRM.

The regions involved in a merge are visually separated using vertical displacement in Figure 3.11. The single lower region is from 2048 while the multiple semi-transparent upper level regions are from 2001.

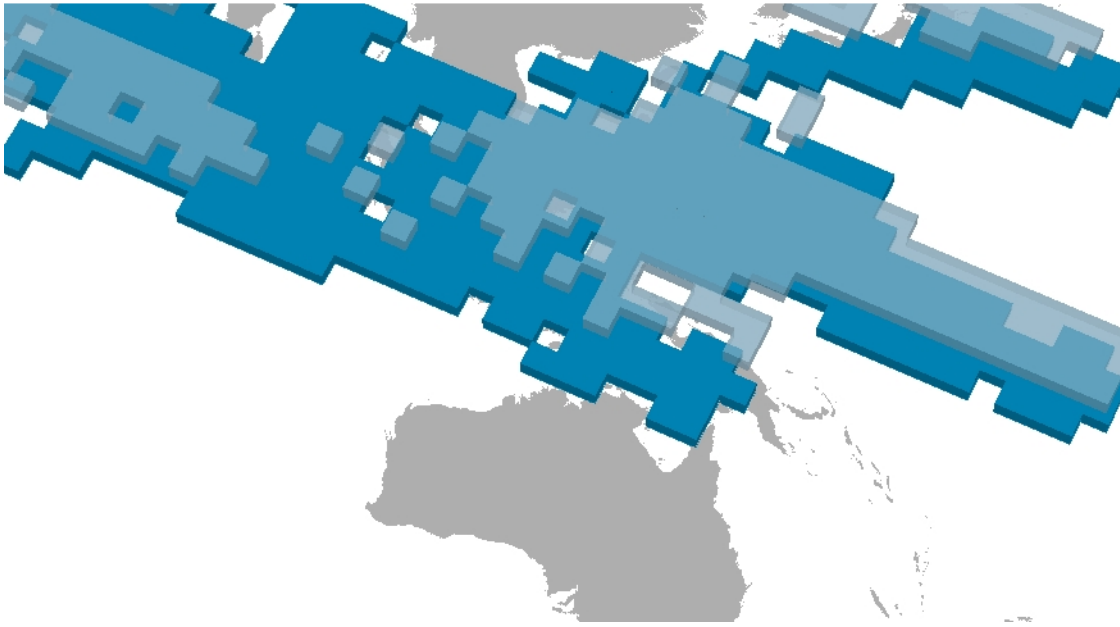


Figure 3.11: Merge from CNRM CM3 213 cm/year regions.

After the calculations, each grid point within regions enclosed by 213 cm/year isohyets are assigned a region ID, divergence value, rotation value, resultant deformation  $D'_1$ , and the deformation angle  $\theta_D$  (Table 3.6).



FID	Shape	VALUE	SUM_F_AREA	vorticobj	divergobj	deform_ang	deform_pri
1	Polygon	14	210474641678	2.79722	-10.3926	-0.610692	12.8152
5	Polygon	42	303645330016	3.03235	-4.43075	1.31644	-9.17179
6	Polygon	49	230971706954	14.9402	27.063101	-0.883933	-32.1581
8	Polygon	63	155491267327	83.570503	70.074097	-0.653175	-66.630699
14	Polygon	105	316108606580	17.2857	-18.475401	-0.027835	12.7012
18	Polygon	133	9442722756640	48.2953	23.5177	-0.60063	-31.692499
20	Polygon	147	78895005796.9	49.388901	4.45629	-0.648897	-32.236099
24	Polygon	175	78738331361	57.423	64.971397	-0.688072	-55.342701
28	Polygon	203	78527444356	35.223598	-43.380199	0.966261	-51.030102
29	Polygon	210	78527444356	31.415501	-20.257799	0.909806	-18.234301
31	Polygon	224	76082636957.1	22.756599	-3.12602	1.05944	-150.146
32	Polygon	231	76082636957.2	45.472	-8.49036	0.174714	-23.957399
33	Polygon	238	207009538234	36.688999	21.4611	-0.544093	-26.355301

Table 3.6: Attribute table for areas of precipitation objects

Because the GCM output products are in latitude and longitude units (NCAR-CCSM3 at  $1.4^{\circ} \times 1.4^{\circ}$  resolution, and CNRM-CM3 at  $2.8^{\circ} \times 2.8^{\circ}$  resolution), the metric extent of these grid cells is not transformed directly to square cells used in GIS data. A Thiessen polygon routine is used to construct two polygon layers in meters: one is based on CCSM3 grid points and the other, CM3 grid points. Both layers are in Robinson projection to provide a balance between areal distortion and shape distortion at the global scale. Because CCSM3 grid points are spaced in a lattice structure, Thiessen polygon routine creates matrices of rectangles that centered at each CCSM3 grid point. The same outcome is applied to the Thiessen polygon layers based on CNRM-CM3 grid points. As shown later in the results, most regions of analysis are in low or mid latitudes and, therefore, are less sensitive to areal or shape distortions in Robinson projection than high latitude area. For each region enclosed by 213 cm/year isohyets, values of kinematic parameters are weighted by the size of respective Thiessen polygons, summed, and then normalized by the area of each region.

### **3.4 Results and Discussion**

The use of kinematics to interpret precipitation patterns enables the comparison of precipitation distribution patterns (Austin & Houze, 1972). Two levels of kinematic properties are examined; one the internal kinematics at grid points within each region and, the other is external kinematics. Internal kinematics measures the internal composition and structure of movement inside a region. In the case of precipitation, internal kinematics characterizes transitions of precipitation at each grid point within a region. External kinematics are attributed to a region enclosed by the threshold isohyets as a whole and characterizes how the region evolved over time. A region might have active internal kinematics with variable precipitation within a region, but externally, the region might remain stationary without significant shifts in location or shape. Both internal kinematics and external kinematics support the assessment of precipitation patterns in space and time and quantification of differences in changes of precipitation patterns from 2001 to 2048 projected by NCAR CCSM3 and CNRM-CM3.

The kinematics of precipitation fields may imply complex interactions between contributing phenomena. Tropical precipitation is a function of water vapor fields, general circulation, orographic lifting and sea surface temperature (Cavazos, 1998). Tropical easterlies transport moisture in the tropics along with a component towards the equator (Chen, 1985). Water transport has a uniform net westward component except for in the tropical and subtropical Indian Ocean regions (Rosen, Salstein, & Peixoto, 1980). The rate of transport increases from the equatorial rate towards a peak at the 25N latitude (Rosen *et al.*, 1980). Mean precipitable water in general decreases from the equator

poleward with the Southern Hemisphere acting as a moisture and latent heat source for the Northern Hemisphere (Rosen, Salstein, & Peixoto, 1979). Tropical rainbands are usually located above regions of warm sea surface temperatures (Manabe, Hahn & Holloway, 1974). The wind field and the water vapor transport field show rotation, convergence, divergence and deformation. The complex interaction of vapor transport, circulation, orographic lifting, and sea surface temperatures, each with unique kinematics, influence precipitation patterns.

Climate change pushes circulation patterns poleward as the Hadley cells increase in size (Mitas & Clement, 2005). Hadley cell shifts affect the Sahel rainfall which is dependent on the northward penetration of the equatorial airmass during the summer (Landsberg, 1975). A similar dependency exists for Antiplano rainfall and the Bolivian high in South America (Lenters & Cook, 1999). The changes in convergence zones in the tropics are associated with a decrease in the frequency of strong updrafts and an increase in weak updrafts (Vecchi & Soden, 2007).

The CNRM CM3 GCM model output includes area encompassed by 213 cm/year isohyets expands from  $42.41 \times 10^6 \text{ km}^2$  in 2001 to  $52.52 \times 10^6 \text{ km}^2$  in 2048 with most of the increase occurring in the Indian Ocean (Figure 3.12).

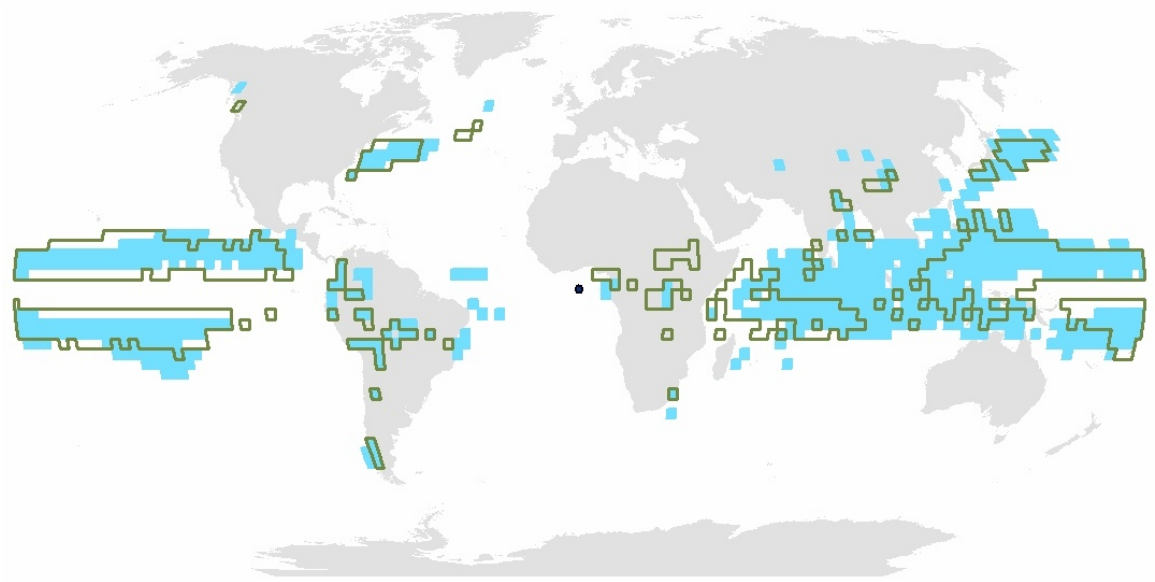


Figure 3.12: CNRM precipitation regions greater than 213 cm/year with 2001 outlined in green and 2048 in solid blue

Regions enclosed by 213 cm/year isohyets from the NCAR CCSM3 products expand from  $39.43 \times 10^6 \text{ km}^2$  in 2001 to  $41.48 \times 10^6 \text{ km}^2$  in 2048 (Figure 3.13) with most of the increase occurring in the Indian Ocean similarly to the CNRM output..

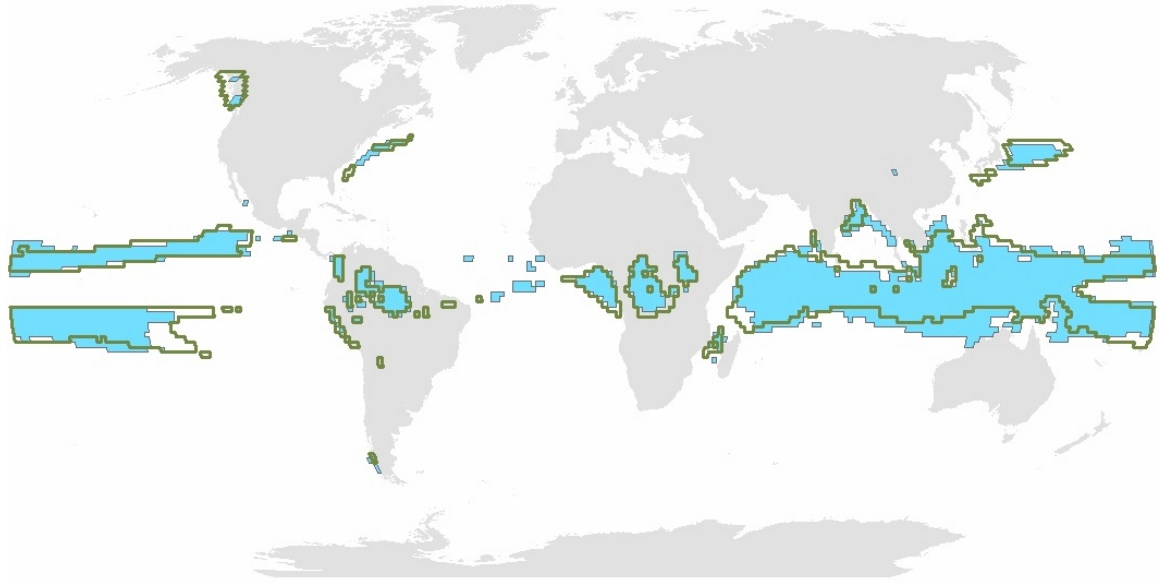


Figure 3.13: NCAR precipitation regions greater than 213 cm/year with 2001 outlined in green and 2048 in solid blue

Figures 3.14-17 illustrates regions indicative of changes in precipitation patterns based on CNRM and NCAR data, respectively. The CNRM model has 16 regions that were deforming with an east-west expansion axis (Figure 3.14).

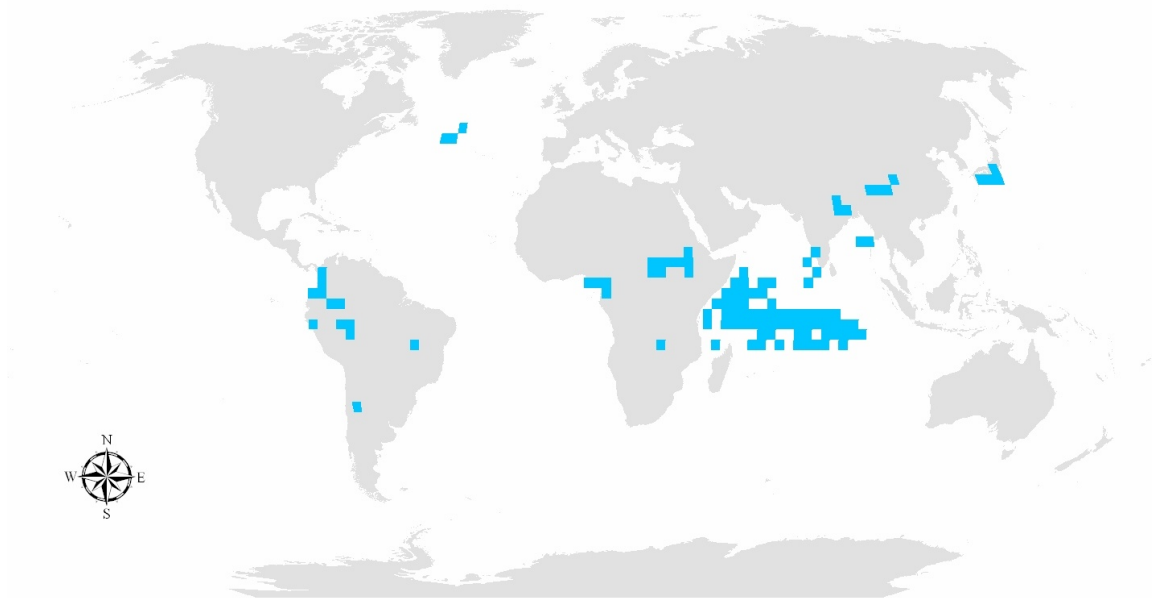


Figure 3.14: CNRM precipitation regions greater than 213 cm/year for 2001 with an east west expansion orientation

An east-west expansion is a possible result of the intensification of regional precipitation driven by increased latitudinal moisture transport that expands a SST or orographic triggered precipitation region. An ITCZ shift likely leads to a north south expansion of a precipitation region. A single large region of size  $4.89 \times 10^6 \text{ km}^2$  over the Indian Ocean and several small regions exhibit east west expansion are displayed in the CNRM output. The CNRM shows a marked increase in the 213 cm/year precipitation extent for the Indian Ocean and the Western Pacific Equatorial Region. The second and third largest regions of east-west expansion are in Africa and in South America for the CNRM output. The NCAR model has 15 regions that deform along an east-west axis of expansion (Figure 3.15).

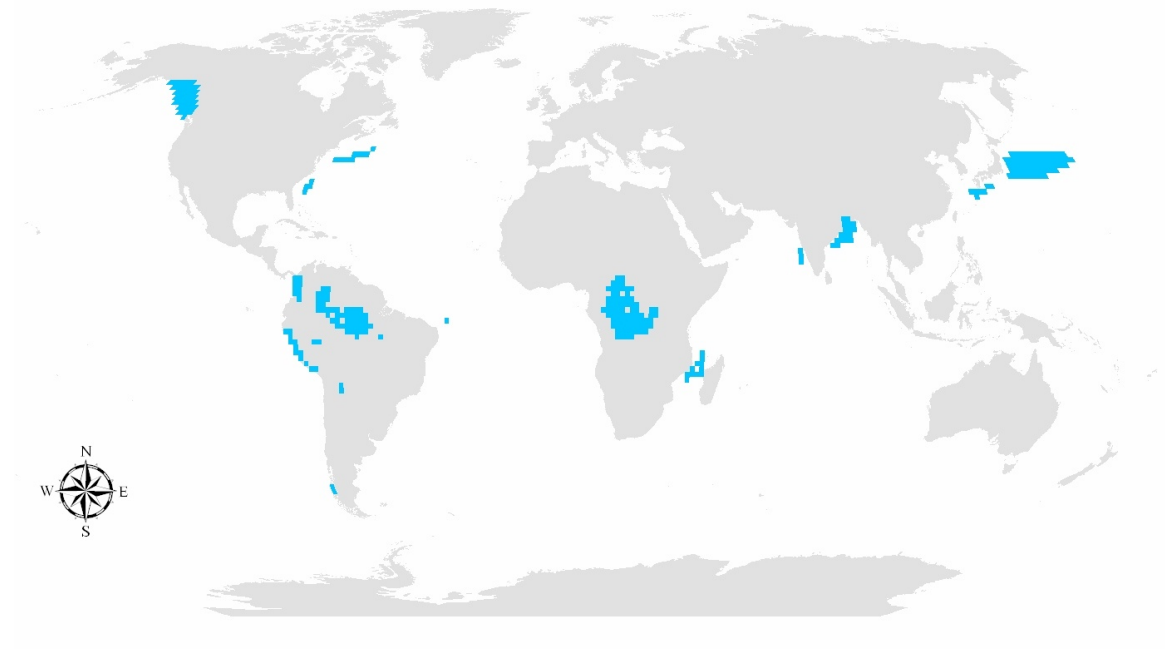


Figure 3.15: NCAR precipitation regions greater than 213 cm/year for 2001 expanding latitudinally (east-west)

The largest region with east-west expansion in the NCAR model is in Africa with a size of  $1.49 \times 10^6 \text{ km}^2$ . The second largest region with east-west expansion is east of Japan in the Pacific, and the third, in South America. The two regions with major non-seasonal water vapor content are northern South America and equatorial Africa (Chen, 1985). The study shows that both CCSM and CNRM model outputs attribute an east-west expansion, which is a possible result of increases in moisture transport. The CNRM Western Pacific Region may be an intensification of a seasonal high water vapor content region (Chen, 1985).

The rotation of annual precipitation regions with large east-west extents are a possible result of zonal mean flow or moisture transport. The zonal flow is easterly at the equator and changing to a westerly at approximately  $30^\circ \text{ N}$  and  $\text{S}$  (Marshall & Plumb,

2008). The westerlies strengthen until 50° N and S (Marshall & Plumb, 2008). The study measures rotation by averaging the shear within the boundaries of the region.

Precipitation regions under the influence of the zonal mean flow would rotate clockwise between 0° and 50° N and counter-clockwise between 0° and 50° S.

The moisture flow in the region in between 50°S and 50°N is also easterly but with increasing magnitude to 25°N or S (Chen, 1985) and consequently has a shear and rotation opposite than that of the zonal mean wind. Increased water vapor transport leads to the expansion of precipitation regions. Regions exhibit the zonal flow rotation direction resulting from zonal shear or opposite direction due to water vapor transport.

The CNRM model had 13 regions with counter clockwise rotation (Figure 3.16).

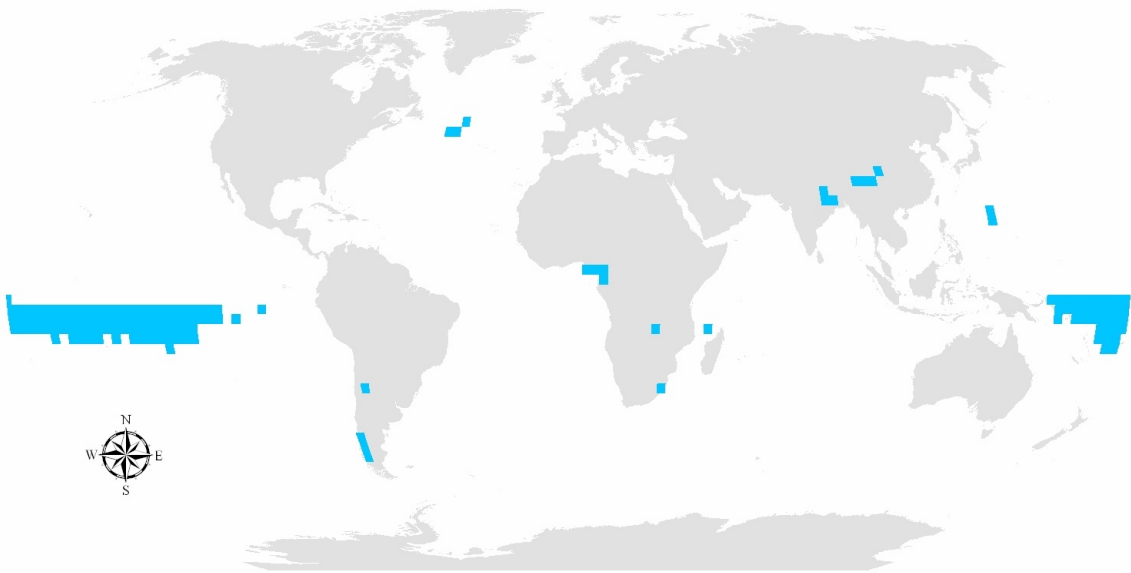


Figure 3.16: CNRM precipitation regions greater than 213 cm/year for 2001 with counter clockwise rotation

Regions of limited east west extent are possibly due to the influences of meridional flow and local annual flow. The CNRM regions with counter clockwise



rotation are mostly in the southern hemisphere, as mean zonal wind shear would indicate, with a large region in the Western Pacific.

There is a region in the western Atlantic with counter clockwise rotation but the center of this location is far enough north for its rotation to be explained by zonal wind influences. There are four regions in the northern hemisphere: one in the western Pacific and three continental regions, with counter clockwise rotation hinting at potential changes in moisture transport. There are several regions in South America and Southern Africa which exhibit counter clockwise rotation in the same direction as Southern Hemisphere zonal wind shear. The NCAR model has fifteen regions with counter clockwise rotation in the Northern Hemisphere at less than 40° N latitude which is the same direction as the vapor transport field (Figure 3.17).

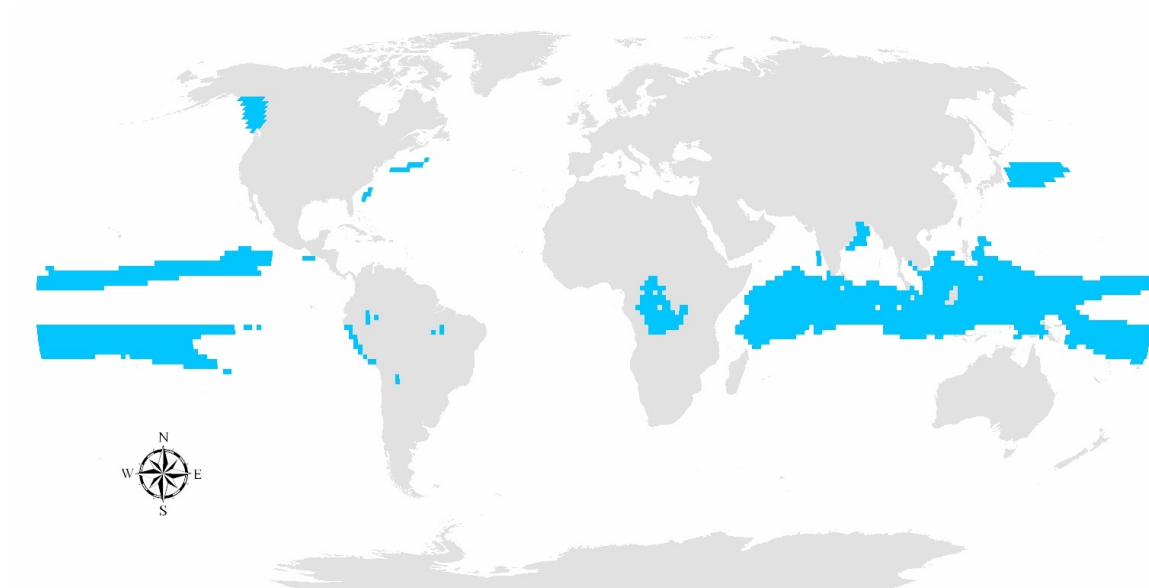


Figure 3.17: NCAR precipitation regions greater than 213 cm/year for 2001 with counter clockwise rotation

These counter clockwise rotating regions include two in the Atlantic off the east coast of the North American Continent at 41° and 36° N, two regions in close proximity

to the Indian Peninsula and two regions in the Pacific east of Asia at approximately 40° N. There is a region shared with the CNRM model in the southern Pacific of clockwise rotation. This rotation is the result of the zonal mean flow shear which is common to both models.

The CNRM CM3 output for the 213 cm/yr isohyets shows that eleven of 34 regions show expansion (Figure 3.18) with the largest being in the southern equatorial Pacific.

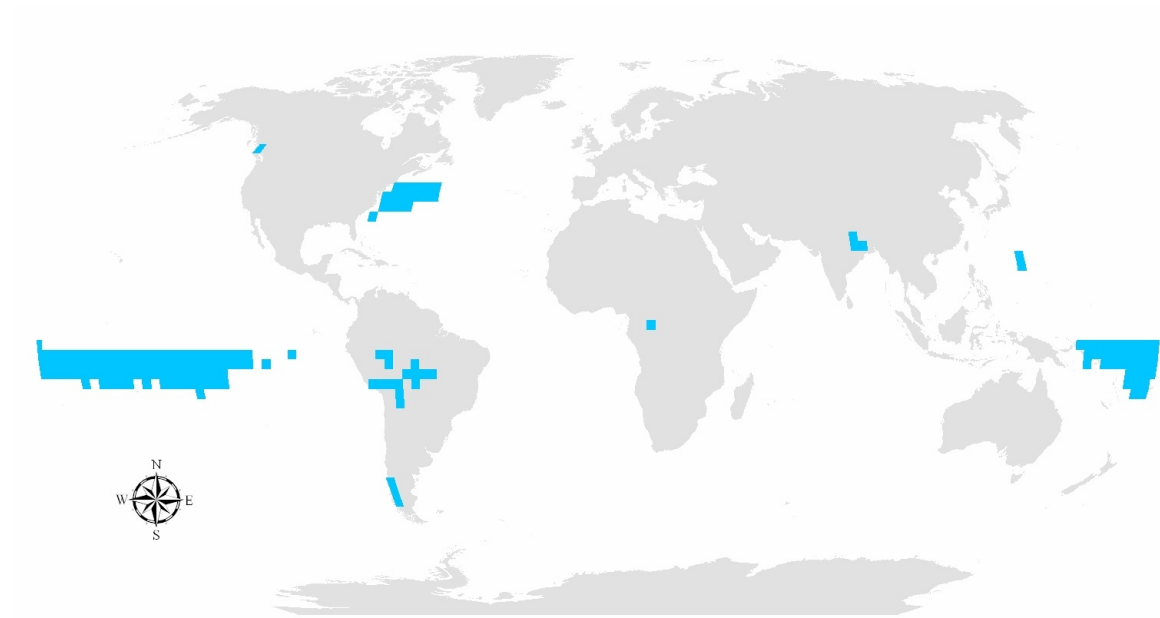


Figure 3.18: CNRM precipitation regions greater than 213 cm/year for 2001 with positive divergence

The NCAR model has very few regions of divergence with the largest being east of Japan in the Pacific (Figure 3.19).

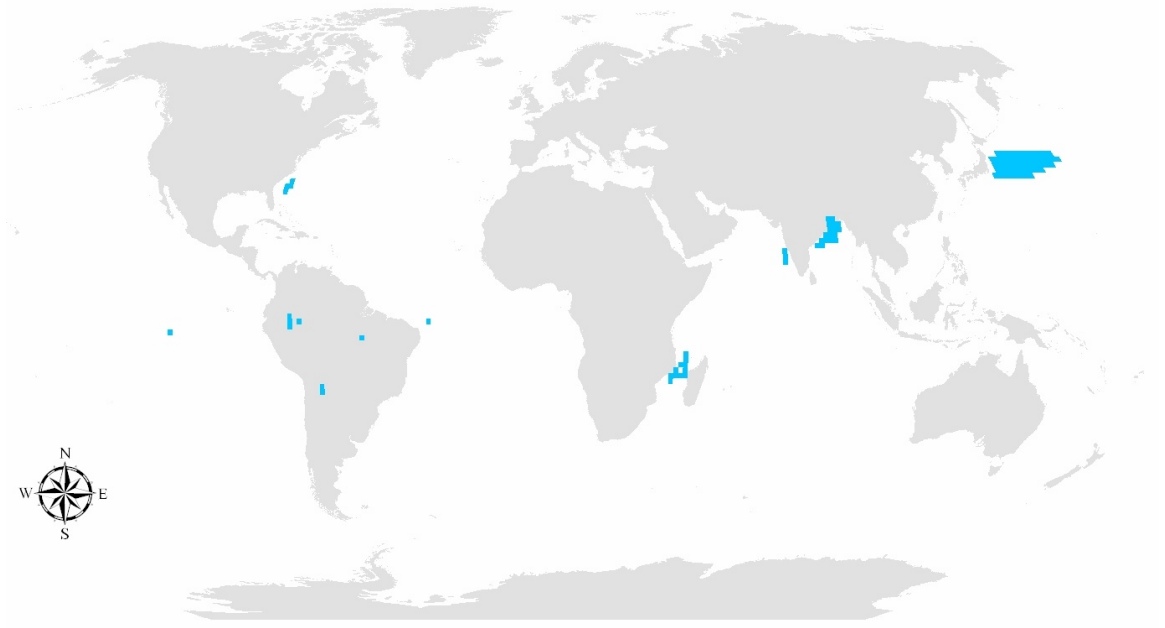


Figure 3.19: NCAR precipitation regions greater than 213 cm/year for 2001 with positive divergence

Though both GCMs show area expansion of regions enclosed by the 213 cm/year isohyets, few regions show divergence. The isohyets flow displacements are generated from twenty different isohyets, not just the isohyets for 213 cm/year. The region of the Indian Ocean that fills in for the 213 cm/year isohyet in the CNRM dataset is diverging as shown by (Figure 3.20) divergence in the north but convergence in the south.

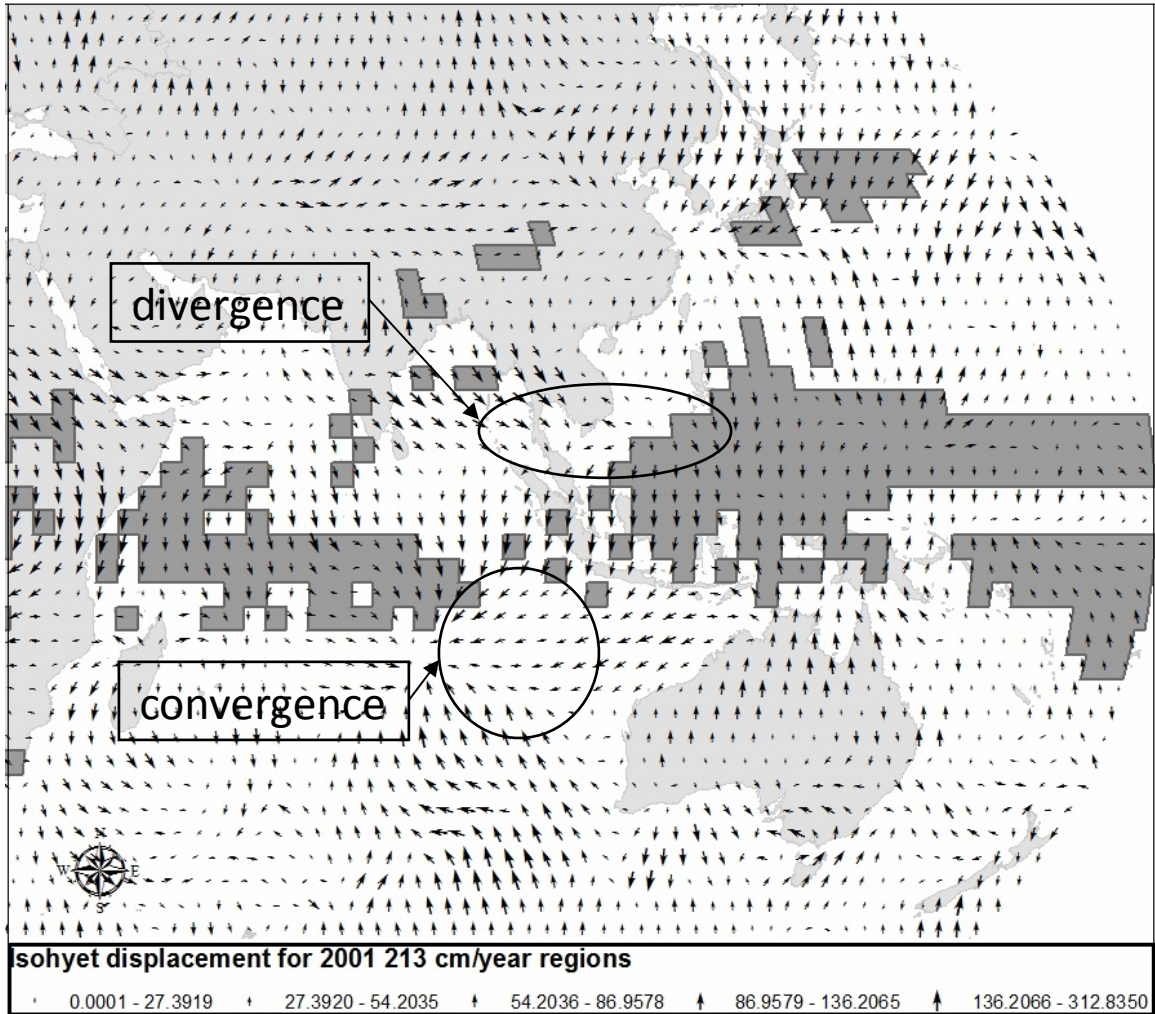


Figure 3.20: External divergence and convergence

The lack of divergence in regions that expand hints that drivers external to the 213 cm/year threshold defined regions may be responsible for the extent changes. The most discernable difference between the two datasets is the high growth rate of 20% for the CNRM 213 region (Figure 3.12) versus 5% for the NCAR 213 cm/year regions (Figure 3.13). The difference is a possible result of differences in the forecasts of SST changes between the two models. Compared to CCSM3, the CNRM shows a larger SST increase in the Indian Ocean which results in higher precipitation increase (Vecchi and Soden 2007). The flow field external to isohyet regions in the CNRM output for the Indian

Ocean mapped the increase in extent and the joining of twelve regions into a single large one (Figure 3.12). The join was recognized as the region mapping table had multiple region IDs in the 2001 column that shared a single region ID in the 2048 column (Table 3.5). Regions involved in a split are also mapped using the region mapping table as well (Figure 3.21).

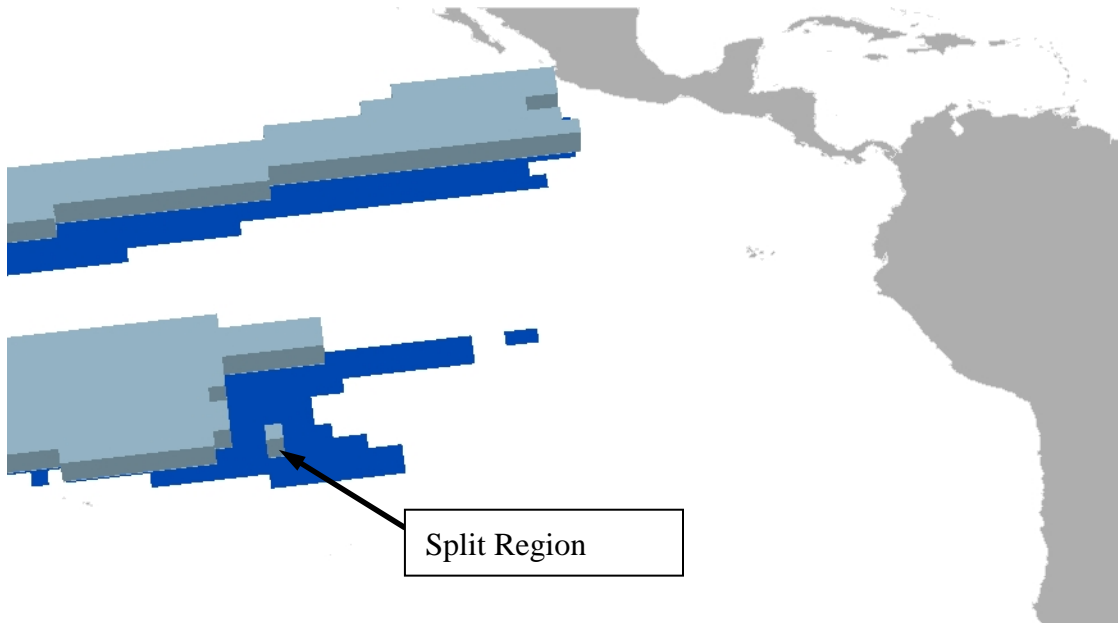


Figure 3.21: Region from 2048 with split into three parts from one. Lower flat level is from 2001.

In addition, regions without an entry in the region association table are either dissipating or emerging. The region association table only contains regions that are associated across two time instances (i.e. 2001 and 2048). Regions in 2001 that are not in the association table are dissipative and regions in 2048 not in the table are emergent. Emerging and dissipating regions are mapped as shown in Figure 3.22 and Figure 3.23. The NCAR emerging dissipating map has emergent locations in the Atlantic as well (Figure 3.23).

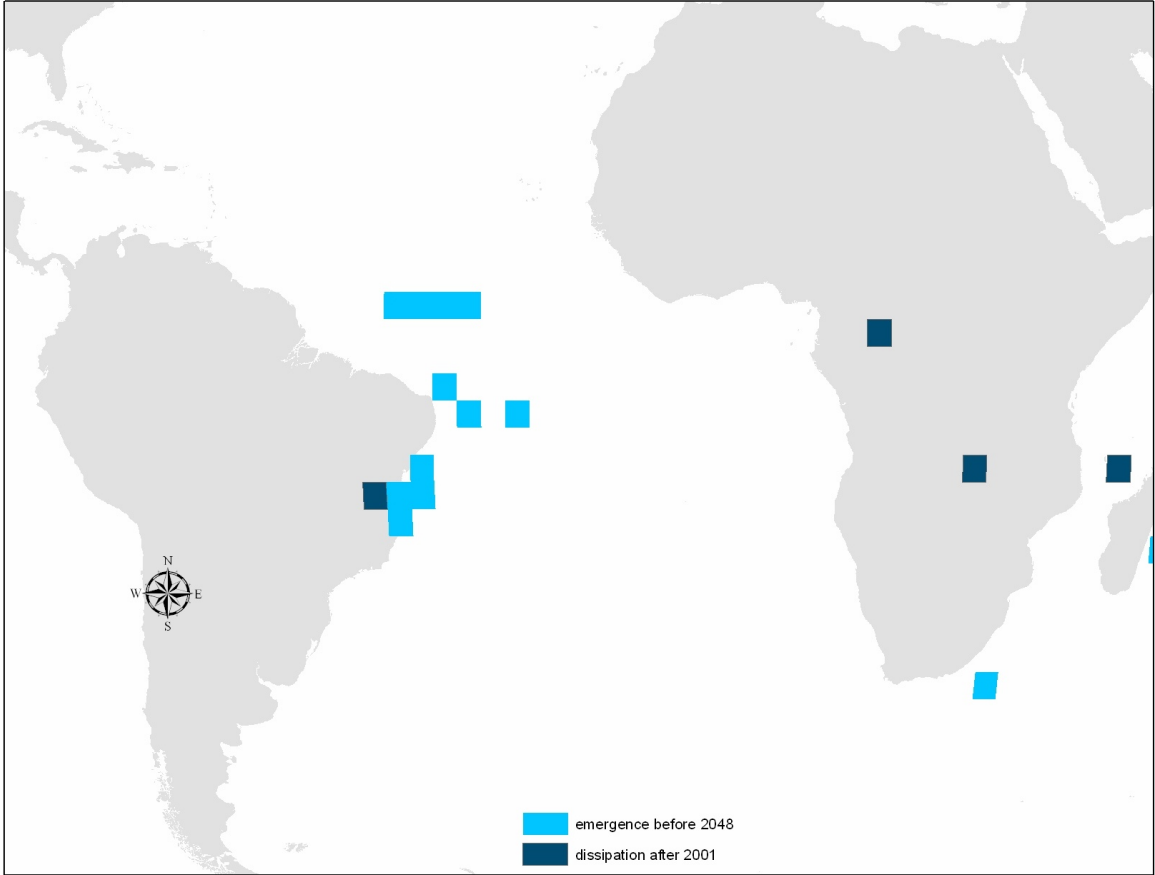


Figure 3.22: CNRM precipitation regions greater than 213 cm/year that emerged or dissipated during the interval 2001-2048

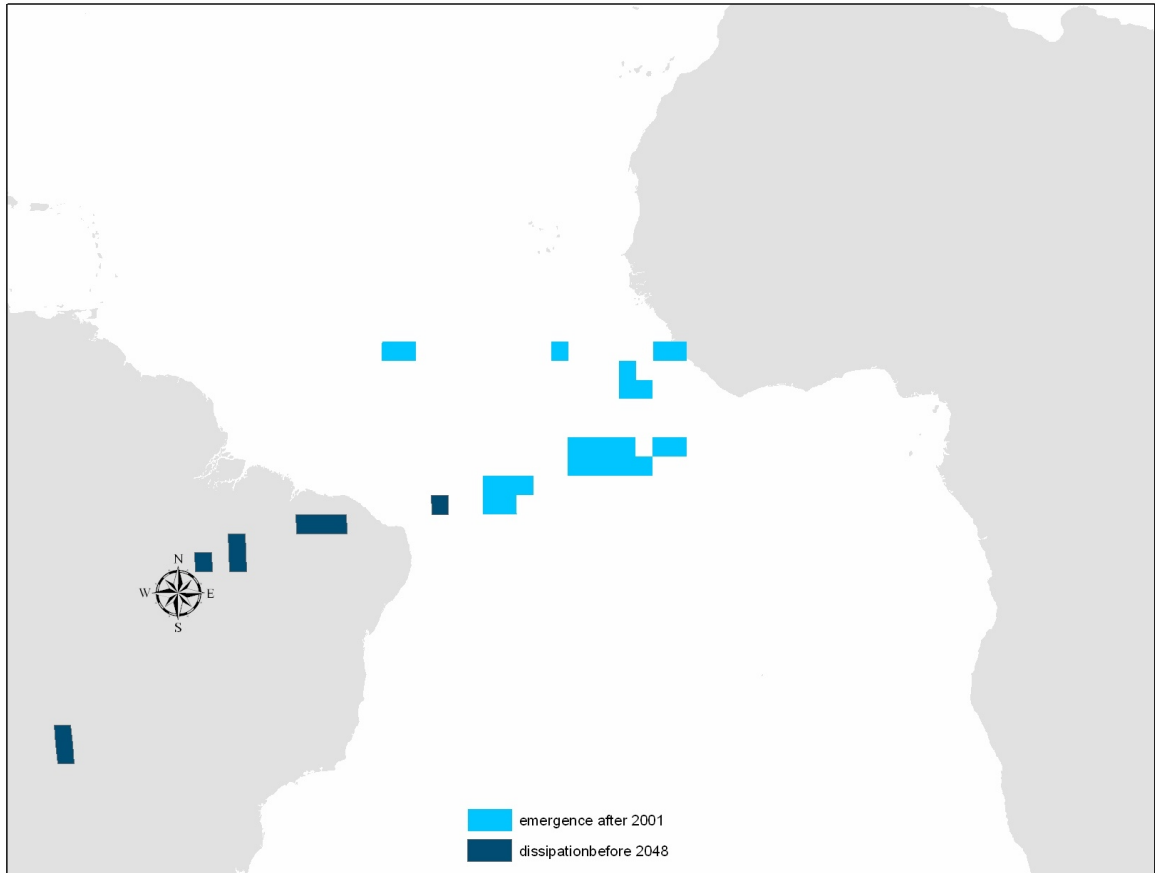


Figure 3.23: NCAR precipitation regions greater than 213 cm/year that emerged or dissipated during the interval 2001-2048

The paired emergent and dissipative regions hint at the amount of variability that exists in the precipitation processes resulting from the driving phenomena. The displacement calculation algorithm proceeds to the next location without determining a displacement value when the displacement line passes through a minima or maxima before locating the position of the isoline in the next time instance.

### 3.5 *Conclusion and Future Work*

The kinematics-based method presented here attempted to measure directly gradual changes in spatiotemporal patterns. Under the assumption that changes in precipitation patterns of regions receiving 213 cm/year of rainfall are gradual from 2001 to 2048, the

research applied the proposed method to evaluate the transition of precipitation patterns projected by NCAR CCSM3 and CNRM-CM3 for Scenario A2 defined by IPCC. Central to the proposed method is the concept of kinematics that characterizes movement patterns. In the case study, isohyets are tracked to determine shifts in isohyets from 2001 to 2048. The shifts are measured by displacement vectors measured along the isohyets and then spatially interpolated to grid points not on a isohyet. Furthermore, the 213 cm/year isohyets are used to form surrogate objects. Kinematic parameters (divergence, rotation, and deformation) are calculated internally at grid points within each identified region and summed to the region as the overall kinematic properties for the region.

Both internal and external kinematic properties are then used to assess spatiotemporal patterns and compare outputs from the two GCM products. Spatial patterns of divergence and rotation are displayed (Figure 3.14, Figure 3.15, Figure 3.16, Figure 3.17) in order to identify patterns of precipitation change between the years 2001 and 2048. The axes of expansion, rotation and divergence provide hints as to the potential drivers for the precipitation extent evolution. The comparison of the CNRM and NCAR output provide indications of the generality of potential drivers of common regions.

Thirteen regions extracted from CNRM 2001 dataset merge into a single region (Figure 3.12) in 2048 as a result of model precipitation intensification in the Indian Ocean. Only three of the thirteen regions have positive divergence. The CNRM region over the Indian Ocean has a negative divergence value, yet the area of greatest expansion was the Indian Ocean in the CNRM model. The growth of precipitation regions is driven by conditions outside the 2001 regions. The major increase in isohyet extent came from outside the 213 cm/year isopleths that existed in 2001 (Figure 3.5).



Long term circulation patterns are likely the determining factor for the precipitation patterns (Van Ulden & Oldenborgh, 2006). Further research comparing general circulation patterns and isohyets displacement patterns may reveal where there are significant differences. The differences may help determine drivers other than general circulation to changes in precipitation patterns.

Future research should include use cases with lower threshold values to determine if the kinematics-based methodology can identify, represent, and analyze spatiotemporal patterns and pattern transitions for temporally average data. The 213 cm/year isohyets result when large numbers of precipitation events affect a location during a single year. Lower thresholds will require temporal averaging to smooth the rapid variation in year to year rainfall.

## References

- Abraham, T., & Roddick, J. F. (1998). Opportunities for Knowledge Discovery in Spatio-Temporal Information Systems. *Australasian Journal of Information Systems*, 5(2), 3-12.
- Austin, P. M., & Houze, R. A. (1972). Analysis of the Structure of Precipitation Patterns in New England. *Journal of Applied Meteorology*, 11, 926-935.
- Bluestein, H. (1992). *Synoptic-dynamic meteorology in midlatitudes: Volume 1, principles of kinematics and dynamics*. New York, NY (United States), Oxford Univ. Press
- Carleton, A. M. (1999). Methodology in Meteorology. *Annals of the Association of American Geographers*, 89(4), 713-735.
- Cavazos, T. (1998) Large-Scale Circulation Anomalies Conducive to Extreme Precipitation Events and Derivation of Daily Rainfall in Northeastern Mexico and Southeastern Texas. *Journal of Climate*, 12, 1506-1523.
- Chen, M.-S., Han, J., & Yu, P. S. (1996). Data Mining: An Overview from Database Perspective. *IEEE Transactions on Knowledge and Data Engineering*, 8, December, 866-883.
- Chen, T. C. (1985) Global Water Vapor flux and Maintenance during FGGE. *Monthly Weather Review*. 113, 1801-1819,
- Chrisman, N. (1998). Beyond the snapshot: changing the approach to change, error and process. In *Spatial and Temporal Reasoning in Geographic Information Systems* (pp 85-93), edited by M. Egenhofer and R. Golledge, Spatial Information Systems (New York, Oxford University Press).
- Claramunt, C., Parent, C., & Thériault, M. (1997). Design patterns for spatio-temporal processes, in S. Spaccapietra and F. Maryanski (Eds.) *Searching for Semantics: Data Mining, Reverse Engineering* ( pp. 415-428).
- Collins, W. D., Bitz, C. M., Blackmon, M. I., Bonan, G. B., Bretherton, C. S., Carton, J. A., Chang, P., Doney, S. C., Hack, J. J., Henderson, T. B., Kiehl, J. T., Large, W. G., McKenna, D. S., Santer, B. D., & Smith, R. D. (2005). The Community Climate System Model: CCSM3, *Journal of Climate*, 19, 2122-2143.
- Fayyad, U. M., Smyth, P., Weir, N., & Djorgovski, S. (1995). Automated Analysis and Exploration of Image Databases: Results, Progress and Challenges. *Journal of Intelligent Information Systems*, 4, 7-25.

- Gold, C. M. (1989): Surface interpolation, spatial adjacency and G.I.S. in: J. Raper (ed.): *Three Dimensional Applications in Geographical Information Systems*. London: Taylor and Francis Ltd. 1989, pp. 2 1-35.
- Landsberg, H. E. (1975). Sahel Drought: Change of Climate or Part of Climate? *Arch. Archiv für Meteorologie, Geophysik und Bioklimatologie*, 23, 193-200
- Lenters, J. D., & Cook, K. H. (1999). Summertime Precipitation Variability over South America: Role of the Large-Scale Circulation. *Monthly Weather Review*, 127, 409-431.
- Manabe, S., Hahn, D. G., & Holloway, J. R. Jr. (1974). The Seasonal Variation of the Tropical Circulation as Simulated by a Global Model of the Atmosphere. *Journal of Atmospheric Sciences*, 31, 43-83.
- Marshall, J., & Plumb, R. A. (2008). *Atmosphere, Ocean and Climate Dynamics, Volume 93: An Introductory Text*. Burlington, MA USA. pg 75.
- Miller, H. J., & Han, J. (2001). Geographic data mining and knowledge discovery: an overview. In H. J. Miller and J. Han (Eds.) *Geographic data mining and knowledge discovery* (pp 3-32). London: Taylor and Francis.
- Mitas, C. M., & A. Clement, A. (2005). Has the Hadley cell been strengthening in recent decades? *Geophysical Research Letters*, 32, 1-12.
- Padmanabhan, B. (2004). The interestingness paradox in pattern discovery. *Journal of Applied Statistics*. 31(8): 1019-1035.
- Peuquet, D. J. (1994). It's About Time: A conceptual Framework for the Representation of Temporal Dynamics in Geographic Information Systems. *Annals of the Association of American Geographers*, 84(3), 441-461.
- Peuquet, D. J. (2001) Making Space for Time: Issues in Space-Time Data Representation. *GeoInformatica*, 5, 11-32.
- Roddick, J. F., & Lees, B. G. (2001). Paradigms for Spatial and Spatio-Temporal Data Mining. *Geographic Data Mining and Knowledge Discovery*. Taylor and Francis. *Research Monographs in Geographical Information Systems*. Miller, H. and Han, J., Eds.
- Rosen, R. D., Salstein, D. A., & Peixoto, J. P. (1979). Variability in the Annual Fields of Large-Scale Atmospheric Water Vapor Transport. *Monthly Weather Review* 107, 26-37.
- Rosen, R. D., Salstein, D. A., & Peixoto, J. P. (1980). Stream Function Analysis of Interannual Variability in Large-Scale Water Vapor Flux. *Monthly Weather Review* 107, 1682-1684.

- Salas-Méllia D., Chauvin F., Déque´ M., Douville H., Gueremy J. F., Marquet P., Planton S., Royer J. F., & Tyteca S. (in review) Description and validation of the CNRM-CM3 global climate model. *Climate dynamics*.
- Selten, F. M., Branstator, G. W., Dijkstra, H. A., & Kliphuis, M. (2004). Tropical origins for recent and future Northern Hemisphere climate change. *Geophysical Research Letters*, 31, L21205
- Shekhar, S., Zhang, P., Huang, Y., & Vatsavai, R. R. (2003). Trends in Spatial Data Mining. as a chapter to appear in *Data Mining: Next Generation Challenges and Future Directions*, H. Kargupta, A. Joshi, K. Sivakumar, and Y. Yesha(eds.), AAAI/MIT Press, 2003.
- Silberschatz, A., & Tuzhilin, A. (1996). What makes patterns interesting in knowledge discovery systems. *IEEE Transactions on Knowledge and Data Engineering*. 8(6), 970-974.
- Smith, B., & Mark, D. M. (1998) Ontology and geographic kinds. *Proceedings, International Symposium on Spatial Data Handling*, Vancouver, Canada. 12-15 July.
- Stefanidis, A., Eickhorst, K., Agouris, P., & Partsnevelos, P. (2003). Modeling and comparing Change Using Spatiotemporal Helixes. *GIS'03*, November 7-8, 2003, New Orleans, Louisiana, USA.
- Steinbach, R., Tan, P. N., Kumar, V., Potter, C., Klooster, S., & Torregrosa, A. (2001). Clustering Earth Science Data: Goals, Issues and Results. *Proc of the Fourth KDD Workshop on Mining Scientific Datasets*.
- Tan, P., Steinbac, M., Kumar, V., Potter, C., & Klooster, S. (2001). Finding Spatio-Temporal Patterns in Earth Science Data. In *KDD Workshop on Temporal Data Mining*, 2001.
- Theisel, H., & Seidel, H.-P. (2003). Feature Flow Fields. *Joint EUROGRAPHICS – IEEE TCVG Symposium on Visualization (2003)*. G.-P Bonneau, S. Hahmann, C.D. Hanse (Editors).
- Thompson, D. S., Nair J. S., Venkata, S. S. D., Machiraju, R. K., Jiang,M., & Craciun, G. (2002). Physics-Based Feature Mining for Large Data Exploration. *Computing in Science and Engineering*, July/Aug 2002, 22-30.
- Van Ulden, A.P., & Van Oldenborgh, G. J.. (2006). Large-scale atmospheric circulation biases and changes in global climate model simulations and their importance for climate change in Central Europe. *Atmospheric Chemistry and Physics*, 6, 863–881.

- Vecchi, G. A., & Soden, B. J. (2007) Global Warming and the Weakening of Tropical Circulation. *Journal of Climate*, 20: 4316-4340.
- Warsi, Z. U. A. (2006) *Fluid Dynamics: Theoretical and Computational Approaches*. 2006. New York. Taylor and Francis.
- Yip, K. & Zhao, F. (1996). Spatial Aggregation: Theory and Applications. *J. Artificial Intelligence Research*, 5: 1–26.
- Yuan, M. (1999). Representing Geographic Information to enhance GIS support for complex spatiotemporal queries. *Transactions in GIS*, 3(2):137-160.
- Yuan, M. (2001). Representing Complex Geographic Phenomena in GIS. *Cartography and Geographic Information Science*, 28(2):.83-96
- Yuan, M., Mark, D. M., Egenhofer, M. J., & Peuquet, D. J. (2005) Extensions to geographic representation. In McMaster R B and Uery E I (eds) *A Research Agenda for Geographic Information Science*. Boca Raton, FL, CRC Press: 129–56

## **Chapter 4: Use Displacement Vectors to Discern Differences in Temperature Change in the 20th Century**

### ***Abstract***

This research develops a new temporal Geographic Information System (GIS) framework to compare General Circulation Model (GCM) products and reanalysis datasets to discern differences in patterns of change and locations of change. The framework incorporates the concept of kinematics to represent the movement of isolines as displacement vectors. Comparison of displacement vectors from the four datasets show differences in isotherm shifts, and the differences are prominent in several well defined regions across the globe. Among the four datasets used in the study, the two reanalysis datasets have the smallest mean of differences in displacement vectors. The CNRM CM3 20C3M dataset contains an Antarctic Cooling that led to most of the differences in displacement vectors against the other datasets. The research shows the effectiveness of displacement vectors analysis to elicit spatial differences in climate patterns among GCMs data and reanalysis data. While temperature data were used in the case study, the proposed method is based on concepts applicable to other isolines of geographic variables (such as isobars or isohyets).

### ***4.1 Introduction***

One challenge of examining GCM products and reanalysis data relates to the massive spatiotemporal data volume and the difficulty of determining patterns of change from a temporal set of gridded data. To meet the challenge, the research transforms gridded datasets to isolines of geographic properties and calculates displacement vectors of these

isolines to capture the rate of change and spatial distribution of change over time. The rate of change is determined by novel applications of image motion detection algorithms to isolines of geographic properties. Furthermore, algorithms are developed to discern regions exhibiting significant differences among data from GCMs and reanalysis.

Displacement vectors offer two key advantages to change analysis. First, displacement vectors capture both rate and direction of change simultaneously. Second, spatial analyses of differences in displacement vectors suggest regions with possible conflicting climate change patterns from the different models. This research focuses on regions characterized by large differences in displacement vectors based on comparisons of data from GCMs and reanalyses. Effects of statistical randomness in differences are reduced through the use of time intervals and spatial filters to smooth local data.

#### ***4.2 Comparison of Model Data in Climate Change Research***

Comparative studies of climate model data are common for enhancing the level of confidence on patterns and effects of climate change. Much research utilizes correlates of climate change such as storm tracks, precipitation, climate classifications and other manifestations of climatology. In each of these comparisons similar climate system response across the different GCMs adds support to the predicted impact of climate change on the manifestation of climatology under study. This research adds the ability to compare and contrast the output of climate models based on the spatiotemporal characterization of scalar climatic fields such as temperature. Comparisons based on manifestations of climate are dependent on the locations and time scales typical of the manifestations. The spatiotemporal characterization developed in this research is only dependent on the temporal span and spatial resolution of the data instead of the

manifestation. The differences between the GCM outputs are used to provide a description of the potential range of the response to climate change.

A consistent poleward shift and intensification of the storm tracks was found in an ensemble of 15 coupled climate models for 21st century climate simulations (Yin, 2005). Ulbrich and Christoph (1999) determined that the North Atlantic Oscillation would shift and there would be increasing storm track activity over Europe due to anthropogenic greenhouse gas forcing by comparing the output of several GCMs. Pinto *et al.* (2007) compared changes in storm tracks and cyclone activity across three SRES ensemble experiments to compare and contrast several GCMs.

Comparison of multiple model outputs helps draw conclusions on regional patterns of climate change. Hansen *et al.* (2006) determined that the increased Equatorial Pacific West–East temperature gradient during the last century might have increased the likelihood of strong El Niños and that, based on the output of future emission scenarios, this may become permanent. Similarly, likely future precipitation pattern changes from climate change were found by van Ulden and van Oldenborgh (2006) when they studied five GCMs and concluded significant differences in circulation patterns would occur. Past work with reanalysis datasets included the determination by Hu and Fu (2007) of a poleward shift in the Hadley cells during the last half a century based on similarities in three meteorological reanalyses and three outgoing long-wave radiation (OLR) datasets. The poleward shift was determined to continue under the regime of anthropomorphic climate change driven by future emission scenarios.

Other research focuses on differences in GCM products. Arzel *et al.* (2006) and Lefebvre and Goosse (2008) identified the uniqueness of CNRM model output in the



Weddell Sea area. Holland and Bitz (2003) determined that the CNRM model produced a slower ice melt rate than the NCAR model. In all researched instances of GCM output comparison the basis is phenomena that enabled the researcher to focus on specific regions to determine similarity or differences between model outputs.

#### *4.2.1 Approaches to Analyze Temporal Gridded Datasets*

Fluid velocity and local trend classifications are commonly used to analyze temporal gridded datasets in earth sciences. For example, Biausser, Grilli, and Fraunié (2004) applied velocity fields to simulate a wave breaking over a sloping ridge. Tan *et al.* (2001) classified the temporal pattern at each grid location to and then searched for spatial correlates among the temporal classes to discern spatiotemporal patterns of soil moisture, temperature, precipitation and net primary productivity.

Expanding upon the ideas of fluid velocity and local trends, this research develops a GIS framework to analyze and compare spatiotemporal patterns based on temporal gridded data. The velocity field of fluid flow has been used in several disciplines as a basis for analysis in addition to fluid mechanics. Astronomy uses an axisymmetric velocity field to help analyze and interpret data about movement of and distances between stars (Brand & Blitz, 1993). This research compares reanalysis climate data and GCM model data. Furthermore, this research extends the concept of flow to shifts in a temperature field characterized by temperature transitions over space. Displacement vectors of temperature change over space represent the direction of the temperature transition and the rapidness of temperature change. Displacement vectors derived from temporal gridded datasets highlight patches of differences in change patterns suggested by GCMs and reanalysis data

#### 4.2.2 *Research Hypotheses and Goals*

The growing availability of temporal gridded datasets from remote sensing, numerical models, and reanalyses poses great challenges for spatiotemporal analysis. Global statistics or clustering analyses allow identification of average trends over the world and spatial patterns at a given time, but the conventional approaches are limited in summarizing how changes progress over space and time. Global and regional statistics mask finer grain changes while cluster analysis requires care when choosing a trend for clustering.

The premise of this research posits the use of displacement vectors as measures of the direction and magnitude of changes over space and time. The chosen geographic attribute, temperature, is representative of continuous fields in which changes are conceptualized as flows. Comparisons of displacement vectors help identify regions of differences among the tested datasets, and hence suggest the need for future study of potential causes. Under the premise, the research tests the following hypotheses with four temperature data sets: two GCM model outputs and two climate reanalyses:

1. The expected values for the differences between the six permutations of pairs of the four displacement sets are significantly different (95% confidence level). The hypothesis is evaluated by applying the F-test to the six difference sets. The difference sets are leptokurtic so a large F value is required to have confidence in the results.
2. The median and box plot interquartile range of the six difference sets are larger between different types of data sources (i.e. GCM data versus reanalysis data) than between same data source types. The standard

deviation does not have meaning for leptokurtic data so a substitute measure, the box plot Interquartile Range (IQR) is used.

3. The displacement vectors themselves reveal meaningful patterns of differences among the four datasets. Differences are substantiated by studies of multiple data sources that have similar conclusions.

The introduction section covers the concepts and approaches in developing the proposed GIS method for spatiotemporal analysis of temporal gridded datasets. The following sections elaborate on the proposed method with temperature data from four climate datasets. The datasets section discusses the sources and nature of the datasets used in the study as well as the rationale and procedures for data selection and processing. The methods section details the proposed method to compute displacement vectors and comparison. The results and discussions section evaluates the expected values of the differences of displacement vectors among the data sources (Hypothesis 1), differences in median and IQR (Hypothesis 2) and relates the research findings to previous climate research (Hypothesis 3). Finally, the chapter concludes with summaries of intellectual contributions of the research and opportunities for future research.

#### ***4.3 Data Sets used in the Study***

Four datasets, two reanalysis products and two GCM products from the Twentieth-Century Climate in Coupled Models experiments (hereafter, 20C3M datasets) are used for this study. The two GCM products are from the National Center for Atmospheric Research (NCAR) Community Climate System Model (CCSM3; Collins *et al.* 2006) and, the other Center National Weather Research (CNRM) global ocean-atmosphere coupled system (CM3; Salas-Mélia *et al.*, in review). Reanalysis data is from the

National Center for Environmental Prediction/National Center for Atmospheric Research (NCEP NCAR; Kalney *et al.*, 1996) and European Centre for Medium-Range Weather Forecasts (ECMWF; Uppala *et al.*, 2005) ERA-40 projects.

Two from each type are chosen to allow comparisons within the reanalysis datasets, within the 20C3M datasets and between the reanalysis and 20C3M datasets. Both the reanalysis datasets and 20C3M datasets are single realizations, not ensembles of multiple realizations, based on historical data observations or GCM model estimates with all the variability of the climate intact. One expects that differences are smaller within a dataset type but larger between the dataset types.

The ERA-40 reanalysis dataset is based on meteorological observations from September 1957 to August 2002 (Uppala *et al.*, 2005). The goal of ERA-40 reanalysis is to provide a uniform analytical technique for meteorological value interpolation through the use of the ECMWF's Integrated Forecast System (IFS; Caires & Sterl, 2003). The heterogeneity of the observations in terms of technique, location and sampling interval remains after the IFS processing. The data collection tools changed significantly over the period of September 1957 to August 2002, with increasing satellite-borne instruments from the 1970s onwards but a declining number of radiosonde ascents since the late 1980s (Uppala *et al.*, 2005). The dominance of satellites corresponds with increased small scale uncertainty in the ERA-40 reanalysis dataset due to the decline in radiosondes and aircraft observations. The decline diminishes the ability to analyse small scale aspects as represented by the vorticity field (Bengtsson *et al.*, 2004). The location and temporal coherence of cyclones captured with satellite data have a wider spread than the

cyclones captured with terrestrial data when compared with the control tracks based on combined surface, terrestrial and satellite data (Bengtsson *et al.* 2004).

On the other hand, NCEP/NCAR re-analysis aimed to produce a 40-year record of global analyses of atmospheric fields for the research and climate monitoring communities (Kalnay *et al.*, 1996) through the recovery of observational data from land surface, ship logs, rawinsonde, pibal, aircraft, satellite and other data sources for the period 1957 through 1999. The data assimilation system used for reanalysis remained unchanged throughout the data auditing and assimilation processes so as to eliminate perceived climate jumps associated with changes in data assimilation systems (Uppala *et al.*, 2005).

The NCEP reanalysis did not use surface temperature (Kalnay & Ming, 2003) whereas the ERA-40 reanalysis did (Uppala *et al.*, 2005). The missing surface forcing did not affect the long term NCEP reanalysis accuracy as Cai and Kalnay (2005) determined that the trends from absent surface forcings, including major volcanic eruptions, are captured in the reanalysis surface data within a few assimilation cycles from the non surface data assimilation.

The initial data assimilation scheme for the ERA-40 reanalysis was more constrained by satellite data than the NCEP scheme which was initially mostly constrained by observation stations (Bromwich & Fogt, 2004). The different assimilation dependencies led to substantial differences in the reanalysis datasets until satellite data became the main data source in the 1970s for both ERA-40 and NCEP. The ERA-40 and NCEP reanalysis products agree closely for most fields (e.g. sea level pressure and zonal winds), especially after 1970 (DeWeaver & Bitz, 2006).

The 20C3M datasets included the Center National Weather Research global ocean-atmosphere coupled system (CNRM- CM3; Salas-Mélia *et al.*, in review) from France and the National Center for Atmospheric Research Community Climate System Model (NCAR- CCSM3; Collin *et al.* 2006) from the United States. The two GCMs were chosen as the different surface grid resolutions (Table 1) gave opportunities for the proposed method of displacement vectors to demonstrate the robustness in analysis of difference in change with respect to grid resolution. The CNRM-CM3 20C3M model includes forcings from ozone, aerosols, GHGs, sulphates, sea salt and desert dust aerosols (Salas-Mélia *et al.*, 2004). The NCAR 20C3M model forcings include ozone, aerosols, GHGs, sulphates, DMS emissions and oxidants (Collins *et al.*, 2006). Both models use the Hadley Centre's global sea-ice and sea surface temperature data set (Raynor *et al.*, 2003) for surface temperature on non land areas (Folland *et al.*, 2002).

Temperature is chosen in this research for two reasons. First, temperature is a spatially continuous property that fits well with the concepts of fields. A good understanding of changes to a field needs effective functions to elicit spatial variations over time, and hence temporal fields of temperature provide a good test case for the proposed displacement vectors. Second, temperature is one key parameter in climate change research. Temperature is a common proxy to evaluate the impacts of anthropogenic causes on climate. Climate observations and modelling efforts produce diverse ranges of climate data and model outputs. Comparison of temperature patterns is important to determining whether suggested patterns of climate change are compatible. Through the case study of changes in temperature fields, this research demonstrates the

effectiveness and value of the proposed method of displacement vectors in identifying differences in spatiotemporal patterns of climate change.

The temperature data for this research was obtained from the Earth System Grid (ESG) data site, the ECMWF data server and the Earth System Research Laboratory. The data are in different grid sizes as a result of balances between output resolution and computation power available in different modelling processes. The effect of horizontal resolution on GCMs have been studied since the 1970s and increased resolution does not lead to a guaranteed improvement in the model ( Manabe *et al.*, 1978; Welck *et al.*, 1971; Miyakoda *et al.*, 1971). Manabe *et al.* (1978) showed that some phenomena, such as low-level westerlies, can degrade with increased resolution. Baumhefner and Downey (1978) showed that increased resolution beyond a limit does not necessarily guarantee better accuracy.

Although for many phenomena, the fidelity of the model varies monotonically with resolution, increasing resolution does not always guarantee an overall improvement in the results. The lack of consistency between models versus resolution suggests that physical parameterizations play a large role, and that parameterizations are best within a limited resolution range. Increasing resolution can lead to degradation of model output if parameterizations are broken by the resolution change. Tibaldi *et al.* (1990) found that the change from medium to high resolution did not always increase the fidelity of a model. The zonal-mean diagnostic did not show improvement for resolution beyond T42, a spectral resolution that approximates to a  $2.8125^\circ \times 2.815^\circ$  grid, in several models (Boyle 1993). Increased resolution, nevertheless, enhances the NCAR CCSM3 products

through the reduction of inaccuracy in Arctic Sea Ice inaccuracies and increasing the resolution of the Arctic Anticyclones modeling. (DeWeaver & Bitz, 2006).

Dataset Name	Organization	Country	Atmospheric Horizontal Resolution	Source
CCSM3	NCAR	USA	256 x 128	Collins <i>et al.</i> (2006)
CNRM-CM3	Meteo-France/CNRM	France	128 x 64	Salas-Melia <i>et al.</i> (2005)
ERA-40	ECMWF	UK	2.5 x 2.5 144 x 73	<a href="http://www.ecmwf.int">http://www.ecmwf.int</a>
NCEP	NCAR	USA	2.5 x 2.5 144 x 73	<a href="http://dss.ucar.edu/pub/reanalysis/">http://dss.ucar.edu/pub/reanalysis/</a>

Table 4.1: Datasets and their horizontal resolution.

A set of isotherms is used as reference features to determine changes in a temperature field. The data extends from 1959 to 1999 for all four datasets. Two temporal averages and a gap are needed to generate means and noticeable changes between the means. The isotherms are fourteen year means using the years 1958-1971 for the 1971 mean and the years 1986-1999 for the 1999 mean. There is a fourteen year gap from 1972 through 1985 so as to provide noticeable changes between the 1971 and 1999 mean value grids. When temperature changes over space, isotherms shift accordingly. The proposed method calculates the displacement vectors of isotherm shifts to measure the direction and magnitude of temperature change; for example, 10<sup>0</sup> C isotherm shift north. The values of reference isotherms used in the case study, (-20, -16, -12, -8, -4, 0, 2, 4, 6, 8, 10, 12, 14, 16, 18, 20, 22, and 26<sup>0</sup>C), are chosen using the Koppen Climate Classification



temperature division lines with further subdivisions to provide a more complete sampling of the scalar temperature field (Figure 4.1).

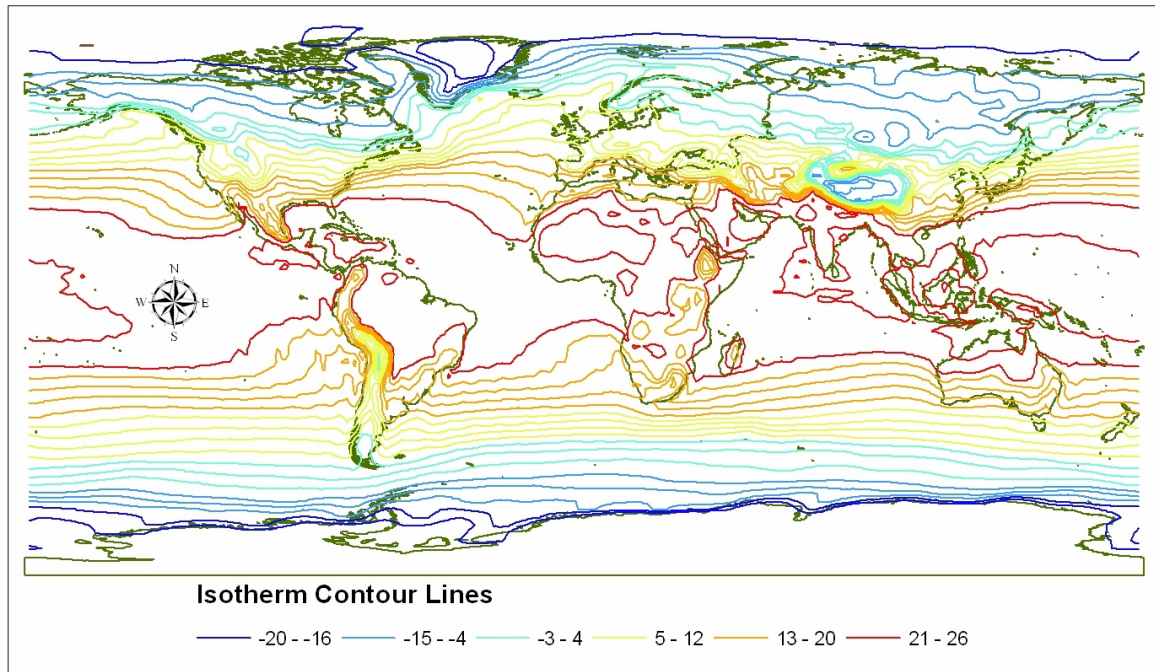


Figure 4.1: Isotherm contour lines from the NCAR NCEP dataset for 1971

The change in climatic temperature drives changes in bioclimatic zones that manifest as changes in morphology (Parmesan & Yohe, 2006). Comparing the changes in climatic temperatures provides insight into the differences between climatic datasets with an emphasis on bioclimatic envelopes.

#### **4.4 *Methods and Methodology***

The proposed method transforms a time series of scalar fields, such as temporal grids of temperature, into displacement vectors to reveal the spatiotemporal patterns of change in the GCM or reanalysis datasets. Conceptually, the proposed technique is applicable to any resolution and interval as long as due consideration is given to the rate

at which the phenomena traverse the data field. The method identifies regions in scalar data that are changing at different rates between two datasets (Figure 4.2).

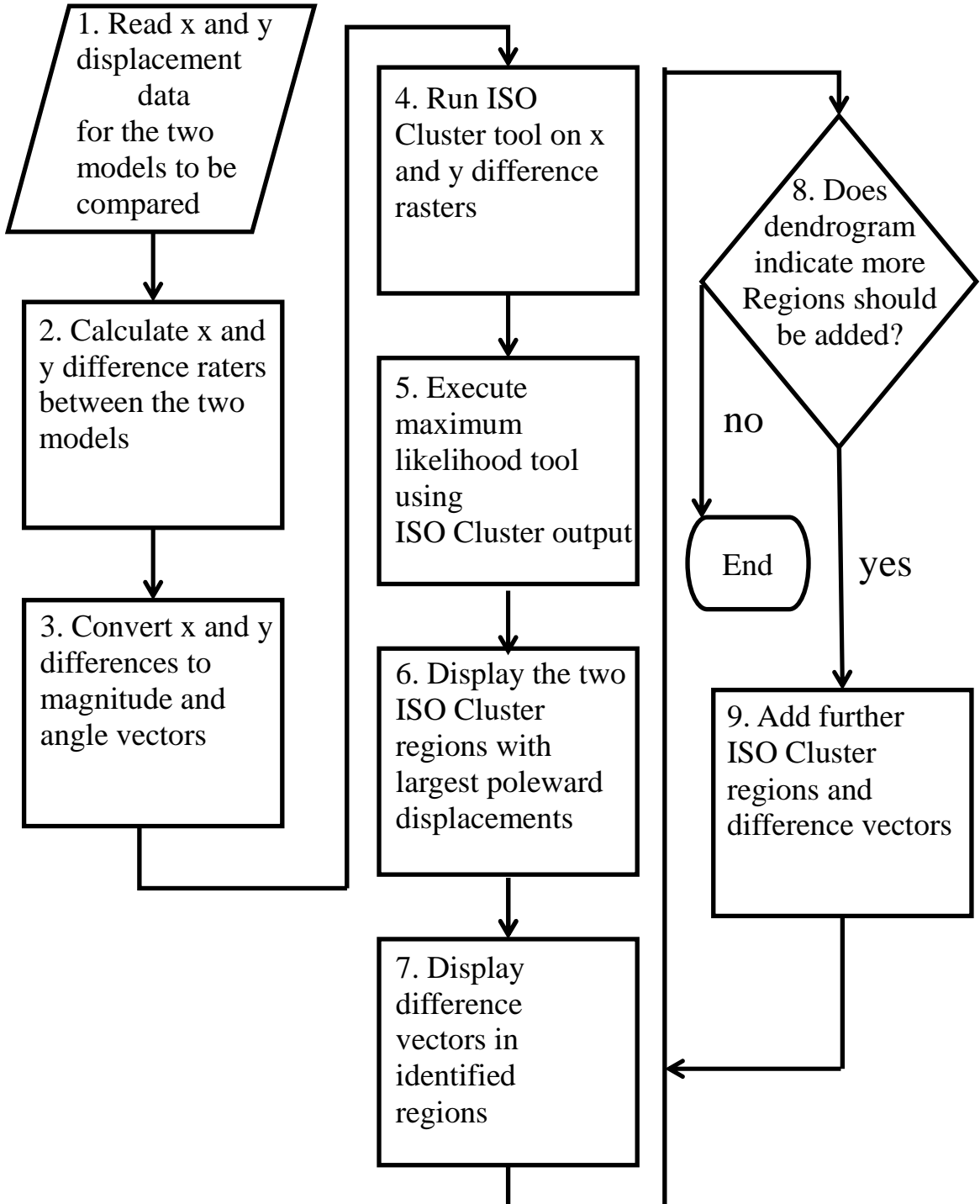


Figure 4.2: Anomalous displacement region identification and display

#### 4.4.1 Displacement Vectors and Comparisons of Differences

This research is built around the concept of kinematics and the utilization of the rich history of kinematic analysis in Meteorology. The foundation of kinematic analysis is the change in velocity for both latitudinal and longitudinal flow (Bluestein, 1992). This research applies kinematics to a virtual flow that reflects the spatiotemporal changes of scalar attributes over the Earth's surface. The kinematic representation utilizes Lagrangian and Eulerian concepts of fluid kinematics to capture the spatiotemporal characteristics of a field. Fiat boundaries based on subjective criteria, isotherms in this study, are used to spatially delineate surrogate objects. The surrogate objects are traced across multiple time instances and displacements calculated for the object's boundaries using optical flow analysis. The displacement vectors for each dataset are calculated based on contour matching from image processing algorithms developed in chapter 2. (Figure 4.3)

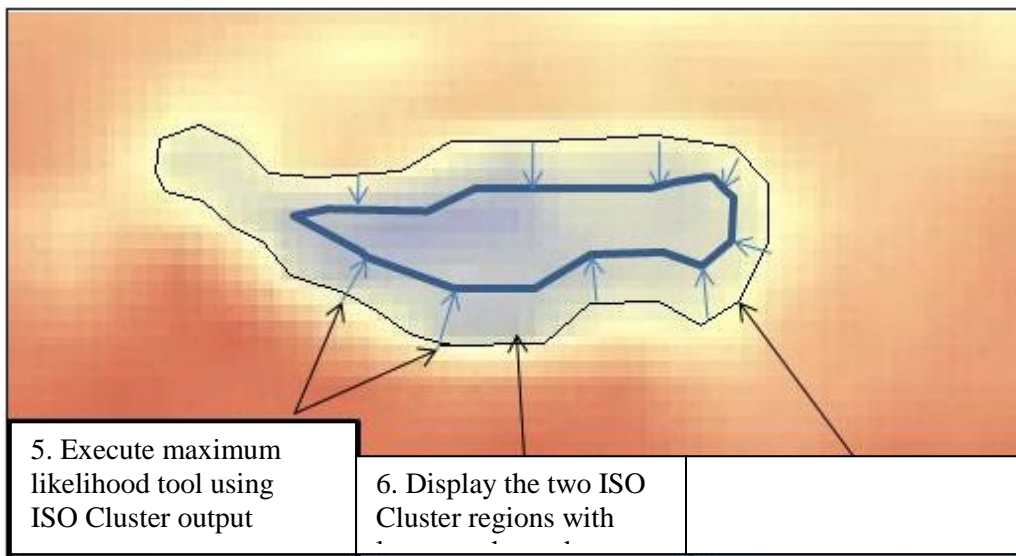


Figure 4.3: Calculating displacement vectors

An attempt is made to create a vector parallel to the local temperature gradient that intercepted a same value isotherm at time  $T_1$  for all grid points on a particular isotherm at time  $T_0$ . Interpolation is used to assign displacements to all grid points without an explicitly calculated displacement. Differences in the displacement vectors for each grid point are then calculated for each pair combination.

The displacement difference vectors contrast the shifts in isotherms in the two datasets being compared. The differences in x and y directions are converted to points with magnitudes and angles at locations.

The Iterative Self Organizing (ISO) clustering tool is used to identify regions of similar differences of displacement vectors based on maximum likelihood classification functions. These identified clusters may relate to underlying geophysical phenomena. All difference vectors outside the defined large vector region are removed from the map to remove the spatial and temporal randomness intrinsic to the models (Caires & Sterl, 2003). The remaining difference vectors are symbolized as arrows with orientation dictated by the displacement vector's direction.

This research utilizes a pairing approach for analysis of differences by comparing the difference in displacement vectors among the four test datasets by examining the six possible pairings. The simplistic approach is taken for this research for two reasons: the number (4) of models in the comparison is manageable for direct comparisons and pair comparison supports the recognition of differences that are unique to a particular model.

#### **4.5    *Results and Discussions***

The differences in displacement vectors between the CNRM 20C3M dataset and the NCEP reanalysis dataset are depicted in Figure 4.4 as a kinematic analysis example.

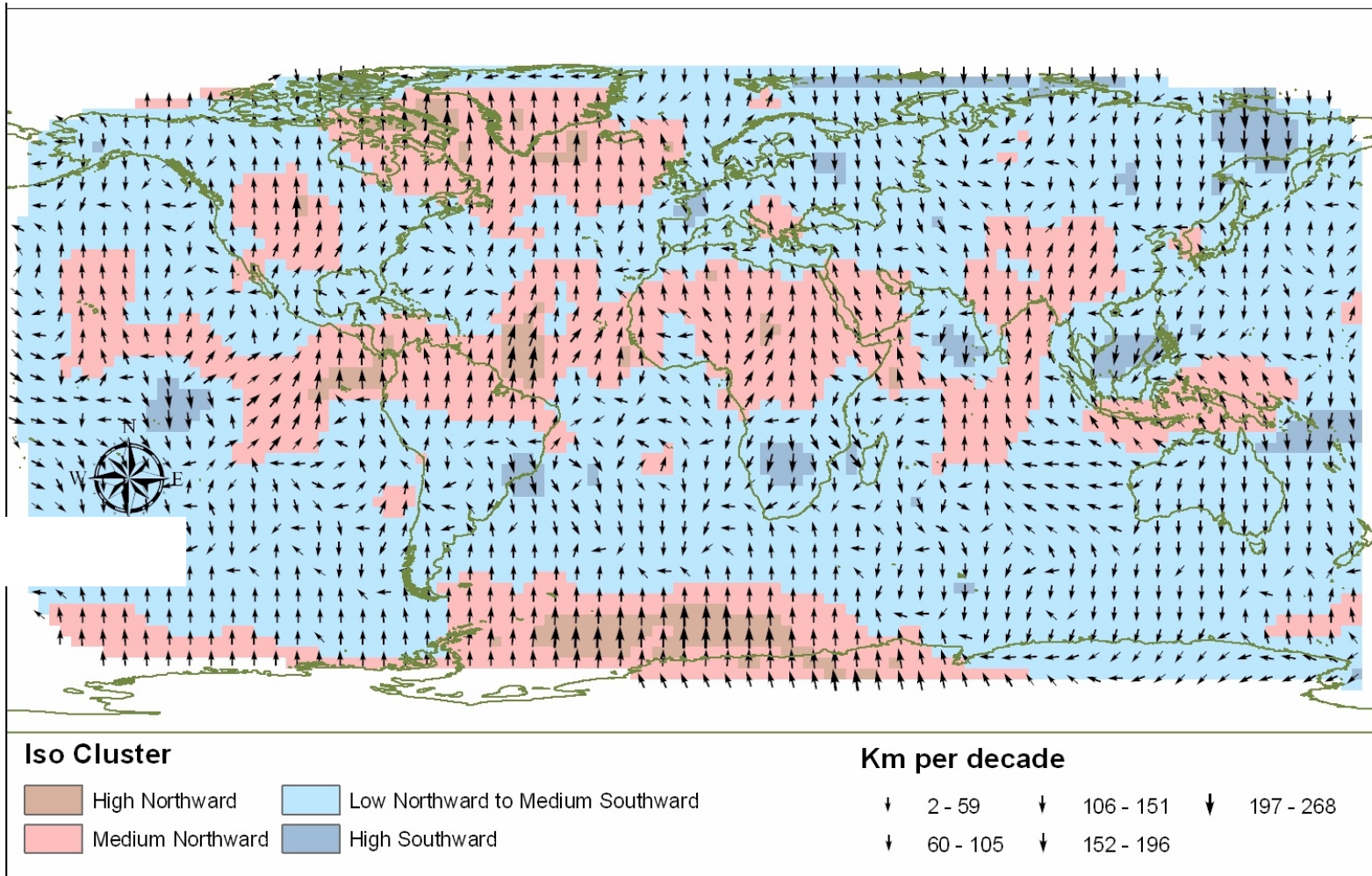


Figure 4.4: CNRM minus NCEP displacement map

The differences are calculated by subtracting the NCEP longitudinal and latitudinal displacement values from the CNRM values. The large magnitude northward arrows in the Weddell Sea, at the center of the map north of the Antarctic, result from the CNRM dataset portraying a northward shift of the isotherms, i.e. cooling. The northward arrows over Africa result from the larger northward shift in isotherms for the CNRM dataset than the NCEP dataset as well. There is good agreement between the two datasets in the southern mid latitudes of the oceans depicted by the light blue in figure Figure 4.4.

#### 4.5.1 The findings

The differences for the six possible permutations of pair kinematic differences of the four datasets were calculated at each grid point. The difference set for each was leptokurtic with a kurtosis value from four to six. The mean and standard deviation do not apply to datasets with such a large deviation from a normal distribution. The box plot interquartile range (IQR) of 25% to 75% is used to compare ranges. The IQR and the median difference are displayed in the table below for comparison purposes (Table 2).

Source Dataset	CNRM 20C	ERA40	NCAR 20C	NCAR NCEP	Median
CNRM 20C		16	11	-9	CNRM 20C
ERA40	67		-4	0	ERA40
NCAR 20C	60	44		-6	NCAR 20C
NCAR NCEP	80	41	52		NCAR NCEP
Box Plot IQR	CNRM 20C	ERA40	NCAR 20C	NCAR NCEP	Source Dataset

Table 4.2: The median and data range of differences in the longitudinal displacement in km/decade

The NCAR CNRM difference dataset histogram is show in Figure 4.5.

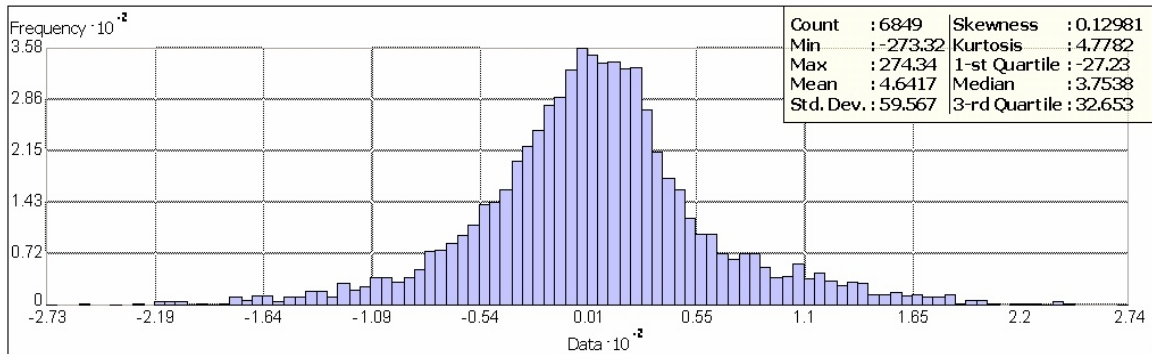


Figure 4.5: Histogram of the NCAR minus CNRM longitudinal displacement. Other difference histograms are similar.

The ANOVA F-test was applied to the 6 differences datasets which had a total of 43776 data points, 5 degrees of freedom in the numerator and 43771 in the denominator. The F-test result was 466 indicating an almost certainty of the datasets having different expected values. The 99.9% confidence level for 5 degrees of freedom in the numerator and 1000 in the denominator is 4.1392. Hypothesis #1 is confirmed.

Comparisons between the two reanalysis datasets and the two 20C3M datasets produced two groups of comparison similarities/differences when the medians and IQR of the longitudinal displacement are evaluated. The reanalysis datasets and the NCAR 20C3M dataset had less difference in longitudinal displacement difference median and IQR, and therefore, the two reanalysis datasets along with the NCAR 20C3M dataset appear to have the most similar spatial patterns of temperature change on the 14-year mean temperature. The kinematic similarity of the NCAR 20C3M dataset with respect to the reanalysis datasets supports the CO<sub>2</sub> forcing built into the NCAR model (Collins *et al.*, 2004). The differences between the CNRM GCM and all the others are the larger



three of the set of six differences. Hypothesis #2 is not confirmed as the differences between the NCAR and CNRM displacements are larger than between NCAR and both reanalysis displacement sets. The finding indicates that the CNRM 20C3M has unique and significant differences, versus the other three datasets, in the movement of isotherms during the period used for this study

#### *4.5.1.1 Similarity maps*

There is general agreement between the maps of the isotherm displacement difference vectors from comparisons between the two reanalysis datasets and the NCAR 20C3M dataset. The similarities between the three datasets include the median and percentile range of the differences calculated by subtracting the longitudinal displacements at all grid points for the datasets being compared. Vector close agreement is defined as within the IQR for the set of differences. The two reanalysis datasets are in close agreement over approximately 77% of the earth's surface (Figure 4.6).

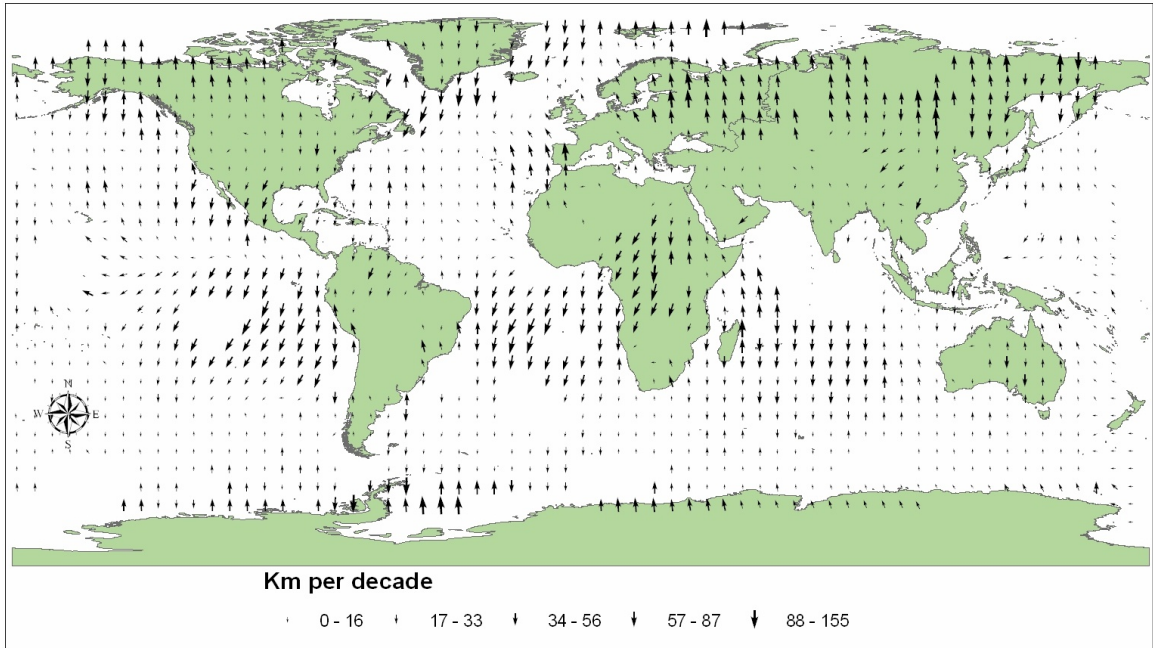


Figure 4.6: Map of ERA40 Displacement minus NCEP Displacement where the difference is within a standard deviation. Locations with a greater difference were left blank for clarity.

The similarities between the reanalysis datasets and the NCAR dataset are widespread and cover approximately 75% of the earth surface for the ERA40 difference and approximately 74% for the NCEP differences (Figure 4.7 and Figure 4.8).

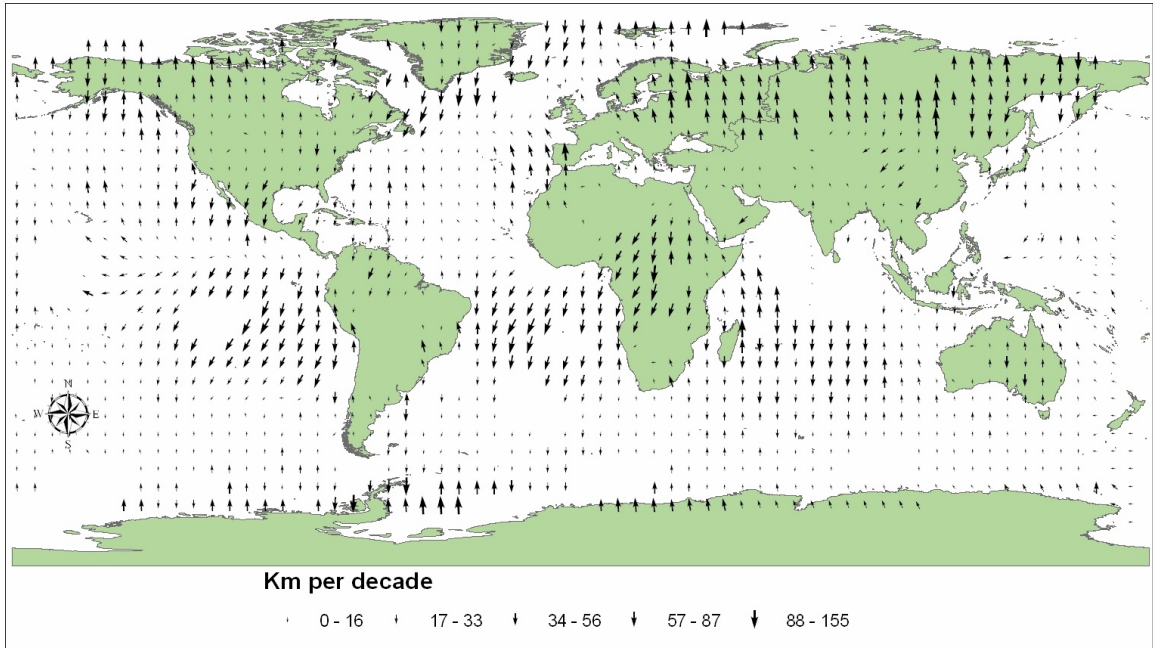


Figure 4.7: Map of EAR40 Displacements minus NCAR 20C3M Displacements where the difference is within a standard deviation. Locations with a greater difference were left blank for clarity.

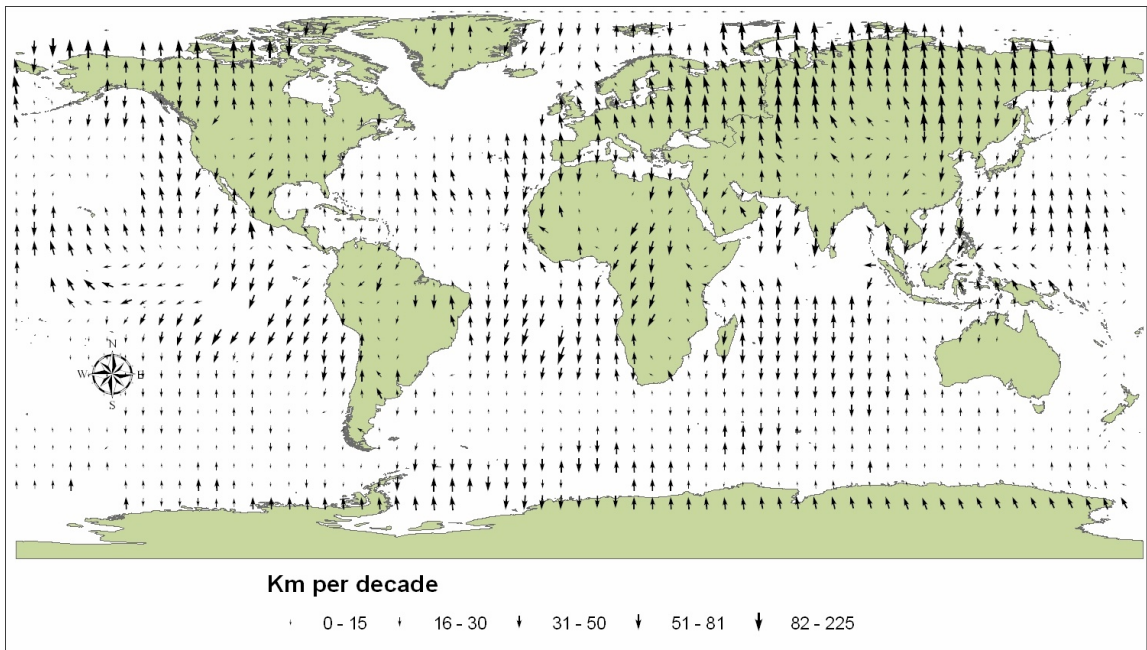


Figure 4.8: Map of NCAR 20C3M Displacement minus NCEP Displacement where the difference is within a standard deviation. Locations with a greater difference were left blank for clarity.

The agreement of the NCAR 20C3M and reanalysis datasets with respect to isotherm movement bolster support for the explicit CO<sub>2</sub> forcing in the NCAR model.

#### 4.5.1.2 Difference maps

The results exhibit clusters of comparatively larger displacements in the Arctic, Antarctic for CNRM, Greenland, Indian Ocean, several ENSO regions and other spatially disjoint regions (Figures 4.9-14). A literature review on the Antarctic and the CNRM CM3 GCM (Figure 4.9, Figure 4.10 and Figure 4.13) locates past research that corresponds to the patch of larger differences in all three comparisons with CNRM products. Additional literature is reviewed for the Arctic, Greenland, the Indian Ocean and ENSO regions with respect to the 20<sup>th</sup> Century climate and the GCMs. Findings from these literature reviews validate several of the regions identified by iso clusters of differences in displacement vectors.

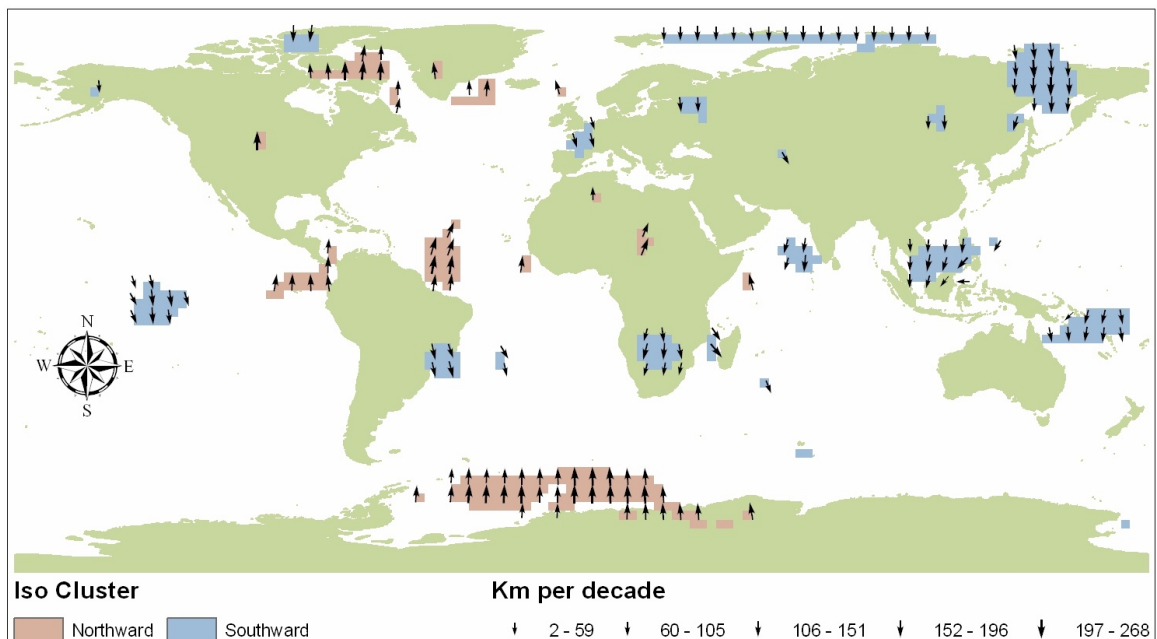


Figure 4.9: CNRM 20C3M minus NCEP large difference regions.

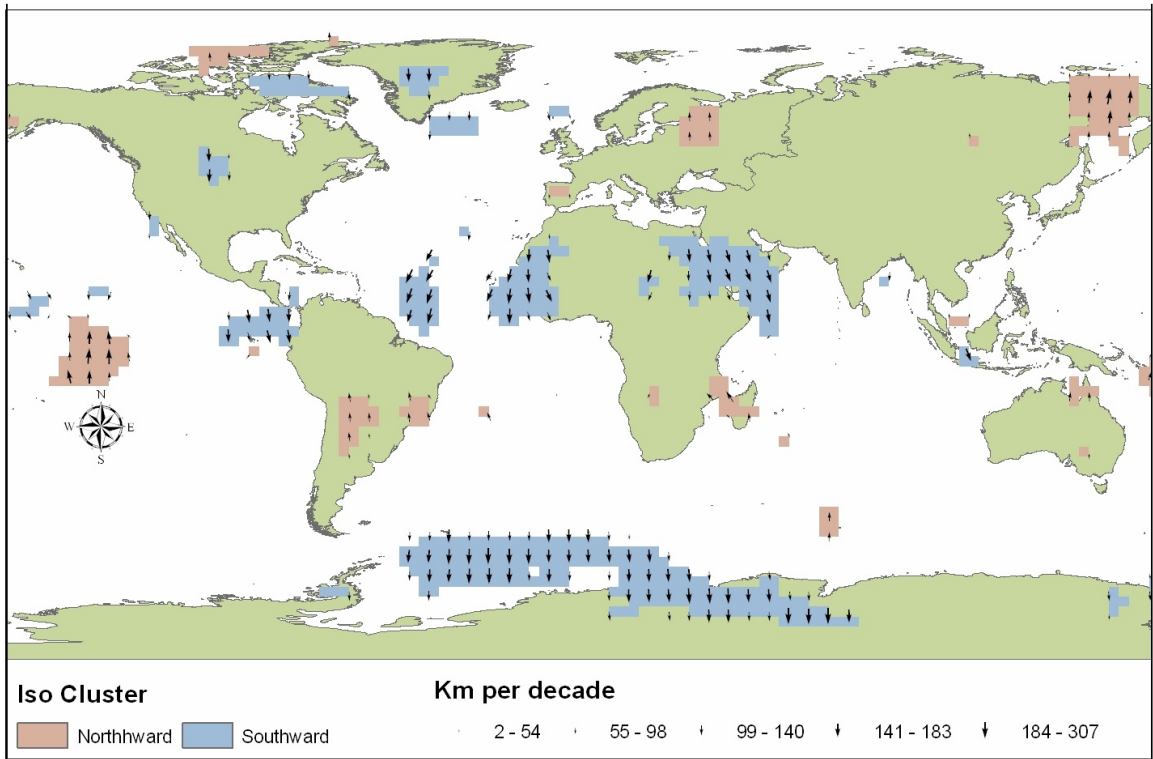


Figure 4.10: ERA-40 minus CNRM 20C3M large difference regions.

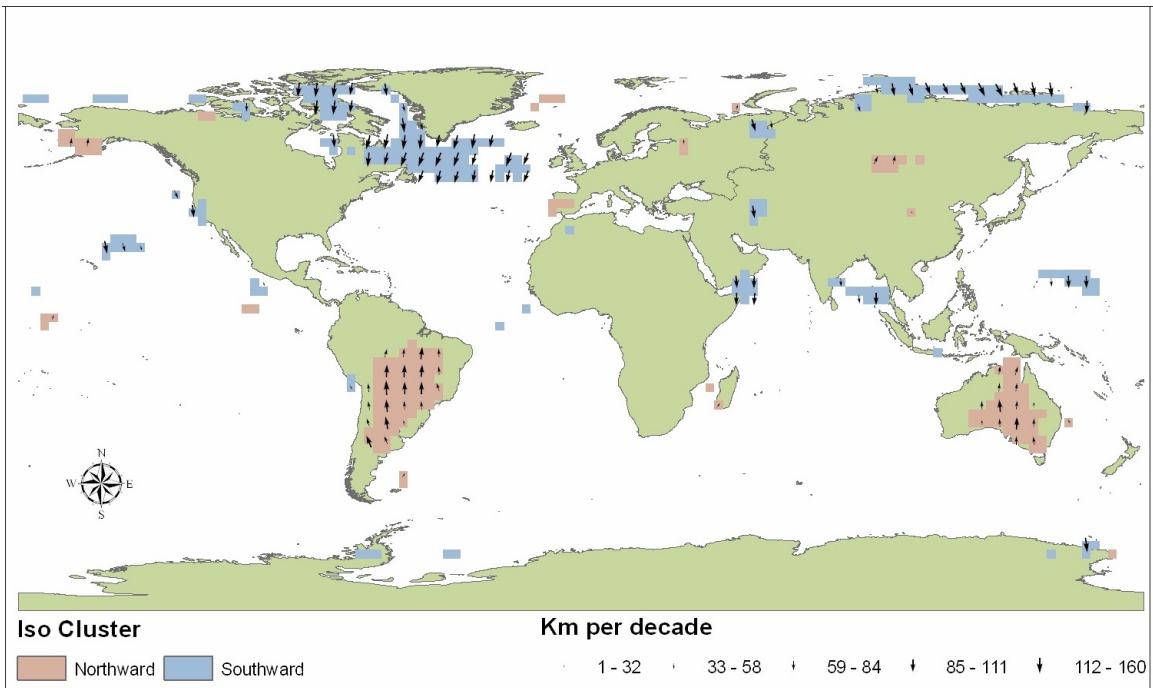


Figure 4.11: ERA-40 minus NCAR 20C3M large difference regions.

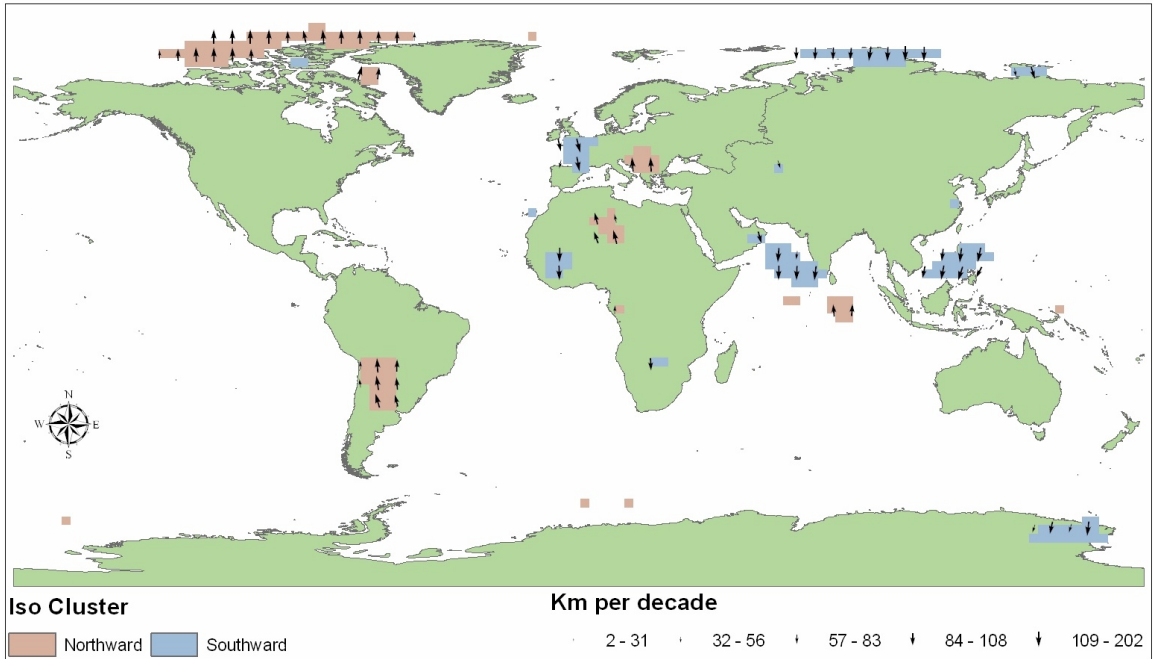


Figure 4.12: ERA-40 minus NCEP large difference regions.

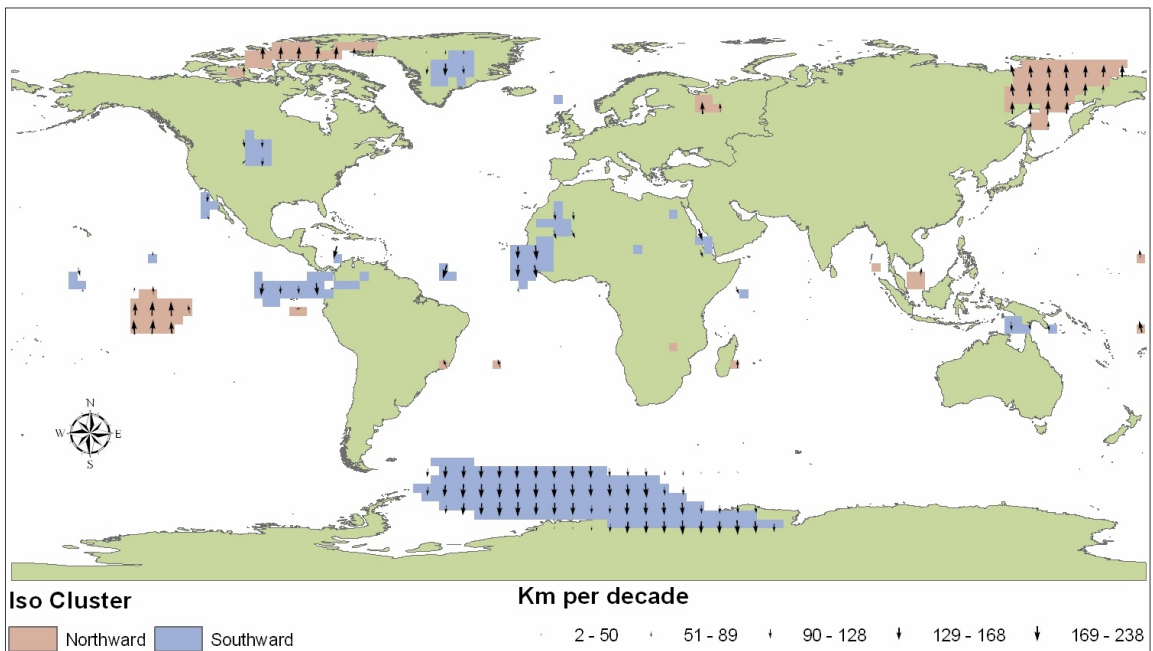


Figure 4.13: NCAR 20C3M minus CNRM 20C3M large difference regions.

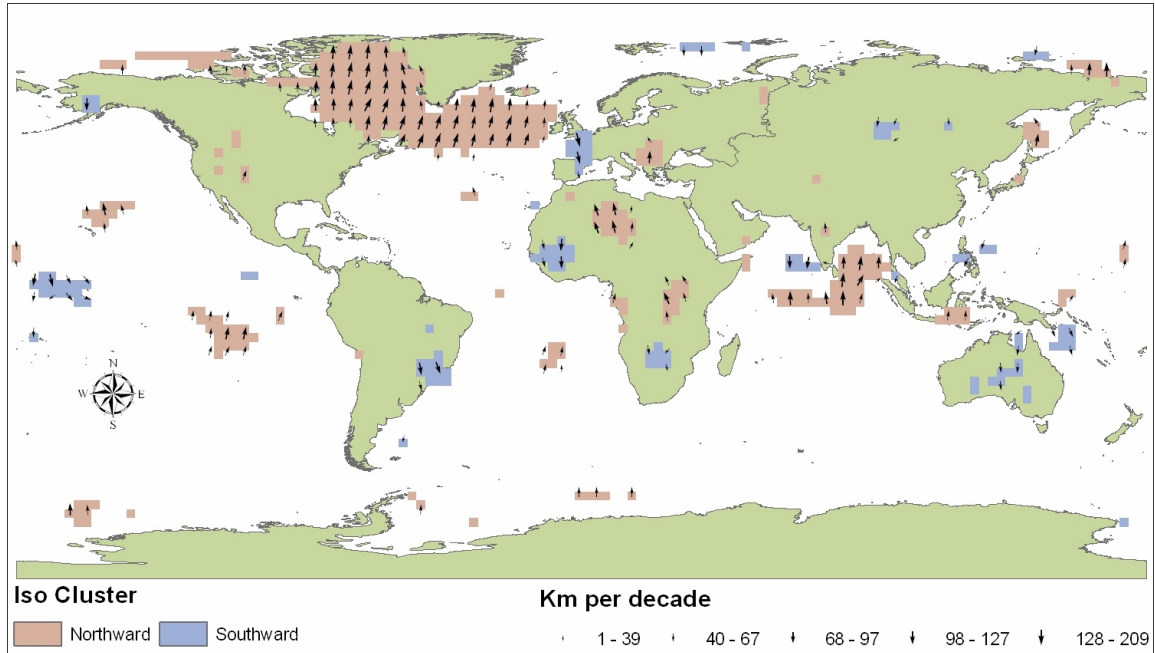


Figure 4.14: NCAR 20C3M minus NCEP large difference regions.

#### 4.5.1.2.1 *Antarctic Regions based on Differences in Displacement Vectors with CNRM data sets*

Differences of displacement vectors from comparing CNRM and any of the other datasets all showed noticeable discrepancy in the Weddell Sea region in the Southern Hemisphere (Figure 4.9, Figure 4.10 and Figure 4.13). The CNRM displacement vectors indicate a cooling in the Weddell Sea portrayed by the northward isotherm movement. The northward push of isotherms in this region is a likely result of an extension of the Weddell Sea ice. Several researchers have found such an extension during the time interval used in this study when examining outputs from the CNRM CM model. Using the CNRM CM3 20C3M dataset, Lefebvre and Goosse (2008) and Arzel *et al.* (2006) both identified a noticeable sea ice increase in the Weddell Sea predicted for the late 20<sup>th</sup> Century. According to the CNRM CM3 the overall global climate is wetter and colder than the observed climate in the 20<sup>th</sup> century (Salas-Mélia *et al.*, 2005). While the

isotherm movement is unique among the four datasets, the finding is supported by the studies of Arzel *et al.* (2006) and Lefebvre and Goosse (2008).

The cooling trend in the Antarctic Sea depicted in the CNRM dataset is supported by several prior studies of the region. Doran *et al.* (2002) concluded that the Antarctic station data show an East Antarctic coast cooling in recent decades. Arzel *et al.* (2006), Lefebvre and Goosse (2008) and Cavalieri, Parkinson and Vinnikov (2003) all suggested that an increase of  $1.3 \cdot 10^5 \text{ km}^2$  in sea ice occurred from 1981-2000 in the Southern Hemisphere. This change was after a period of noticeable decreases in Antarctic Sea ice over the period 1973–1977 (Cavalieri *et al.*, 2003), indicating the changes in sea ice extent were short term fluctuations not long term trends. Causal mechanisms for the Antarctic Sea Ice growth are attributed to atmospheric variations in the 1970s that included appreciable changes in tropospheric circulation at middle and high latitudes in the Southern Hemisphere (Hurrell & Van Loon, 1994). Though only the CNRM dataset shows the Antarctic sea ice changes, observations actually support the CNRM portrayal of Weddell Sea temperature changes during the last forty years.

#### 4.5.1.2.2 *NIÑO3.4 Region based on Differences in Displacement Vectors with CNRM datasets*

A common region, NIÑO3.4, appears in comparisons of displacement vectors with CNRM datasets (Figure 4.9, Figure 4.10 and Figure 4.13). The NIÑO3.4 regions are attributable to the model's implementation of the El Niño–Southern Oscillation (ENSO) teleconnection which is considered a dominant pattern of ocean–atmosphere variability with substantial global climate impacts. Studies on the climate of the 21<sup>st</sup> century showed



that anthropomorphic CO<sub>2</sub> emissions could result in a wide range of effects on the ENSO phenomena.

Climate change predictions on regional to continental scales are hampered by low fidelity in handling physical processes, such as ENSO, in climate system models (Joseph & Nigam 2006). The majority of coupled GCMs strongly underestimated the equatorial sea surface temperature signature of the ENSO variability (Latif *et al.*, 2001; Rao & Sperber, 2002). Contrarily, the modeled equatorial negative response to the east of the SST anomaly in the central Pacific is too strong when compared to the reanalysis data (van Oldenborgh, Philip, & Collins, 2005). No definitive studies that would attribute the NIÑO3.4 area differences in Figure 4.9, Figure 4.10 and Figure 4.13 to a specific model or models were found. The appearance of the NIÑO3.4 region for all comparisons involving CNRM suggests that an investigation of the CNRM implementation of ENSO may yield interesting results.

#### *4.5.1.2.3 Arabian Sea Region identified from Differences in Displacement Vectors with NCEP datasets*

The three comparisons of displacement vectors with NCEP datasets (Figure 4.9, Figure 4.12 and Figure 4.14) show a common region of large northward displacement in the Arabian Sea just west of the tip of India. There are two potential mechanisms for the region; a stronger monsoon season, which is usually followed by cooler than normal SSTs in the Arabian Sea, and the influence of the Indian Ocean Dipole, a pattern of coupled ocean–atmosphere interaction, which affects zonal SST gradients along the equator (Saji, Xie & Yamagata., 2006). These mechanisms are represented differently in GCMs' representations of mixed layer physics in the Indian Ocean (Saji *et al.*, 2006).

The NCEP reanalysis dataset has a greater difference when contrasted with the other three datasets than when they have when contrasted with each other. This is a surprising result as the ERA-40 and NCEP reanalysis datasets were expected to be in close agreement with each other. The two reanalysis products agree closely for most fields, especially after 1970. (DeWeaver & Bitz, 2006).

#### *4.5.1.2.4 Middle East Region Identified by Differences in Displacement Vectors between ERA-40 and CNRM 20C3M datasets*

Large magnitude difference vectors for the Middle East Region emerge in the comparison of displacement vectors based on the ERA-40 reanalysis dataset and CNRM C20C dataset (Figure 4.10). The Middle East is difficult for GCMs to model as the region has high natural inter-annual variability with a complex topography with multiple mountain ranges and inland seas (Evans, Smith & Oglesby 2004; Evans, 2009). The NCAR 20C3M comparisons do not exhibit the large magnitude difference region in the Middle East (Figure 4.11, Figure 4.13 and Figure 4.14). The lack of good observational data and the challenges to GCMs modelling for the region suggests a shortage of quality climate datasets for the region. The Middle East region recognized by the proposed method suggests an area of interest to climate change research.

#### *4.5.1.2.5 Greenland and North Atlantic Region based on Differences of Displacement Vectors with NCAR 20C3M datasets*

The differences of displacement vectors based on NCAR 20C3M and the reanalysis datasets show large magnitude difference regions in the vicinity of Greenland (Figure 4.11 and Figure 4.14). The largest region in this area resulted from the comparisons based on NCAR 20C3M and the NCEP datasets. The differences of displacement vectors show

a large area of the Northern Atlantic at approximately  $57^{\circ}$  latitude along the Baffin Bay, Davis Straits and Labrador Sea. These differences are indicative of disagreement on how rapidly the sea surface temperatures in the region increased during the 20<sup>th</sup> century. The departure of NCAR 20C3M from ERA-40 in displacement vectors also suggests a smaller region of disagreement around Greenland (Figure 4.11).

Around the area of inland Greenland, displacement vectors from the CNRM CM3 dataset exhibit warming differences from the other three datasets (Figure 4.9, Figure 4.10 and Figure 4.13). Holland and Bitz (2003) determined that the CNRM model produced a slower ice melt rate than the NCAR model. The differences in displacement vectors suggest a higher rate of northward flow in the CNRM datasets than the other three datasets. This flow difference is in the opposite direction than what would be expected given the slower ice melt in the CNRM dataset. This is explained when isotherms used in the datasets are examined. The  $-20^{\circ}\text{C}$  isotherm from the NCAR 20C3M for 1971 (Figure 4.15) and 1999 (Figure 4.16) is confined to the Greenland region and shrinking.

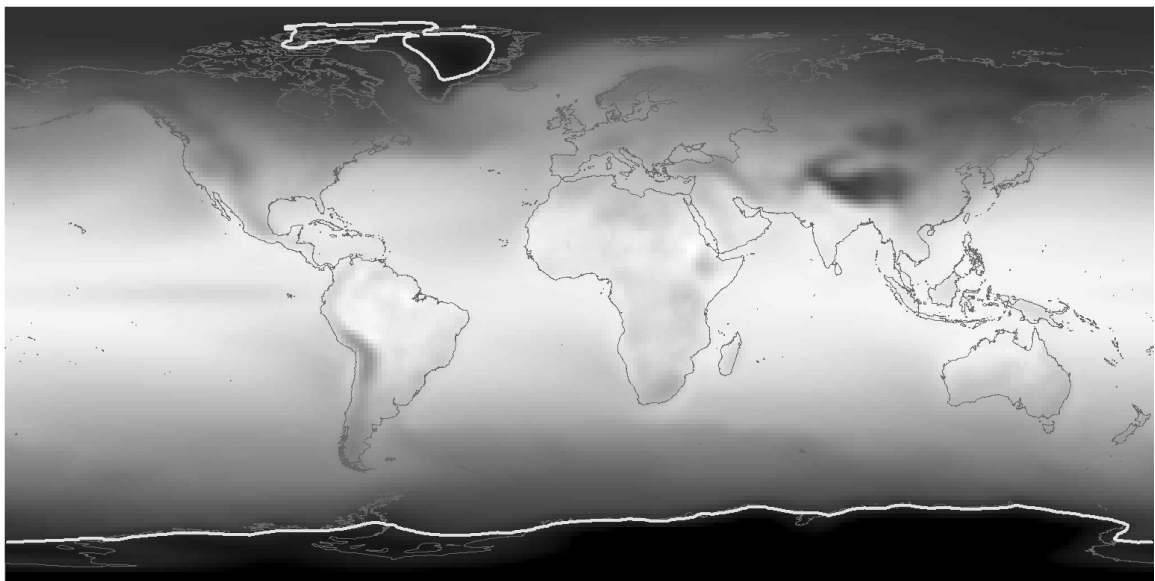


Figure 4.15: NCAR 20C3M  $-20^{\circ}\text{C}$  isotherm for 1971

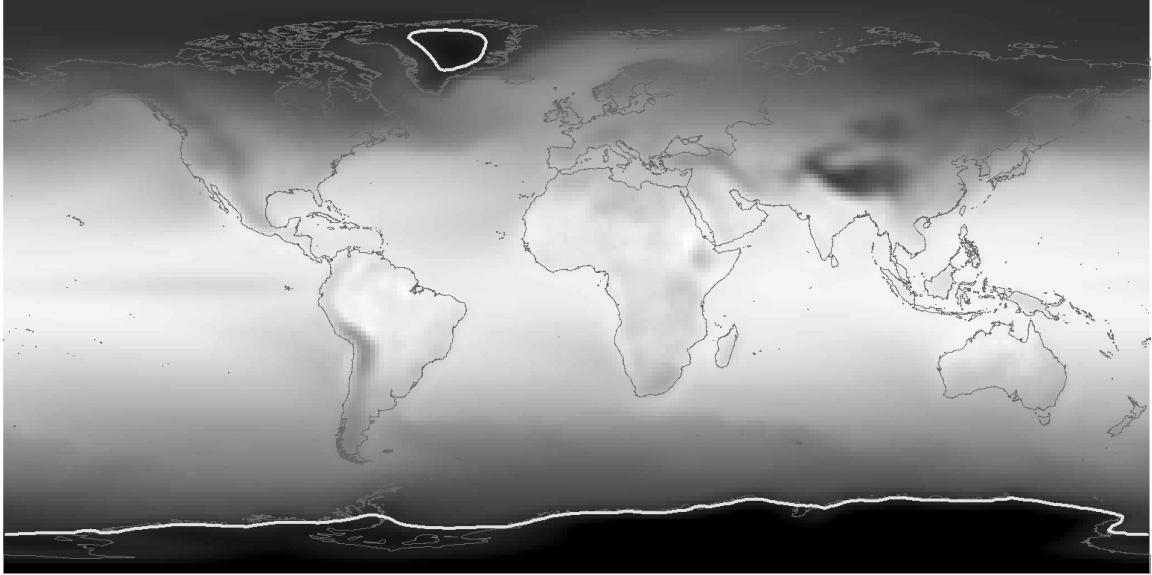


Figure 4.16: NCAR 20C3M -20°C isotherm for 1999

The result is a ring of displacement with the northern boundary of the -20°C region generating displacements to the south. A similar region around Greenland is evident in both reanalysis datasets as well. The differences seen in the Greenland region are the result of all but the CNRM 20C3M dataset having displacement vectors with a southern orientation. The CNRM dataset has a -20°C isotherm in the Arctic that changes little from the 1971 position to the 1999 position (Figure 4.17) and generates very small magnitude displacement vectors in the Arctic region. The smaller displacement vectors are a result of slower ice melt in the CNRM dataset (Holland & Bitz, 2003).

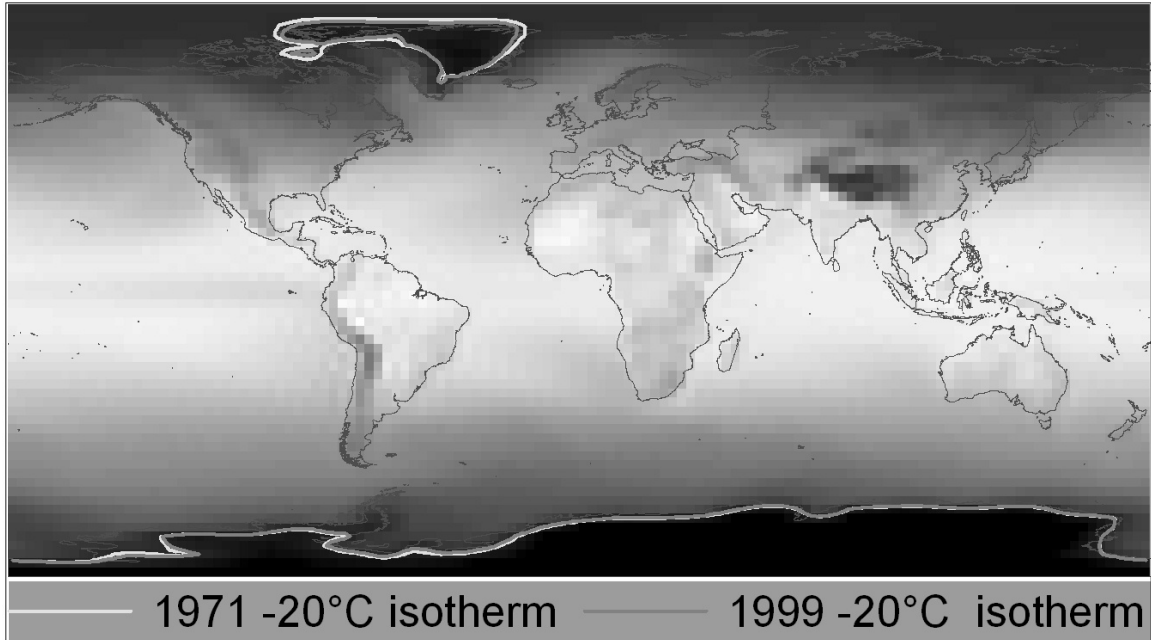


Figure 4.17: CNRM 14 year mean -20°C isotherms for 1971 and 1999.

*4.5.1.2.6 Equatorial Regions off of the northern coast of Brazil and eastern coast of Columbia Region*

The CNRM 20C3M dataset show large displacement of Sea Surface Temperature (SST) around two areas: (1) equatorial regions off the northern coast of Brazil, and (2) eastern coast of Columbia in South America (Figure 4.9, Figure 4.10 and Figure 4.13). No research was found to address any of these areas. These areas maybe additional areas of interest for further climate change research.

*4.5.1.2.7 Australia and South America Regions*

Differences of displacement vectors from the ERA-40 datasets in comparison with NCAR 20C3M and NCEP datasets suggest regions of interest in inland South America and Australia (Figures Figure 4.11 and Figure 4.12). No past research about potential differences caused by modeling issues was found to address potential climate mechanisms in these regions.

#### 4.5.1.2.8 *The Verkhoyansk Range in East Siberia*

The CNRM 20C3M dataset shows a smaller northward displacement indicating a lower rate of warming for Verkhoyansk Range in east Siberia (Figure 4.9, Figure 4.10 and Figure 4.13). The CNRM dataset exhibits a slower warm up in the area which is likely due to slower ice melt in the CNRM dataset (Holland and Bitz 2003).

#### 4.6 *Summary, Intellectual Contribution and Future Study*

The research applies displacement vectors to evaluate differences in climate products from two GCM models and two reanalysis datasets. The research demonstrates that displacement vectors effectively elicit meaningful change patterns from temporal gridded datasets. Hypothesis #1, that the expected values for the differences between the six permutations of pairs of the four displacement sets are significantly different, is confirmed. Hypothesis #2 is not validated as climate patterns are not more similar within the same types of data sources (such as comparison within GCM products or within reanalysis products) than data sources from different realizations (i.e. GCM products versus reanalysis data). Differences of displacement vectors are greatest when comparisons are made with the CNRM 20C3M dataset. The other 20C3M dataset, from NCAR, has change patterns that were more similar with the two reanalysis datasets than with the CNRM dataset. Hypothesis #3 is confirmed by the discovery of the primary cause of the uniqueness of the CNRM displacement set. The impact of the Weddell Sea cooling, captured in the CNRM output but missing in the other three datasets, is the primary cause of this unexpected result. Arzel *et al.* (2006), Lefebvre and Goosse (2008) documented the Weddell Sea cooling in the CNRM dataset and along with Cavalieri *et*

*al.* (2003) provide evidence that the cooling was a real event in the Antarctic. The equal level of similarities of climate change patterns between the reanalysis datasets and NCAR 20C3M dataset supports the inclusion of Green House Gases and other forcings in the NCAR model. Overall, the proposed method of displacement vector allows the researcher to quickly locate potential regional differences among the two GCM and two reanalysis datasets. The method identified and geographically located the Antarctic cooling and unique Arctic cooling pattern contained in the CNRM output.

The proposed method uses displacement vectors to capture change in continuous fields. Central to the proposed method is the concept of flows that progressively move across a continuous field. By extracting isolines of flows from temporal gridded datasets, the research defines displacement vectors as shifts in contours of defined values over space and time. The method successfully captured the spatiotemporal characteristics of a scalar field as portrayed across a time interval. The method can be applied to any scalar that is continuous in nature as long as the time between grid instances is chosen so as to exhibit a change that generates noticeable displacement vectors.

The proposed method can be further used to analyze the members of an ensemble and of the mean ensemble value to assess the similarity of climate change projections for IPCC scenarios. This research uses the distribution function of the entire set of differences between two different GCMs. Further research will focus on more than two sets of displacement values at regions and grid points. Displacement vectors for the ensemble should fall within the envelope of displacement vectors aggregated from the members of the ensemble as a validation of the proposed method. Regions of large

differences in displacement vectors suggest different assumptions or parameterizations in climate models and provide opportunities for further investigations.



## **References**

- Arzel, O., Fichefet, T., & Goosse, H. (2006). Sea ice evolution over the 20th and 21st centuries as simulated by current AOGCMs. *Ocean Modeling*, *12*, 401–415.
- Baumhefner, D., & Downey, P. (1978). Forecast intercomparisons from three numerical weather prediction models. *Monthly Weather Review*, *106*, 1245-1279
- Bengtsson, L., Hodges, K. I., & Hegemann, S. (2004). Sensitivity of the ERA40 reanalysis to the observing system: determination of the global atmospheric circulation from reduced observations. *Tellus*, *56A*, 456-471.
- Biausser, B., Grilli, S. P., & Fraunié, P. (2003). Numerical Analysis of the Internal Kinematics and Dynamics of Three-dimensional Breaking Waves on Slopes. *Proceedings of The Thirteenth (2003) International Offshore and Polar Engineering Conference Honolulu, Hawaii, USA, May 25–30, 2003*.
- Bluestein, H. (1992). *Synoptic-dynamic meteorology in midlatitudes: Volume 1, principles of kinematics and dynamics*. New York, NY (United States), Oxford Univ. Press
- Brand, J., & Blitz, L. (1993). The Velocity Field of the Outer Galaxy. *Astronomy and Astrophysics*, *275(1)*, 67-90.
- Bromwich, D. H., & Fogt, R. L. (2004). Strong Trends in the Skill of the ERA-40 and NCEP–NCAR Reanalyses in the High and Midlatitudes of the Southern Hemisphere, 1958–2001. *Journal of climate*, *17*, 4603-4619.
- Boyle, J. S. (1993). Sensitivity of dynamical quantities to horizontal resolution for a climate simulation using the ECMWF (Cycle 33) model. *Journal of Climate*, *6*, 796-815
- Cai, M., & Kalnay, E. (2005). Can reanalysis have anthropogenic climate trends without model forcing? *Journal of Climate*, *18*, 1844–1849.
- Caires, S., & Sterl, A. (2003). Validation of ocean wind and wave data using triple collocation, *Journal of Geophysical Research*, *108(C3)*, 3098.
- Cavalieri, D. J., Parkinson, C. L., & Vinnikov, K. Y. (2003). 30-Year satellite record reveals contrasting Arctic and Antarctic decadal sea ice variability. *Geophysical Research Letters*, *30(18)*, 1-4.
- Collins, W. D., Bitz, C. M., Blackmon, M. I., Bonan, G. B., Bretherton, C. S., Carton, J. A., Chang, P., Doney, S. C., Hack, J. J., Henderson, T. B., Kiehl, J. T., Large, W. G., McKenna, D. S., Santer, B. D., & Smith, R. D. (2006). The Community Climate System Model: CCSM3, *Journal of Climate*, *19(11)*, 2122-2143.

- DeWeaver, E., & Bitz, C. M. (2006). Atmospheric circulation and its effect on Arctic sea ice in CCSM3 simulations at medium and high resolution. *Journal of Climate*, *19*(11), 2415-2451.
- Doran, P. T., Prisco, J. C., Lyons, W. L., Walsh, J. E., Fountaink, A. G., McKnight, D. M., Moorhead, D. L., Virginia, R. A., Wall, D. H., Clow, G. D., Fritsen, C. H., McKay, C. P., Andrew N., & Parsons, A. N. (2002). Antarctic climate cooling and terrestrial ecosystem response. *Letters to Nature*, *415*, 517-520
- Earth System Grid at the National Center for Atmospheric Research. (2007). Monthly surface temperature data CNRM and NCAR GCMs. Retrieved from <http://www.earthsystemgrid.org/home.htm>.
- Evans, J. P. (2009). 21st century climate change in the Middle East. *Climatic Change*, *92*, 417–432.
- Evans, J.P., Smith, R.B., & Oglesby, R.J. (2004). Middle East climate simulation and dominant precipitation processes. *International Journal of Climatology* *24*, 1671–1694.
- Folland, C.K., Shukla J., Kinter J., & Rodwell, M. J. (2002). C20C: The Climate of the Twentieth Century Project. *CLIVAR Exchanges*, *7*(2) (June 2002), 37-39.
- Hansen, J., Sato, M., Ruedy, R., Lo, K., Lea, D. W., & Medina-Elizade, M. (2006). Global Temperature Change. *Proceedings of the National Academy of Science*, *103*(39), 14288-14293.
- Holland, M.M., & Bitz, C.M.. (2003) Polar amplification of climate change in coupled models. *Climate Dynamics*, *21*(3-4), 221-232.
- Hu, Y., & Fu, Q. (2007). Observed poleward expansion of the Hadley circulation since 1979. *Atmospheric Chemistry and Physics* *7*(19), 5229-5236.
- Hurrell, J. W., & van Loon, H. (1994) A modulation of the atmospheric annual cycle in the Southern Hemisphere. *Tellus*, *46A*, 325–338.
- Joseph, R., & Nigam S. 2006. ENSO Evolution and Teleconnections in IPCC's Twentieth-Century Climate Simulations: Realistic Representation? *Journal of Climate*. *19*, 4360-4377.
- Kalnay, E., Kanamitsu, M., Kistler, R., Collins, W., Deaven, D., Gandin, L., Iredell, M., Saha, S., White, G., Woollen, J., Zhu, Y., Leetmaa, A., Reynolds, R., Chelliah, M., Ebisuzaki, W., Higgins, W., Janowiak, J., Mo, K., Ropelewski, C., Wang, J., Jenne, R., & D. Joseph. (1996) The NCEP/NCAR 40-Year Reanalysis Project. *Bulletin of the American Meteorology Society*, *77*, 437–471.

- Kalnay E., & Ming C. (2003). Impact of urbanization and land-use change on climate, *Nature*, 423, 528-31.
- Lefebvre, W., & Goosse, H. (2008). Analysis of the projected regional sea-ice changes in the Southern Ocean. *Climate Dynamics* 30, 59–76.
- Latif, M., Sperber, K., Arblaster, J., Braconnot, P., Chen, D., Colman, A., Cubasch, U., Cooper, C., Delecluse, P., Dewitt, D., Fairhead, L., Flato, G., Hogan, T., Ji, M., Kimoto, M., Kitoh, A., Knutson, T., Le Treut, H., Li, T., Manabe, S., Marti, O., Mechoso, C., Meehl, G., Power, S., Roeckner, E., Sirven, J., Terray, L., Vintzileos, A., Voß, R., Wang, B., Washington, W., Yoshikawa, I., Yu, J., & Zebiak, S. (2001). ENSIP: the El Niño simulation intercomparison project. *Climate Dynamics*, 18(3-4), 255-276.
- Manabe, S., Hahn, G., & Holloway, J. L. 1978. Climate simulations with GFDL spectral models of the atmosphere. *Report of the JOC study conference on climate models: performance, intercomparison and sensitivity studies*. GARP Publication 22(1), 41-94. WMO, Geneva.
- Miyakoda, K., Strickler, R. F., Nappo, C. J., Baker, P. L., & Hembree, G.D. (1971). The effect of horizontal grid resolution in an atmospheric circulation model. *Journal of Atmospheric Science*, 28, 481-499
- Parmesan C., & Yohe G. (2003). A globally coherent fingerprint of climate change impacts across natural systems. *Nature*, 421, 37–42
- Pinto, J. G., Ulbrich, U., Leckebusch, G. C., Spanghel, T., Reyers, M., & Zacharias, S. (2007). Changes in storm track and cyclone activity in three SRES ensemble experiments with ECHAM5/MPI-OM1 GCM. *Climate Dynamics*, 29, 195-210.
- Rao, K. A., & Sperber K. (2002) Simulation of the El Niño Southern Oscillation: Results from the Coupled Intercomparison Project, *Climate Dynamics*, 19, 191-209.
- Rayner, N.A., Parker, D.E., Horton, E.B., Folland, C.K., Alexander, L.V., Rowell, D.P., Kent, E.C., & Kaplan, A. (2003) Global analyses of sea surface temperature, sea ice, and night marine air temperature since the late nineteenth century. *Journal of Geophysical Research*, 108(D14), 4407
- Saji, N. H., Xie, S.-P., & Yamagata, T. (2006). Tropical Indian Ocean Variability in the IPCC Twentieth-Century Climate Simulations. *Journal of Climate*. 19, 4397-4416
- Salas-Méllia D., Chauvin F., Déque´ M., Douville H., Gueremy J. F., Marquet P., Planton S., Royer J. F., & Tyteca S. (2004) XXth century warming simulated by ARPEGE-Climat-OPA coupled system

- Salas-Méllia, D., Chauvin, F., Déqué, M., Douville, H., Gueremy, J. F., Marquet, P., Planton, S., Royer, J. F., & Tyteca, S. (in review). Description and validation of the CNRM-CM3 global coupled model. *Climate Dynamics*.
- Tan, N.-P., Steinbach, M., Kumar, V., Potter, C., Klooster, S., & Torregrosa, A. (2001). Finding Spatio-Temporal Patterns in Earth Science Data. *In KDD Workshop on Temporal Data Mining, 2001*.
- Tibaldi, S., Palmer, T., Brankovic, C., & Cubasch, U. (1990). Extended-range predictions with ECMWF models: Influence of horizontal resolution on systematic error and forecast skill. *Quarterly Journal of the Royal Meteorology Society*, 116, 835-866
- Ulbrick, U., & Christoph, M. (1999). A shift of the NAO increasing storm track activity over Europe due to anthropogenic greenhouse gas forcing. *Climate Dynamics*, 15(7), 551-559.
- Uppala, S. M. , Kållberg, P. W. , Simmons, A. J. , Andrae, U. , Da Costa Bechtold, V. , Fiorino, M. , Gibson, J. K. , Haseler, J. , Hernandez, A. , Kelly, G. A. , Li, X. , Onogi, K. , Saarinen, S. , Sokka, N. , Allan, R. P. , Andersson, E. , Arpe, K. , Balmaseda, M. A. , Beljaars, A. C. M. , Van De Berg, L. , Bidlot, J. , Bormann, N. , Caires, S. , Chevallier, F. , Dethof, A. , Dragosavac, M. , Fisher, M. , Fuentes, M. , Hagemann, S. , Hólm, E. , Hoskins, B. J. , Isaksen, L. , Janssen, P. A. E. M. , Jenne, R. , McNally, J.-F. Mahfouf, J.-J. Morcrette, N. A. Rayner, R. W. Saunders, P. Simon, A. A. P., Sterl, Trenberth, K. E. , Untch, A. , Vasiljevic, D. , Viterbo, P., & Woollen, J. (2005). The ERA-40 re-analysis. *Quarterly Journal of the Royal Meteorological Society*, 131(612), 2961-3012.
- van Oldenborgh, G. J., Philip, S., & Collins, M. (2005). El Niño in a changing climate: a multi-model study. *Ocean Science Discussions*, 2, 267–298.
- van Ulden, P., & van Oldenborgh, G. J. (2006). Large-scale atmospheric circulation biases and changes in global climate model simulations and their importance for climate change in Central Europe Atmos. *Atmospheric Chemistry Physics*, 6, 863–881.
- Yin, J. (2005). A consistent poleward shift of the storm tracks in simulations of 21<sup>st</sup> century climate. *Geophysical Research Letters*, 32, L18701
- Wellck, R. E., Kasahara, A., Washington, W. M., & De Santo, G. ( 1971) Effect of Horizontal Resolution in a Finite-Difference Model of the General Circulation. *Monthly Weather Review*, 99, 673–683.

## Acknowledgements

*NCEP Reanalysis data provided by the NOAA/OAR/ESRL PSD, Boulder, Colorado, USA, from their Web site at <http://www.cdc.noaa.gov/>*

## **Chapter 5: The Similarity of the Variability Characteristics of Datasets Produced by Applying the Temporal Geographic Information System Framework to GCM output with that of Trends Embedded in GCM Output**

### ***Abstract***

Separability and variability of the kinematic representation is evaluated for model dependence and similarity to trend variability. The variability of temporal change in General Circulation Models (GCM) output has been evaluated using trends at fixed locations. A new temporal Geographic Information System (GIS) framework, based on the concept of kinematics, characterizes change using the motion of virtual particles of fixed value. The framework is applied to eight realizations of the National Center for Atmospheric Research (NCAR) Community Climate Systems Model (CCSM3) GCM and one realization from the Center National Weather Research (CNRM) global ocean-atmosphere coupled system (CM3) GCM from the Twentieth-Century Climate in Coupled Models (20C3M) datasets to generate displacement datasets. Eight sets of seven NCAR members are used to form Single Mode Ensembles (SME) for the analysis of the impact on grid point displacement range of adding a NCAR or CNRM realization. The F-test determined that the different expected value for the larger number of grid points with increased range when adding a CNRM realization versus a NCAR realization is significant. The GCM dependent difference indicates that displacement datasets from one GCM can be distinguished from another by the differences in the displacement vectors. The standard deviation is used to measure areal variability. Displacement vector spread and range are

compared for a collection of eight NCAR realizations, constituting a SME and the set of nine realizations ( the eight NCAR realizations and a CNRM realization) a Mixed Model Ensemble (MME). Grid point range and spread increases when adding the CNRM realization to the SME as the combination is a bimodal distribution. In contrast, the northern hemisphere, southern hemisphere, northern hemisphere land, northern hemisphere sea, southern hemisphere land and southern hemisphere sea all exhibit a decrease in spread when the CNRM realization is added to the SME to form a bimodal MME. These results are similar to the results of trend variability analysis done in several papers. The variability characterizations of the trend and kinematic representation are similar as both represent the changes in the GCM data.

### **5.1 Introduction**

The new temporal GIS framework characterizes the kinematics of isolines embedded in gridded datasets of geographic properties as displacement vectors. The vectors support kinematic analysis by capturing both rate and direction of change. Displacement vectors datasets from multiple realizations of the same General Circulation Model (GCM) are expected be more similar to each other than to different GCM datasets if the framework characterizes a model's dynamics. In addition the variability characteristics of displacement vectors derived from Single Model Ensembles (SME) and Multiple Model Ensembles (MME) are compared to the variability of trend characterization of SME and MME datasets. The variability of temporal change in General Circulation Models (GCM) output has been evaluated using trends at fixed locations (Tebaldi, & Knutti, 2007; Gleckler *et al.*, 2008; Lambert, & Boer, 2001; Zhou, & Yu 2006). The variability of

trends and displacement vectors are expected to have similar scale dependencies; scales in this study include grid point, hemisphere sea, hemisphere land, entire hemispheres and global. Global mean poleward displacement variability is compared to global mean trend by using an inverted longitudinal axis in the southern hemisphere. The inverted axis keeps the predominately poleward displacement in the two hemispheres from cancelling each other.

## **5.2 Hypothesis**

The differences between realizations from different GCMs are larger than between realizations from the same model (Barnett 1999). The temporal GIS framework displacement datasets should reflect this larger inter model difference when the range of displacements is compared at the grid point level. The first research hypothesis is:

- 1) The F-test determines if there is a statistically significant difference in the number of grid points of the CNRM realization versus an NCAR realization outside the current range of a SME. The SME is composed of seven NCAR realizations that do not include the NCAR realization being compared against the range. A 95% confidence level is used to allow leptokurtic distributions.

A climatic variable simulated in GCMs can be used as a basis for a variability characteristic comparison between displacement vectors and trends at multiple spatial extents. Additional hypothesis are:

- 2) MME displacement variability will more often exceed SME displacement variability at the grid point level. The MME has a bimodal distribution as it has displacement datasets from two different GCMs.



- 3) SME displacement variability will exceed MME displacement variability at the hemisphere, hemisphere land and hemisphere sea as does trend variability. Spatial averaging will filter the point bimodal distributions in the MME displacements.

The introduction section covers the focus of this paper, the similarity of displacement datasets from the same GCM versus a different GCM along with the comparison of trend and displacement vector variability. The concepts and approaches of the temporal GIS framework are discussed in previous chapters. The choice of climatic variable and a discussion of studies of trend variability provide background for the research hypotheses. The datasets section discusses the sources and nature of the datasets used in the study as well as the rationale and procedures for data selection and processing. The methods section provides an overview of the process for computing displacement vectors covered in detail in previous chapters. The results and discussions section evaluates the effect of dissimilar GCMs on displacement grid point data range (Hypothesis 1), the variability of displacement vectors for a SME versus a MME at the grid point scale (Hypothesis 2) as well as at the hemisphere, hemisphere land and hemisphere sea scale (Hypothesis 3). This chapter concludes with a summary of the findings that increase confidence in the framework displacement vector representation.

### **5.3 *Model variable choice***

Quantifying climate change can be done using primary climate variables including surface air temperature and precipitation. Temperature and precipitation are first order drivers of climate change and induce secondary effects that include weather extremes, sea ice thinning, ocean circulation changes and glacier retreat. In addition temperature and

precipitation are the best-observed variables over large scales with relatively long historical records (Sheffield & Wood, 2008). Models are assessed by evaluating fidelity to historical observations, model convergence and inter model agreement (Giorgi & Mearns, 2002). Gleckler, Taylor, and Doutriaux (2008) compared model differences from historical records to determine that models simulate temperature best, mean sea level pressure less well and, precipitation worst. General circulation models predict first order drivers such as temperature and precipitation better than the secondary effects.

This research uses surface air temperature changes over a 42 year period, 1958-1999 inclusive, captured by a spatiotemporal representation. The model's temperature output is transformed into displacement vectors that capture the spatiotemporal changes of the 1958-1972 and 1985-1999 means of the surface temperature. The displacement vectors from the temporal temperature data capture the dynamics of the GCM. Dataset displacement ranges from different models are compared to demonstrate the separability of datasets from different GCMs. Finally the displacement variability at multiple scales is compared with trend variability to show similar scale dependencies.

#### **5.4    *Variability***

Model created uncertainty arises from four main areas: parameterization, implementation, lack of theoretical knowledge and stochasticity (Knutti, Furrer, Tebaldi, Cermak, & Meehl, 2010). Parametric uncertainty results when small scale processes that cannot be captured by the large scale model are described empirically rather than resolved. Implementation uncertainty is caused by the model's imperfect representation of dynamics which fail to match the real world observations. A third source of uncertainty results from incomplete theoretical understanding of a process such as the impact of

aerosols on cloud formation (Knutti *et al.*, 2010). The first three sources of uncertainty cause differences between the outputs for different models as well as differences between same model realizations that can be reduced through the model refinement. Stochastic uncertainty is an additional differentiator between models and between same model realizations that is an inherent uncertainty characteristic of the model. Unlike the other sources of uncertainty, variability is a desired part of the model. Variability creates the frequency of oscillatory events such as the North Atlantic Oscillation (NAO) and the Arctic Oscillation (AO) (Holland, 2003).

Model emulated variability may be of low fidelity with markedly different frequencies and magnitudes than exist in the observed data. Variability magnitudes for the NAO and AO are less in the models than in the real world (Holland 2003). Comparing different models highlights additional variability due to the inclusion of different physical processes or differing implementations of the same processes. Combining results from multiple models in an ensemble set that is analyzed as a collective entity leads to further reduced variability (Tebaldi, & Knutti, 2007; Gleckler *et al.*, 2008; Lambert, & Boer, 2001). The multiple model ensemble is extensively used even though the ensemble mean exhibiting less error than any single ensemble member is a possible result of problems with the modeling of internal variability according to Kirtman and Shulka (2002).

An ensemble data set is a collection of set members where the member sets contain time dependent data from spatial state variables generated by computational models. Delworth and Knutson (2000), Dia *et al.* (2001) and many others determined that individual realizations of a Single Model Ensemble (SME) can show considerable

difference between runs. Delworth and Knutson (2000) emphasized the SME mean instead of data from a single realization due to the large internal variability in the simulated time series of global mean surface temperature for the 20th century. Barnett (1995) determined that due to sometimes large internal model variability of a single simulation the predications of an inter-annual climate event or general climate using the single realization is unreliable and a poor depiction of the model's capabilities. The averaging resulting from ensemble construction reduces the impact of the internal variability on the state variables.

The SME approach leads to closer adherence to recorded global means values for temperatures and other climatic primary variables. The SME does not correct for the three non-variability uncertainty sources but rather provides an output that is less dependent on the initial conditions and model internal variability. Small variations in initial and boundary conditions are not consequential for long term climate prediction (Knutti *et al*, 2010). Giorgi and Francisco (2002) determined that 30 year global means of climatic variables did not vary substantially between different realizations of a SME.

Past research determined multiple model ensembles provide superior forecasts than any single model ensemble, in terms of skill, reliability, and consistency, when considering primary variables or secondary effects (Tebaldi, & Knutti, 2007; Gleckler *et al.*, 2008; Lambert, & Boer, 2001). The inclusion of different models in a Multiple Model Ensemble (MME) dataset has a large impact on the fidelity for temperature and long wave radiation. The impact of multiple models is predominately a reduction in variance magnitude which results in higher correlation coefficients for trends (Johnson, & Sharma 2008).

#### 5.4.1 *SME versus MME*

Variations among outputs from a single model ensemble (SME) set result from differences in input conditions while variation from a multiple model ensemble (MME) set also include parameterization, implementation and theoretical uncertainty. Kunckel et al (2006) determined that internal intra-model variability is dominant at the regional scale with trends that varied by up to 1.8°C per century. Delworth and Knutson (2000) determined that internal variability generated 0.50°C of the observed 0.53°C per 35 years trend from 1910-1944. Uncertainty from a model's climate sensitivity and other inter model differences add uncertainty to the same model realization differences resulting from internal model variability (Allen, Stott, Mitchell, Schnur, & Delworth, 2000; Kattenberg *et al.*,1996). Internal variability closely matches regional variability for model climate yet MME averages with structurally different models exhibit better large scale agreement with observations (Meehl *et al.*, 2007). Though MMEs exhibit higher correlation with historical temperatures the increased state variable range at the grid points can delay change recognition due to the increase in the magnitude required for a change to be statistically significant ( Delworth, & Knutson, 2000; Sheffield, & Wood, 2008).

Variability is smoothed when members of an ensemble are averaged, reducing the difference between the ensemble mean and recorded values. Analysis of multiple 1000-yr control runs of the Geophysical Fluid Dynamics Laboratory model suggested that intra-model variability is much smaller than inter-model variability (Barnett, 1999). Inter-model variability is in addition to the internal variability which according to some previous papers (Delworth, & Knutson, 2000) matches observed large scale trends. The

dominate source of uncertainty in a simulation of average regional temperature is inter-model variability with inter-scenario and internal model variability having a lesser impact (Giorgi, & Fransicso, 2000). Zonal means showed larger differences between 5 models than between the same model (Delworth, & Knutson, 2000). The total effect of internal variability and inter-model differences leads to excess variability at the global scale.

#### 5.4.2 *Scale of region, range, variability and spread*

The correlation of a model ensemble with the recorded mean climate trends appears to be dependent on the scale of the region being compared. Among eight realizations of the NCAR CCSM2 analyzed by Zhou and Yu (2006), correlations for the global mean Surface Air Temperature (SAT) range from 0.79 to 0.87, the mean Northern Hemispheric from 0.69 to 0.82, and those for the SAT averaged over China range from 0.23 to 0.44. Spatial and temporal averaging mask internal variability which dominates single realization climate changes modeling at the regional (length of approximately 103 km) and smaller scales (Dai *et al.* 2001). The decrease in data samples averaged within a region at finer resolution reduces the smoothing of variability. The spread of model's climate output for the Chinese region is larger than the spread for the Northern Hemisphere and for the globe (Zhou, & Yu, 2006). This suggests that as the scale of the region used to compare model realization outputs diminishes the spread increases.

Averaging reduces the variability that is an intrinsic characteristic of climate phenomena.

Using ensembles improves the correlation as the amplitude of random variations is modulated by the averaging (Zhou, & Yu, 2006). The resulting higher correlation is a product of a better phase relationship, not necessarily a better simulation of the surface air temperature values. Working with ensembles increases the correlation with trends but

decreases the amplitude. The amplitude of a single realization, equal to the variability of recorded climatic variables at the regional scale, is greater than that of an ensemble.

### **5.5 *Data Sets used in the Study***

The research uses model output data from the Twentieth-Century Climate in Coupled Models (20C3M) project located in the World Climate Research Program's Coupled Model Intercomparison Project Phase 3 (WCRP CMIP3) data archive. The 20C3M simulations are driven by historical greenhouse gas concentrations, sulphate-aerosol loadings and other forcings since the start of the industrial revolution. The 20C3M project produces multiple models with ensembles with multiple realizations for each model. The two GCM products used are based on the National Center for Atmospheric Research (NCAR) Community Climate Systems Model (CCSM3; Collin *et al.* 2006) and the Center National Weather Research (CNRM) global ocean-atmosphere coupled system (CM3; Salas-Mélia *et al.*, in review). The research uses eight realizations of the NCAR CCSM ensemble and a single CNRM-CM3 realization.

### **5.6 *Methods and Methodology***

The research uses individual grid points with a size of  $1.4^{\circ} \times 1.4^{\circ}$  degrees. The CNRM CM3 model data has half this resolution,  $2.8^{\circ} \times 2.8^{\circ}$  degrees, so CNRM displacements are interpolated to match the NCAR CCSM resolution (See appendix A for a discussion of potential interpolation artifacts). A set of isotherms is used as reference features to determine changes in a temperature field. The isotherms are from fourteen year means using the years 1958-1971 for the 1971 mean and the years 1986-1999 for the 1999 mean. There is a fourteen year gap from 1972 through 1985 to provide noticeable

changes between the 1971 and 1999 mean value grids. When temperature changes over space, isotherms shift accordingly. Displacement vectors are calculated for isotherm shifts to measure the direction and magnitude of temperature change; for example, 10<sup>0</sup> C isotherm shift north. The values of reference isotherms used in the case study, (-20, -16, -12, -8, -4, 0, 2, 4, 6, 8, 10, 12, 14, 16, 18, 20, 22, and 26 <sup>0</sup>C), are chosen using the Koppen Climate Classification bioclimatic boundary temperature demarcation lines with further subdivisions to provide a more complete sampling of the scalar temperature field.

Varying amounts of point estimates are made in the ensembles due to the difference in isotherm movement. This variation is a result of the tracing algorithm and the resolution of the GCM. The algorithm utilizes threshold defined boundaries from one time interval mean to a second. No displacement calculation is done if a grid point on a threshold defined isotherm has not shifted to a different grid location. The NCAR realizations generated displacement for 3707 to 6268 of the 32000 grid points. The variable number is expected as the members of the ensemble are initialized with different values and generate different dynamics. Slower rates of isotherm movement generate less displacement vector calculations. The following figure shows the location of all displacement vectors calculated from an example run (Figure 5.1).



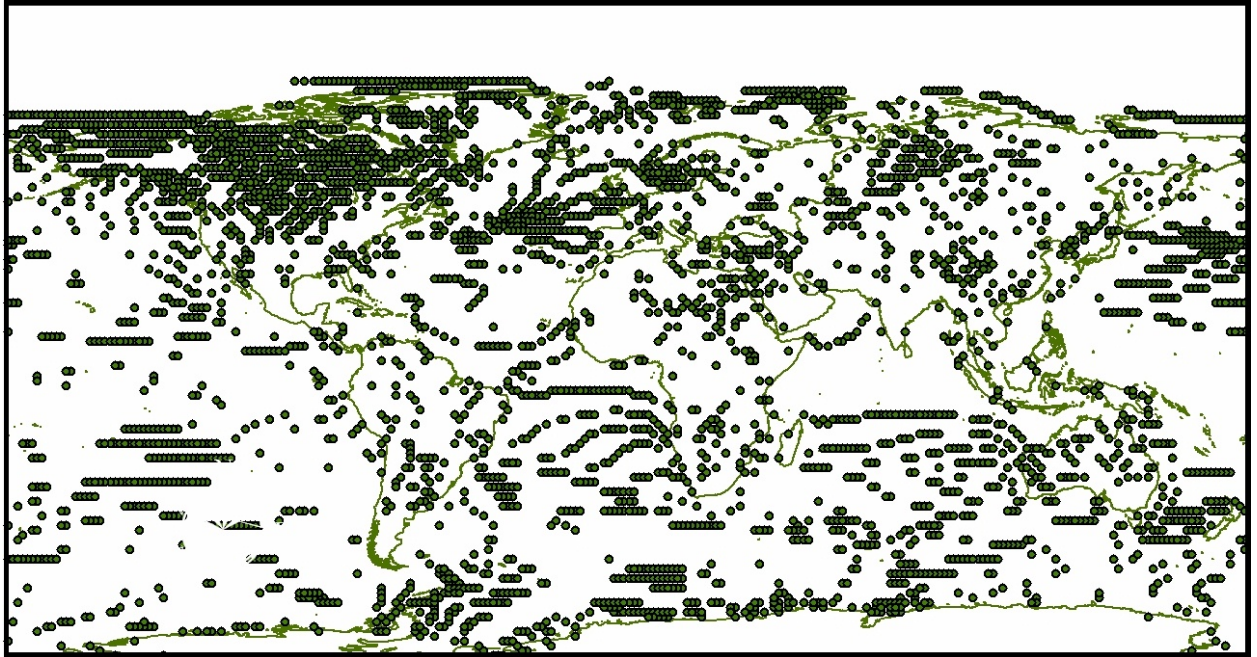


Figure 5.1: Grid points for NCAR #1 realization with calculated displacements

The map of calculated displacements (Figure 5.2) shows more rapid change over continental areas, in particular in Alaska.

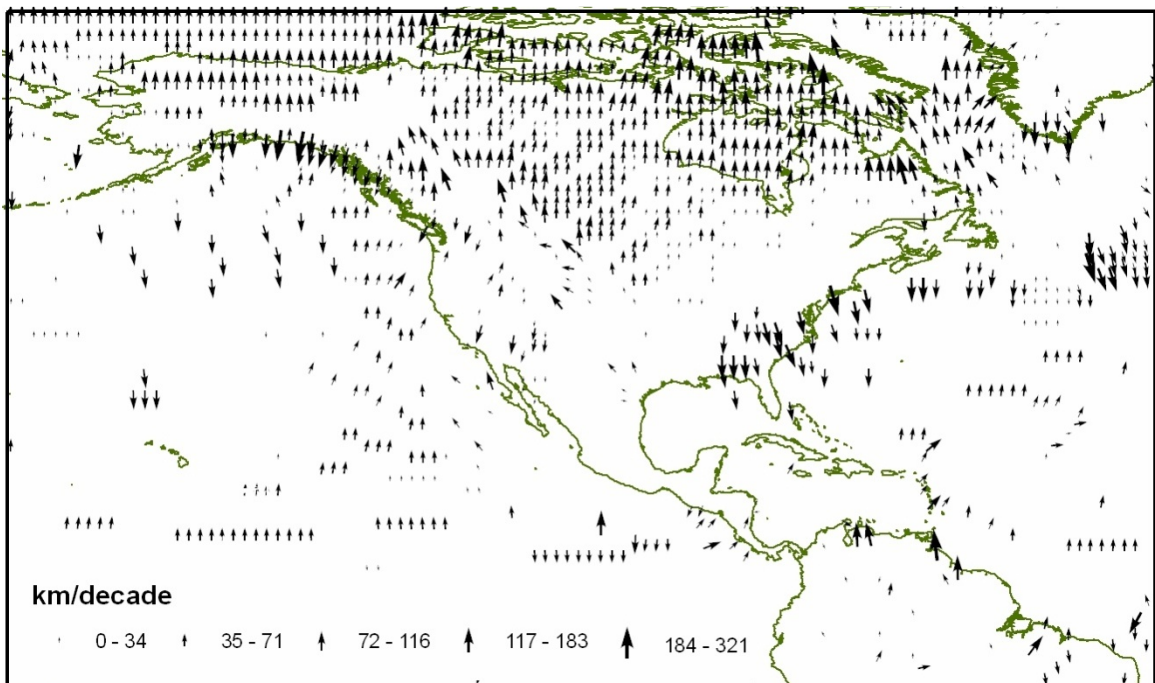


Figure 5.2: NCAR #1 realization North American region displacements

The displacement vectors are replaced with the poleward displacement component to simplify analysis. The poleward displacements are on a regular grid but the locations actually calculated by the displacement algorithm are irregular. Natural neighbor interpolation was used to fill in missing grid points. Any clustering of the variance maximums resulting from the application of the natural neighbor algorithm to the 3707 to 6268 calculated grid points are between grid points with explicitly calculated displacements.

### **5.7 Results**

The spatiotemporal representation captures the changes in 14 year means at the beginning and end of the period 1958 through 1999 inclusive. Nine maps of the isotherm motion from the eight NCAR realizations and the CNRM realization are made (Figure 5.3).

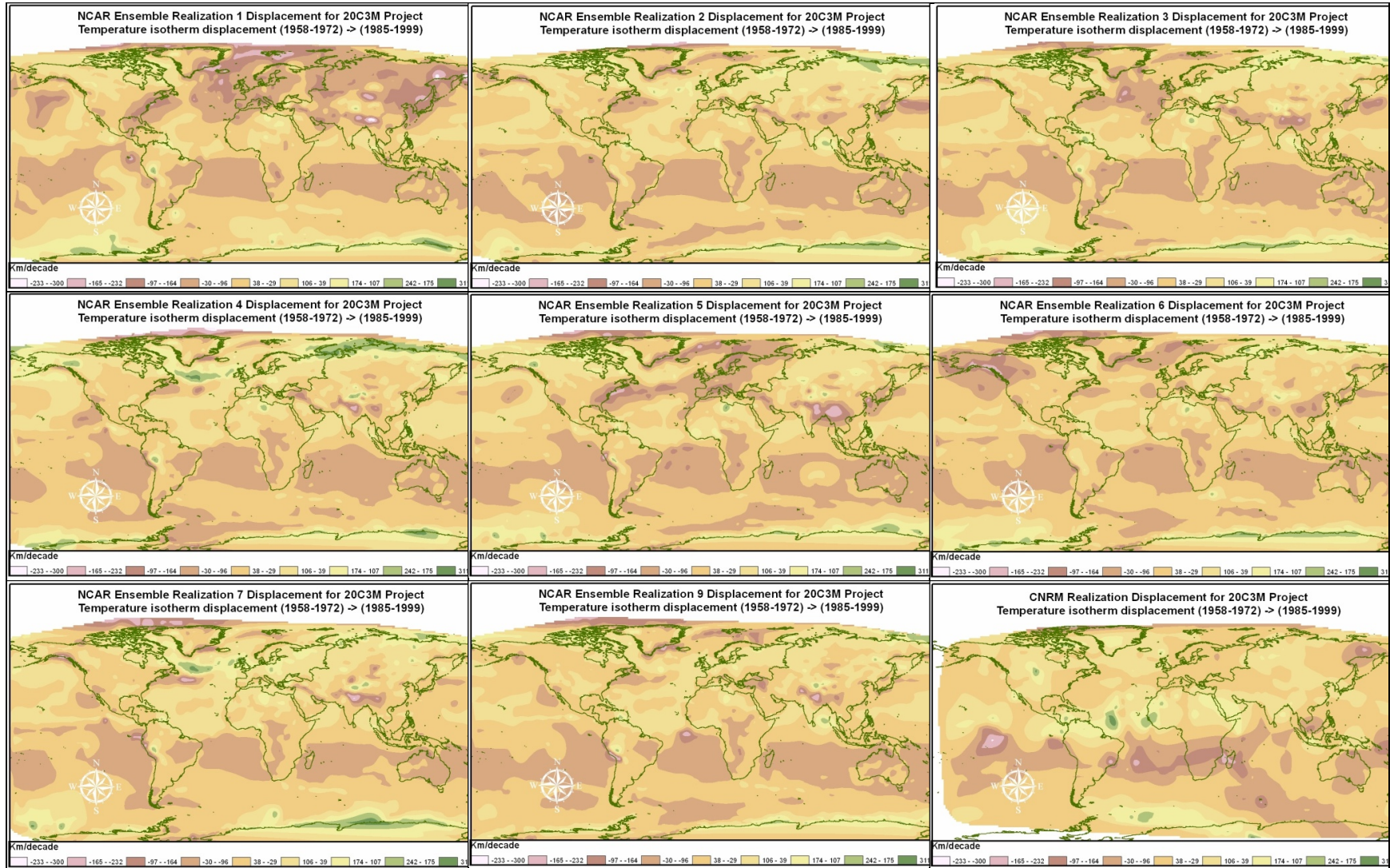


Figure 5.3: Displacement maps for 8 NCAR CCSM realizations and the CNRM realization

A set of eight SMEs is created by taking all permutations of seven NCAR realizations from the set of eight available realizations. The NCAR realization missing from each permutation is evaluated to determine the number of grid points for which the missing NCAR realization is outside the range of the seven member SME. The CNRM realization is then evaluated to determine the number of grid point locations for which the realization is outside the range of the SME (Table 5.1).

SME formulated by leaving out NCAR realization #	Number of grid points for which the missing NCAR realization is outside the range of the SME	Number of grid points for which the CNRM realization is outside the range of the SME
1	12573	16761
2	5250	14586
3	4310	14490
4	8614	14887
5	7937	15094
6	5975	14751
7	7983	14798
9	5370	14647

Table 5.1: Grid points count for range expansion when 8th NCAR realization or CNRM realization was added

The F-test is applied to the two sets to determine whether the grid point intergroup variability is the same as the intra-group variability. The result, 63.7, is much larger than the .01 critical value of 8.862 for the F-test with 1 degree of freedom in the numerator and 14 degrees in the denominator. The two range exceeded sets are shown to have different expected values. The significant difference in range exceeded expected values implies a difference in the displacement datasets that is model dependent. The combination of NCAR displacements and CNRM displacement likely leads to a bimodal distribution with increasing range and variance. The range in 52% of the grid point

locations had an increase when the CNRM data was added to the eight member NCAR SME (Figure 5.4). Adding a ninth member to a sample set is expected to fall outside the range of the original set a proportional percentage or about 11% of locations.

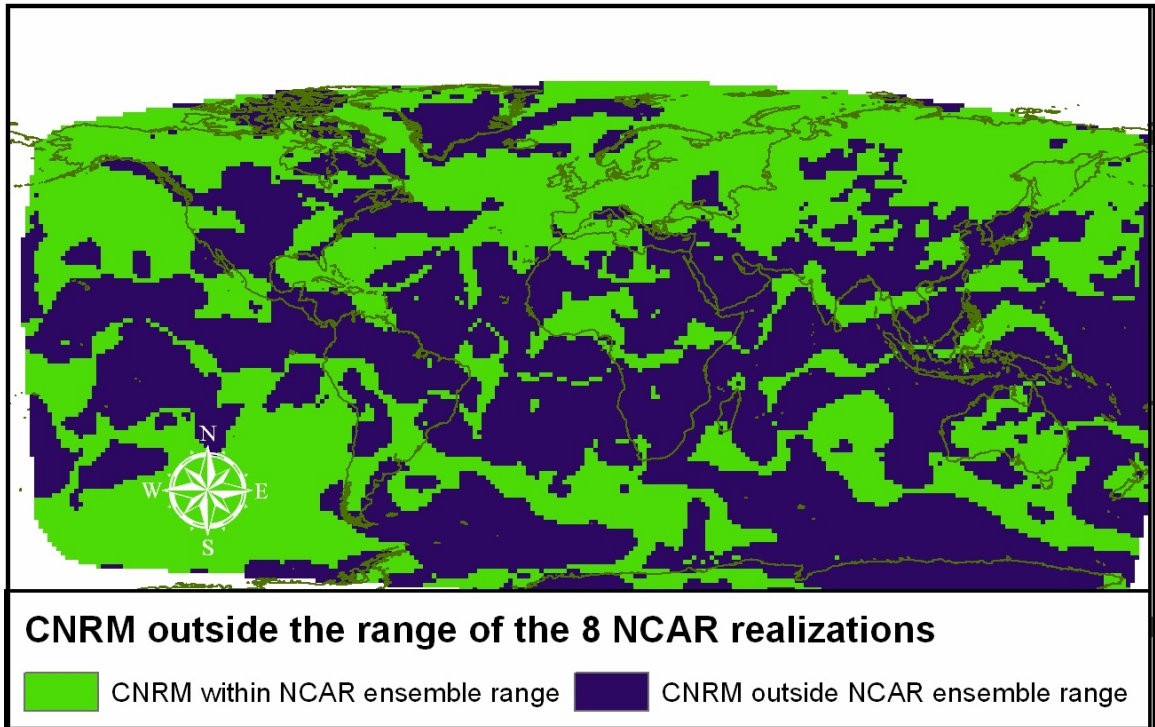


Figure 5.4: CNRM dataset values contained by SME range of data at the grid point resolution

The map showing where there is an increase in range in the MME versus the SME is almost identical to the map showing the 60% of grid points where MME spread is larger than the SME (Figure 5.5). The increase in sample size from the eight to the nine normally results in a decrease in variance unless the ninth sample has a different expected value.

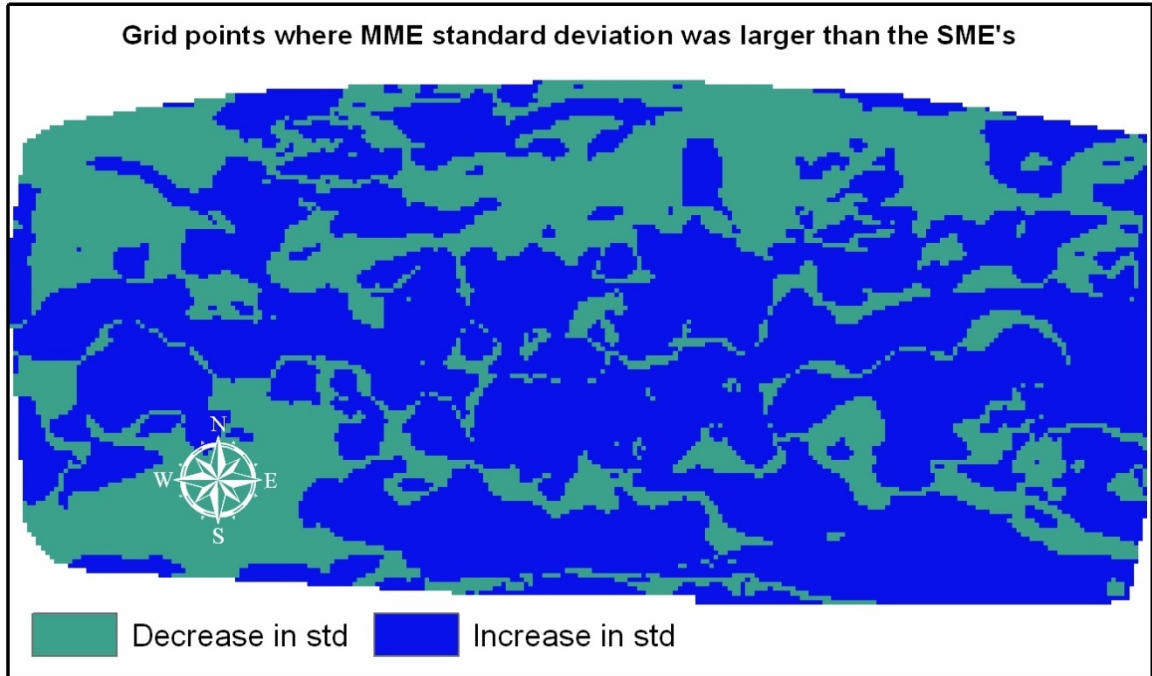


Figure 5.5: Grid points where the MME dataset values have a larger standard deviation than the SME displacements dataset

The variance of region means is then compared for the eight member SME and the nine member MME. Determining mean regional displacements requires the area weighting of the grid points on the Earth's surface. Weighting is done by filling the Robinson projection of a 128 (longitudinal) by 256 (latitudinal) grid in the World Geodetic Survey 1984 coordinate system with Thiessen polygons. Grid point data are weighted by the area of the corresponding Thiessen polygon. The area weighted displacement spread, standard deviation (Zhou and Yu 2006), for the single realization from the CNRM-CM3 model are compared to the NCAR model realizations displacement spread. The CNRM global spread is larger than all but NCAR realization 1, the northern hemisphere spread is larger than all but NCAR 1,4 and 5 realizations whereas the southern hemisphere displacement spread is greater than all of the NCAR realizations (Table 5.2).

Hemisphere	NCAR #1	NCAR #2	NCAR #3	NCAR #4	NCAR #5	NCAR #6	NCAR #7	NCAR #9	CNRM
Global	58	49	50	52	55	50	56	44	57
Northern	62	49	49	53	59	48	52	44	53
Southern	53	46	49	46	50	51	54	43	58

Table 5.2: Spread for the 8 NCAR and the CNRM hemisphere realization dataset in km/decade

A SME is formed from the eight NCAR displacement datasets. A MME is formed by combining the CNRM displacement dataset with the SME. The use of MMEs to increase global, hemisphere, hemisphere land, and hemisphere ocean trend correlations indicates that at these scales the displacement spread in the MME is less than the SME. In contrast, the spread of the MME is larger than the SME at the grid point.

The displacements for the eight members of NCAR CCSM ensemble are averaged to obtain an ensemble mean at each grid point (Figure 5.6).

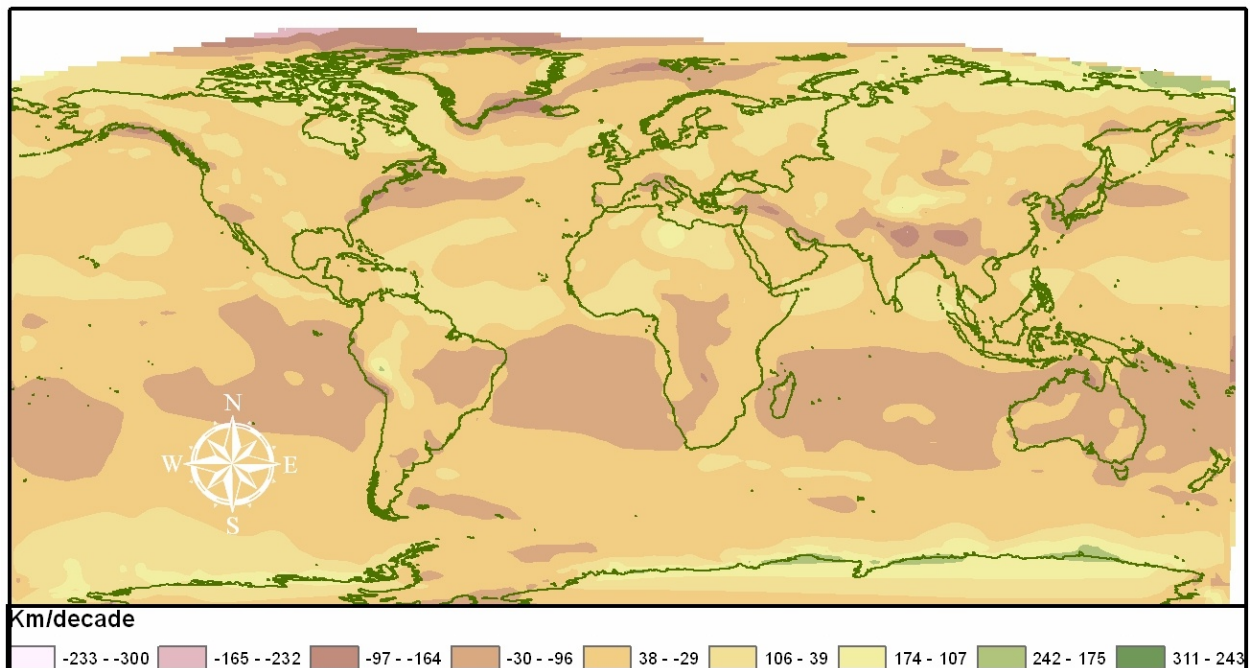


Figure 5.6: Poleward displacement of isotherms from NCAR 20C3M SME.

The SME has a northern hemisphere mean area weighted northward displacement of 22 km/decade with a spread of 42. The SME southern hemisphere displacement exhibits a southern displacement of -6 km/decade with a spread of 10. The lower southern spread is a likely result of more uniform isotherms and isotherm motion over the sea surface.

The displacements for the eight NCAR realizations with the CNRM realization MME are then averaged to obtain an ensemble mean (Figure 5.7).

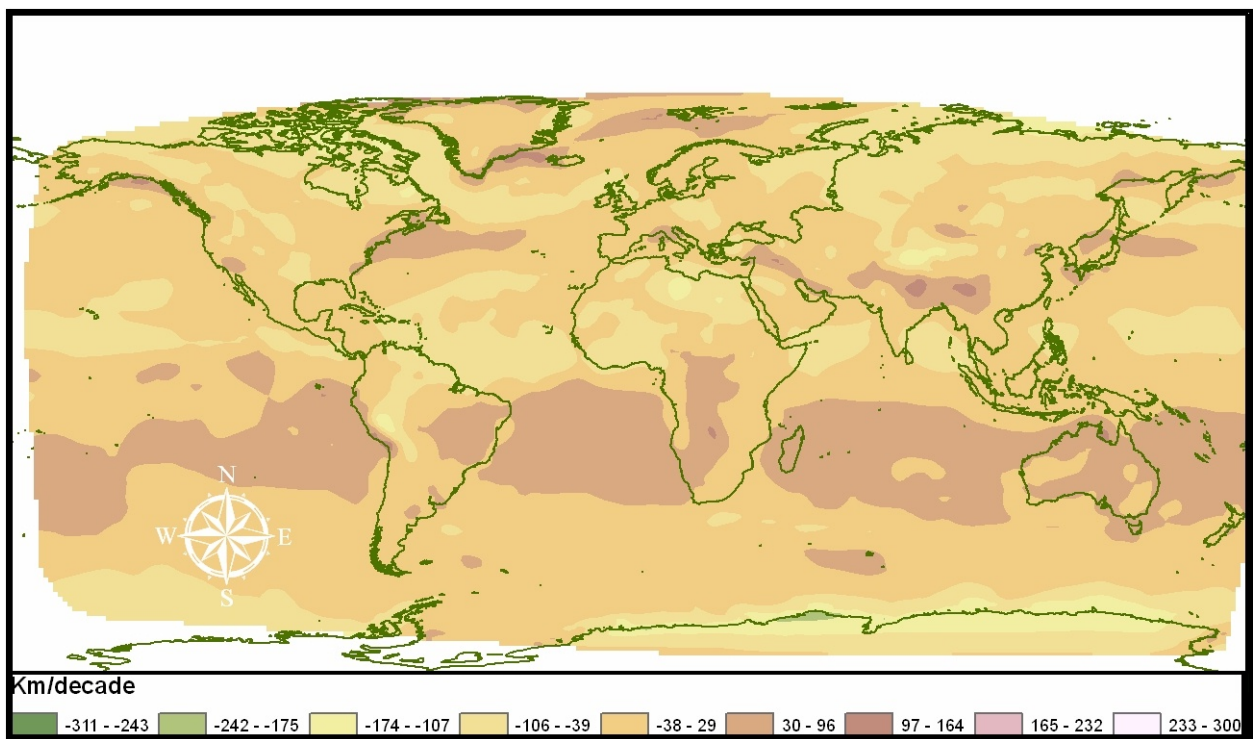


Figure 5.7: Poleward displacement of isotherms from NCAR/CNRM MME.



The global, northern, and southern hemisphere spread for the MME and SME is listed in table 5.3.

Model	Global	Northern Hemisphere	Southern Hemisphere
SME	42	38	44
MME	39	34	40

Table 5.3: Spread for mean global, northern, and southern hemisphere displacements in km/decade.

The spread decreases for the MME versus the SME even though the grid point distributions of the MME are bimodal. The land and ocean hemisphere displacement spreads for the MME and the SME are listed in table 5.4.

	Northern Hemisphere		Southern Hemisphere	
	Land	Ocean	Land	Ocean
SME	42	33	59	37
MME	38	32	55	34

Table 5.4: Spread for land and ocean in both hemispheres.

The hemisphere spread for land and ocean also shows a decrease in spread in the MME versus the SME for northern and southern hemisphere land and sea. Spatial averaging at some scales removes the increased spread at the grid point scale from the bimodal MME distribution.

## 5.8 Discussion

The displacement datasets have different expected values for the number of grid points with an expanded range when a same model realization was added to a SME versus a different model. This demonstrates that displacement datasets from the CNRM and NCAR GCMs are likely distinguishable using grid point range differences. The CNRM displacement is outside of the range of seven NCAR displacements compared to an

eightth NCAR realization a statistically significantly larger proportion. Chapter four established the difference between these two GCMs is large and it is uncertain if other GCM pairs will have similar differences.

Adding the CNRM to the set of eight NCAR realizations increases the range and variance at the grid point resolution. The combination of the NCAR and CNRM datasets results in a bimodal distribution. The poleward displacement range of the CNRM northward motion is -110 to 86 km/decade which is smaller than the NCAR realization's range of -110 to 107 km/decade. Although the NCAR has a larger global range the addition of the CNRM dataset adds to grid point range and to variability.

The increase in spread at the majority of locations when a MME is formed by adding the CNRM data to the NCAR SME is in contrast to the spread of regions. All hemisphere regions, hemisphere land regions and hemisphere ocean regions showed a decrease in both range and spread in the MME. This is consistent with the previous research by Zhou and Yu (2006) on the spread of trend data for regions at the sub continental scale and larger. An ensemble mean, single or multiple model, is better than any single realization with respect to variation as the mean modulates the extremes from the single realizations.

## **5.9 Conclusion**

The displacement differences for multiple GCMs are evaluated at the grid point and larger scales. Single realization displacements are compared to sets of displacements to determine if the single realization is outside the range of the set. The count of grid points in an NCAR or CNRM realization outside the range of a seven member SME shows a difference that is dependent on the GCM realization added. The F-test determined as

statistically significant the difference counts resulting from adding a same model realization versus a different model realization confirming hypothesis #1. The displacement datasets for the isotherm changes in the CNRM GCM and the NCAR GCM produce significantly different datasets that affect grid point range. The comparison of increased range grid points counts needs to be done with GCMs other than the pair used for this research to verify the separability of GCM displacement datasets. Research using multiple realizations for both models will also strengthen the finding as the comparison for this research used a single CNRM realization.

This research also focuses on spread to examine the interaction of scale, variability and ensemble type. Displacement variability is shown to have similar characteristics to that of trend variability. At the grid point level the addition of a different model to an ensemble leads to increased variability and increased range in the majority (60% and 52%) of locations confirming hypothesis #2. The impact on the global, hemisphere and sub hemisphere temperature displacements from adding a different model to an ensemble is a reduction in variability and range in all regions confirming hypothesis #3. The reduction in variability and range when spatial averaging is done matches trend data research reports.

## References

- Allen, M. R., Stott, P. A., Mitchell, J. F. B., Schnur, R., & Delworth, T. L. (2000). Quantifying the uncertainty in forecasts of anthropogenic climate change. *Nature* 417, 617–620.
- Barnett, T. P. (1995). Monte Carlo Climate Forecasting. *Journal of Climate*, 8, 1005-1022.
- Barnett, T. P., (1999): Comparison of Near-Surface Air Temperature Variability in 11 Coupled Global Climate Models. *Journal of Climate*, 12, 511-518
- Bluestein, H. (1992). *Synoptic-dynamic meteorology in midlatitudes: Volume 1, principles of kinematics and dynamics*. New York, NY (United States), Oxford Univ. Press
- Collin, W. D., Bitz, C. M., Blackmon, M. I., Bonan, G. B., Bretherton, C. S., Carton, J. A., Chang, P., Doney, S. C., Hack, J. J., Henderson, T. B., Kiehl, J. T., Large, W. G., McKenna, D. S., Santer, B. D., & Smith, R. D. (2005). The Community Climate System Model: CCSM3, *Journal of Climate*, 19, 2122-2143.
- Dai, A., Wigley, T. M. L., Boville, B. A., Kiehl, J. T. & Buja, L. E. (2001): Climates of the twentieth and twenty-first centuries simulated by the NCAR Climate System Model. *Journal of Climate*, 14, 485–519.
- Delworth, T. L., & Knutson, T. R. (2000). Simulation of early 20th century global warming. *Science*, 287, 2246–2250.
- Giorgi, F., & Francisco, R. (2000). Evaluating Uncertainties in the Prediction of Regional Climate Change. *Geophysical Research Letters*, 27(9), 1295-1298.
- Giorgi, F., & Mearns, L. O. (2002). Calculation of Average, Uncertainty Range, and Reliability of Regional climate Changes from AOGC Simulations via the “Reliability Ensemble Averaging” (REA) Method. *Journal of Climate*, 15, 1141-1158.
- Gleckler, P. J., Taylor, K. E., & Doutriaux, C. (2008): Performance metrics for climate models. *Journal of Geophysical Research*, 113, D06104.
- Holland, M. M. (2003). The North Atlantic Oscillation–Arctic Oscillation in the CCSM2 and Its Influence on Arctic Climate Variability. *Journal of Climate*, 16, 2767-2781
- Johnson, G., & Sharma, A. (2009). Measurement of GCM skill in Predicting Variables Relevant for Hydroclimatological Assessments. *Journal of climate*, 22, 4373-4382

- Kattenberg, A., Giorgi, F., Grass, H., Meehl, G.A., Mitchell, J.F.B., Stousser, R.J., Tokioka, T., Weaver, A.J., & Wigley, T.M.L. (1996) Climate models ± Projections of future climate. In: Houghton, J.T., Filho, L.G.M, Callandar, B.A., Harris, N., Kattenberg, A., Maskell, K. (eds) *Climate change 1995*. Cambridge University Press, Cambridge, UK, pp 285-357
- Kirtman, B. P., & Shukla, J. (2002). Interactive coupled ensemble: A new coupling strategy for CGCMs. *Geophysical Research Letters*, 29(10), 1367
- Kolstad, E. W., & Bracegirdle, T. J. (2008). Marine cold-air outbreaks in the future: an assessment of IPCC AR4 model results for the Northern Hemisphere. *Climate Dynamics*, 30 (7-8), 871-885.
- Kunkel, K. E., Liang, X. Z., Zhu, J., & Lin, Y. (2006). Can CGCMs Simulate the Twentieth-Century “Warming Hole” in the Central United States? *Journal of Climate*, 19, 4137-4153
- Knutti, R., Furrer, R., Tebaldi, C., Cermak, J., & Meehl, G.A. (2010), Challenges in combining projections from multiple climate models. *Journal of Climate*, 23, 2739–2758.
- Lambert, S. J., & Boer, G. J. (2001): CMIP1 evaluation and intercomparison of coupled climate models. *Climate Dynamics*, 17, 83–106.
- Meehl G. A., Stocker T. F., Collins W. D., Friedlingstein P., Gaye A. T., Gregory J. M., Kitoh A., et al. Global climate projections. In: Solomon S., Qin D., Manning M., Chen Z., Marquis M., Averyt K. B., Tignor M., et al., editors. *Climate Change 2007: The Physical Science Basis* (Contribution of Working Group 1 to the Fourth Assessment Report of the Intergovernmental Panel on Climate Change) ed S Solomon *et al* (Cambridge: Cambridge University Press) pp 747–845
- Salas-Méllia, D., Chauvin, F., Déqué, M., Douville, H., Gueremy, J. F., Marquet, P., Planton, S., Royer, J. F., & Tyteca, S. (in review). Description and validation of the CNRM-CM3 global coupled model. *Climate Dynamics*.
- Sheffield, J., & Wood, E. F. (2008). Projected changes in drought occurrence under future global warming from multi-model, multi-scenario, IPCC AR4 simulations. *Climate Dynamics*, 31, 79–105
- Tebaldi, C., & Knutti, R. (2007). The use of the multi-model ensemble in probabilistic climate projections. *Philosophical Transactions of the Royal Society B: Biological Sciences*, A365, 2053–2075
- WCRP CMIP3. The WCRP CMIP3 multi-model dataset archive at the Program for Climate Model Diagnostics and Intercomparison. [http://www-pcmdi.llnl.gov/ipcc/diagnostic\\_subprojects.php](http://www-pcmdi.llnl.gov/ipcc/diagnostic_subprojects.php).

Zhou, T., & Yu, R. (2006). Twentieth-Century Surface Air Temperature over China and the Globe Simulated by Coupled Climate Models, *Journal of Climate* 19, 5843-5858.

## **Chapter 6: Conclusion**

### ***6.1 Introduction***

A temporal Geographical Information Systems (GIS) framework for dynamic fields or gridded data provides a representation that supports temporal analysis. GIS spatiotemporal research has been predominately object and event oriented whereas the spatiotemporal analysis of fields or gridded data requires a different approach. This research demonstrates a kinematic representation based on velocity that describes the spatiotemporal characteristics of a time varying scalar field. Statistical and reanalysis tools such as those at the NOAA Earth System Research Laboratory support fixed location analysis without direction. Representing change over space and time using a vector representation captures direction along with magnitude at fixed locations.

#### ***6.1.1 The Kinematic Representation Applied to Spatiotemporal Analysis***

The spatiotemporal analysis of large datasets from satellites and 4D finite element models is difficult with current techniques. Researchers utilize known spatiotemporal phenomena, such as ENSO, to focus their analysis of GCM output on a subset of the data. A second approach uses regional and grid point trends at fixed locations (Zhou & Yu, 2006). The spatiotemporal representation developed for this research enables analysis without requiring a higher level abstraction such as gales, cyclonic storms or other spatiotemporal phenomena. In contrast to fixed locations trends this Lagrangian approach tracks the apparent motion of fixed value virtual particles. The result is displacement vectors with both magnitude and direction in contrast to the scalar magnitude of trends. The kinematic representation is applied to the surface temperature in the outputs of two

GCMs in chapter two. Regions are formed by aggregating rapid displacement grid points in temperature displacement maps. The regions are compared for similarities in location across the two GCMs. In contrast, chapter three uses displacements to characterize fiat objects defined by isohyets in two GCM's datasets. The characteristics of the objects are used to compare the output of GCM precipitation data. Chapter four introduces displacement difference vectors which have different expected values, medians and box plot interquartile ranges for different dataset pairs. Differences between reanalysis datasets are smallest but unexpectedly the difference between the two GCMs is as large as between the GCM and reanalysis datasets. Finally in chapter five the variability characteristics for ensembles are examined. The values from one GCM displacement dataset are shown to cluster at the grid point scale when compared to a second GCM. The displacement variability is similar to region trend variability at several scales. Details of the findings are in the following sections.

## **6.2**    *Summary of findings*

### *6.2.1 Representing Continuous Temporal Geographic Fields using Fluid Kinematic Concepts*

The temporal GIS framework is applied to the IPCC A2 scenario output for two different GCMs, the (French) Center National Weather Research (CNRM) Global Coupled System (CM3; Salas-Mélia *et al.*, in review) and the (U.S.) National Center for Atmospheric Research (NCAR) Community Climate System Model (CCSM3; Collin *et al.*, 2006). The spatiotemporal information elicited by the temporal GIS framework characterizes the changes embedded in the GCM datasets. The characterizations are compared and



contrasted with each other and to previous works by others to provide support for the representations.

#### *6.2.1.1 Displacement analysis of Project Temperature for Scenario A2 during the period of 2030-2090*

Histograms of the longitudinal displacement vectors show a bimodal distribution with modes for both the northern and southern displacements for both CNRM data (Figure 2.8, p.36) and the NCAR data (Figure 2.12, p.41). The southern hemisphere shows a wider spread of displacement magnitudes than the northern hemisphere for the CNRM data while the NCAR data's southern hemisphere displacement magnitude is less than the northern hemisphere. The assignment of the displacement mode to the northern hemisphere and the southern hemisphere is done using a longitudinal displacement map that shows the spatial distribution of the longitudinal component for CNRM (Figure 2.8, p.36) and NCAR (Figure 2.13, p. 42). The CNRM and NCAR displacements suggest a distributed moderate warming trend in the northern hemisphere with some northern areas showing southward movement that are the possible result of local minima. Large displacements occur at multiple locations at approximately 67°N in both models. The CNRM southern hemisphere motion is more varied with more rapid warming in the subtropical and temperate zones with cooling bordering the polar region. The NCAR southern hemisphere displacements are smaller and less varied with the exception of just south of the equator. The differences are the likely result of different sea ice models in the two GCMS. Latitudinal displacement for both models is dominated by widespread small shifts of magnitude 33km/decade or less (Figure 2.10, p.38 and Figure 2.15, p.44).

Iso cluster (de Smith, Longley & Goodchild, 2007) analysis discerns clustered large displacements and large convergence/divergence rates for both CNRM (Figure 2.11, p. 39) and NCAR (Figure 2.16, p.45). The northern band of rapid motion at 67° in both models is a possible result of rapid change at the Polar Regions (Holland & Bitz, 2003). Sea surface temperature changes due to a strengthening monsoon are possibly captured by the rapid change portrayed over the Arabian Sea in the CNRM output. The rapid change highlighted by the CNRM model in the south western coastal region of Arica may be the result of increased western flow from the Sahara due to global warming (Semazzi & Song, 2001). The NCAR displacements in the South Atlantic Ocean portray rapid warming seen in earlier version of the NCAR CCSM by Carril, Menede, and Nunez (1997). In the CNRM output regions of divergence over Indonesia and Niño 3 may indicate the ENSO process is changing due to anthropomorphic climate change (IPCC 2001). The NCAR output has a divergence region east of Brazil that is a possible result of a shift in the Inter-Tropical Convergence Zone (ITCZ), (Labraga, 1997).

Differences in the displacement maps for the two models suggest very different patterns of -16° C isotherms indicating that the Arctic ice in the NCAR model has melted to a greater extent than in the CNRM CM3 model. Holland and Bitz (2003) determined that in the earlier versions of these two GCMs the CNRM model produced a slower sea ice melt rate than the NCAR model and it is likely that this difference persists in the current model versions.

The result of applying the kinematic representation to spatiotemporally characterize a time dependent scalar field is successful. Several regions of similarity and

differences have potential underlying phenomena identified that support the kinematic differences.

### *6.2.2 Applying the Kinematics-based Methodology to Represent and Analyze Spatiotemporal Patterns of Precipitating Change*

This research applies a method based on kinematics, originally designed for the analysis of changes in temperature patterns, to emphasize spatiotemporal transitions of precipitation. Areas of high precipitation, in the A2 scenario defined by the International Panel for Climate Change (IPCC), are aggregated into objects. Concepts of kinematics are used to track the direction and movement of these objects over space and time. Instead of examining precipitation patterns at individual time frames, patterns of precipitation changes are examined through linking objects across time steps similarly to the flow field defined by Theisel and Seidel (2003). Divergence, deformation and rotation, measures for internal kinematics of an object, are used to measure shifts in the rates of emergence, dissipation, splitting and merging that may be indicative of the effects of large scale circulation patterns on precipitation. The three-domain model of Yuan (1999) is expanded by adding the rate of internal changes in fiat objects (i.e. precipitation areas) to bring insights into changes in precipitation patterns.

#### *6.2.2.1 Eliciting Spatiotemporal Patterns*

Optical flow analysis is applied to annual isohyets of the values 10, 20, 30, 40, 50, 60, 70, 80, 90, 100, 110, 120, 130, 140, 150, 161, 178, 213 and 284 cm/year in the years 2001 and 2048 to calculate displacement vectors (Figure 3.2, p. 69 and Figure 3.3, p. 69). Precipitation features defined by a given threshold of 213 cm/year, which include areas with annual precipitation 213cm or greater, are formulated from CNRM and NCAR data

for IPCC climate change analysis (Figure 3.5, p.73 and Figure 3.13, p.88). The threshold is set to a level that shows change over the time interval without exhibiting spatiotemporal discontinuities. Displacement vectors are used to calculate the kinematic parameters  $\partial u/\partial x$ ,  $\partial u/\partial y$ ,  $\partial v/\partial x$  and  $\partial v/\partial y$  (Equation 3.2-5, p.74) to determine divergence (Equation 3.6, p.75), deformation (Equation 3.10, p.77), and rotation (Equation 3.7, p. 75), at each point location. The values of these kinematic parameters are weighted by the size of each grid point's respective Thiessen polygons, summed, and then normalized by the area of each region. Displacement vectors determined between the two region's boundaries (Figure 3.2, p. 69 and Figure 3.3, p. 69) represent precipitation transitions over space and time and are used to associate regions from one time to the next (Figure 3.10, p. 82) (Table 3.5, p. 83).

#### *6.2.2.2 Results Interpretation*

Internal and external kinematics of fiat objects are compared and contrasted for both CNRM and NCAR datasets. Kinematic characterizations are validated by finding research by others that supports the characterizations. Both models (Figure 3.12, p.87 and Figure 3.13.14, p88) show an expansion of the 213 cm/year objects in the Indian Ocean. The CNRM model shows east-west expansions that are the possible result of increase latitudinal moisture transport or an orographic triggered precipitation. The CNRM model has an east-west expansion region in western Africa overlapped by an expansion region in the same location for the NCAR data.

The lack of divergence in expanding regions in both GCMs hints that drivers external to the 213 cm/year threshold defined regions drive the extent changes. The most discernable difference between the two datasets is the high growth rate of 20% for the

CNRM 213 region (Figure 3.12, p.87) versus 5% for the NCAR 213 cm/year regions (Figure 3.13, p.88). The difference is a possible result of differences in the forecasts of SST changes. Paired emergent and dissipative regions are discovered that are the likely result of the variability that exists in precipitation processes (Figure 3.22, p.97 and Figure 3.23, p.98).

The temporal framework supports all six classifications of Claramunt, Parent and Theriault (1997); location, attribute, extent, mutation, movement and evolution; as well as a seventh from Peuquet (1994); branching. These seven classifications enable the articulation of differences in datasets based on the characteristics assigned to virtual objects by the framework.

### *6.2.3 Discerning Differences in Temperature Change in the 20th Century datasets*

The temporal framework is applied to four datasets, two reanalysis products and two GCM outputs from the Twentieth-Century Climate in Coupled Models (20C3M). The reanalysis datasets are from the National Center for Environmental Prediction/National Center for Atmospheric Research (NCEP NCAR; Kalney *et al.*, 1996) and European Centre for Medium-Range Weather Forecasts (ECMWF; Uppala *et al.*, 2005) ERA-40 projects. The 20C3M datasets are from the CNRM CM3 GCM and the NCAR CCSM3 GCM. Temperature is chosen as the variable of interest as it is spatially continuous property that fits well with the concepts of fields and is a key anthropomorphic climate change parameter. The temporal GIS framework is used to create displacement vectors of temperature change over reference isotherms (-20, -16, -12, -8, -4, 0, 2, 4, 6, 8, 10, 12, 14, 16, 18, 20, 22, and 26 °C) (Figure 4.1, p.116), representing the direction and magnitude of the temperature transitions.

The displacement vectors enable the spatial analysis of differences in vectors between model pairs to suggest regions with conflicting climate change. The difference in displacement vectors among the four datasets is analyzed by examining the six possible pairings. Differences in the displacement vectors for each grid point are calculated for each pair combination to contrast the isotherm shifts in the pair being studied. Regions of large displacement vector differences based on comparisons of data from GCMs and reanalyses are highlighted. The Iterative Self Organizing (ISO) clustering tool is used to identify regions of significant differences based on maximum likelihood classification functions. The research tests the following hypotheses:

1. The expected values for the differences between the six permutations of pairs of the four displacement sets are significantly different (at the 95% confidence level). The hypothesis is evaluated by applying the F-test to the six difference sets. The difference sets are leptokurtic so a large F value is required to have confidence in the results.
2. The median and box plot interquartile range (IQR) of the six difference sets are larger between different types of data sources (i.e. GCM data versus reanalysis data) than between same data source types. The standard deviation does not have meaning for leptokurtic data so the IQR is used.
3. The displacement vectors themselves reveal meaningful patterns of differences among the four datasets. Differences are validated by studies of multiple data sources that have similar conclusions about climate change patterns.

The six difference sets, formed from six permutations of the four displacement sets, have a non-normal distribution with kurtosis values of between 4 and 6 (Figure 4.5, p.123). The expected values for the six difference sets are shown to be distinct with a confidence level much larger than 95%. The statistical characteristics of the leptokurtic difference sets are compared using median and the IQR. More agreement between reanalysis displacement datasets is expected as the reanalysis products process historical data in order to create their datasets. The reanalysis difference set has the smallest median and IQR of the six datasets partially confirming hypothesis #2. The difference dataset for the two 20C3Ms has the second largest median and the third largest IQR which negates hypothesis #2. The comparison of the CNRM dataset with the NCAR NCEP dataset produces the third largest median difference and largest IQR (Table 4.2, p.123). The performance of the NCAR 20C3M versus either reanalysis is better than the NCAR NCEP versus CNRM comparison. Hypothesis 3 is verified when the possible reason for the CNRM GCM uniqueness is discovered using the difference maps. A potential reason for the large differences for pairs with the CNRM model is the sea ice model of the CNRM GCM (Lefebvre & Goosse, 2008).

The similarities between the reanalysis datasets and the NCAR dataset cover approximately 75% of the earth surface for the ERA40 difference and approximately 74% for the NCEP differences (Figures Figure 4.7 and Figure 4.8, p.126). The kinematic similarity of the NCAR 20C3M dataset with respect to the reanalysis datasets supports the CO<sub>2</sub> forcing built into the NCAR model (Collins *et al.*, 2003).

The differences between the CNRM GCM and all the other three datasets are the largest of the set of six differences (Figure 4.9-15, p.127). The difference maps for

CNRM CM3 versus any other dataset have anomalous regions in the Weddell Sea region in the Antarctic and eastern Russia. Lefebvre and Goosse (2008) determined that the CNRM CM3 C20C data shows a sea ice increase in the Weddell Sea for the late 20<sup>th</sup> Century. Though the CNRM model is the exception in the Antarctic Sea Ice region it is not erroneous. Doran *et al.* (2002) determined that the Antarctic station data show an East Antarctic coast cooling in recent decades. Arzel, Fichefet and Goosse(2006), Lefebvre and Goosse (2008) and Cavalieri *et al.* (2003) all determined that the observations indicate a slight increase in sea ice extent from 1981-2000 of about  $1.3 \cdot 10^5 \text{ km}^2$  in the Southern Hemisphere. The temporal framework is successful in capturing the uniqueness of the CNRM dataset.

#### 6.2.4 *Variability of Displacement Vectors Compared to Fixed Location Trends*

The variability of trends at fixed location in GCM output is compared to that of the kinematic representation of the GCM. The variability should be similar as both represent the dynamics in the GCM data. The temporal GIS framework is applied to eight realizations of the NCAR CCSM GCM and one realization from the CNRM CCM GCM from the 20C3M datasets. Eight sets of seven NCAR members are used to form Single Model Ensembles (SME). The effect on grid point range of adding an eighth NCAR or the single CNRM realization displacements to the SME is analyzed. The following hypotheses are evaluated:

- 1) There is a statistically significant difference in the number CNRM realization grid point displacements outside the range of the SME versus for an NCAR realization. The SME is composed of seven NCAR realizations that do not



include the NCAR realization being compared. The F-test at more than 95% confidence level is desired to account for non-normal distributions.

- 2) MME displacement variability more often exceeds SME displacement variability at the grid point level. The MME has a bimodal distribution as it has displacement datasets from two different GCMs.
- 3) SME displacement variability will exceed MME displacement variability at the global, hemisphere, hemisphere land and hemisphere sea as does trend variability. Spatial averaging will filter the point bimodal distributions in the MME displacements.

The F-test evaluation of the larger number of grid points with increased range for the added CNRM realization versus an added NCAR realization (Table 5.1, p.159) indicating a much higher than 95% confidence level of the two sets having different expected values confirming hypothesis #1. Displacement vector spread, measured as the standard deviation, is compared for a SME of eight NCAR realizations and a MME consisting of the SME plus the CNRM realization. Areal averages at the global, hemisphere and regional scale show a decrease in spread for the MME versus the SME (Table 5.3, p164 and Table 5.4, p.164) confirming hypothesis #3. In contrast, grid point range and spread is larger for the MME than for the SME in the majority of grid points (Figure 5.4, p.160 and Figure 5.5, p.161) confirming hypothesis #2. The results are similar to the results of trend variability analysis in several papers. The kinematic framework and trend analysis have similar variability characteristics at different scales.

### **6.3 Concluding Remarks**

The framework developed in this dissertation enables the kinematic characterization and analysis of spatiotemporal fields, in which anomalous regions are identified by inspection after small magnitude differences have been removed. Subsequent efforts in the research investigate potential underlying phenomena and analyse the validity of identified anomalous regions. Regions exhibiting differences between different datasets hint at the fundamental difference in sea ice models between the CNRM GCM and the other datasets as described by Holland and Bitz (2003). The areal variability characteristics of the representation applied to GCM output are determined to be similar to the characteristics of areal trends.

The utility of the proposed representation beyond the existing temporal GIS approaches is shown by six spatiotemporal transitions, including split and merge, to threshold defined objects (Figure 3.4, p.72). Objects are characterized with deformation orientation, rate of divergence and vorticity using the representation. The translation characterization is demonstrated through the comparison of two different GCM datasets.

Four datasets, two reanalysis and two GCM, are compared by calculating six maps of the differences between the permutations of the datasets. The F-test established there are different expected values for the difference sets. The median and IQR are compared to establish that the two reanalysis have the smallest difference while all differences with the CNRM GCM have large differences. The regions of large differences in the six maps lead to the identification of the probable reason for the unique CNRM data.

Nine realizations of two different GCMs are compared for variability and range. Comparing the effect of adding a same model realization and a different model

realization on the range of seven member Same Model Ensemble indicate the displacement datasets are separable by GCM. The variability characteristics of the kinematic representation match that of trend data at fixed points.

### 6.3.1 Future research

Several limitations in the proposed framework call for future research. The framework developed in this dissertation cannot calculate displacement vectors for complex shapes. Displacement vectors for complex changes such as merges and splits in the isotherms are also not captured. An isotherm ring that disappears by the next interval leads to displacements that cannot be calculated by the algorithm as no ending location for the vectors can be determined. The limits of the temporal framework are dependent on the time interval and the displacement magnitude. Objects that move more than half of the objects length parallel to the motion generate erroneous displacements (Figure 6.1).

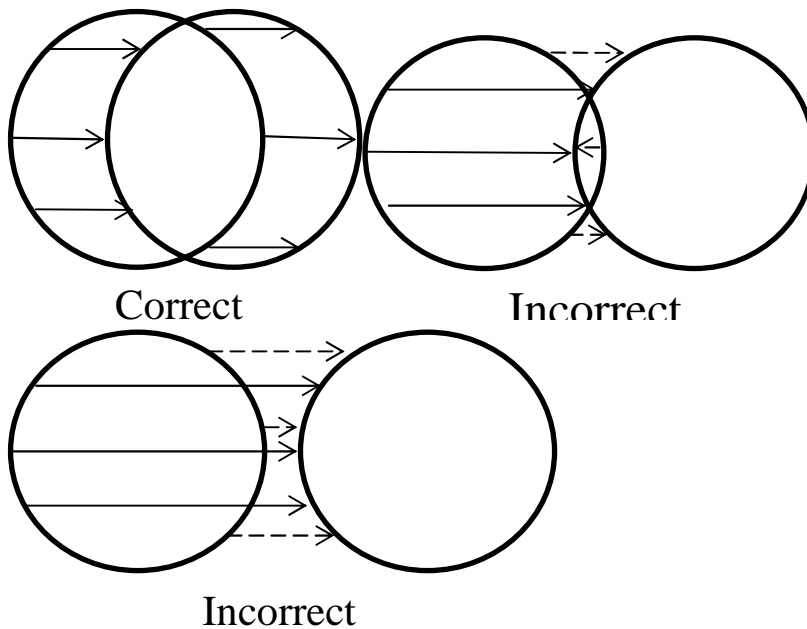


Figure 6.1: Displacements with incorrect magnitudes. Correct displacement are solid arrows, incorrect are dashed arrows.

All displacements should be the same in the figure 6.1, but the local maximum or minimum contained within the object may result in errors. A fiat object of a circular isoline implies a minimum or maximum that is internal to the object. The solid arrows have the correct length while the dashed arrows are incorrect. The error introduced to the displacement values does not increase as the object shift magnitude increases further. The differences between the actual displacement and the measures remain constant after the displacement is greater than the total length of the object.

The framework requires spatially continuous data for a field. Spatially repetitive patterns will cause the algorithm to generate erroneous displacements. Local maxima or minima can halt the displacement calculation algorithm, while the user needs to be aware of these limitations and with careful choices of time intervals avoid errors due to excessive displacement. The spatially repetitive patterns are more difficult to remedy as fiat objects that are larger than the spatial lag of reoccurring patterns will generate errors regardless of the displacement. If the spatially lag in the repetitive pattern is larger than the fiat objects, careful selection of interval will allow the kinematic algorithm to be used.

While applications for the temporal framework can be limited by the spatial and temporal restrictions mentioned above, most of phenomena in human and physical geography are potential applications for the temporal framework. Physical geography is the study of change across the earth's surface and amenable to analysis with the framework. For terrain analysis, ontological features, such as mountains or slopes, can serve as surrogate features. For land cover analysis, different land cover types may be used for surrogate objects. For climate, isolines of atmospheric properties, such as isotherms or isobars, are good candidates for surrogate objects. The population density of

organisms is an attribute that is used by in biogeography and in urban planning. Other human geography applications include the spread of disease, growth of cities and population, growth of commerce, and economics with respect to the biophysical environment. An outstanding restriction on applications of the framework is the time interval versus displacement magnitude and the field periodicity.

An alternative approach to the optical flow algorithm used to determine displacement vectors in the proposed framework is the active contours algorithm (Kass, Witkin, & Terzopoulos, 1987). Active contours are used in the field of image processing to locate and track contours and edges that define an object of interest. Active contours resolve gaps and other minor discontinuities in a boundary. The active contour algorithm (a. k. a. snake algorithm) uses energy field functions derived from the image to flow towards lines, edges and endpoints. The energy function for boundaries is formulated in ways that vary from a simple gradient formulation to more complex formulations such as the Laplacian of a Gaussian. Determining the energy function that is successful for a given image is difficult. In addition, local minima within the image and spline energy formulation are avoided with a careful choice of an external force (Kass, Witkin, & Terzopoulos, 1987). Choosing the energy field function and the force function require multiple iterations.

The potential applications of the temporal framework can be broadened by an algorithm that uses curvature along the boundary and pairs the curvature at points to equivalent points on a later boundary removes the gradient or gradient energy function requirement. The approach applies a spatial filter to the boundary grid points to reduce the number of curvature points to be matched across the interval. In addition, the

approach uses an energy function based on the sum of the distances between the many possible point pairings to arrive at an optimal solution. For example, the curvature approach will allow the application of the proposed temporal framework to classifications such as the Köppen climate zones. Yet, the expanded application is subject to the constraint that some of the paired boundaries curvature must be similar in the different snapshots in order for the curvature approach to be successful. The aforementioned algorithms are examples that show how the proposed temporal GIS representation can improve the analytical capabilities of the existing GIS platforms. Research into new algorithm development is needed to advance GIS analytical capabilities for complex and dynamic geographic phenomena beyond the current capabilities of the conventional GIS technology.

## References

- Arzel , O., Fichefet, T., & Goosse, H. (2006). Sea ice evolution over the 20th and 21st centuries as simulated by current AOGCMs. *Ocean Modeling*, *12*, 401–415.
- Carril, A. F., Menede, C. G., & Nunez, M. N. (1997). Climate Change Scenarios Over the South American Region: an Intercomparison of Coupled General Atmosphere-Ocean Circulation Models. *International Journal of Climatology*, *17*, 1613-1633.
- Cavalieri, D. J., Parkinson, C. L., & Vinnikov, K. Y. (2001). 30-Year satellite record reveals contrasting Arctic and Antarctic decadal sea ice variability. *Geophysical Research Letters*, *30*(18), 1-4.
- Claramunt, C., Parent, C., & Thériault, M. (1997). Design patterns for spatio-temporal processes," in S. Spaccapietra and F. Maryanski (Eds.) *Searching for Semantics: Data Mining, Reverse Engineering*, pp. 415-428.
- Collin, W. D., Bitz, C. M., Blackmon, M. I., Bonan, G. B., Bretherton, C. S., Carton, J. A., Chang, P., Doney, S. C., Hack, J. J., Henderson, T. B., Kiehl, J. T., Large, W. G., McKenna, D. S., Santer, B. D., & Smith, R. D. (2005). The Community Climate System Model: CCSM3, *Journal of Climate*, *19*, 2122-2143.
- de Smith, M.J., Longley, P.A., & Goodchild, M.F., 2007. *Geospatial analysis: A comprehensive guide to principles, techniques and software tools*. Winchelsea: Winchelsea Press. Pg 105.
- Doran, P.T., Prisou, J.C., Lyons, W.B., Walsh, J.E., Fountain, A.G., McKnight, D.M., Moorhead, D.L., Fritsen, C.H., McKay, C.P., & Parsons, A.N. (2002). Antarctic climate cooling and terrestrial ecosystem response. *Nature*, *415*, 517–520.
- Goodchild, M. F. (1992). Geographical data modeling. *Computers & Geosciences*, *18*, 401-408.
- Holland, M.M., & Bitz, C.M. (2003). Polar amplification of climate change in coupled models. *Climate Dynamics*, *21*(3-4): 221-232.
- IPCC, Climate Change (2001). *The scientific basis. Contribution of Working Group I to the Third Assessment Report of the Intergovernmental Panel on Climate Change*. Albritton, D. L., Meira Filho, L. G., Cubasch, U., Dai, X.; Ding, Y., Griggs, D. J., Hewitson, B., Houghton, J. T., Isaksen, I., Karl, T.; McFarland, M., Meleshko, V. P., Mitchell, J. F. B., Noguier, M., Nyenzi, B. S., Oppenheimer, M., Penner, J. E., Pollonais, S., Stocker, T., Trenberth, K. E., Maskell K., & Johnson C.A. (eds) Cambridge University Press, Cambridge, UK pp 881
- Kalnay, E., Kanamitsu, M., Kistler, R., Collins, W., Deaven, D., Gandin, L., Iredell, M., Saha, S., White, G., Woollen, J., Zhu, Y., Leetmaa, A., Reynolds, R., Chelliah, M., Ebisuzaki, W., Higgins, W., Janowiak, J., Mo, K., Ropelewski, C., Wang, J.,

- Jenne, R., & D. Joseph. (1996) The NCEP/NCAR 40-Year Reanalysis Project. *Bulletin of the American Meteorology Society*, 77, 437–471.
- Kass, M., Witkin, A., & Terzopoulos, D. (1987). Snakes: Active contour models. *International Journal of Computer Vision*, 1(4), 321-331.
- Labraga, J. C. (1997). The Climate Change in South America Due to a Doubling in the CO<sub>2</sub> Concentration: Intercomparison of General Circulation Model Equilibrium Experiments. *International Journal of Climatology*, 17, 377–398
- Langran, G., & Chrisman, N. R. (1988). A Framework for Temporal Geographic Information. *Cartographica*, 25(3), 1-14.
- Lefebvre, W., Goosse, H. (2008). Analysis of the projected regional sea-ice changes in the Southern Ocean. *Climate Dynamics* 30, 59–76.
- Peuquet, D. J., (1994). It's About Time: A Conceptual Framework for the Representation of Temporal Dynamics in Geographic Information Systems. *Annals of the Association of American Geographers*, 84(3), 441-461.
- Salas-Mélia, D., Chauvin, F., Déqué, M., Douville, H., Gueremy, J. F., Marquet, P., Planton, S., Royer, J. F., & Tyteca, S. (in review). Description and validation of the CNRM-CM3 global coupled model. *Climate Dynamics*.
- Semazzi, F. H. M., & Song, Y. (2001). A GCM study of Climate Change induced by Deforestation in Africa. *Climate Research* 17, 169-182.
- Theisel, H. and Seidel, H.-P. (2003). Feature Flow Fields. Joint EUROGRAPHICS – IEEE TCVG Symposium on Visualization (2003). G.-P Bonneau, S. Hahmann, C.D. Hanse (Editors).
- Uppala, S. M. , KÅllberg, P. W. , Simmons, A. J. , Andrae, U. , Da Costa Bechtold, V. , Fiorino, M. , Gibson, J. K. , Haseler, J. , Hernandez, A. , Kelly, G. A. , Li, X. , Onogi, K. , Saarinen, S. , Sokka, N. , Allan, R. P. , Andersson, E. , Arpe, K. , Balmaseda, M. A. , Beljaars, A. C. M. , Van De Berg, L. , Bidlot, J. , Bormann, N. , Caires, S. , Chevallier, F. , Dethof, A. , Dragosavac, M. , Fisher, M. , Fuentes, M. , Hagemann, S. , Hólm, E. , Hoskins, B. J. , Isaksen, L. , Janssen, P. A. E. M. , Jenne, R. , Mcnally, J.-F. Mahfouf, J.-J. Morcrette, N. A. Rayner, R. W. Saunders, P. Simon, A. A. P., Sterl, Trenberth, K. E. , Untch, A. , Vasiljevic, D. , Viterbo, P., & Woollen, J. (2005). The ERA-40 re-analysis. *Quarterly Journal of the Royal Meteorological Society*. 131(612), 2961-3012.
- Yuan, M. (1999). Representing Geographic Information to enhance GIS support for complex spatiotemporal queries. *Transactions in GIS*, 3(2), 137-160.
- Zhou, T. and Yu, R. (2006). Twentieth-Century Surface Air Temperature over China and the Globe Simulated by Coupled Climate Models. *Journal of Climate*, 19, 5843-5858.





## **Appendix A**

### ***A.1 Introduction***

The sampling technique for this research uses boundaries of virtual objects defined by threshold values. The percentage of grid points sampled is a function of the number of threshold values used to delineate virtual object boundaries. Grid points without calculated displacement values are assigned displacements using the natural neighbor interpolation algorithm. Patterns in the resulting displacement map could be the result of the interpolation algorithm instead of the data's spatiotemporal dynamics. Confidence in using interpolation can be increased by demonstrating that higher sampling level leads to a more detailed depiction of the displacement shown in maps using low levels. Feature similarity that is independent of sample percentage would support the assertion that the interpolation technique does not generate noticeable artefacts.

### ***A.2 Background***

The sampling technique for this research uses aggregation to form virtual objects and then traced grid points on the objects' boundaries. The best performance, when tracing changes in environmental data, is achieved using isoline tracking for fronts and range aggregation for hot spot tracking (Solis & Obraczka, 2005). This research combines the two approaches, using aggregation to form virtual objects and then tracking the virtual object boundaries which are approximate isolines. Interpreting data using samples from the data isolines results in DEM's exhibiting terraces or stripping (Persson, Pilesjo & Eklundh, 2005). The displacements calculated for this research are independent of the isoline based values used to sample the data, surface temperature. The calculated

displacement values have significant variance along a single isotherm. The longitudinal displacement values for the single isoline of 0°C range from 130km/decade southward to 126 km/decade northward. The maps output with missing displacement values assigned using the natural neighbor interpolation also do not generate terracing (Figure A.1, A.2 and A.3).

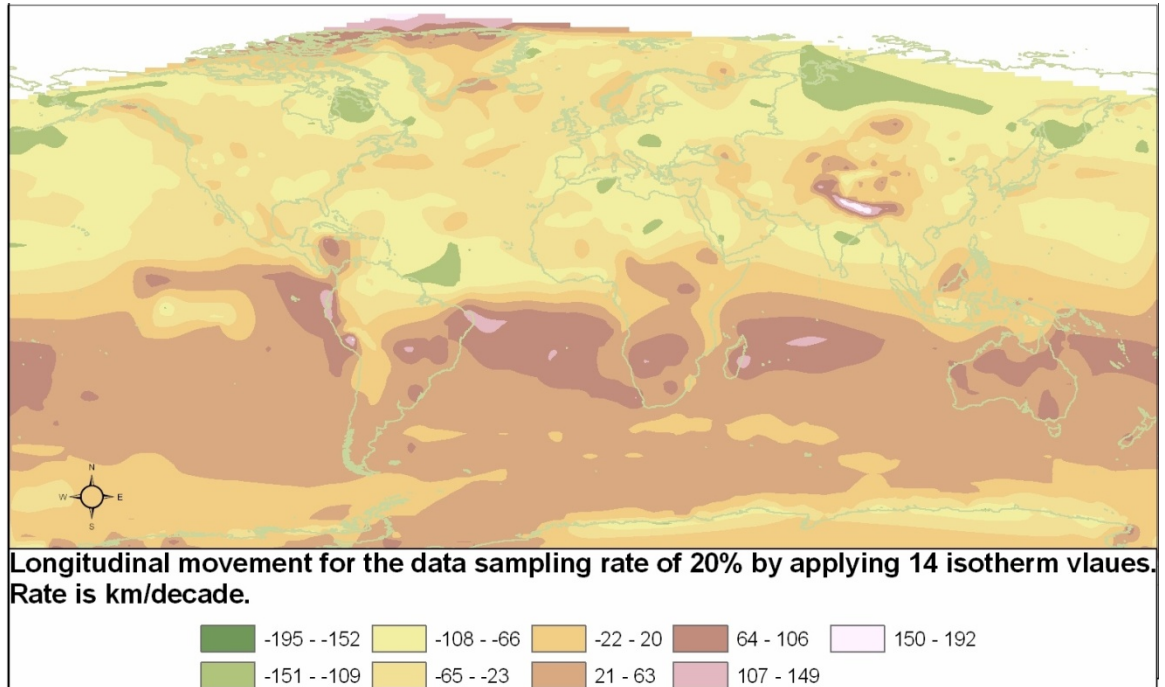


Figure A.1: Longitudinal moment based on a sampling of 20% of the grid locations

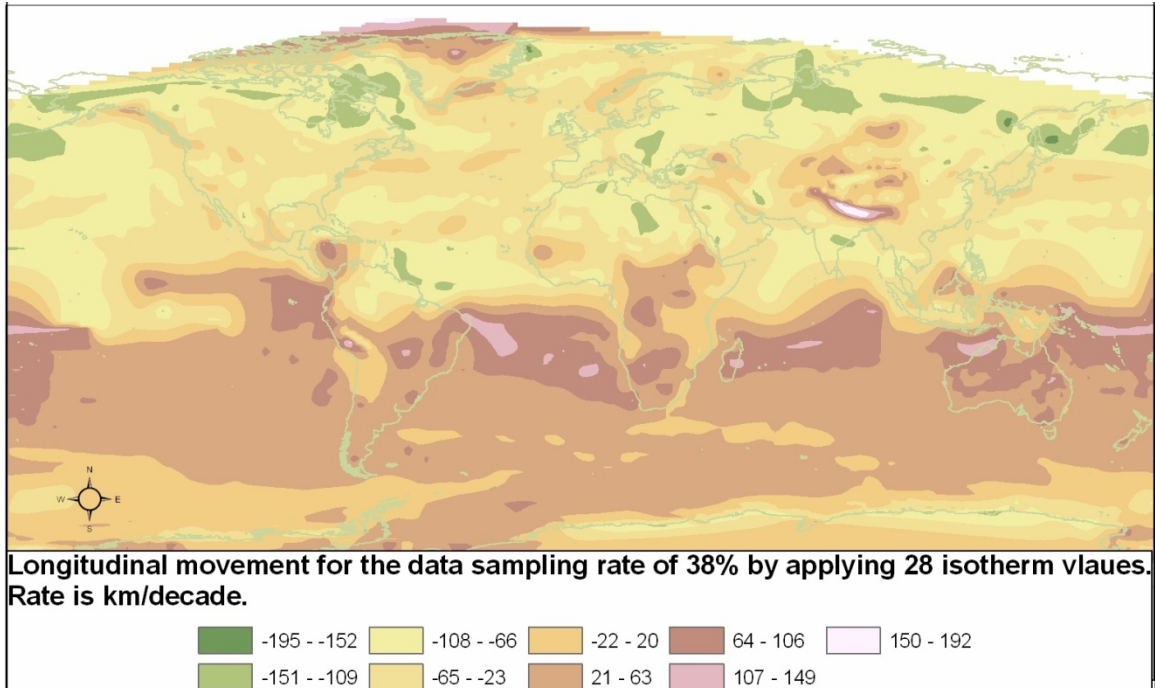


Figure A.2: Longitudinal moment based on a sampling of 38% of the grid locations

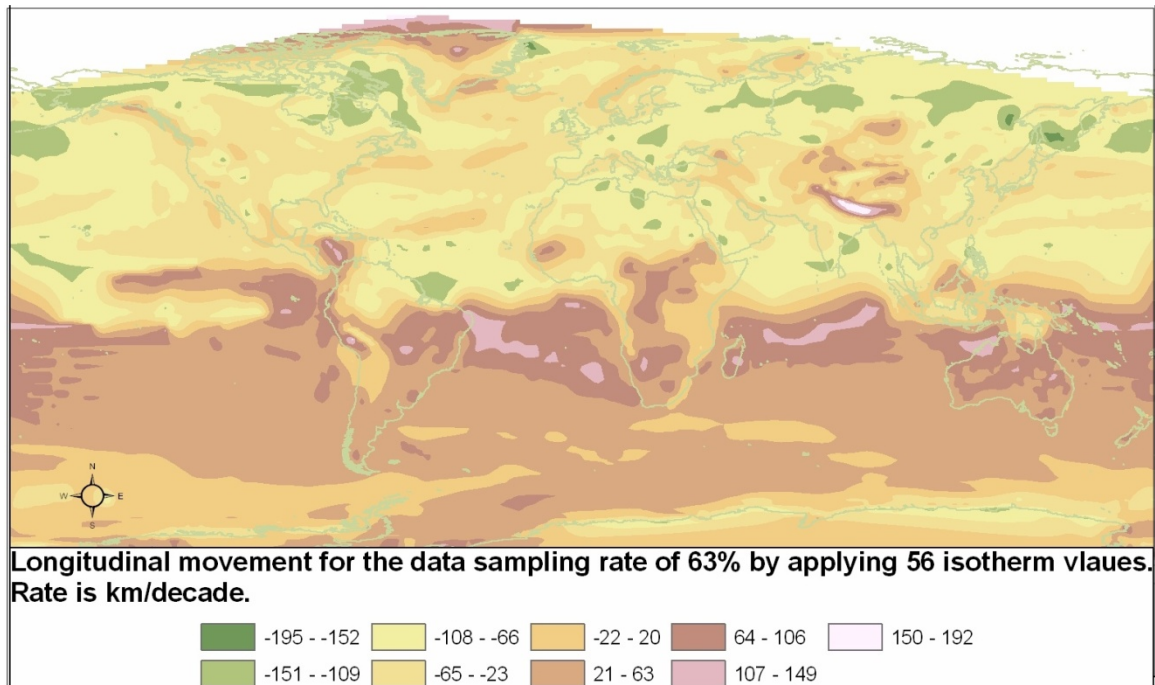


Figure A.3: Longitudinal moment based on a sampling of 63% of the grid locations

### ***A.3 Procedure***

Maps of longitudinal displacement at three levels of sampling are generated from the same dataset and then compared. Comparisons are done qualitatively, by looking for significant feature differences across the sampling levels, and quantitatively, by comparing difference vectors between two different sampling levels. Higher sampling rates enable the discernment of finer details in the displacement field features. The general distribution pattern of displacement remains consistent. Multiple sampling percentages generate consistent results but with better definition of extremes as the sampling level increases. Lower sampling level maps are quantitatively compared to maps with a higher sampling level by taking the difference between the two maps displacement values. The differences between 20% and 38% are compared with 38% and 63%.

### ***A.4 Results and discussion***

Figures 1, 2 and 3 are the output of the kinematic representation longitudinal displacement using 20%, 38% and 63% sampling. Utilization of virtual object boundaries limits the ability of achieving a given sampling level precisely. The shapes of extreme regions' change as the sampling percentage increase but the results are similar across the three different sampling percentages. Sampling by threshold value leads to more fluidity in regions defined by extreme values than sampling by regular spatial resolutions as extreme regions have closely spaced isolines. There is a similarity of structures with regions remaining in the same location as evidenced by the three maps at different sampling levels (Figures A.1, A.2 and A.3).

There are noticeable differences between the displacement map based on a 20% sampling rate and the map based on a 38% sampling rate but the regions of extreme longitudinal displacement have similar locations and shapes. The differences between the longitudinal displacement have similar locations and shapes. The differences between the sampling rates are compared to zero instead of the mean displacement difference as the goal was to highlight any difference between the two displacement maps, not just where there are unusual displacement differences. As sampling approached 100% of the grid points the differences with the 100% sampling would approach 0 as well. A difference map shows the absolute value of the difference between the 20% and 38% sampling displacement values (Figure A.4).

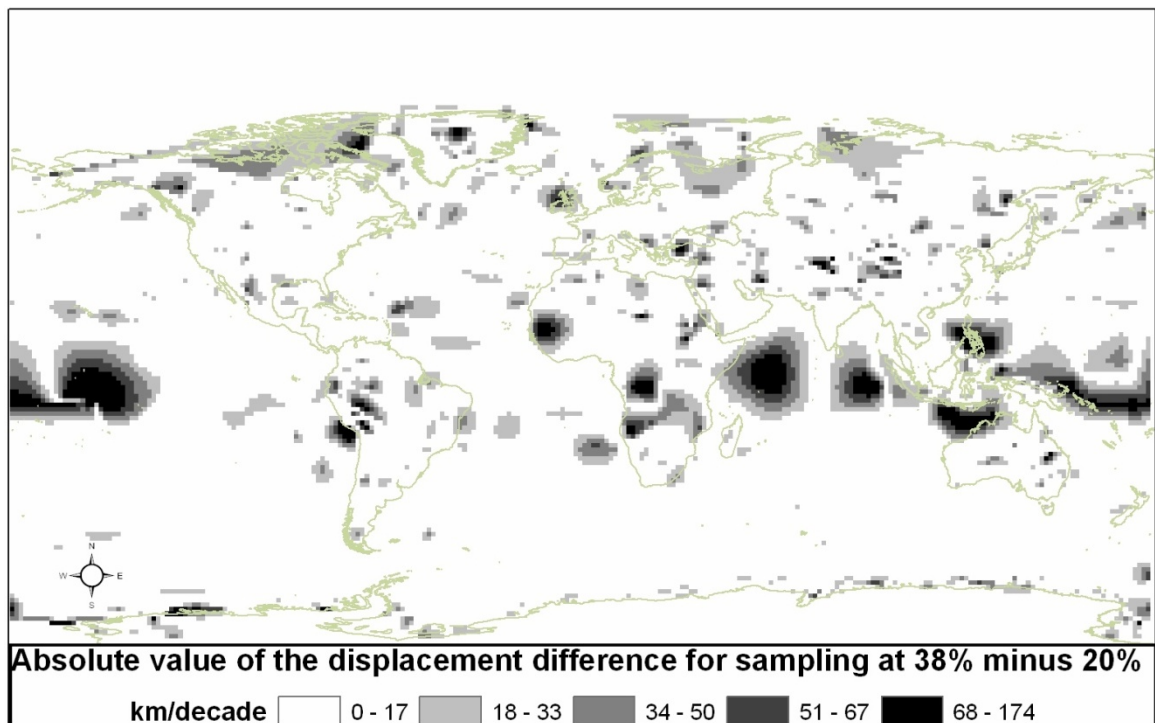


Figure A.4: Absolute value of the differences between displacement for 38% sampling minus 20%

As with the 20% sampling versus the 38% sampling maps, there are noticeable differences between the displacement map based on a 38% sampling rate and the 63% sampling rate. Regions of extreme longitudinal displacement have similar locations and

shapes. A difference map of the absolute value of the difference between the 38% sampling values from the 63% sampling values is shown below (Figure A.5).

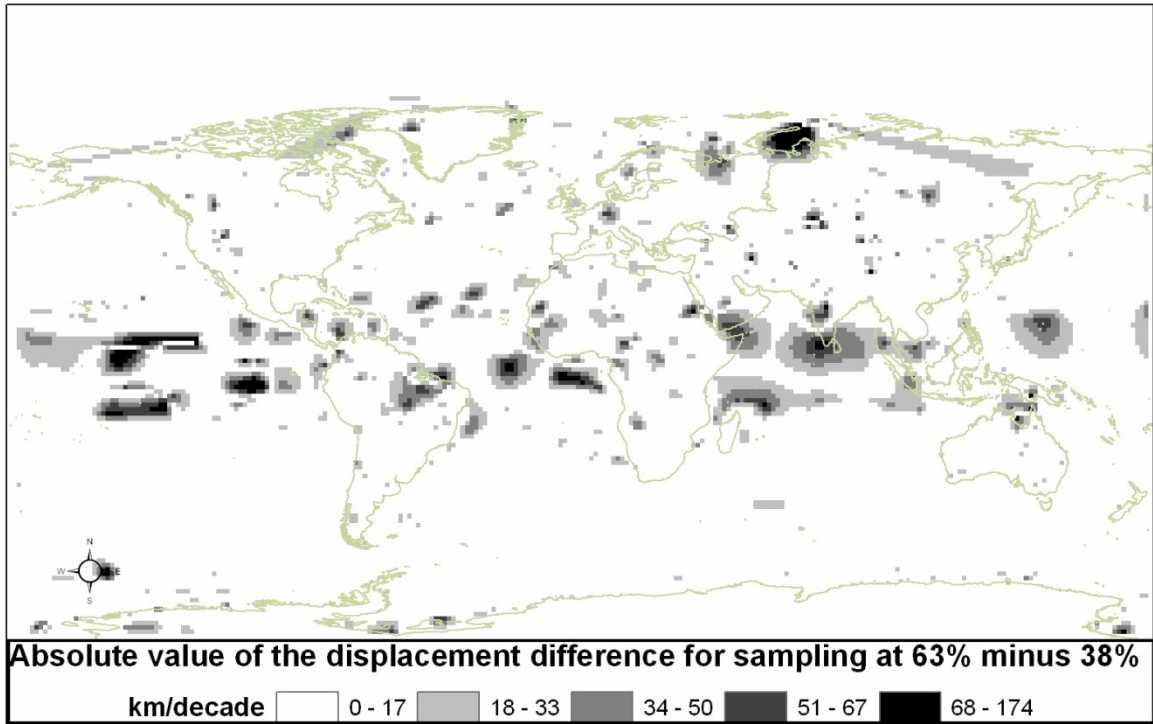


Figure A.5: Absolute value of the differences between displacements from 63% sampling and 38% sampling

The decrease in the number of grid points in five difference ranges for the 63% and the 38% sampling rate versus the difference between the 38% and the 20% sampling rate is in table A.1.

Displacement Difference km/decade	Grid point count change from 63% and 38% difference versus the difference between the 38% and 20% sampling.
0-17	+1879
18-33	-846
34-50	-375
51-67	-205
>67	-272

Table A.1: Change in difference count when sampling at 63% and 38% versus 38% and 20%.

The larger displacement difference ranges all have a decreased count with increasing sampling rates with a corresponding increase in the smallest displacement range. The mean deviation for the 63% versus the 38% sampling rate is 35 km/decade and 53 km/decade for the 38% versus 20%. Both displacement range counts and mean deviation show improvement as the sampling percentage increases.

#### ***A.5 Conclusion***

Concerns about the sampling technique based on virtual objects defined by threshold values are reduced by examining multiple sampling percentages for the same data. The sampling percentage is a function of the number of threshold values used to delineate virtual objects. Higher sampling level leads to a more accurate depiction of the displacement while lower levels of sampling lead to maps that exhibited similarities to maps with higher sampling levels. The ratio of change, defined by the absolute value of the difference between the two sampling levels' maps at each point, improved as the sampling level increase. The number of grid points with a displacement difference that is less than 17 km/decade increased by 1879 while all other displacement difference value ranges decreased with the region of largest difference decreasing in count by 67%. The mean deviation also showed improvement changing from 53 to 35 as sampling rates is increased. Visual inspections of the displacement maps also showed qualitatively that the displacements were similar regardless of the sampling percent.



#### **6.4**    *References*

Persson, A., Pilesjo, P., & Eklundh, L. 2005. Spatial Influence of Topographical Factors on Yield of Potato. *Precision of Agriculture*, 6(4), 341-357.

Solis, I., & Obraczka, K. (2005) Efficient continuous mapping in sensor networks using isolines. *Mobiquitous*, pp 325–332.